

Computer simulation of precipitation kinetics in solid metals and application to the complex power plant steel CB8

Revised form No. 1

By
Hans-Joachim Rajek
Institute for Material Science, Welding and Forming
Graz University of Technology

A dissertation submitted for the degree
Doktor der technischen Wissenschaften
at Graz University of Technology, Austria
November 2005

Acknowledgements

I would like to thank everybody at the institute for accompanying and supporting me during my time there. There are many interesting, encouraging and happy moments to remember with my friends in Graz. I am very grateful to Prof. Horst Cerjak who provided financial support and together with all members of the *IWS* created an enjoyable working environment.

It is with pleasure that I thank Prof. Harry Bhadeshia for admitting me as a member of the *PT* group. It was a very nice place to be and I made many friends there.

Of course I am especially grateful to Dr. habil. Ernst Kozeschnik for teaching me, supporting me and discussing so many refreshing subjects over a beer or two. It was really great to work with you my friend!

Finally I would like to thank Monika for her support and patience, especially during the last year where I misused so many weekends as work-ends.

Joachim Rajek

Contents

Contents	I
1 Introduction.....	1
1.1 Economical and ecological considerations	1
Ecological impact	2
1.2 Technical background and solutions.....	3
1.2.1 Service challenges.....	4
Creep mechanisms, microstructure.....	5
1.2.2 Fabrication challenges	7
1.2.3 Material developments in Europe	8
1.3 A typical steam power plant today	9
2 Motivation and Objectives	13
Motivation.....	13
Objectives	13
3 Current state of precipitation kinetics modelling	15
3.1 Treatments of computer simulation of precipitation kinetics	15
Sharp interface methods.....	15
Spinodal decomposition theory	15
Coupled <i>Johnson-Mehl-Avrami</i> equations.....	16
<i>Wagner Kampmann</i> model	16
Multi-component, local equilibrium approach	16
3.2 Precipitates in Cr-steels for power-plant application.....	16
3.2.1 Nucleation sites.....	16
3.2.2 Precipitate microstructure and alloying fundamentals.....	21
Ferrite stabilizing elements	21
Austenite stabilizing elements	21
Precipitate phases.....	22
3.3 Theoretical treatment of precipitation.....	23
3.3.1 Interfacial energy γ	23
Nature of interfacial energy	24
Calculation of solid-solid interfacial energy.....	28
Calculation of solid-liquid interfacial energy	36
3.3.2 Measuring the interfacial energy of solid-solid interfaces.....	37
Measurement of dihedral angles	37
Equilibrium shape	37
Coarsening	37
Zero strain, zero creep method	38
4 Classical precipitation kinetics and the new model	39
4.1 Classical precipitation kinetics	39
4.1.1 Nucleation	39
4.1.2 Growth	42
4.1.3 Coarsening	43
4.2 The <i>SFFK</i> Model	45
4.2.1 Software implementation.....	46
4.2.2 Precipitate nucleation.....	48

4.2.3	Precipitate growth	49
4.2.4	Example of a precipitate kinetic simulation.	50
4.3	Calculation of interfacial energy γ	52
4.3.1	Model systems	54
4.3.2	Complex systems	56
5	Introductory simulations.....	58
5.1	Isothermal simulations	58
5.1.1	Fe-C system	58
5.1.2	Fe-Cu system	60
5.1.3	Ageing simulation of two heat resistant Cr steels.....	63
	Heat treatment of 2¼% Cr steel.....	65
	Heat treatment of 3% Cr steel.....	68
	Composition variations	69
5.2	Heat treatments	71
5.2.1	Thermal history of P92	71
	Results and discussion of the complex heat treatment	72
	Results and discussion of the simple annealing simulation.....	75
	Comparing both simulations.....	76
5.2.2	Thermal history of GX-12	76
6	Precipitation kinetics of the <i>COST</i> steel <i>CB8</i>	78
6.1	Experimental information	79
	Specimen in „as-cast” condition (No. 1)	80
	Specimen in „austenitised” condition (No. 4)	82
	Specimen in „tempered” condition (No. 7)	83
	Specimen in „as-received” condition (No. 13)	84
	Specimens after creep testing and exposure at 650°C (2000h to 7000h)	84
	Specimen after creep testing and exposure at 650°C (16000h).....	85
6.2	Thermodynamic equilibrium analysis of the steel <i>CB8</i>	86
6.2.1	Thermodynamic equilibrium analysis (Fe-Data).....	87
	<i>CB8</i> Phase fraction diagram	87
	<i>CB8</i> Phase diagrams	90
6.2.2	Comparing thermodynamic databases	94
6.2.3	Thermodynamic equilibrium analysis (modified TCFE 3).....	97
	<i>CB8</i> Phase diagrams	97
	<i>CB8</i> Phase fraction diagram	98
6.2.4	Calculated interfacial energies γ	99
6.2.5	Microsegregation – Scheil-Gulliver simulation.....	100
6.3	Thermal history of <i>CB8</i>	103
6.3.1	Numerical Simulation	104
6.3.2	Results and Discussion	105
	Interfacial energy and nucleation site saturation	109
	Evolution of the precipitate and matrix composition during simulation	110
	Precipitate populations.....	111
	Comparing coarsening rates.....	113
6.3.3	Comparing two cooling rates from austenitising.....	114
6.3.4	Comparing two austenitisation temperatures.....	117
6.3.5	Comparing two annealing/tempering temperatures	119
6.3.6	Comparing two service temperatures	121

7	Summary, Conclusions, Outlook.....	123
8	Bibliography	125
9	Appendix.....	134
9.1	Thermal history of GX-12	134
9.2	Scripts	141
9.2.1	Thermal history of P92	141
	Master script	141
	System setup and austenitising (P92_600_1_austenitising_setup.mcs)	141
	Tempering and annealing (P92_600_2_annealing.mcs).....	147
9.2.2	Thermal history of CB8	148
	Master script	148
	System setup and casting simulation (CB8_173_1_setup_casting.mcs)	149
	Austenitising simulation (CB8_173_2_reheating.mcs)	157
	Austenitising simulation (CB8_173_3_austenitising.mcs).....	158
	Heat treatment simulation (CB8_173_4_ht.mcs)	158
	Annealing simulation (CB8_173_5_service.mcs)	159
9.3	Maybe unfamiliar.....	160

1 Introduction

1.1 Economical and ecological considerations

The highly industrialized and especially all newly industrialised countries are faced with a growing demand for electricity. There are many technologies available to provide this energy. The transportation of electrical energy is cost intensive and produces additional wastage. Also storing electrical energy in the magnitude needed for our life is not possible now. Therefore a decentralized production of this energy is necessary which strongly depends on local factors like: Availability and price of plant technology, primary energy, labour and financial capacity as well as ecological considerations.

At present the backbone of the worldwide electricity production are fossil fired steam power plants (*SPP*). Within this group especially lignite fired stations show a new boom, because of the worldwide availability and the low price of lignite compared to gas. 40% of the world demand of electricity is generated with lignite fired steam power stations. The only other option that can meet the worldwide demand of energy now is nuclear power, which is undesirable in Europe due to public exerting pressure on the authorities. Fig. 1 a) illustrates the expected development in the European Union for the next decades. The electricity consumption will increase by 1,5% every year and new power plants have to be installed. Due to political reasons the existing nuclear energy capacity will be reduced and the total power of fossil fired power plants will rise. Water and wind energy technologies will increase but are not able to meet this demand.

Fig. 1 b) shows the expected worldwide energy demand. Especially Asia and America, but also Western Europe, will need more electrical energy. A worldwide plus of 66% up to 2020 is expected.

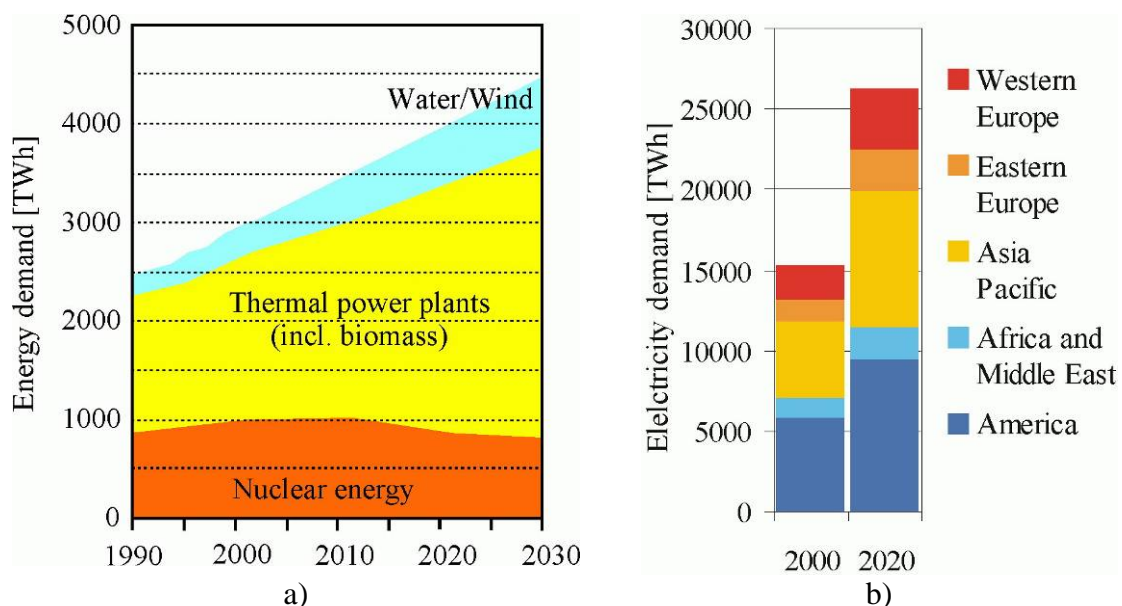


Fig. 1: a) Electricity generation options in the EU up to 2030. The growth in consumption is about 1,5% per year. b) Growth in electricity demand by regions. A plus of 66% is expected. Source: VGB figures and facts about electricity generation 2004

Ecological impact

Burning fossil fuels generates huge amounts of flue gas and ash that has to be cleaned expensively or simply released to the atmosphere. Many economies have ratified the *Kyoto protocol* of 1987 and have committed themselves to reduce greenhouse gas emissions drastically. The protocol became effective on the 16. February 2005 with 141 countries participating*. Typical greenhouse gases emitted by burning fossil fuel are CO_2 and NO_x . Fig. 2 shows the increasing total CO_2 emissions over the last century and the corresponding increase of the global mean temperature.

As illustrated in Fig. 3 increased steam parameters in *SPP* lead to a reduction in greenhouse gas emissions which is highly appreciated. This is due to increased plant efficiency and therefore less effort of fuel per mega-watt. The figure shows the combined reduction of CO_2 , NO_x and SO_x emissions in different stages of power plant developments [1].

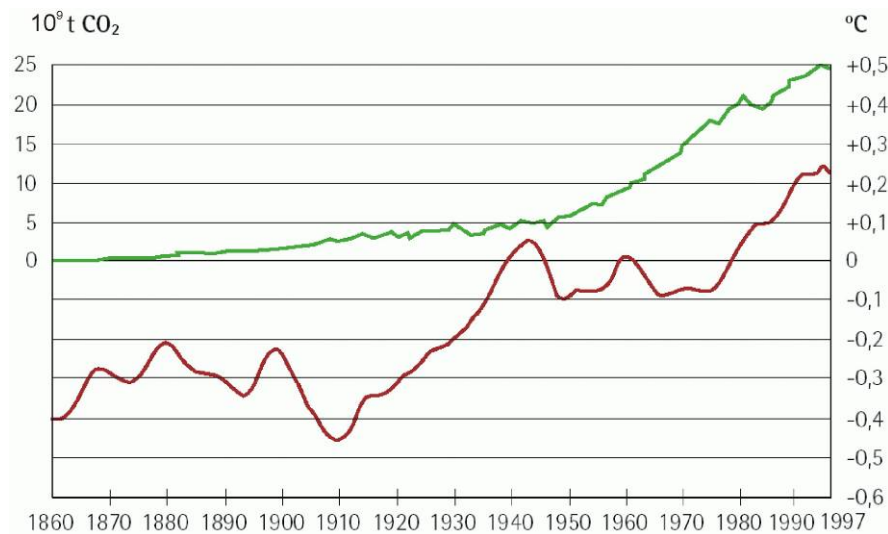


Fig. 2: Global mean temperature (red line) and amount of CO_2 emitted (green line) over the past century [2].

Increased steam parameters (increased efficiency) reduce also total operational costs, which is the main driving force for intensive international work to improve power station design. A high intellectual effort and costly investigations are applied to increase the efficiency of thermal power plants without significantly increasing investment costs. These collaborative research programs for example are *COST* [3] in Europe, *EPRI* [4] in the US and *Ultra-steel* in Japan.

Old sub critical plants existing in newly industrialising countries have a net efficiency of about 30% and produce too much greenhouse gases. Whereas the more than 500 worldwide super critical (*SC*) plants in operation reach a net efficiency of 40%. One percent increase in efficiency reduces by two percent specific emissions such as CO_2 , NO_x , SO_x and particulates. Fig. 4 shows how modern technologies can reduce the environmental pollution by downstream flue gas cleaning. It has to be pointed out that this technology can be installed in existing old stations but they are expensive, therefore a generous financial support by wealthy industrial nations (i.e. Europe, USA, Japan) is necessary to protect our own environment. These demands become more challenging after all because our society asks for a more easy and luxurious live.

* The largest green house gas producers USA, China and India do not take part.

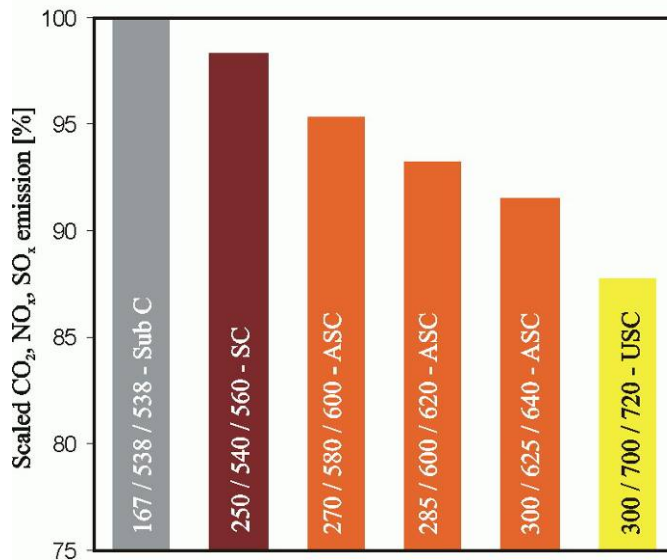


Fig. 3: The potential of exhaust reduction of some greenhouse gases by increased steam parameters for equal power output. The numbers are live steam pressure [bar] / live steam T[°C] / reheat steam T[°C]. Sub denotes sub critical steam conditions, SC, ASC and USC stand for super critical, advanced super critical and ultra super critical steam conditions, respectively.

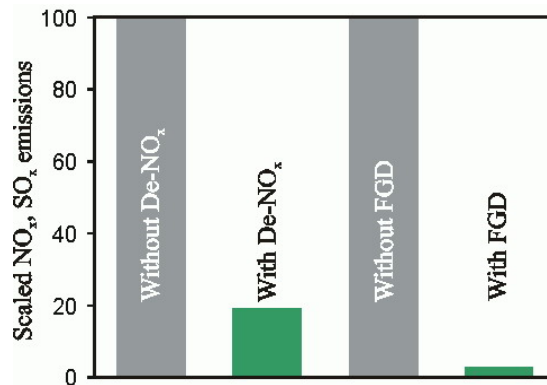


Fig. 4: Reduction of NO_x and SO_x by means of flue gas cleaning. FGD denotes flue gas desulphurisation [1].

1.2 Technical background and solutions

A thermal power plant converts the potential energy stored in fossil or nuclear fuels to electrical energy. First fuel combustion or nuclear fission is used to generate super-heated steam which is injected into steam turbine sets. During expansion the steam pressure and temperature decreases and thereby runs the turbine. This mechanical energy is finally converted into electrical energy by the generators.

In 1947 Sir Oliver Lyle explained why steam is ideal to store and transport heat in industrial applications [5] and in this case steam power plant applications. Steam possesses many outstanding qualities:

- Very high heat content
- Gives up heat at constant temperature
- Produced from water (cheap and plentiful)
- Clean, odourless, tasteless
- It's heat can be used over and over again
- Can generate power, then be used for heating
- Can be readily distributed and easily controlled

These considerations are still correct and except for military applications thermal power plants use water as heat carrier. The expressions „sub critical” and „supercritical” describe the operational range of a steam power plant and refer to the thermodynamic condition of the steam/water circulating in the plant. The critical point of water is defined by a pressure of 221,2bar and a temperature of 374,4°C. There is no clear distinction between the liquid and the gaseous phase of water beyond this point.

Steam power plants can be classified by their efficiency. The *Carnot* process is the most efficient and therefore ideal process for thermal engines. Engineering design tries to run a power plant as close to the *Carnot* process as possible. This is achieved by several heat regeneration and preheating units in the water/steam cycle. The maximum efficiency μ after *Carnot* is determined by T_{in} and T_{out} , the mean temperature where the heat is transferred to the water/steam and the mean temperature of the condenser, respectively.

$$\mu = \frac{T_{in} - T_{out}}{T_{in}} \quad (1)$$

T_{out} is the temperature of air (cooling tower), seawater or rivers that cool the condenser depending on the location and design of the power plant. From both the economical and the ecological point of view it is necessary to raise the operation temperature T_{in} to increase the efficiency.

1.2.1 Service challenges

There are several mechanisms limiting the life of *SPP* components under high temperature operation conditions, for example high temperature corrosion (fire side), oxidation (steam side), thermal fatigue and creep. Especially the later is of great interest and discussed in more detail.

Some *SPP* components need to resist high temperatures and mechanical stresses over a long time. Changing loads including also numerous shut downs and start ups are necessary to run smaller units economical. This leads to inhomogeneous temperature distributions and thermal stresses especially in thick walled components and hence thermal fatigue. The thick walled components are turbine casings, headers and live steam pipes. The service at high temperatures and internal pressures result in a time depending deformation (creep).

Different types of materials are available which can withstand these loads. Co-base alloys, Ni-base alloys, austenitic steels and ferritic/martensitic steels. The Co- and Ni-base alloys withstand the highest temperatures and oxidizing environments but, beside the extremely high costs, up to now components in the size needed for an *SPP* can not

be cast or forged. These materials are used in smaller gas turbines for aviation and small stationary power plants or single turbine blades. Castings and forgings needed for large *SPP* are hence made of steel.

Austenitic steels are superior to ferritic/martensitic steels considering some properties, for example the corrosion resistance at high temperatures. There are some investigation programs going on to further develop austenitic steels for *SPP* application [6]. Compared to martensitic steels the thermal expansion coefficient of austenitic steels is higher and the thermal conduction coefficient lower. Therefore thick walled components made of austenitic steels develop high thermal stresses during instationary loads which results in thermal fatigue and early failure. Martensitic 9-12% Cr-steels are used in modern super critical thermal power plants due to the best property spectrum. Kukutschki [7] gives an overview of relevant ferritic/martensitic chromium steels.

Creep mechanisms, microstructure

A creep mechanism is briefly introduced and on the basis of martensitic steels, the favourable creep resistant microstructure shall be explained. Constant mechanical stress at high temperatures over a long time leads to an irreversible creep deformation and later creep damage. Creep can be divided into three stages, where the first stage is characterized by a decreasing creep rate due to strengthening effects because of increasing dislocation density.

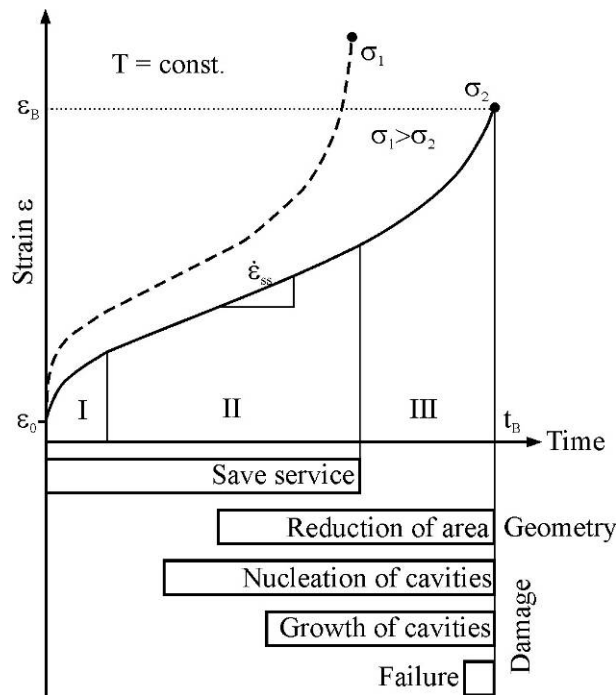


Fig. 5: Sketch of creep strain at two stress levels. ϵ_0 is the initial elastic strain, $\dot{\epsilon}_{ss}$ is the steady state creep rate, t_b is the rupture time, ϵ_b is the strain at rupture.

A stationary creep rate is established during the second stage. The strengthening and weakening processes, formation and annihilation of dislocations, respectively, neutralize each other. During the last stage the creep rate accelerates because of increasing damage of the microstructure. Voids, which already nucleated during the second stage, grow and coalesce finally forming micro cracks. Fast growing micro cracks lead to failure. This process is illustrated in Fig. 5 [8].

SPP components are replaced due to safety reasons at the end of the secondary stage (stationary creep). A typical creep rate for a power plant application is about $3 \cdot 10^{-11} \text{s}^{-1}$ which is equivalent to 2% elongation over 30 years service time [9]. Martensitic steels often show modified creep behaviour at high stresses and/or high temperatures. To refer to the classical subdivision into three parts, these steels do not show a distinct steady state creep with a constant creep rate. The primary - or transient - stage (creep rate drops) is more or less directly followed by the tertiary stage (creep rate rises). The transition between these stages is marked by the technically important minimum creep rate. This behaviour can be explained by the creep strengthening based on finely distributed precipitates which act as obstacles for dislocation movement [10, 11]. Investigations show that the minimum creep rate is inversely proportional to the duration of the transient creep and hence to the onset time of accelerated creep and therefore to the time of rupture (Fig. 6).

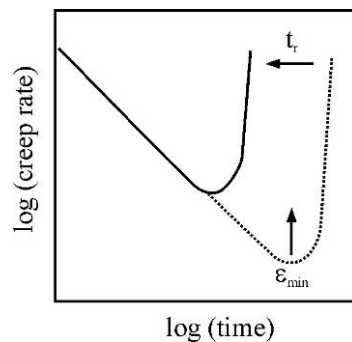


Fig. 6: A sketch of the creep rate over time of 9-12% Cr steels. A lowered minimum creep rate ϵ_{min} prolongs the primary creep stage and delays the onset of catastrophic tertiary creep.

During the fabrication heat treatment of martensitic steels a high density of dislocations is introduced due to the martensitic transformation after austenitisation. As a result of the microstructure evolution during creep the dislocations move. This movement is hindered by obstacles in terms of fine dispersed precipitates (MX particles) and the boundaries of narrow martensite laths as well as prior austenite grain boundaries.

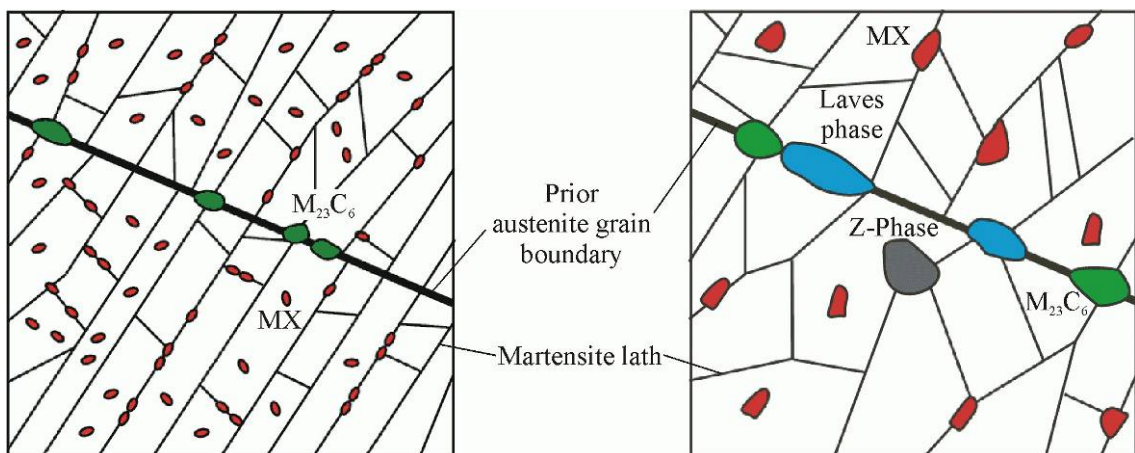


Fig. 7: Illustration of the microstructure evolution during creep deformation. The left sketch depicts the microstructure in the „as-received” condition; the right side shows the microstructure in crept condition.

In order to reduce the free energy of the system the lath boundaries migrate and polygonalise, which results in a loss of creep strength. The migration of these boundaries is obstructed especially by $M_{23}C_6$ precipitates which pin them down. Besides the precipitation hardening effect the matrix is strengthened by addition of solution hardening elements like Mo or W.

The goal of alloy design and heat treatment optimisation is to introduce a high dislocation density into a microstructure which shows a fine martensite lath structure with fine dispersed and stable precipitates to preserve the high dislocation density and subgrain structure as long as possible. But the precipitates start to coarsen at high temperatures during service due to diffusional processes. Sometimes second phases, which are thermodynamically more stable, form and dissolve the MX and/or $M_{23}C_6$ precipitates (Z phase) or dilute the matrix of strengthening elements (Laves phase), which is of course harmful for creep resistance. These degradations are illustrated in Fig. 7. On the left side one can see an idealised microstructure in the „as-received” condition, the right side depicts the situation after a long service at high temperature and stress.

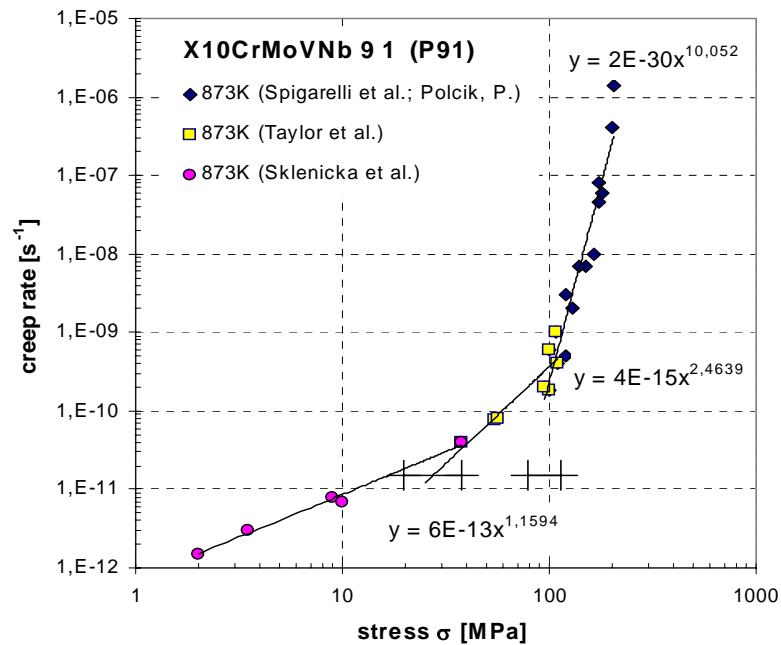


Fig. 8: Stress dependence of measured and experimentally evaluated secondary creep rates of the steel P91 [3, 12-14].

The creep tests at stresses similar to the service conditions in an *SPP* component are very time consuming (>10a). To gain results earlier, these tests are performed at higher mechanical stresses which lead to an accelerated creep behaviour (σ_I in Fig. 5). It is well known that the creep rates are stress depending. The results of short time creep tests at higher stresses hence may lead to an overestimation of the creep behaviour at lower stresses [14]. Partially, this is controlled by a transition in the stationary or minimum creep rate exemplarily shown for the steel *P91* at 600°C in Fig. 8.

1.2.2 Fabrication challenges

Large *SPP* components are castings and forgings in the size up to 60t. The design of turbine casings, rotors, tubes and valve bodies has to be considerate of manufacturabil-

ity (casting, forging, joining), repairability and of course inspectability (estimation of residual life). In the field of manufacturability more information about casting is given for example by Hanus [15] and an insight in forging technology is given by Zeiler et al. [16]. Due to different working conditions a variety of materials is in use which have to be joined mostly by means of bolting or welding. Welding large components can be a critical process which leads to new challenges and problems but often it is the best or only choice. The improvement of welding technology including welding consumables is as extensive as the development of new base materials. An overview about investigations in the field of welding of creep resistant martensitic steels for *SPP* applications gives Letofsky [17, 18].

1.2.3 Material developments in Europe

In 1950 the first creep resistant 12% Cr steel was developed for the operation up to 10000h in gas turbines. After 1970 the 9% Cr steel *P91* was developed at Oak Ridge National Laboratory (USA) with Mo and lowered C. Later V, Nb and N have been increased to stabilise the carbonitrides. A lowered C content increased the weldability of this alloys [1]. In Japan W was alloyed additionally and tempering temperatures were reduced. This led to a good combination of strength and toughness and even better creep strength.

Beginning in 1984 the first research collaborative in the field of material design *COST* 501* for advance steam power plant projects started developing a series of 9-12% Cr steel alloys. To improve the oxidation resistance the Cr content was raised and, to reduce δ -ferrite formation, parallel the Ni content was increased. Recent investigations reveal that B can improve the creep properties by reducing the coarsening of $M_{23}C_6$ precipitates. A series of boron alloyed steels was introduced (*CB2-CB11*). The actual *COST* research program is *COST 536* and will go on until 2009. The history of these developments in Europe can be found for example in the paper by Scarlin et al. [19].

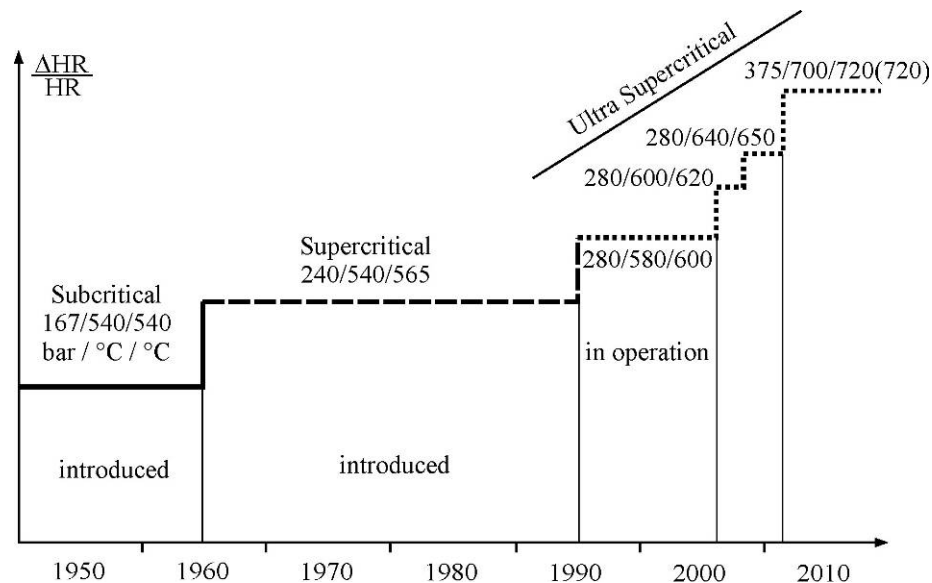


Fig. 9: The increased heating rate *HR* over the decades by raising the steam parameters (live steam pressure / live steam temperature / reheat steam temperature) [20].

* *COST*...Cooperation in Science and Technology

1.3 A typical steam power plant today

In 1824 *Carnot* made statements about heat engine cycles and work fluids, which are: No heat engine can have a higher efficiency than one operating in a *Carnot* cycle (dashed lines in Fig. 10 a) and no heat engine can generate work without net rejection of heat to a low-temperature reservoir. Steam power plants, or *SPP*, run the *Rankine* cycle as illustrated in a temperature-entropy diagram like Fig. 9. Compared to the ideal *Carnot* cycle where the working fluid is compressed and expanded isothermally and adiabatically, it is very easy to fully condense the vapour and compress the liquid to boiler pressure in a relatively small pump (*Rankine* cycle).

An *SPP* optimised for electricity production consists of typical components and only few see the high pressures and temperatures that define the *SC* or *USC* condition. These components are the super heater pipes, the main steam pipes to the high pressure turbine, the reheater steam line and the intermediate pressure turbine set. The efficiency of the thermodynamic process of a thermal power plant describes how much of the energy that is fed into the cycle is converted into electrical energy. In a sub critical *SPP* (Fig. 10 a) the steam needs to be separated from water in the steam-drum of the boiler before the steam is superheated and led into the high pressure stage of the turbine. Anyhow the live steam is super heated by the hot flue gases and injected into the high pressure turbine. As a consequence of the high steam parameter the live steam is completely dry which prevents erosion on the turbine blades.

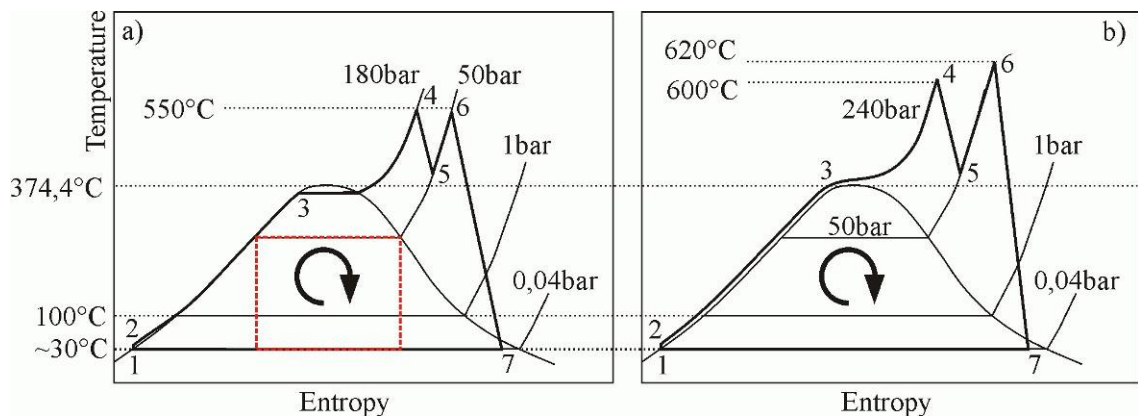


Fig. 10: *T-s* diagram of the *Rankine* cycle: a) *T-s* diagrams of a sub critical steam power plant. The red box symbolises the *Carnot* cycle where T_{in} corresponds to 50bar pressure and T_{out} is $\sim 30^{\circ}\text{C}$. b) A supercritical power plant, the boiler pressure is 240bar, the condenser pressure is 0,04bar. The area inside the cycle represents the gross energy. The critical point of water is marked by a temperature of $374,4^{\circ}\text{C}$ and 221,2bar.

As described by equation 1 the efficiency can be increased basically by increasing the operating pressure which shifts the cycle to the left at the same maximum temperature or by a higher mean temperature where the heat is transferred to the medium (T_{in}) by superheating the steam. Super critical *SPP* are operating with these steam parameters (Fig. 10 b). Superheating has another advantage in this case, because the moisture content in the steam leaving the last turbine stage is reduced, which reduces erosion corrosion. Another method to increase the cycle efficiency is feedwater preheating by extracting (bleeding) steam at various stages of the turbine sets. A beneficial side effect is deaeration of the feedwater which reduces corrosion in the boiler due to dissolved gases

that leak in at the condenser ($p < 1\text{bar}$). The feedwater preheating is not illustrated in Fig. 10.

Fig. 11 shows the water/steam cycle in a modern supercritical power plant. Starting with point 1 in Fig. 10 the simplified cycle is introduced now. The condensate pump feeds the water ($30^\circ\text{C}/1\text{bar}$) into the condensate tank; first the water is preheated in the economiser (E) which additionally increases the boiler efficiency. The economiser is the last heating surface before the flue gas leaves the boiler. The boiler consists of the components inside the dashed line in Fig. 11. The low-pressure feedwater preheaters utilize steam from the low pressure stage(s) to further raise the condensate temperature. Thereby steam from the LP stage condensates and is fed into the condenser system. Dissolved gases are removed in the condensate tank by means of steam extracted from the IP turbine(s). This is very important because dissolved oxygen and CO_2 are responsible for corrosion in the feedwater system. The gas-solubility of water is zero when the temperature reaches the boiling point. This process also preheats the condensate in the storage tank. In case of emergencies the volume of the tank has to be large enough to ensure cooling of the boiler tubes for about 10min. One of the largest energy consumers in the power plant is the feedwater pump. This device is often driven by an own steam turbine and needs maybe 6% of the plant power total energy output. A boiler of a 750MW power plant for example needs about $1000\text{m}^3\text{h}^{-1}$ feedwater at a pressure of 280bar ($1 \rightarrow 2$, in Fig. 10). Now the water temperature is further increased by the high-pressure feedwater heaters utilizing steam from the HP turbine stage exhaust.

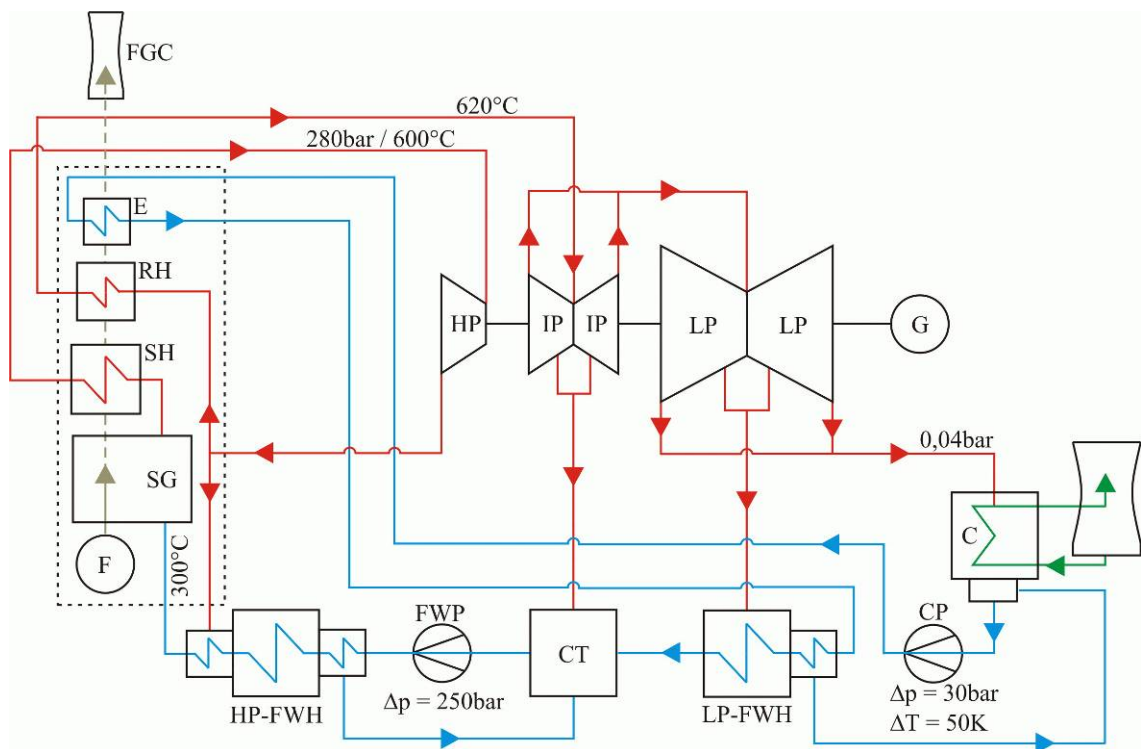


Fig. 11: The simplified scheme of a typical steam power plant. Typical components (incomplete): Steam generator (SG), super-heater (SH), high pressure turbine (HP), reheater (RH), intermediate pressure turbine (IP), low pressure turbine (LP), generator (G), condenser and cooling tower (C), condensate pump (CP), low pressure feedwater heater (LP-FWH), condensate tank with deaeration unit (CT), feedwater pump (FWP), high pressure feedwater heater (HP-FWH), flue gas cleaning (FGC), fuel storage and processing (F).

Depending on the water pressure the boilers show different designs. While sub critical power plants using drum-type boilers are limited in their load change rate due to the boiler drum, supercritical power plants using once-through boilers (*Benson* type) can achieve quick load changes when the turbine is of suitable design. In general every boiler of an *SPP* is a large chamber surrounded by waterwalls.

Inside the chamber the fuel is burned and in the lower section the radiation heats the waterwalls and hence the water inside (2→3). Later the hot flue gas (600 to 1500°C) heats the superheater (3→4) tubes, the reheater tubes and the economizer tubes by means of convection. The steam (and water) is collected in the headers of each boiler section. The superheated steam is sent to the high pressure turbine stage. The materials applied in the superheater, the superheater headers, the main steam pipe to the *HP* turbine (Fig. 12) and the turbine itself face the highest temperatures and pressures. The wall thickness of the *HP* turbine section should be as low as possible and should avoid massive material accumulation in order to increase the thermal flexibility (low thermal stresses) and hence fast load changes with low risk of thermal fatigue.

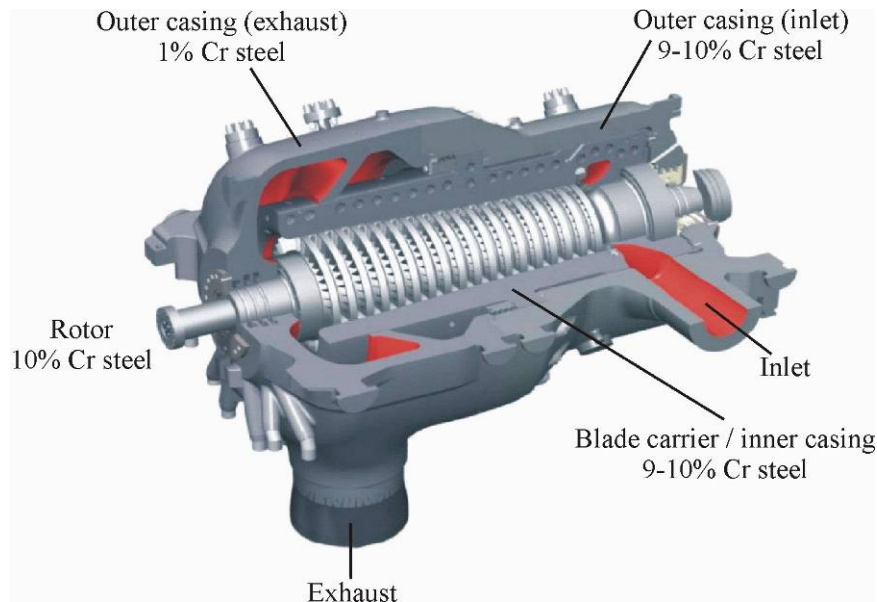


Fig. 12: Cross section of a high pressure turbine with axial divided barrel design for 300bar / 600°C steam conditions. The outer casing on the exhaust side is cooled by exhaust steam (Design: Siemens Power Generation).

In the turbine the steam expands between the blades of the rotor and inner casing and cools down (4→5). Thereby the potential energy of the steam is converted into kinetic energy during expansion which drives the generator. Depending on the steam pressure and temperature the turbine design is optimized. The steam is then reheated (5→6) and again fed into another turbine section (*IP* stage, 6→7, Fig. 13). The low pressure stage(s) of the turbine set expand (6→7) the steam to the condenser pressure (>20mbar). Finally the wet steam is cooled and fully condensed again (7→1). The condenser located under each *LP* stage is cooled with cooling water, which itself is cooled by means of air (cooling tower) or water (river, sea). Depending on the environmental temperature of the *SPP* location and hence the cooling conditions, the total efficiency varies up to 1%.

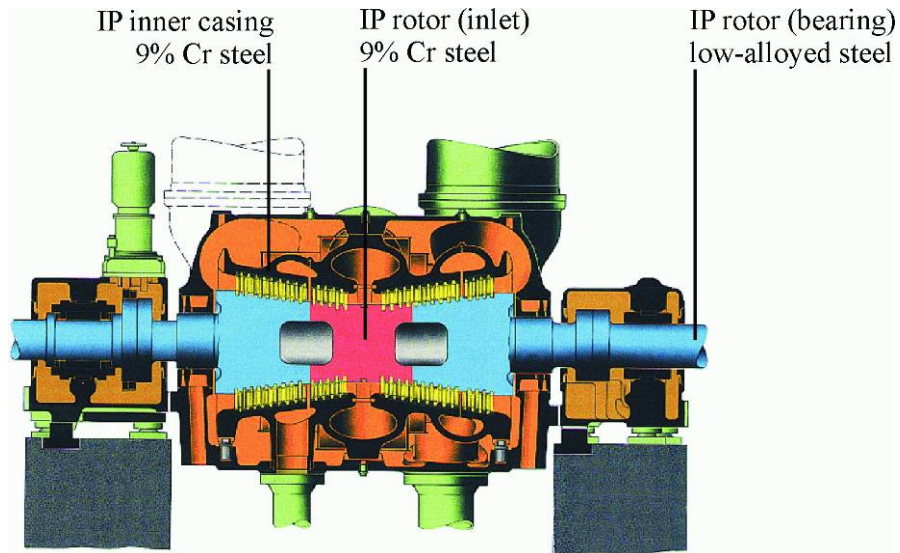


Fig. 13: Longitudinal section through a welded double flow intermediate pressure rotor. Depending on the demands different materials are used. The welded rotor consists of a 9% Cr steel where the reheated steam is injected into the *IP* turbine, the cooler ends are made of a low-alloyed steel (Design: Alstom Power Ltd.).

A comparison of the water/steam cycle equipment in sub critical and supercritical coal fired power plants shows that the major differences are limited to a small number of components. The equipment in the high pressure feedwater train, downstream of the feedwater pumps shows a different design in *USC* plants compared to sub critical plants. These components represent less than 6% of the total value of a coal fired power plant [1] and therefore should not prevent a revamp.

2 Motivation and Objectives

As mentioned in chapter 1 extensive and expensive efforts are made to improve the materials applied in thermal power plants. With knowledge and experience about how the microstructure is changing during high temperature (and high pressure) service and what would be the ideal microstructure, the demand for simulation- and investigation-tools did rise too. The introduction of several microscopy [21, 22] methods, creep testing procedures and computational tools prepared the next step in alloy design. A reasonable merging of the available techniques leads to a comprehensive approach to the development and improvement of 9-12% Cr steels [4].

Motivation

Over the last years a comprehensive R&D strategy has been pursued at the Institute for Materials Science, Welding and Forming*, Graz University of Technology, which covers the experimental characterisation of the creep behaviour up to refined microstructure investigations and advanced modelling. Through the multidisciplinary character of the approach, a broad understanding of the physical mechanisms operating in 9-12% Cr steels during creep can be achieved.

Now the state of the art is utilization of sophisticated technologies like energy filtering transmission electron microscopy, in-situ hot tensile testing compared with scanning electron microscopy [23], on-line creep rate measurement, finite element methods and thermodynamic calculations [24, 25]. Precipitation modelling efforts have reached a level where the prediction of the microstructural evolution is applicable in the field of complex alloys. Chapter 3.1 briefly introduces the precipitation kinetic approaches, an overview about creep modelling is given by Weinert [26].

In general, modelling promises to be a powerful tool in the activity field of materials science, under the absolute prerequisite of a physically reliable basis of the models and secure materials data. Reliable databases are necessary for equilibrium thermodynamics and kinetic calculations and hence the quantification of alloy developments with computer support. To provide real advance in the development of creep resistant materials, simultaneously, additional statistical analysis on basis of a large extent of carefully assessed experimental data is more than ever necessary.

Objectives

The objective of this thesis is therefore to scrutinise, test and apply a novel precipitation kinetics model introduced in chapter 4.2 and to simulate the thermal history of a complex 9-12% Cr-steel for power plant application. These tests comprehend the isothermal annealing simulation of well understood model binary two phase alloys and complex steels which show overlapping precipitation of multiple phases (chapter 5.1). In a next step the heat treatment simulation of simple alloys and also a complex steel was performed (chapter 5.2). The experience gathered with these calculations directly influenced the development of the software *MatCalc* [27], which was used for the simulations. Finally the model was utilized to predict the interacting evolution of precipitation reactions in the complex 9-12% Cr steel *CB8* developed in the *COST 522* [28] program during an industrial heat treatment and service. The simulation parameters and thermodynamic databases were calibrated on published data of microstructural investigations

* <http://iws.tugraz.at>

of annealed and creep tested specimens. This simulation was compared with measured data provided by Plimon [29], Dimmler [8] and Sonderegger [30] (chapter 6.3).

3 Current state of precipitation kinetics modelling

3.1 Treatments of computer simulation of precipitation kinetics

The microstructure of alloys determines its properties, for example the strength at elevated temperatures or oxidation resistance. The microstructure itself is depending on the manufacturing process and considering steels, the heat treatment. Steels are the most important commercial alloys and structural materials. During a heat treatment or under service conditions at elevated temperatures they often show complex sequences of precipitates. A proper prediction of the evolution of the microstructure during manufacturing and service is therefore necessary to improve the properties and estimate the lifetime of a component.

Many attempts to predict the precipitation kinetics in steels have been published. However, modelling the evolution of microstructure in three dimensions using systems large enough to yield data that provide applicable information is challenging. Most works consider a single precipitate, or uniform precipitate population, as an equilibrium phase. A recent review about the state of the art of precipitation kinetic modelling is provided by Thornton and co-workers [31]. They present a summary of work done in the field of the sharp interface method and the diffuse interface method to describe the motion of an interface. This corresponds to the classical nucleation theory and spinodal decomposition theory.

Sharp interface methods

The classical sharp interface methods assume local equilibrium at the precipitate/matrix interface even though the bulk phases are not in equilibrium. The precipitate growth kinetics, and therefore the velocity of the interface, is evaluated from the flux balance into and out of the precipitate. The rate of transformation is either controlled by the diffusional transport of elements to and from the interfaces or by the interface mobility. A solution of the diffusion equation can be found for fixed precipitate geometries (i.e. ellipsoids, sphere, etc.). Since such solutions neglect some aspects of interfacial energy, they are not generally able to predict changes in the shape of the precipitate. The benefit of this technique is the possibility to take into account the multi-component long-range diffusion of all elements including all interactions between them. A corresponding algorithm is implemented in the software *DICTRA* [32]. Other approaches utilizing the sharp interface method are *Monte Carlo* models [33] and *Ising* models [34].

Spinodal decomposition theory

The diffuse interface method is an alternative approach to modelling an interface. This method utilizes a field variable smoothly changing across the interface. The interface is not considered sharp but has a temperature depending finite width. The properties, for example composition, of the adjacent phases change smoothly over the interface thickness. There are several advantages using diffuse interface methods. For instance, topological changes, such as particle splitting or merging, are naturally handled. The model is very flexible for it is possible to include various physical effects (e.g. elastic stresses) [31]. First principle calculations [35] may support the dilute interface method. Many studies have examined *Ostwald* ripening in solid-solid systems including misfit strain via numerical solutions to the *Cahn-Hilliard* equation [36].

Coupled *Johnson-Mehl-Avrami* equations

The *Johnson-Mehl-Avrami* approach treats the precipitation kinetic problem as an overall kinetic theory [37-41]. These models utilize a number of semi-empirical parameters which not necessarily have a clear physical significance. Therefore the kinetic coefficients in the mathematical formulation have to be fitted for each alloy and process. Extrapolations and predictions for new alloys are uncertain and limit the application. The original formulation of this type of model can not cope with precipitation kinetic reactions where a number of precipitate phases interact simultaneously.

Robson and Bhadeshia [42, 43] and Fujita and Bhadeshia [44] presented a kinetic theory capable to deal with simultaneous reactions in power plant steels. In this work, the *Johnson-Mehl-Avrami* theory has been applied to describe the kinetics of a single phase, utilizing *MTDATA* [45] to predict the chemical driving forces (see chapter 5.1.3). These models only need little computing power, which is a major benefit.

***Wagner Kampmann* model**

Wagner and Kampmann [46] presented a model that accurately describes the entire course of precipitation within the framework of classical nucleation and growth theory. In the so-called „numerical model” (*KWN*), the rate equations for the change of particle radius and number density are numerically integrated and no simplifying assumptions need to be made. The extension into multi-component systems proves to be difficult. In many applications effective diffusion coefficients relating to the slowest diffusing species are introduced. To the knowledge of the author, no attempt has been made yet to apply the *KWN* to a description of the precipitate evolution in modern 9-12% Cr-steels.

Multi-component, local equilibrium approach

In order to overcome the problems of multi-component precipitation kinetics a more sophisticated model has to be used. Ågren developed a method [47] for the simulation of the diffusional reactions in multicomponent systems utilizing *DICTRA* [32]. Gustafson and Hättestrand [48] published simulation results where they applied this model to the coarsening kinetics in advanced creep resistant steels (*P92*, *PI22*). They discussed the calculated influence of some elements on the coarsening rates of MX and $M_{23}C_6$ particles. This technique is limited to simulating interactions between a very limited number of particles, usually two or three, due to a high demand on computational resources (see chapter 5.2.1). Schneider and Inden [49] performed kinetic simulations utilizing *DICTRA* analyzing the competitive growth of cementite, M_7C_3 , $M_{23}C_6$ and Laves phase in alloys similar to 9-12% Cr steels containing up to 5 elements.

3.2 Precipitates in Cr-steels for power-plant application

3.2.1 Nucleation sites

A vital point when simulating the kinetics of distributed precipitates in solid metals is knowledge about the number and type of available nucleation sites. Several types of nucleation sites are provided by the metallic microstructure. Investigations reveal that certain phases nucleate on one or more of the available sites. Every nucleation site represents a different energy level which strongly influences nucleation and later to smaller extent growth and coarsening of the precipitates. Especially the inhomogeneous crystal structure at grain boundaries are potential nucleation sites because of a higher energy state and enhanced diffusivity along the boundary. Subsequently, the different nucleation sites and the calculation of their density with *MatCalc* will be explained.

The kinetic model implemented in this software is of a statistical type and therefore the microstructure only exists as type and number of nucleation sites. To estimate the correct number of nucleation sites, first, a shape of variable size has to be found capable filling the simulated volume without any gaps. There are some solid bodies that satisfy this demand, like cuboids, rhomboids, truncated octahedrons and the tetrakaidecahedron a 14-sided polyhedron (Fig. 14). The latter was first used by Lord Kelvin [50] analysing the behaviour of foams. The proposed shape fills space with a minimum of volume loss and a minimum of surface area. A slightly altered version of this body is used in *MatCalc* having no curved surface areas. This body is able to depict the known austenitic and ferritic-martensitic microstructure quite well. Furthermore, this body can be shrunk and stretched to simulate the martensitic lath structures.

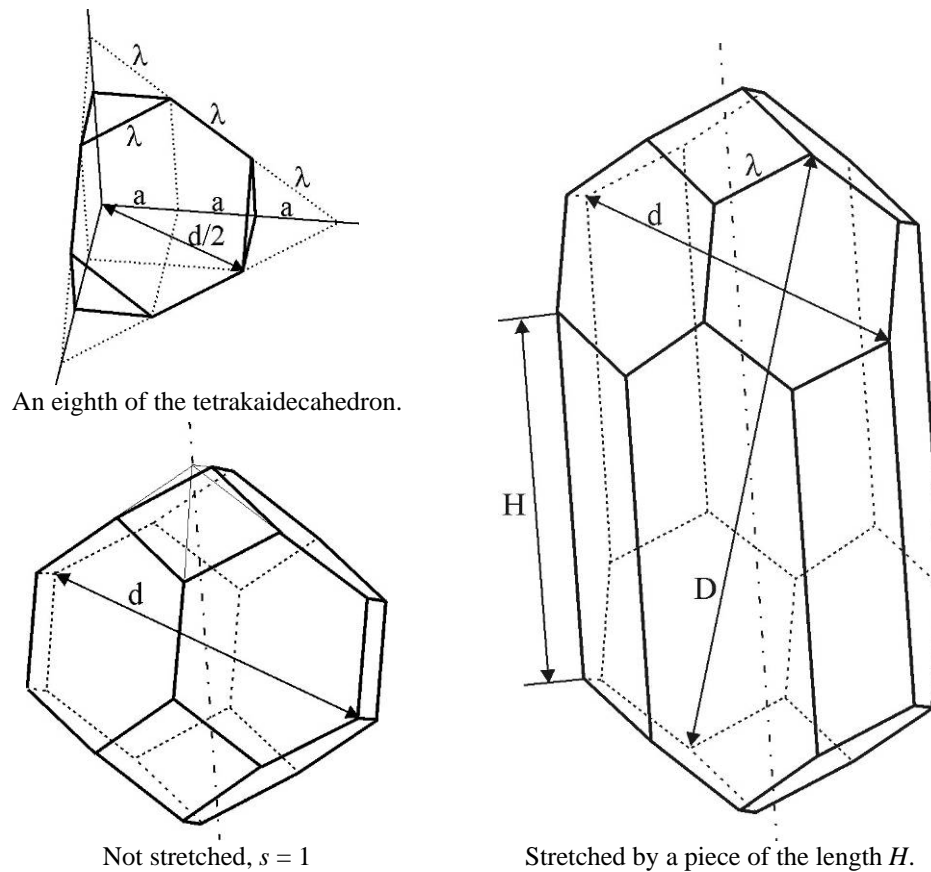


Fig. 14: A sketch of the tetrakaidecahedron utilized in *MatCalc* to calculate the number of nucleation sites. Construction, original and stretched version.

The line segments a and λ in Fig. 14 can be calculated as follows:

$$\lambda = \frac{d}{\sqrt{10}}, \lambda = \sqrt{2} \cdot a, a = \frac{d}{\sqrt{20}} \quad (2)$$

It is useful to define a ratio of two diameters if the body should be stretched to simulate a microstructure with elongated grains such as rolled materials, textures resulting from casting or martensite laths. This ratio s should be defined to be comparable with eventually measured data:

$$s = \frac{D}{d} \quad (3)$$

By stretching the tetrakaidecahedron with a prism, the value H can be computed:

$$H = \left[\sqrt{\left(\frac{D}{2}\right)^2 - \frac{d^2}{20} - \frac{d}{\sqrt{5}}} \right] \cdot 2 \quad (4)$$

The systems simulated with *MatCalc* have the size of 1m^3 and consist of a vast number of these bodies. The number of nucleation sites is calculated for a single body, marked with a horizontal line, and for bodies building a composite, according to equations 5 to 8. The considered body shall be completely surrounded by other tetrakaidecahedrons. The error introduced by not taking into account the nucleation sites on the surface of the 1m^3 cube (6m^2) is negligible. L denotes the total length of all edges in the simulated volume.

$$\bar{L} = 40 \cdot \lambda + 8 \cdot H, \quad L = \bar{L} \cdot \frac{1}{3} \quad (5)$$

The surface area of an isolated body is \bar{A} , and A stands for a body in the composite.

$$\bar{A} = 6 \cdot (1 + 2 \cdot \sqrt{3}) \cdot \lambda^2 + 2 \cdot \lambda \cdot (2 \cdot H + \lambda), \quad A = \bar{A} \cdot \frac{1}{2} \quad (6)$$

The volume of one body is calculated by:

$$\bar{V} = V = 8 \cdot \sqrt{2} \cdot \lambda^3 + 6 \cdot \lambda^2 \cdot H \quad (7)$$

Every body is surrounded by four neighbours therefore the number of corners is reduced to six.

$$\bar{C} = 24, \quad C = 6 \quad (8)$$

To calculate the number of each type of nucleation site, the total number of bodies building the simulated volume of 1m^3 has to be known.

$$n = \frac{1 \cdot \text{m}^3}{V} \quad (9)$$

The different types of nucleation sites applied in *MatCalc* are introduced now:

2-dimensional

- Grain boundaries, adjacent planes of grains (*GB*)
- Subgrain boundaries, adjacent planes of sub grains (*SGB*)
- Other precipitates or inclusions

1-dimensional

- Atoms on a dislocation line (*D*)
- Grain boundary edges, contact edge of three grains (*E*)

0-dimensional

- Grain corners, contact point of four grains (*C*)
- Single bulk atoms (*B*)

In general every substitutional atom of the bulk can be a nucleation site. Therefore, it is necessary to know the number of atoms in the system per unit cell depending on the crystal structure:

$$a_{bcc} = \sqrt[3]{\frac{a_{0BCC}^3}{2}}, a_{fcc} = \sqrt[3]{\frac{a_{0FCC}^3}{4}} \quad (10)$$

It is necessary to calculate an adapted lattice parameter a_j by calculating the volume of the unit cell, where j stands for *bcc* or *fcc*, ferrite and austenite, respectively, the important matrix phases for this work.

$$A_z = a_j^2 \quad (11)$$

$$V_z = a_j^3 \quad (12)$$

The total number n_B of bulk substitutional atoms is then:

$$n_B = \frac{V}{V_z} \cdot n \quad (13)$$

Similar considerations lead to the number of atoms on the surface area n_{GB} , the edges n_E and the corners n_C of the tetrakaidecahedron.

$$n_{GB} = \frac{A}{A_z} \cdot n \quad (14)$$

$$n_E = \frac{L}{a_j} \cdot n \quad (15)$$

$$n_C = C \cdot n \quad (16)$$

The number of atoms along the dislocations can be calculated using:

$$n_D = \frac{\rho}{a_j} \quad (17)$$

Where ρ is the dislocation density in $[\text{m}^{-2}]$. Tab. 2 shows the calculated number of nucleation sites for an austenitic and a martensitic matrix phase. The size of bodies is chosen to meet real values and derives the number of bodies. For comparison the *fcc* and *bcc* grains are compared although the subgrain structure and the dislocation density in austenite is very different to ferrite.

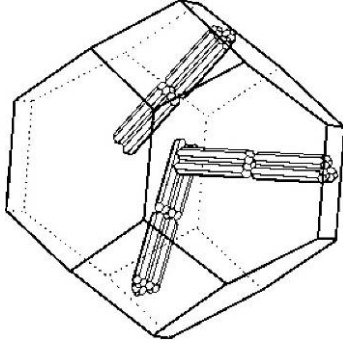


Fig. 15: A representative of a primary austenite grain boundary with three typical martensite lath bundles. The orientation is not fundamental just the number of nucleation sites.

Tab. 1: Number of grains and sub grains in a stretched tetrakaidecahedron with sub-grain structure. Grain size $d=100\mu\text{m}$, $s=1$. Subgrain size $=0,1\mu\text{m}$, $s=100$.

Number of grains (bodies)	$2,795 \cdot 10^9 \text{m}^{-3}$
Number of sub grains	$1,672 \cdot 10^{19} \text{m}^{-3}$

Tab. 2: Number of nucleation sites $[\text{m}^{-3}]$ in a stretched tetrakaidecahedron with sub-grain structure. Dislocation density in Austenite $\rho = 10^{11} \text{m}^{-2}$, Dislocation density in Ferrite $\rho = 10^{14} \text{m}^{-2}$, Grain size is $100\mu\text{m}$, $s = 1$. Subgrain size is $0,1\mu\text{m}$, $s = 100$.

Nucleation sites $[\text{m}^{-3}]$	Matrix phase		
	Ferrite (<i>bcc</i>)	Austenite (<i>fcc</i>)	
	$a_0=2,87 \cdot 10^{-10} \text{m}$	$a_0=3,515 \cdot 10^{-10} \text{m}$	
	$a_{bcc}=2,27 \cdot 10^{-10} \text{m}$	$a_{fcc}=2,214 \cdot 10^{-10} \text{m}$	
Bulk atoms (<i>B</i>)	$8,46 \cdot 10^{28}$	$9,211 \cdot 10^{28}$	Total system
Dislocation lines (<i>D</i>)	$4,39 \cdot 10^{23}$	$3,58 \cdot 10^{20}$	Total system
Grain boundary (<i>GB</i>)	$7,75 \cdot 10^{22}$	$8,20 \cdot 10^{22}$	Primary austenite grain
Grain boundary edge (<i>E</i>)	$5,17 \cdot 10^{24}$	$5,32 \cdot 10^{16}$	Primary austenite grain
Grain boundary corner (<i>C</i>)	$1,003 \cdot 10^{20}$	$1,677 \cdot 10^{10}$	Primary austenite grain
Subgrain boundary (<i>SGB</i>)	$2,066 \cdot 10^{26}$	/	Martensite lath

3.2.2 Precipitate microstructure and alloying fundamentals

Complex 9-12% Cr steels contain many different phases precipitating either in the austenitic and/or martensitic matrix. These phases consist of elements which are introduced into the alloy for certain reasons like stabilising phases, increasing hardenability or oxidation resistance. The expected properties of these phases and the desired effects of the elements are introduced.

During cooling from melting temperature, the matrix phase of martensitic Cr steels undergoes major phase transformations and hence appears in different crystal structures. First, δ ferrite solidifies and transforms to austenite (γ) which itself transforms to martensite. Depending on the chemical composition, a certain amount of δ ferrite may not transform to austenite. According to Abe [51] for instance, an elevated δ ferrite fraction reduces toughness, creep resistance and forgeability of heat resistant Cr steels. The favourite matrix microstructure of creep resistant steels is tempered martensite with a high dislocation density and a tailored precipitate distribution. Therefore a number of alloying elements is added to stabilize the ferritic phase and simultaneously to prevent δ ferrite formation. The elements only seldom have just one planned purpose and usually, the elements influence different aspects of the material properties. Moreover they mutually influence the effect of each element.

Ferrite stabilizing elements

These elements widen the region where ferrite exists in the phase diagram; however excess quantities stabilize δ ferrite, which is unwanted. The ferrite stabilizing effect is therefore compensated by austenite stabilizing elements. Ferrite stabilizing elements are:

Chromium, which forms a series of carbides (see below). To ensure corrosion and oxidation resistance a chromium level of 9 to 12% is necessary for modern power plant steels. Chromium reduces the critical cooling rate to guarantee full martensitic transformation; therefore cooling at still air provides a fully martensitic structure even in thick-walled castings (fully air hardenable).

Molybdenum stabilizes the M_2C carbide and increases the strength of the matrix via solid solution strengthening. An elevated Mo content leads to a higher Laves phase fraction.

Silicon is added to remove oxygen during pouring and solidification. The silicon oxide floats as slag on the liquid metal and can easily be removed. Si reduces the ferrite lattice parameter [52] which increases the lattice mismatch between the matrix and the precipitates. This effect alters the precipitation kinetics and increases the precipitation hardening effect.

Vanadium is a strong carbide and nitride forming element. VN precipitates (or MX carbonitrides) show a high solubility temperature, they form above austenitising temperature and thereby limit austenite grain coarsening.

Tungsten is added to heat resistant steels in order to increase the solute strengthening effect by substituting Fe in the matrix [53]. This element also stabilizes the Laves phase like Mo.

Austenite stabilizing elements

These elements stabilize the austenite phase and are therefore added to balance the ferrite formers to prevent large amounts of δ ferrite. As mentioned above, these steels undergo several transformations from austenite to ferrite and back again to obtain the favourable microstructure. Therefore the δ ferrite fraction has to be limited.

Nickel does not form any precipitates in 9-12% Cr steels but is reported to accelerate Laves phase formation [54]. In alloys recently introduced Ni is replaced by Co, which is, however, expensive.

Cobalt has the same effect as Ni and furthermore does not lower the transformation temperature (A_{c1}). Co presumably lowers the self diffusivity of Fe in the ferritic matrix. Both effects increase the stability of the microstructure. This element does not form precipitates in the creep resistant steels and increases the strength at elevated temperatures.

Manganese strongly reduces the critical cooling rate (air hardenability) and contributes in a series of carbides.

Carbon is the most important alloying element for steels generally. It forms many carbides and increases the strength and hardenability. This element occupies the interstitial sites in ferrite as well as austenite. The austenitic matrix, which can dissolve more carbon due to more interstitial sites, reaches the martensite start temperature* during cooling the austenite (*fcc*) transforms into the body centred tetragonal *bct* without any diffusional process [55]. The carbon is hence trapped in the martensitic structure which is highly strained. During tempering, carbides form, which reduces the carbon concentration in the martensite and therefore the strain (tempered martensite). Castings and forgings are never flawless and at least repair welds are necessary. To prevent cracking in the heat affected martensitic zone of weldings, the carbon content is generally limited to 0,15wt% [56] or at least 0,2wt%.

Nitrogen also occupies the interstitial sites of the austenitic and ferritic matrix. The complex MX precipitates are formed by N together with C. These precipitates are the backbone of the precipitation hardening effect in power plant steels. The MX precipitates have a high solubility temperature but partly dissolve during austenitisation, which allows controlling their size and hence distribution. As mentioned in chapter 1.2.1 the diameter and average distance of precipitates is crucial in slowing down the dislocation movement.

Precipitate phases

The desired precipitate phases are carbides (M_7C_3 , $M_{23}C_6$) and carbonitrides (MX, M_2X) to increase the creep resistance and hold back microstructure degradation. Typical carbide forming elements are Nb, Cr and Mo whereas Al, V and Ti form very stable nitrides. Especially during service, but sometimes already during the heat treatment, unwanted precipitates can form and may deteriorate the creep properties dramatically. Considering 9-12% Cr steels, these are the intermetallic phases Laves and Z.

M_7C_3 is rich in Cr and has a trigonal structure. Usually, in a 9-12% Cr steel this phase only occurs in alloys with high chromium content. M_7C_3 coarsens rapidly and is metastable and replaced by $M_{23}C_6$ during the heat treatment (see for example chapter 6.3). $M_{23}C_6$ is a chromium rich carbide with *fcc* structure. The typical nucleation sites are prior austenite grain boundaries and martensite lath boundaries. The purpose of these precipitates is to pin the former austenite grain boundaries and lath boundaries and prevent grain and subgrain coarsening which stabilizes the microstructure. They tend to coarsen at a high rate compared to the MX precipitates. There are investigations going on to increase N and highly reduce the C content of 9% Cr steels to prevent extensive $M_{23}C_6$ formation. This would preserve the chromium content in the matrix and also increase the MX phase fraction.

* M_s of CB8 is about 250°C, depending on the actual composition.

Abe [57] reports about alloy designing utilizing Boron. This element is known to segregate to grain boundaries and also occurs in $M_{23}C_6$ precipitates, which is supposed to reduce the coarsening rate [58, 59]. A controlled boron-nitrogen ratio is necessary to prevent BN formation, thus lower N levels are adjusted in B alloyed heat resistant steels.

MX carbonitrides are finely dispersed in the whole matrix of 9-12% Cr steels and they also decorate the martensite lath boundaries and subgrain boundaries. They pin these boundaries and prevent substructure degradation. On the other hand they act as obstacles for the moving dislocations. MX have also an *fcc* structure and show a high solubility temperature, so they do not dissolve completely during the austenitising heat treatment and thereby hinder grain-coarsening during this heat treatment step. The size and distribution of these precipitates can be controlled by devised tempering treatments. MX show a low coarsening rate at elevated temperatures, which significantly increase the creep resistance.

Laves phase is found in two variants, depending on the composition of the Cr steel. In W containing Cr steels, Laves phase contains more W than Mo (steel *P92* for example, chapter 5.2.1). Steel *CB8* does not contain W, therefore one of the major elements of Laves phase is Mo. In *CB8* Laves phase occurs during service after some thousand hours and tends to coarsen rapidly [60] (see chapter 6.1, 6.2 and 6.3). When the size of these particles exceeds a certain level, they can not contribute to the precipitation hardening effect any more and the negative influence is stressed. Furthermore Laves phase depletes the matrix from Mo and W, which are added for the matrix strengthening effect. The Laves phase has an A_2B structure where A stands for Fe, Cr and Si and B stands for Mo and W. This phase nucleates at prior austenite grain boundaries and martensite lath boundaries. Later, the Laves phase precipitates are reported to nucleate also on other precipitates [61]. As mentioned above this phase is undesired as soon as it coarsens too rapidly because large precipitates do not contribute to the precipitate strengthening effect.

Z phase occurs in some martensitic Cr steels after some thousand hours of service at elevated temperatures. The structure of Z phase can be written as $Cr(Nb,V)N$. This phase does not contribute to any strengthening effect but dissolves the MX precipitates. Thereby the particle strengthening effect and the creep resistance is reduced dramatically. Danielsen and Hald [62] reported that a single Z phase precipitate can consume up to 2000 MX precipitates.

3.3 Theoretical treatment of precipitation

3.3.1 Interfacial energy γ

Precipitates in solid matter are separated from the embedding matrix by a narrow area that is denoted as the interfacial region. Whenever this region expands or shrinks, energy is either consumed or released. This energy is the product of the specific interfacial energy γ [Jm^{-2}] and the interfacial area A [m^2] between precipitate and bulk material. The interfacial energy is a vital parameter for kinetic simulations. Even small variations of this parameter can have a massive impact on nucleation and also strongly influence growth and coarsening of precipitates. Usually the value of this energy is not known, since it depends on the crystallography of precipitate and matrix, on the chemical composition of involved phases, on their misorientation and finally degree of coherency. Commonly, a mean value of the interfacial energy is used in numeric simulations, which is denoted an effective interfacial energy γ . It is of great importance, therefore, to evaluate possibilities to predict these parameters from existing data (e.g. thermody-

namic databases). To treat the problem of multi-component, multi-phase, multi-particle precipitation kinetics on a most physical basis it is necessary to predict the interfacial energies of the precipitates depending on the actual system state. First an introduction is given to explain the general nature of an interface and interfacial energy, subsequently various theories for predicting interfacial energies are explored.

Nature of interfacial energy

Typically there are two different kinds of interfaces: Free interfaces, often denoted as surfaces, which divide liquids from gases or solids from gases. In contrast, internal interfaces separate liquid-liquid, liquid-solid or solid-solid phases, where the solid-solid interface is of particular interest for this work.

The interface in a solid metal is described as a dividing surface that interrupts a periodic lattice arrangement, or separates homogeneous phases of varying composition and/or crystal structure. The surface is a two-dimensional object; an interface is a very narrow, three-dimensional object. Interfaces in solid metals can be grain boundaries separating two grains of the same phase or interfaces between two different phases, also called interphase boundaries. In our context, interphase boundaries separate precipitates and matrix phase.

The thermodynamics of surfaces was first described by Gibbs [63]. The surface difference free energy is defined as a reversible work per unit area to create a surface. There is a distinct to the surface stress which is a reversible work per area to expand a surface elastically [64]. A comprehensive summary of the phenomenon „interface” can be found in the textbook by Murr [65].

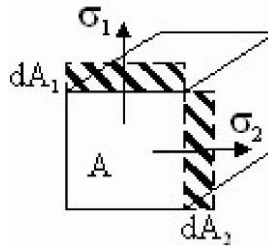


Fig. 16: Reversible deformation of a crystal surface (area) element.

Whenever new surface is created, the surface/interfacial energy has to be expended by the system. A typical example for such a process is the growth of a precipitate in a solid matrix, a general definition of this energy has been given by Shuttleworth [66]:

An initially stress free solid body is deformed, by applying a certain force. This introduces a change in the surface area A . The work against the surface tension σ is then equal to the change in Helmholtz surface free energy F_A .

$$\sigma_1 \cdot dA_1 + \sigma_2 \cdot dA_2 = d(A \cdot F_A) \quad (18)$$

The surface stresses are σ_i [Nm^{-2}], A_i are the newly formed surfaces (Fig. 16). The free surface energy F_A is defined as $F_A = H_A - T \cdot S_A$, where H_A is the total surface energy, S_A is the surface entropy and T is the absolute temperature. For symmetrical crystals i.e. isotropic solids, the surface stresses are equal in each direction and identical to the surface tension [Nm^{-2}].

$$\gamma_s \cdot dA = d(A \cdot F_A) \rightarrow \gamma_s = F_A + A \cdot \left(\frac{dF_A}{dA} \right) \quad (19)$$

Shuttleworth showed that for isotropic solids the surface energy (γ_s) is equal to the surface tension as in the case of a pure liquid. If a liquid drop is deformed isothermally the surface energy stays constant because atoms constantly migrate from the bulk to the surface keeping the surface structure constant. Therefore, dF_A in equation 19 is zero. This is the reason why the surface energy and surface tension is identical for liquids. Therefore in the case of liquids, these two quantities are often referred to by the common name „surface tension”.

In the case of metallic solids surface energy and surface stress are not equal: Solids, especially at lower temperatures, can not easily rearrange atoms on the surface because of low diffusivity. Moreover, shear forces can be applied to solids and therefore dF_A is not zero and hence the surface energy is not equal to the surface tension of solids. The introduction of a surface tension in terms of interfaces is only valid when the process of interface creation is reversible. This is at least correct for liquid-solid interfaces. Furthermore the interfacial energy of metallic solids depends on the misorientation over the crystal interface, as discussed for example by Wulff [67]: An isolated monatomic single crystal surrounded by its own vapour will adopt a shape that minimizes its total surface energy. The values of the surface energy can be plotted in a system of spherical coordinates. The inner tangent planes of the surface energy distribution determine the equilibrium shape of the crystal (Fig. 17). These are usually symmetrical polyhedrons, cuboids, disks or spheres.

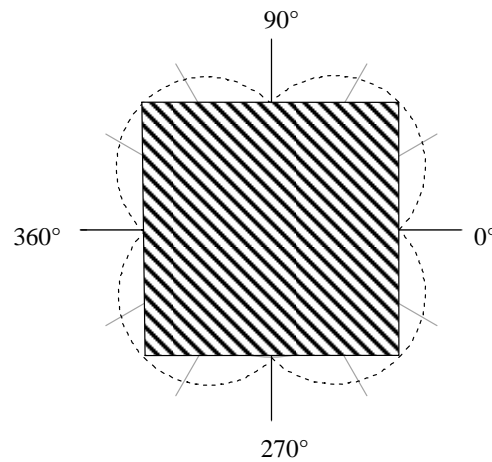


Fig. 17: Example of a two-dimensional Wulff [67] construction. The dashed line indicates the orientation dependent interfacial energy value. The hatched square illustrates the corresponding equilibrium shape of the crystal.

The assumptions of Wulff are valid for perfect single crystals. If these crystals form a polycrystalline microstructure, the interfacial energies strongly depend on the type of the solid-solid interface. As mentioned already, one has to consider crystal structure, coherency and orientation of the adjoining bodies.

Coherency effects influence the interfacial energy in two ways. The interfacial energy contribution can be divided into a mechanical part and a chemical part. The chemical part is depending on the type of atoms that are bonded across the interface and the par-

ticular bond energy between the atoms. The mechanical part arises from the difference between the crystallographic structures of the precipitate and the matrix which introduces elastic strain [68]. The level of these two energies depends on the coherency between the two crystal structures separated by the interface. The coherency level, and therefore the properties of precipitate / matrix interfaces, usually lies between the value for a fully coherent and a fully incoherent interface.

Fully coherent precipitates

These interfaces do not show misfit dislocations on the precipitate / matrix interface and there are no broken bonds across the interface. An interface is said to be fully coherent if each atomic plane in one crystal, that intersects the interface, is matched by another plane on the opposite side of the interface [69].

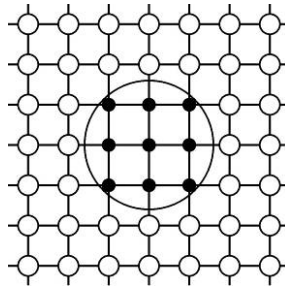


Fig. 18: Fully coherent precipitates, no broken bonds. The interface is indicated by the circle.

Interface energy with this specification is only of chemical nature, because there is no structural difference. Fully coherent precipitates occur whenever there is no or only insignificant lattice mismatch, at least in one direction. Especially small precipitates often meet this condition; see for example the *Guinier-Preston** (*GP*) zones. If there is no lattice mismatch at all these interfaces show identical, usually very low, interfacial energy values in every direction (Fig. 18). Consequently, these precipitates are usually spheres, for example in the Al 4at% Ag model alloy.

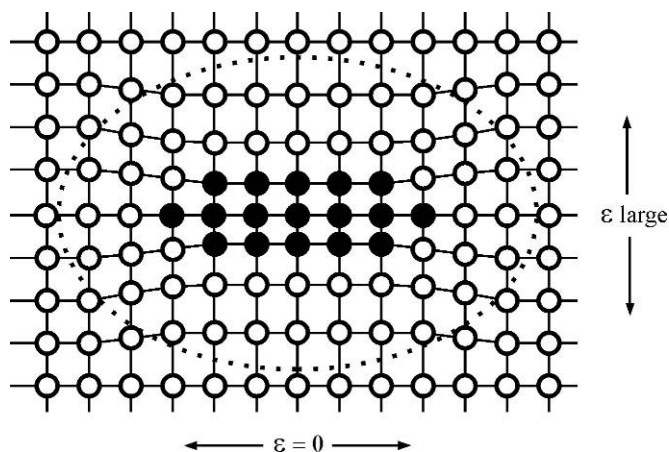


Fig. 19: Coherent precipitate with different lattice parameters only in vertical direction. The volume influenced by the lattice misfit is marked by the dotted line.

* e.g.: Al-Cu system with monatomic, plate shaped, Cu layer in (100) plain. Fully coherent with matrix, typical diameter of 3-10nm.

If the lattice parameters differ, considerable strain energy can be the result. Because of the different lattice structure of precipitate and matrix, the lattice will be deformed elastically, depending on the Young's modulus and also depending on the orientation in the lattice. For example, a situation where a particle has a similar lattice parameter in horizontal direction but not in vertical direction is illustrated in Fig. 19. To keep the misfit energy a minimum these precipitates arrange in horizontal direction and develop plate or needle like shapes. Similar misfits in every direction will also lead to a spherical particle.

Incoherent precipitates

They usually show a large lattice mismatch and a minimum of bonds with the surrounding matrix. According to the Wulff construction these particles are often symmetrical polyhedrons. Incoherent precipitates introduce mainly elastic stresses because only few interface bonds exist.

This problem was solved analytically for an ellipsoidal shaped precipitate for example. The level of the strain energy is depending on a shape factor and can be described as a ratio of precipitate length and diameter [70]. Theory predicts that platelets have a minimum and spheres provide maximum strain energy if the precipitate phase is elastically softer than the matrix, regardless of the orientation relationship and elastic anisotropy. For a hard particle embedded in a softer matrix, the sphere represents the minimum strain energy shape [71].

During the evolution of a precipitate, it is very likely that the effective interfacial energy changes depending on the actual size and composition of the particle. A small precipitate will probably start with fully coherent interfaces and introduce only low elastic strain, despite a possible lattice misfit. During growth, some interfaces can transform into semi coherent interfaces to reduce the elastic strain energy. This coherency loss is accompanied by the formation of vacancies and / or misfit dislocations in the interface.

Semi coherent precipitates

Semi coherent precipitates share some coherent and some incoherent interfaces with the matrix, depending on the crystal orientation. The value of the interfacial energy depends on this orientation. The equilibrium shape as predicted by the Wulff theorem depends on the possible local growth and on the local elastic strain. These particles do often have plate or needle like shapes (Fig. 20).

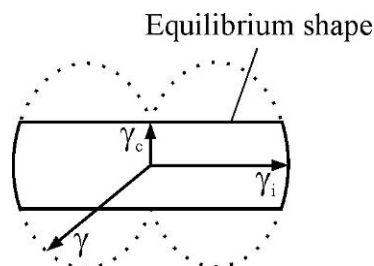


Fig. 20: Semi coherent precipitates, Wulff construction of the equilibrium shape based on the interfacial energy plot. γ_i and γ_c is the maximum incoherent and coherent specific interfacial energy respectively.

Precipitates on grain boundaries

Precipitates on grain boundaries represent a special case because they are located on the junction of two or more different crystal orientations and maybe also different lattice parameters in case of interphase boundaries. Fig. 21 shows different possibilities of interfaces on an even grain boundary.

Summarizing these findings, the interfacial energy is depending on crystallographic and chemical parameters and is not a single scalar value in general. For practical reasons an effective interfacial energy is often introduced in computer simulations.

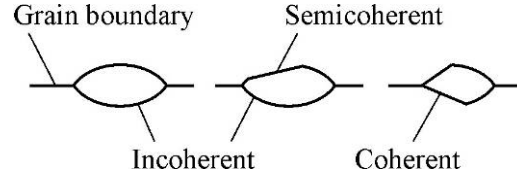


Fig. 21: Precipitates on a grain boundary with different possibilities of interfaces.

Subsequently published work shall be summarized, describing the phenomenon interfacial energy. Possibilities to calculate the values for the interfacial energy are discussed.

Calculation of solid-solid interfacial energy

Nearest neighbour, broken-bond hypothesis

Bragg and Williams [72] studied the total free energy of a binary system with a crystal structure. They assumed that this energy is equal to the sum of all bond energies. This is exactly valid if there is no difference in the crystal structure between precipitate and matrix and hence the precipitate is fully coherent. For simplicity the bond energy mentioned here only considers nearest neighbours in the lattice. Becker [73] defined the bond energy U for such a system containing N atoms and the free energy per atom f based on the same assumptions. Becker's approach is presented in more detail now. A solid solution crystal contains statistically distributed atoms A and B , the total number of atoms is N . The concentration of each species can be written in terms of a parameter α .

$$\begin{aligned} \text{Atoms } A: & N \cdot \alpha \\ \text{Atoms } B: & N \cdot (1 - \alpha) \end{aligned} \quad (20)$$

Depending on the combination of neighbouring atoms, different bond energies exist: V_{aa} , V_{ab} , V_{bb} are the bond energies between A - A , A - B and B - B bonds respectively. With Z being the number of nearest neighbour atoms per bulk atom in the lattice, every A -atom has approximately $Z \cdot \alpha$ neighbours and every B -atom has $Z \cdot (1 - \alpha)$ neighbours. The number of each bond type can hence be written as:

$$\begin{aligned} A - A: & \frac{1}{2} \cdot N \cdot Z \cdot \alpha^2 \\ B - B: & \frac{1}{2} \cdot N \cdot Z \cdot (1 - \alpha)^2 \\ A - B: & N \cdot Z \cdot \alpha \cdot (1 - \alpha) \end{aligned} \quad (21)$$

Summation of the terms in equation 21 after multiplication with V_{aa} , V_{ab} and V_{bb} yields the total bond energy of the system U :

$$U = N \cdot Z \cdot \left[V \cdot \alpha \cdot (1 - \alpha) + \frac{1}{2} \cdot V' - \frac{1}{2} \cdot V_{\delta} \cdot (1 - 2 \cdot \alpha) \right] \quad (22)$$

The V terms in joules per atom are defined as:

$$\begin{aligned} V &= V_{ab} - \frac{1}{2} \cdot (V_{aa} + V_{bb}) \\ V' &= \frac{1}{2} \cdot (V_{aa} + V_{bb}) \\ V_{\delta} &= \frac{1}{2} \cdot (V_{aa} - V_{bb}) \end{aligned} \quad (23)$$

The term containing V' does not depend on the composition α but only shifts U over the whole composition range. Therefore the V' term is neglected, because the value of the interfacial energy depends on the energy difference and the parallel shift is automatically removed. As a simplification, V_{aa} is considered to be equal to V_{bb} which makes V_{δ} zero. For all following considerations, only V is relevant, which indicates how much more strongly A - A and B - B neighbours are bonded than A - B pairs.

The entropy S is defined by the Boltzmann equation using the expression W which indicates the number of possibilities how $N \cdot \alpha$ atoms of type A and $N \cdot (1 - \alpha)$ atoms of type B can be arranged on N lattice sites.

$$S = k \cdot \ln|W| \quad (24)$$

$$W = \frac{N!}{(N \cdot \alpha)! [N \cdot (1 - \alpha)]!} \quad (25)$$

The entropy can be simplified using the Stirling formula ($\ln|N!| \cong N \cdot \ln|N| - N$) to

$$S = -k \cdot N \cdot [\alpha \cdot \ln|\alpha| + (1 - \alpha) \cdot \ln|1 - \alpha|] \quad (26)$$

The total free energy of the crystal is defined as $U - T \cdot S$. The total free energy per atom is defined as:

$$f(\alpha) = V \cdot Z \cdot \alpha \cdot (1 - \alpha) + k \cdot T \cdot [\alpha \cdot \ln|\alpha| + (1 - \alpha) \cdot \ln|1 - \alpha|] = \frac{U - T \cdot S}{N} \quad (27)$$

The values of $f(\alpha)$ are symmetrical to the composition 0,5 because the bond energies V_{aa} and V_{bb} are considered to be equal. The minima of equation 27 calculated for different temperatures add up to the phase diagram shown in Fig. 22. The graphical construction of the driving force of a nucleus with composition β in the matrix α at the temperature T_2 is shown (dashed line).

The intersection C of the tangent to $f(\alpha)$ in α with the vertical through the arbitrarily chosen nucleus composition β defines the value of the driving force $C - f(\beta)$.

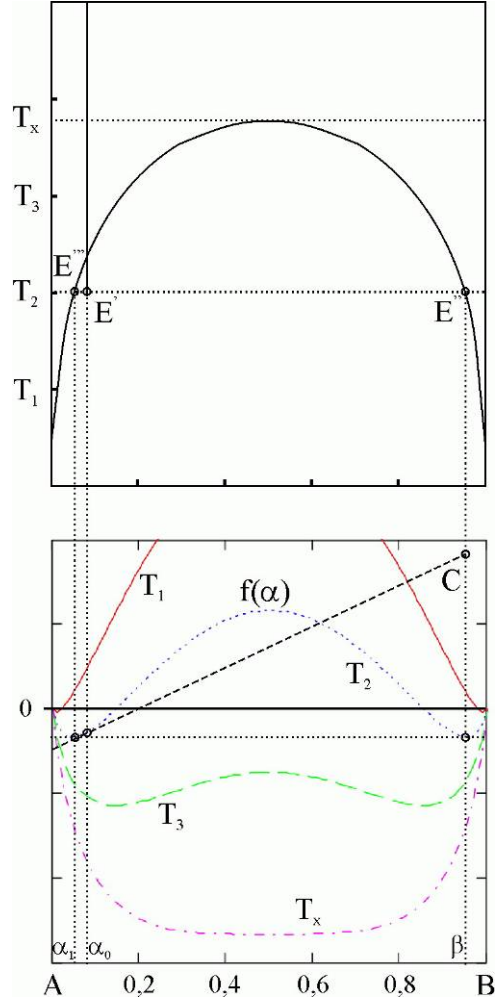


Fig. 22: The phase diagram of the AB crystal and the corresponding free energy diagram at different temperatures.

After definition of the total system energy, the precipitation of a B rich particle at a constant temperature T and the related free energy change is discussed. Therefore, a second phase with the initial composition β is introduced:

The B -rich super saturated solid solution with the initial composition α_0 is forming one nucleus by random walk of atoms in the matrix. In other words, due to diffusion the concentration of A atoms can reach the β -composition by chance. If a small cube with the composition β reaches a critical size this nucleus is stable and will not dissolve again. The length of this cube shall be a and the cube then contains $n=a^3$ atoms. Due to the formation of this nucleus the free energy of the system F increases and can be divided into two terms. One term is related to the volume of the nucleus F_V the other term F_S relates to the nucleus surface.

$$F = F_V + F_S \quad (28)$$

F_V of a thermodynamic stable precipitate phase is negative, which is displayed in Fig. 22 and can be derived from $f(\alpha)$. F_S is positive and determined by the specific interfacial energy.

When evaluating F_V it has to be considered that during precipitation the initial alloy of N atoms with the composition α transforms into two phases. One phase represents the nucleus/precipitate, containing n atoms with the composition β , the other phase is the matrix containing $N-n$ atoms. The matrix composition α can be calculated from the mass-balance.

$$N \cdot \alpha = (N - n) \cdot \alpha_0 + n \cdot \beta \quad (29)$$

or*

$$\alpha_0 - \alpha = \frac{n}{N} \cdot (\beta - \alpha_0) \quad (30)$$

The volume related term of the total free energy F_V can be written as:

$$F_V = [n \cdot f(\beta) + (N - n) \cdot f(\alpha)] - [N \cdot f(\alpha_0)] \quad (31)$$

Because N is much larger than n , the value of $\alpha_0 - \alpha$ is very small. Therefore $f(\alpha)$ can be written as a series neglecting second order and higher terms:

$$f(\alpha) = f(\alpha_0) - \frac{df(\alpha_0)}{d\alpha} \cdot (\alpha_0 - \alpha) \quad (32)$$

This leads to:

$$F_V = -n \cdot \left[f(\alpha_0) - f(\beta) + \frac{df(\alpha_0)}{d\alpha} \cdot (\beta - \alpha_0) \right] \quad (33)$$

The value of the F_V term in square brackets indicates the distance of point C to the value $f(\beta)$ in Fig. 22 which represents the driving force for this nucleus in the matrix. It can also be observed that only B -rich nuclei can form in the A -rich matrix because other nucleus compositions do not provide a positive driving force. When the phase fraction of the β -phase rises, driving force is reduced according to the tangent construction in Fig. 22.

During precipitation and growth, new interfaces are formed and existing interface area is increased. This changes the total system energy which is taken into account by the surface related term F_S of the total free energy. The definition of F_S can be illustrated by considering two cubes that are cut out of the phases A and B respectively. The cubes have an equal volume of a^3 and are exchanged between phase A and B . Thereby new interfaces between the two phases are introduced without changing the phase fraction. A total interface area of $2s = 12a^2$ is established and, as discussed earlier, bonds have to be broken and rebuilt in both phases A and B . The number of broken bonds and newly formed bonds can be derived as shown in Tab. 3:

* The original equation by Becker [73] differs, but the result is the same.

Tab. 3: The number of bonds when phase B is forming an interface with phase A.

	A-A bonds	B-B bonds	A-B bonds
Broken in A	$N \cdot \alpha^2$	$N \cdot (1 - \alpha)^2$	$N \cdot 2 \cdot \alpha \cdot (1 - \alpha)$
Broken in B	$N \cdot \beta^2$	$N \cdot (1 - \beta)^2$	$N \cdot 2 \cdot \beta \cdot (1 - \beta)$
Formed A-B	$2 \cdot N \cdot \alpha \cdot \beta$	$2 \cdot N \cdot (1 - \alpha) \cdot (1 - \beta)$	$2 \cdot N \cdot \alpha \cdot (1 - \beta) + \beta \cdot (1 - \alpha)$

The value of F_S is defined by the difference between the total bond energy of the system before and after the exchange of the cubes, hence the establishment of the interface. The number of newly built bonds minus the number of broken bonds on the cube surface multiplied with the according bonding energies leads to the value of F_S .

$$F_S = N \cdot \frac{s}{2} \cdot \left[2 \cdot \alpha \cdot \beta \cdot V_{aa} + 2 \cdot (1 - \alpha) \cdot (1 - \beta) \cdot V_{bb} + 2 \cdot (\alpha \cdot (1 - \beta) + \beta \cdot (1 - \alpha)) V_{ab} \right. \\ \left. - \alpha^2 \cdot V_{aa} \quad (1 - \alpha)^2 \cdot V_{bb} \quad - 2 \cdot \alpha \cdot (1 - \alpha) \cdot V_{ab} \right. \\ \left. - \beta^2 \cdot V_{aa} \quad - (1 - \beta)^2 \cdot V_{bb} \quad - 2 \cdot \beta \cdot (1 - \beta) \cdot V_{ab} \right] \quad (34)$$

The first line represents the energy obtained by the newly built bonds, the other two lines stand for the broken bonds in the matrix A and the precipitate phase B. Collecting the terms leads to,

$$F_S = s \cdot V \cdot (\alpha - \beta)^2 \quad (35)$$

where V is the term from equation 23. With equations 33, 34, $n=a^3$ and $s=6a^2$ equation 28 can be finally written as:

$$F = -a^3 \cdot \left[f(\alpha) - f(\beta) + \frac{df}{d\alpha}(\alpha) \cdot (\beta - \alpha) \right] + 6 \cdot a^2 \cdot V \cdot (\alpha - \beta)^2 \quad (36)$$

Equation 36 describes the total free energy of the system depending on the cube size. Becker assumed that the total free energy of a binary two phase system is equal to the sum of all bond energies. Moreover, the crystal structures of the phases have to be identical and the interfaces between matrix and precipitates are sharp. Thus, the composition in both phases is constant up to the interface. This yields a fully coherent interface with no misfit strain and no broken bonds and thus the maximal possible chemical interfacial energy. He also explained that during the formation of a precipitate in a matrix bonds are broken and new bonds established. This leads to a difference of the system enthalpy before and after this kinetic reaction or F in equation 36 before and after the precipitation reaction.

Becker's approach was utilized by Turnbull [74] who defined the specific interfacial energy between two phases and did set the bond energy V in equation 36 equal to the enthalpy of solution ΔE^0 . Turnbull points out that this definition is only correct for a temperature of 0K and only considering the chemical contribution. Lattice misfit is not taken into account because Becker assumed perfect coherency.

$$\Delta E^0 = N_A \cdot z_s \cdot \left[V_{ab} - \frac{1}{2} \cdot (V_{aa} + V_{bb}) \right] \quad (37)$$

N_A is Avogadro's number; z_s is the coordination number of an atom on the precipitate surface which denotes the number of nearest neighbours of an atom on the surface. This approach is used in abbreviated and extended versions by many authors for a vast number of calculations (e.g. Nishizawa et al. [75]). In principle, these attempts differ only in how the enthalpy of mixing is predicted.

$$\gamma_c^0 = \frac{z^*}{z_l} \cdot \frac{N_s \cdot \Delta E^0}{N_A} \quad (38)$$

The value of the interfacial energy γ can be derived as shown in equation 38, where N_s is the number of atoms per unit area forming the interface, z^* is the number of bonds per interface atom across the interface and z_l is the number of nearest neighbours in the precipitate in bonds per atom. As indicated by the subscript c and the superscript 0 , this is strictly the chemical interfacial energy at the temperature 0K. An interpretation of this equation can be given by splitting into two parts:

The factor z^*/z_l in equation 38 is taking crystallography into consideration. The more bonds established across the interface (high value of z^*), the higher the interfacial energy. The higher the number of bonds per atom in the bulk of the precipitate z_l , the lower is γ . Influence by shape of the interface is not considered nor how many precipitates share. The right term in equation 38 describes the energy per atom. $\Delta E^0/N_A$ is the enthalpy of mixing for one atom of the system. Multiplying with N_s leads to the total energy of the interface. Servi and Turnbull [76] expanded equation 38 to the form:

$$\gamma_c^0 = \frac{N_s \cdot (z_l - z_s) \cdot \Delta E^0 \cdot (c_p - c_l)^2}{N_A \cdot z_l} \quad (39)$$

The different composition c_p and c_l between the precipitate and the matrix respectively are considered, they utilized this equation to calculate the values of the interfacial energies for Co enriched precipitates in the Cu-Co system. The factor $z_l - z_s$ replaces z^* and represents the maximum number of cross-bonds per surface atom. Considering an {111} interface in an *fcc* crystal $z_s=9$ and $z_l=12$, which leads to $z^*=3$.

To conclude, ΔE^0 can be calculated from *CALPHAD* type databases [77] which allows to predict the specific chemical interfacial energy of any system. This approach is used to derive the interfacial energies of complex Cr-steels as well as model alloys and described in chapter 4.3.

Variations of the nearest neighbour, broken-bond approach

Hillert [78] extends the simple nearest neighbour, broken-bond model allowing one-dimensional composition changes and thereby predicting periodically modulated structures in ordering and precipitation systems. Unfortunately he does not provide a value for interfacial energy.

Shiflet et al. [79] discuss and expand the work of Servi and Turnbull [76] concerning nucleation of spherical particles in the Cu-Co System. Their model is using a regular solution* to determine the enthalpy of mixing ΔH .

* Regular solution: Mixing of components is an endo- or exothermic process, as a result of changing atom distances and neighbours. The thermal energy, or enthalpy of mixing ΔH_{mix} , is absorbed or released.

$$\gamma = N_s \cdot z^* \cdot \Delta x^2 \cdot \Delta H \quad (40)$$

$$\Delta H = \frac{\Omega}{Z \cdot N_A} \quad (41)$$

They also mention that it is known that this model is „incorrect in principle, since once the temperature and pressure of the system are specified the interfacial thickness (the width of the region in which composition differs from that of either of the bulk phases) is no longer an independent variable” [82].

Lee and co-workers [80] describe four methods to measure the regular solution parameter Ω which is independent of temperature and composition [81]. This allows to calculate the enthalpy of mixing of a binary system with symmetrical free energy curves. Cahn and Hilliard [82] as well as Lee and Aaronson [83] show that the coherent interfacial energy strongly depends on Ω . They employ a nearest neighbour, broken-bond model to calculate the concentration profile across a specific coherent interface and furthermore the interfacial energy. A precise computation of the free interfacial energy is possible if the exchange of atoms across the interface is considered, building new bonds and breaking existing bonds until equilibrium is reached. This discrete-lattice-approach allows taking all the neighbouring atoms into account, the results show that the anisotropy of the interfacial energy for an *fcc* crystal is temperature dependent. Beginning at 0K where the ratio between the maximum values is 1,3 to less than 1,006 when the temperature is 75% of the precipitate solubility temperature.

Yang and Enomoto [84, 85] use a discrete lattice plain, nearest neighbour, broken-bond model to calculate the interfacial energy of carbides and nitrides in austenite depending on the crystallographic orientation. They point out that the chemical contribution of γ is much higher than the grain boundary free energy of the matrix, because of the usually large composition difference between precipitate and matrix. Furthermore precipitates containing heavy metallic atoms tend to have a higher interfacial energy because the bonding enthalpy ΔH_m is larger. They also observed that nitrides have a higher chemical interfacial energy than carbides because of a more negative formation enthalpy ΔH_f . The influence of the entropy term can be neglected because the volume expansion of the interface is responsible for the value of the entropy. Thus the interface between austenite and nitrides/carbides is very narrow, the same holds true for ferrite. This also denotes that the concentration of solute atoms can be regarded as constant up to the interfacial plane, therefore the interfacial energy is more or less only depending on the bond energy between bulk and interfacial region. This is not predicted by the model of Cahn and Hilliard [82].

Miedema and de Broeder [86] assume that the interfacial energy for pure metals can be described by the work of adhesion with simple thermodynamic calculations. Their approach is based on the fact that the relative difference of the interfacial energy between the liquid state and the solid state is independent of the metal. This allows predicting the interfacial energy of pure solid metals based on the values for their liquid state. This is again only valid for 0K, therefore a temperature dependent entropy term was added. They further assume that for two solids with different lattice parameters the geometrical term is comparable with the energy of a high angle grain boundary. The enthalpy of such a boundary is about 30% of the zero temperature surface energy [74].

The calculations of Miedema and co-workers [86-88] do not show extensive difference between pure metals interfacial energies of gas-solid interfaces to gas-liquid interfaces. Therefore the interfacial energy for gas-solid interfaces, including a temperature de-

pendency, can be derived from experimental values based on liquid metals. Therefore the interfacial energy for a solid-solid interface between pure metals can be roughly calculated:

$$\gamma_{SS}^{AB} = 0,15 \cdot (\gamma_A^{S,o} + \gamma_B^{S,o}) + \gamma_{SS}^{chem} \quad (42)$$

Their values are in good agreement with experimental data.

Diffuse interface approach

The diffuse interface approach considers the interface as a volume, not only a two-dimensional layer, between the bulk and the precipitate. The interface is extended over a certain number of lattice planes, the width of which is temperature dependent. In this approach the interface is not sharp but diffuse with a composition profile from the matrix bulk composition to the precipitate composition.

Cahn and Hilliard [82] developed a continuum method to calculate the free energy of a non-uniform system, regarding composition and density. They consider a flat interface between two phases with a variable thickness and a concentration gradient depending on the temperature, the higher the temperature, the wider the interface. At the solubility temperature the interface thickness is infinite.

Leo and Hu [89] investigate the solid-solid interface by using a continuum approach. The minimisation of the total energy, bulk and surface, leads to a mixed interfacial structure of coherent and incoherent interfaces. A value for the interfacial energy is not acquired.

Kahlweit [90] provides equations describing the free enthalpy of mixing of an inhomogeneous strictly regular solution of a two phase system. He calculates the interfacial energy also based on the nearest neighbour, broken-bond hypothesis. This model shows the same diffuse interface for higher temperatures as the continuum approach of Cahn and Hilliard [82] and a sharp interface at lower temperatures as assumed by Becker [73].

Other approaches

Some work is concentrated on special locations or orientations of precipitates, like precipitation on dislocations and the associated strain field influencing them (Wang and Shiflet [91]). Such calculations are used to explain the atomic arrangement of *fcc* metals with one mono-layer of *bcc* deposit (Gotoh et al. [92]).

Monte Carlo simulations can predict anisotropic as well as thermal dependencies of binary interfaces with a defined crystallographic orientation [93, 94].

The *ab initio* calculations (atomistic approach) are also used to simulate interfacial phenomena, up to now limited to special cases and not for universal use. Unfortunately, macroscopic values for the interfacial energy are difficult to obtain with this approach [95-97].

Gupta [98] combines the interface energy phenomenon with the ratio of diffusivity in the lattice D_l and along the interface D_i .

$$\gamma = \frac{1}{2} \cdot R \cdot T \cdot \left(\ln \frac{|D_i|}{|D_l|} \right) \quad (43)$$

This calculation of the interfacial energy γ is only valid for pure metals, as well as the expression for grain boundary energy γ_b :

$$\gamma_b = \frac{71 \cdot T_m}{2 \cdot a^2 \cdot N_A} \quad (44)$$

He argues that the diffusion process in general is related to the melting temperature T_m .

Calculation of solid-liquid interfacial energy

Spaepen [99] and Spaepen and Meyer [100] developed a structure model to calculate the solid-liquid surface free energy σ . The model is dealing with dense random packing of hard spheres (liquid) which can be characterized as maximum short range density (*hcp*) and a close-packed crystal plane stated as maximum long range density (*fcc*). The surface energy at the melting temperature T_m can be derived via the configurational entropy difference between the bulk and the surface.

Holland-Moritz [101] examined undercooled Al-base melts. To predict the interfacial energy he used an adapted model proposed by Spaepen and Meyer [99].

$$\sigma = \frac{N_i}{N_s} \cdot \frac{\Delta S_{ef}(Bulk) - S_{ef}(i)}{\Delta S_f} \Delta H_f \quad (45)$$

N_i is the number of atoms in the interface, N_s the number of atoms in the first layer of the solid phase. $S_{ef}(i)$ is the configurational entropy per atom of the interface, $\Delta S_{ef}(Bulk)$ is the difference of the configurational entropy between liquid and solid per atom and ΔS_f is the entropy of fusion per atom.

Nishizawa and co-workers [102] estimated the interfacial energies between ceramics and liquid metal. They used the Becker [73] approach and an extended version to second nearest neighbour bonds.

Digilov [103] described his „corresponding-state” approach to predict the surface tension properties of pure solid and liquid metals. The surface tension is linearly scaled with the melting temperature and the atomic volume of the solid phase at the melting point.

Butler's equation:

Many authors used the equation first introduced by Butler [104] to calculate liquid-solid surface energies σ [105-116]. Butler investigated the case of a single layer of molecules at the interface which have different physical properties from those in the bulk.

The equations are based on chemical potentials* which can be accessed by using the CALPHAD [77] method.

$$\begin{aligned} \sigma &= \sigma_A + \frac{R \cdot T}{A_A} \ln \left(\frac{1 - X_B^s}{1 - X_B^b} \right) + \frac{1}{A_A} \cdot (G_A^{E,s} - G_A^{E,b}) \\ \sigma &= \sigma_B + \frac{R \cdot T}{A_B} \ln \left(\frac{X_B^s}{X_B^b} \right) + \frac{1}{A_B} \cdot (G_B^{E,s} - G_B^{E,b}) \end{aligned} \quad (46)$$

R is the gas constant, T the absolute temperature, σ_i is the surface tension and A_i the molar surface area of the pure element i (in this case Element A or B). $G_i^{E,b}$ is the partial

* $\mu \sim RT \ln X$

excess free energy of i in the bulk, $G_i^{E,s}$ is the partial excess free energy of i in the surface. X_i^b is the mole fraction of i in the bulk.

3.3.2 Measuring the interfacial energy of solid-solid interfaces

Jones [117] and Tyson [118] provide extensive lists of solid-vapour, solid-liquid and liquid-vapour interfacial energies for pure metals. These values are measured utilizing different investigation methods:

Measurement of dihedral angles

The grain boundaries aspire an energy balance and thus certain angles between the grain boundaries are adjusted by migration. This angle ideally depends on the grain boundary energy only and by measuring these angles the grain boundary energy can be calculated. These measurements only lead to feasible results for the precipitate matrix interfacial energy when the precipitate is located on a grain boundary and is of significant size [119]. It is possible to calculate the interfacial energy between grains of different phases too, but only relative values for the interfacial energies can be deduced.

Gjostein et al. [120] predicted the ratio of ferrite to austenite interfacial energies in Fe-C alloys by measuring the dihedral angles between the grains. They point out, that the value of the interfacial energy is depending on the C adsorption in the interface.

Equilibrium shape

Particles surrounded by their own vapour tend to generate the equilibrium shape according to the Wulff theorem [67] during growth in order to minimize the surface energy (see chapter 3.3.1). The direction depending interfacial energy can then be calculated by measuring the shape parameters of such isolated particles.

Coarsening

Measuring the coarsening rate of precipitates during an annealing treatment is presumably the most precise and sophisticated method to derive interfacial energy values of precipitates in a matrix. The coarsening behaviour of precipitates located in a solid matrix is described accurately by Lifshitz, Slyozov [121] and Wagner [122] (*LSW* theory). Specimens are annealed at a constant temperature. At planned intervals samples are generated and the mean radii of the precipitates are measured. According to the *LSW* theory the mean radius rises parabolically with time.

$$r^3(t) - r^3(t_0) = K_R^{LSW} \cdot t \quad (47)$$

t is the absolute time, K_R^{LSW} is the rate constant for an ideal solution and r is the mean radius of the precipitates. The rate constant can be written as:

$$K_R^{LSW} = \frac{8 \cdot D \cdot V_\beta \cdot c_\alpha^e \cdot \gamma}{9 \cdot R \cdot T} \quad (48)$$

D is the diffusion coefficient of the solute atoms in the matrix, V_β is the molar volume of the precipitate phase, c_α^e is the equilibrium matrix composition and γ is the specific interfacial energy. R is the gas constant and T the absolute temperature (see chapter 4.1.3). These data allow calculating the product of the diffusion coefficient and interfacial energy according to the *LSW* theory, assuming that the other values are known. The accuracy of this method is depending on the correct value of the diffusion coefficients.

Ardell [123] developed a method to calculate the interfacial energy and the diffusion coefficient independently. He analyses therefore the mean radii and parallel the changes of the matrix composition or the phase fraction of the precipitate phase.

Polat et al. [124] evaluated the changes of the phase fraction and the particle radius during coarsening of a Ni-12,5 at% Si alloy using X-ray diffraction data simultaneously. By utilizing equations of the *LSW* theory, a separated calculation of the diffusion coefficient and the interfacial energy is possible.

Marsh et al. [125] did similar investigations for a Ni-12,5 at% Al alloy, their γ values are in good agreement with calculations presented in ref. [126].

Zero strain, zero creep method

Jones [127] described the zero creep method to measure grain boundary- and surface energies of metals and alloys. Specimens consisting of single crystals attached to each other forming a „bamboo” structure are creep tested. The load is directed normal to the grain boundaries along the single crystal-chain. Measuring the creep rate allows to predict the grain boundary energies between the crystals. This method could in principle provide interfacial energy values for matrix precipitate interfaces but under some restrictions: Concerning shape, the interfaces need to be parallel or normal to the applied stress, the grain size should be equal to the usual interphase spacing, and the microstructure must be stable during the experiment.

Murr and co-workers [128] describe their experiment to obtain the interfacial energy values and linear temperature coefficients of a 304 stainless steel (18% Cr 10% Ni) with the zero creep method.

4 Classical precipitation kinetics and the new model

4.1 Classical precipitation kinetics

On the basis of a hypothetical binary alloy the classical cluster-kinetics approach the processes of nucleation, growth and coarsening is explained. The equilibrium condition of this system consists of an A -rich matrix phase α with the composition c_α^e and a B -rich precipitate phase β with the composition c_β^e (Fig. 23). For a general overview see for example the chapter by Wagner and co-workers [129] in the textbook by Kostorz.

4.1.1 Nucleation

When an alloy is homogenized at a temperature T_0 and then quenched to the temperature T_1 into a meta-stable region where a miscibility gap exists, the matrix phase α is said to be supersaturated (c_α^0). A positive driving force exists to decompose the single-phase system towards the thermodynamic equilibrium state, i.e. two separated phases α and β . The *Gibbs* energy diagram and the matching phase diagram can be seen in Fig. 23.

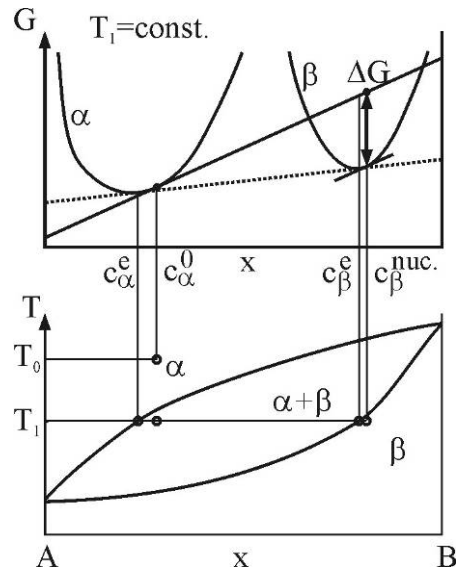


Fig. 23: The *Gibbs* free energy of a hypothetical binary two phase system is depicted in the upper graph. The corresponding phase diagram of this system can be seen below.

Performing the tangent construction for the supersaturated condition in the upper graph in Fig. 23 leads to the highest possible driving force for the nucleus. According to classical thermodynamics, the driving force can be illustrated by drawing a tangent to the *Gibbs* energy graph of the matrix phase through the c_α^0 state. The parallel to this tangent to the *Gibbs* energy curve of the precipitate marks the composition $c_\beta^{nuc.}$. The most favourable composition of the nuclei in the matrix with the composition c_α^0 is therefore $c_\beta^{nuc.}$. The driving force ΔG for nucleation, growth and coarsening is defined as the sum of a chemical contribution and a mechanical contribution [129].

$$\Delta G = \Delta f_{ch} + \Delta f_{el} \quad (49)$$

Considering coherent interfaces, the elastic contribution to the driving force f_{el} can be computed:

$$\Delta f_{el} = 2 \cdot \gamma \cdot \left(\frac{1+\nu}{1-\nu} \right) \cdot \delta^2 \quad (50)$$

The chemical contribution to the driving force strongly depends on the matrix composition:

$$\Delta f_{ch} \approx - \frac{R \cdot T}{V_\beta} \ln \left| \frac{c_\alpha}{c_\alpha^e} \right| \quad (51)$$

R is the gas constant and T the absolute temperature. V_β is the molar volume of the precipitate phase. c_α^0 and c_α^e are the actual system composition and the equilibrium matrix composition, respectively. ν is Poisson's ratio and δ the lattice misfit between the matrix and the precipitate crystal structure.

Due to diffusion random walk of atoms small particles with the composition c_β^{nuc} form when atoms are attached to each other by compositional fluctuations. The interface between nuclei and matrix is assumed to be sharp.

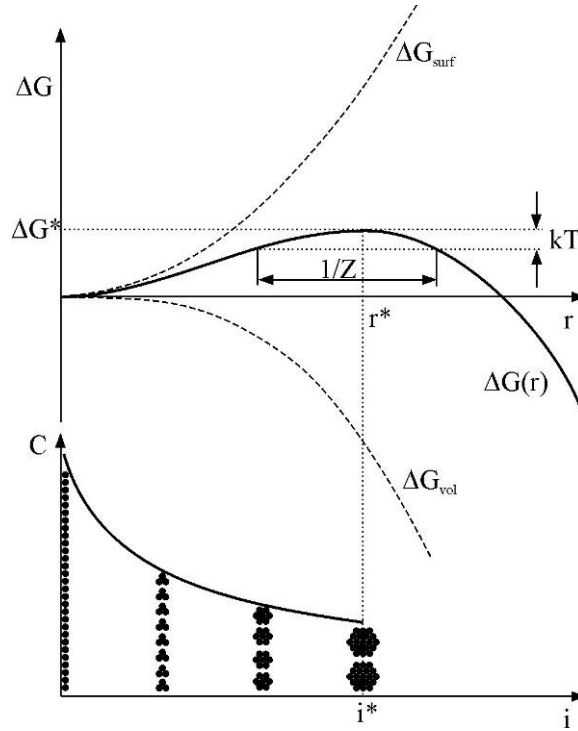


Fig. 24: The total energy of a nucleus drawn over the radius and the cluster size distribution up to the critical radius r^* and the critical number of atoms i^* , respectively.

The formation of precipitates is of course changing the total free energy of the system, where the level of the energy of a nucleus is volume and surface dependent (equ. 52). The left term of this equation is related to the nucleus volume and accounts for the gain of *Gibbs* energy due to the formation of the droplet (ΔG_{Vol} , negative contribution). The energy related to the second term has to be expended to form a new interphase boundary

area (ΔG_{Surf} , positive contribution). These two energy contributions determine the shape of the total free energy curve of the nucleus as depicted in Fig. 24.

$$\Delta G(r) = (\Delta f_{ch} + \Delta f_{el}) \cdot \frac{4 \cdot \pi}{3} \cdot r^3 + 4 \cdot \pi \cdot r^2 \cdot \gamma \quad (52)$$

γ is the specific interfacial energy, r is the nucleus radius. The nuclei here are treated as spheres and can be classified by their size. As illustrated in Fig. 24, the nuclei have a size distribution C . Clusters with a size r^* , are in unstable equilibrium and the free energy decreases if the system contains clusters which are smaller or larger than r^* . Therefore only clusters which are larger than r^* overcome the activation barrier for nucleation ΔG^* . According to the *Becker-Döring* theory [130] a decay of nuclei with $r > r^*$ is still likely. This is accounted for by the *Zeldovich* factor Z . A nucleus is supercritical when the size is larger than the size range indicated by $1/Z$ in Fig. 24.

$$r^* = -\frac{2 \cdot \gamma}{\Delta G} \quad (53)$$

$$\Delta G(r^*) = \Delta G^* = \frac{16 \cdot \pi}{3} \cdot \frac{\gamma^3}{\Delta G^2} \quad (54)$$

It is obvious that the interfacial energy γ strongly influences nucleation (see chapter 3.3.1). The time-dependent nucleation rate J^* is given by:

$$J^*(t) = Z \cdot \beta^* \cdot N_0 \cdot \exp\left(-\frac{\Delta G^*}{k \cdot T}\right) \cdot \exp\left(-\frac{\tau}{t}\right) \quad (55)$$

β^* is the atomic impingement rate, N_0 the number of available nucleation sites. The simulation time is t , k is the Boltzmann constant, T is the absolute temperature, and τ is the incubation time. The gradient of the driving force ΔG within the region $1/Z$ is rather small and the cluster will move across this region predominantly by random walk with the jump frequency β^* . The expected time to cover the distance $1/Z$ is identified with the incubation time τ [131].

$$\tau = \frac{1}{2 \cdot \beta^* \cdot Z^2} \quad (56)$$

$$\beta^* = \frac{4 \cdot \pi \cdot r^{*2} \cdot D \cdot c_\alpha}{a^4} \quad (57)$$

a is the mean atomic distance of the matrix phase, the other values are explained above. The atomic impingement rate β^* is the effective rate, or probability, with which the atoms change from the matrix to the nucleus surface. Equation 57 holds true for spherical nuclei and a binary system as proposed by Russel [131].

4.1.2 Growth

Now suppose stable nuclei exist in the matrix. The nuclei are very small and therefore the matrix is still supersaturated. The precipitates grow by attaching atoms to their surface and thereby depleting the matrix until the equilibrium phase fraction is reached. During pure growth the total number of precipitates stays constant.

Every precipitate is surrounded by a concentration field as shown in Fig. 25 a) and all atoms move according to the Brownian motion. For example atoms located at point „1” in the concentration field preferably move towards the interface (point „2”) due to the concentration gradient. Once attached to the precipitate it is very unlikely that they are detached again during growth.

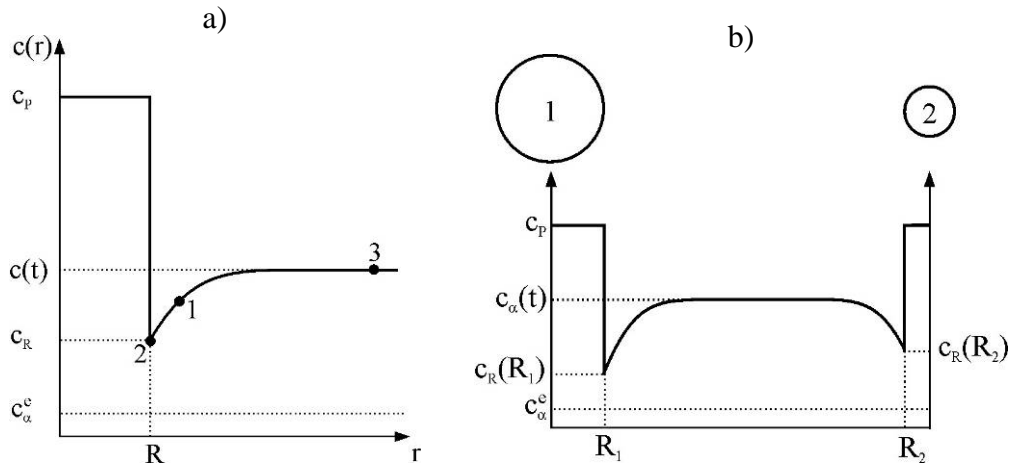


Fig. 25: a) Schematic concentration field in the matrix surrounding a nucleus with radius R and composition c_p . b) Sketch of the diffusion fields in the vicinity of two precipitates with different radii. The composition at the interface $c_R(r)$ is predicted by the *Gibbs Thomson* equation (equ. 58).

According to the *Gibbs Thomson* equation (equ. 58), the composition c_R of the matrix phase at a curved interface is different from that of the flat interface and depending on the precipitate radius r .

$$c_R(r) = c_\alpha^e \cdot \exp\left(\frac{2 \cdot \gamma \cdot V_\beta}{R \cdot T} \cdot \frac{1}{r}\right) \quad (58)$$

This equation holds true when the solid solution shows regular solution behaviour. The driving force is constantly reduced during growth as can be seen in Fig. 26.

The matrix composition changes during growth from c_α^0 to c_α^1 because element B is removed from the matrix to form the B -rich precipitates. Also the precipitate composition providing the highest driving force is changed from c_β^0 to c_β^1 . The precipitate equilibrium composition is therefore changing during growth and also the precipitates can have a composition gradient across the radius.

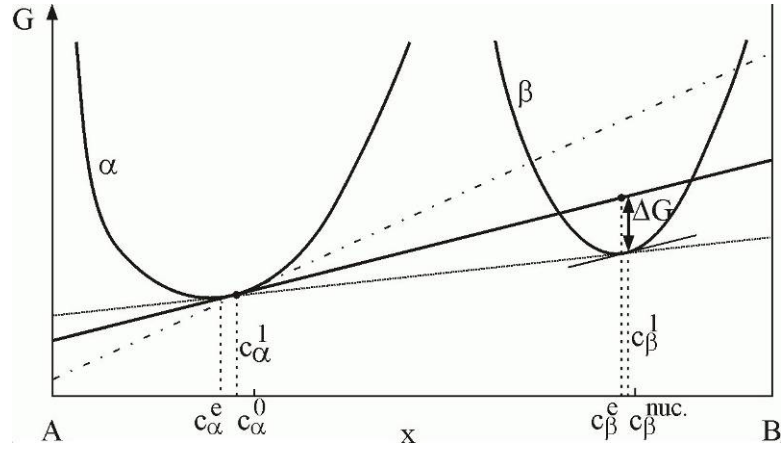


Fig. 26: The *Gibbs* free energy change of the discussed system during growth is shown. The dash dotted line visualizes the initial situation as described in Fig. 23.

The rate at which the precipitates grow can be controlled either by the rate at which atoms are supplied to the particle/matrix interface by diffusion or by the rate at which they cross the interface [132]. It is commonly assumed that the mobility of the interface is sufficiently high in order to allow the solute concentration at the curved interface c_R to achieve local equilibrium. In this case diffusion is the rate controlling step of the growth of stable coherent nuclei in homogeneous precipitation reactions. The radius evolution of a single precipitate over time can be described by:

$$r(t) = \left(2 \cdot \frac{c_a(t) - c_a^e}{c_\beta - c_a^e} \right)^{1/2} \cdot (D \cdot t)^{1/2} \quad (59)$$

D is the diffusion coefficient of the solute atom in the matrix.

4.1.3 Coarsening

After pure growth has stopped, the matrix is depleted and a near-equilibrium phase fraction of the precipitate phase β is reached. The precipitate distribution is usually left shifted and during a *transient stage* this distribution is rearranged to a right shifted distribution. During the transient stage the mean radius as well as the precipitate number stay constant.

The last stage during a precipitation reaction is referred to as coarsening or *Ostwald ripening*. In this regime, the scaled precipitate distribution is time invariant, or self-similar. Scaling is done by the average particle radius.

For the following remarks it is assumed that lattice diffusion is the rate controlling process. The solute content $c_R(r)$ of the matrix at a small precipitate R_2 with a large ratio of surface to volume is larger than that at a large precipitate R_1 as described by the *Gibbs Thomson* equation (equ. 58). Due to the different solute concentration at small precipitates and at larger precipitates a solute flux occurs from small to large precipitates. This leads to a size-dependent growth rate $r(t)$ which is positive for large precipitates ($c_a(t) > c_R$) and negative for small precipitates ($c_a(t) < c_R$). The growth rate becomes zero for precipitates with $c_a(t) = c_R$ which are in unstable equilibrium with the matrix.

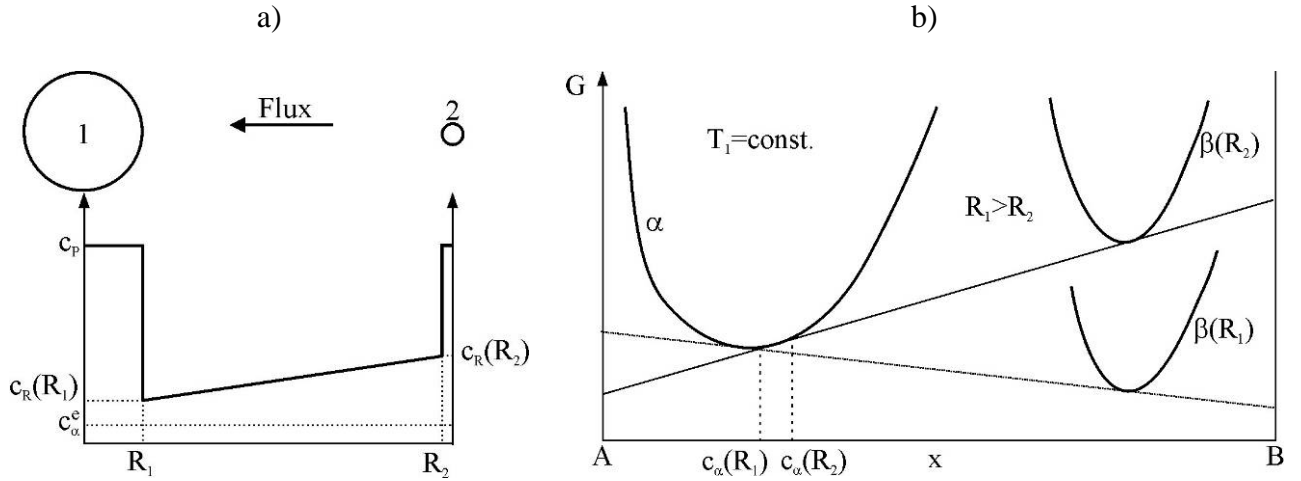


Fig. 27: a) Schematic concentration profile in the matrix between two precipitates with different size. b) The *Gibbs* free energy of the system is lower for large precipitates. This depicts the situation during coarsening.

Hence, driven by the release of excess interfacial energy, larger precipitates will grow at the expense of smaller ones which dissolve again giving rise in the change of the precipitate size distribution. This process is called coarsening and reduces the precipitate number density while the mean radius is increasing. Fig. 27 b) illustrates this situation, it can be seen that large precipitates lead to a lower total *Gibbs* energy.

Coarsening is a multi particle diffusion problem described theoretically by Lifshitz and Slyozov [121] and Wagner [122], based on a continuity equation and the differential form of equation 59. The assumptions made by them are: Both phases are dilute, the precipitate volume is near zero, the precipitates are spheres and the phase fraction of the precipitate phase is constant. The latter confines the *LSW* theory to the late stages of a precipitation reaction.

$$r^3(t) - r^3(t_0) = K_R^{LSW} \cdot t \quad (60)$$

The rate constant K_R^{LSW} for an ideal solution and the dilute solution limit is given by:

$$K_R^{LSW} = \frac{8 \cdot D \cdot V_\beta \cdot c_\alpha^e \cdot \gamma}{9 \cdot R \cdot T} \quad (61)$$

D is the diffusion coefficient of the solute atoms in the matrix, V_β is the molar volume of the precipitate phase, c_α^e is the equilibrium matrix composition and γ is the specific interfacial energy. R is the gas constant and T the absolute temperature.

Coarsening as described above is also characterized by a time invariant shape of the scaled precipitation distribution as shown in Fig. 28. The x-axis shows the scaled radius, which is the radius of each precipitate class divided by the mean radius. In these terms each precipitate class contains a certain number of precipitates with similar size. The y-axis is the number frequency of precipitates in each class. The *LSW* shape of the precipitate distribution for zero volume fraction is given by:

$$f(x) = x^2 \cdot \left(\frac{3}{3+x}\right)^{\frac{7}{3}} \cdot \left(\frac{\frac{3}{2}}{\frac{3}{2}-x}\right)^{\frac{11}{3}} \cdot e^{\left(\frac{-x}{\frac{3}{2}-x}\right)} \cdot \frac{4}{9} \quad (62)$$

The *LSW* theory is valid for systems with a phase fraction near zero where the growth rate is only a function of the particle size. Research results are published for example by Fan et al. [133] or Marsh and Glicksman [134] dealing with systems with a finite volume fraction (non-zero). This influences the shape of coarsening precipitate distribution as well as the coarsening rate. Local diffusional interactions result in spatial correlations which are not random. As a result of the increased volume fraction shrinking precipitates are more close to growing precipitates. Therefore the concentration gradients are higher and as a consequence the rate of growing and shrinking is increased.

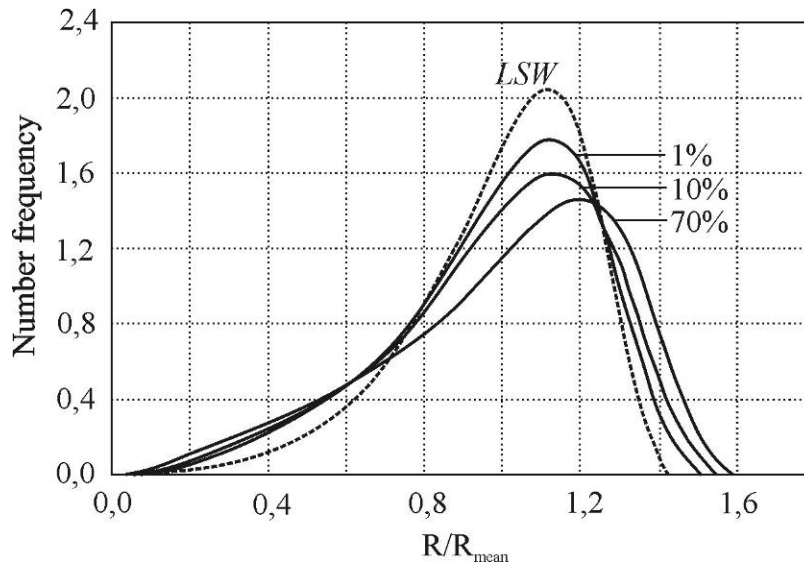


Fig. 28: Steady-state (time invariant) precipitation distributions at various volume fractions. The *LSW* shape of the precipitate distribution for a zero volume fraction is also shown [134].

4.2 The *SFFK* Model

The simulation of the evolution of precipitates during heat treatment of industrial alloys has been a challenge to researchers for considerable time. Since such reactions can involve the concurrent nucleation, growth, coarsening and change in chemical composition of various types of precipitates, a comprehensive treatment becomes usually rather complex. Recently, a theoretical model has been developed that describes the evolution of such systems as a function of temperature and microstructure. The theoretical foundation of this novel model is based on the *Onsager* extremal thermodynamic principle, which postulates that a thermodynamic system evolves with a constraint maximum *Gibbs* free energy dissipation. The theory behind the model has been described by Svoboda et al. [135]. First simulations and the application of this model to various problems are discussed in the accompanying paper [136]. Subsequently, a brief summary of the essential features of the model is presented, which was applied in all simulations described in this thesis.

4.2.1 Software implementation

The model developed in ref. [135] has been implemented into the thermo-kinetic software *MatCalc* [27]. This software evaluates the multi-component thermodynamics of the system from *CALPHAD* type databases [137] and provides chemical potentials and driving forces of all phases as well as the diffusivities of all elements as a function of chemical composition and temperature. Based on these data, the evolution of the radius and composition of the precipitates can be calculated.

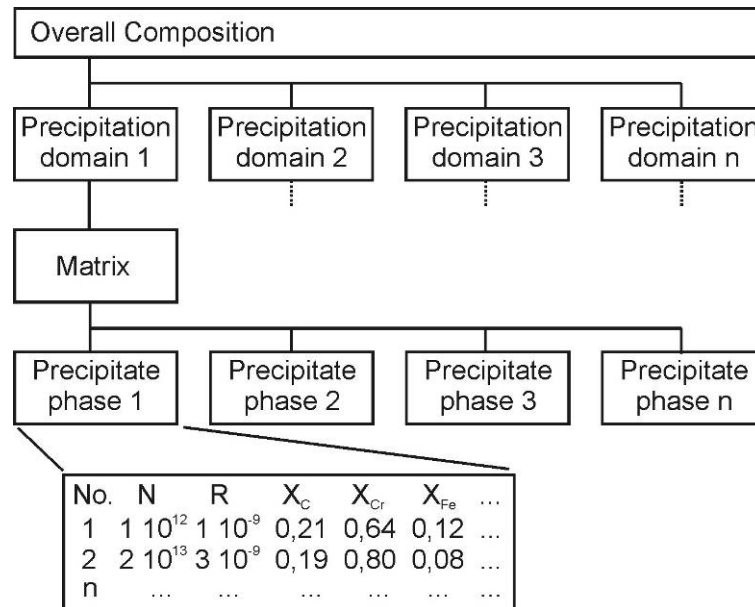


Fig. 29: The schematic structure of the *MatCalc* precipitation kinetics model.

MatCalc organizes a system in precipitation domains. Examples for precipitation domains are e. g. grain boundaries, the grain interior, or two matrix phases in a duplex microstructure. At least one precipitation domain has to be defined and every domain consists of a matrix phase and contains at least one precipitate phase. The microstructure of a domain has to be defined to provide the number of available nucleation sites (see chapter 3.2.1). This microstructure is defined by grain size, subgrain size, grain and subgrain elongation factors and the dislocation density. The matrix phase of the precipitation domain is the phase which usually has the highest phase fraction. This phase is the element pool over which the elements are exchanged between precipitates during kinetic reactions. In the simulations described in chapters 5.2.1 and 6.3 two domains are defined to describe the phase transformations of the matrix from austenite to martensite and back during an industrial heat treatment. The matrix phase of one precipitation domain is *fcc*, which has a higher solubility for most alloying elements and different diffusion coefficients than the second matrix phase, *bcc*. Combined with different dislocation densities and different grain sizes, the real microstructure of the complex power plant steel can be described accurately.

A precipitation domain should contain at least one precipitate phase. The number of precipitate phases is not limited. Also more phases of the same kind are possible, to distinguish $M_{23}C_6$ precipitation on grain boundaries and subgrain boundaries for example.

Every precipitate phase is defined by a set of parameters which is explained now:

- Number of size classes [m^{-3}]
This is a number $n \geq 1$. Usually, it is not necessary to consider more than 250 classes. n can be seen as the accuracy of the description of the precipitate distribution. The precipitates in the same class have the same radius R and composition X_i . Every class contains a certain number of precipitates N . The total number of precipitate changes during the kinetic reaction due to nucleation, dissolution and rearrangement of classes due to computational reasons.
- Strain energy [Jm^{-3}]
If a precipitate has a different molar volume than the matrix phase, a mechanical strain can be introduced. This energy contribution is considered by a volume related factor λ , the strain energy (see equ. 68).
- Interfacial energy [Jm^{-2}]
This is the value of the effective interfacial energy as used in the model (see equ. 68). This value can be estimated from thermodynamic databases, see chapters 3.3.1 and 4.3.
- Interface mobility [$\text{m}^4\text{s}^{-1}\text{J}^{-1}$]
The rate at which the precipitates grow can be controlled either by the rate at which atoms are supplied to the particle/matrix interface by diffusion or by the rate at which the atoms cross the interface [132]. The latter is depending on the interface mobility. All simulations done in the course of this work are diffusion controlled and therefore the interface mobility is set to a high value and thereby not a rate-limiting factor.
- Matrix diffusion enhancement *MDEF*
The ability of the atoms to move in the crystal structure of the phases by exchanging lattice positions is defined by the diffusion coefficients stored in the mobility database. Accelerated diffusion or short-circuit diffusion can occur on certain diffusion paths. Precipitates located on or in the vicinity of dislocations or grain boundaries can grow and dissolve faster due to the faster diffusion along these crystal imperfections. This effect is more noticeable at low temperatures and when the grain size is small and/or the dislocation density high. Gustafson and Hättestrand [48] point out that the microstructure can influence the diffusivity. Grain- and sub grain-boundaries act as high diffusion-paths and accelerate the kinetic reactions for precipitates located on these boundaries. Their investigations and simulations did not confirm higher coarsening rates due to increased diffusivities. However, this circumstance can be considered in the simulation by increasing the matrix-diffusion-enhancement-factor.
- Nucleation site(s)
Every precipitate phase needs at least one nucleation site if nucleation should be possible. Nucleation can be prevented artificially when no nucleation site is defined to analyse pure growth or dissolution for example. The available nucleation sites and their properties are described in chapter 3.2.1.
- Inactive radius factor *IRF*
A diffusion field is developed around each growing precipitate with a composition gradient towards the surface (see Fig. 25 a) in chapter 4.1.2). Inside such a diffusion field, nucleation is retarded due to lowered driving forces. This fact is accounted for by establishing a spherical volume around each precipitate and disabling nucleation inside this sphere. The radius of this sphere is the radius of the precipitate in the cen-

tre multiplied with the inactive radius factor. Values between 1 and 5 are reasonable, higher values are possible.

- Diffusivity in precipitate *IPDCF*

The diffusion coefficients are usually not known for the precipitate phases. It is assumed that diffusion is slower in the precipitate due to a more perfect lattice with fewer vacancies and different atomic bonding. To capture the temperature dependence of the diffusion coefficient the diffusivity inside the precipitates is argued to be the same as in the matrix phase (mobility database) but multiplied with a factor. This factor is set to values between 10^{-6} and 1. In our simulations, a value of 0,025 was chosen.

4.2.2 Precipitate nucleation

In the computer simulation of the evolution of precipitates, time is discretised into small time steps [138]. To guarantee numerical stability, the length of these steps is limited by maximum step length of certain parameters like the radius change of a precipitate or the change of the driving force. The flow chart of *MatCalc* is depicted in Fig. 30. After initializing the system where all precipitate phases and the precipitation domain are set-up, the simulation can start and the first time step is calculated. In each of the steps, it is checked if nucleation occurs. The number of newly formed precipitates is evaluated from classical nucleation theory (see chapter 4.1.1), which has been adapted to apply to multi-component systems.

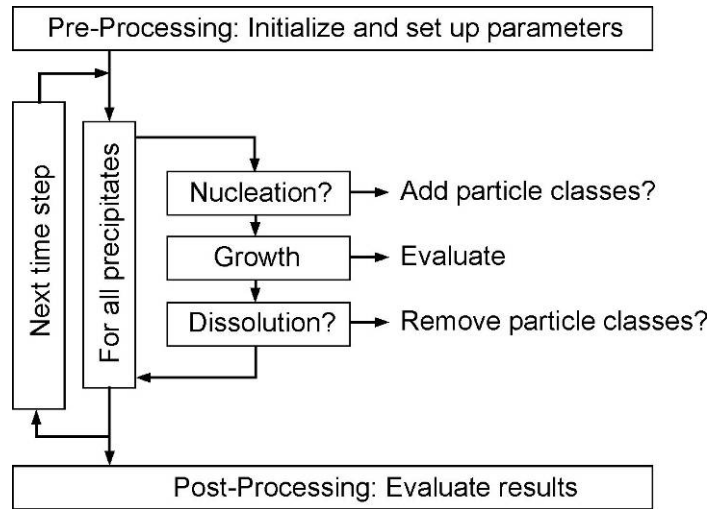


Fig. 30: Flow chart of *MatCalc* precipitation simulation.

If new precipitates form, the number ΔN of these precipitates is calculated from

$$\Delta N = J \cdot \Delta t \quad (63)$$

with J being the nucleation rate given by

$$J = J_s \exp\left(-\frac{\tau}{t}\right) \quad (64)$$

J_s is the steady state nucleation rate according to the *Becker-Döring* theory and τ is the incubation time to form a critical nucleus. J_s and τ are given by [139]

$$J_s = Z\beta^* N \exp\left(-\frac{G^*}{kT}\right) \quad (65)$$

and

$$\tau = \frac{1}{2\beta^* Z^2} \quad (66)$$

Z is the *Zeldovich*-factor, N is the number of nucleation sites, G^* the critical energy for nucleation, k is the Boltzmann constant and T the absolute temperature. The atomic attachment ratio β^* can be calculated from [135]:

$$\beta^* = \frac{r^*}{4\pi V^2} \left(\sum_{i=1}^n \frac{(c_i^P - c_i^M)^2}{c_i^M D_i} \right) \quad (67)$$

r^* is the critical radius, A is the surface area of the nucleus, V is the molar volume of the substitutional components. n is the number of elements in the precipitate, c_i^P and c_i^M are the concentrations of element i in the precipitate and matrix, respectively. D_i is the corresponding diffusion coefficient.

4.2.3 Precipitate growth

As soon as a nucleus has reached a radius larger than r^* , the evolution of its radius and composition can be calculated based on the new model described in chapter 4.2.2 [135]. Consider an n -component system with an arbitrary number m of spherical precipitates of different size, composition and phase type. The total *Gibbs* free energy G of this system can be written as

$$G = \sum_{i=1}^n N_{0i} \mu_{0i} + \sum_{k=1}^m \frac{4\pi\rho_k^3}{3} \left(\lambda_k + \sum_{i=1}^n c_{ki} \mu_{ki} \right) + \sum_{k=1}^m 4\pi\rho_k^2 \gamma_k \quad (68)$$

N_{0i} is the number of moles of component i in the matrix phase, μ_{0i} the corresponding chemical potentials, λ_k the elastic strain energy due to lattice misfit, ρ_k the radius of precipitate k , c_{ki} the concentration of component i in the precipitate k , μ_{ki} the corresponding chemical potentials and γ_k the interfacial energy. The first term on the right side is the sum of the chemical potentials of all atoms in the matrix. The middle term is the precipitate volume related part of the *Gibbs* energy. The right term takes the interface between precipitate and matrix into account.

During a precipitation reaction, the excess *Gibbs* free energy stored in the system is lowered until equilibrium is reached. Three dissipative processes Q , are considered in the *SFFK* model:

- Q1: Migration of interfaces characterized by their mobilities M_k
- Q2: Diffusion of all components in the precipitates
- Q3: Diffusion of all components in the matrix

with

$$Q_1 = \sum_{k=1}^m \frac{4\pi\rho_k^2 \dot{\rho}_k^2}{M_k} \quad (69)$$

$$Q_2 = \sum_{k=1}^m \sum_{i=1}^n \frac{4\pi RT \rho_k^5 \dot{c}_{ki}^2}{45c_{ki} D_{ki}} \quad (70)$$

$$Q_3 = \sum_{k=1}^m \sum_{i=1}^n \frac{4\pi RT \rho_k^3 (\dot{\rho}_k (c_{ki} - c_{0i}) + \rho_k \dot{c}_{ki} / 3)^2}{c_{0i} D_{0i}} \quad (71)$$

The maximization of the *Gibbs* free energy dissipation rate \dot{G} predicted by the *Onsager* thermodynamic extremal principle is given by [140]:

$$\dot{G} + Q_1 + Q_2 + Q_3 = 0 \quad (72)$$

$$\frac{\partial G}{\partial \rho_k} + \frac{1}{2} \frac{\partial Q}{\partial \dot{\rho}_k} = 0 \quad (73)$$

$$\frac{\partial G}{\partial c_{ki}} + \frac{1}{2} \frac{\partial Q}{\partial \dot{c}_{ki}} + \sum_{j=1}^{p_k} \nu_{kj} a_{kij} = 0 \quad (74)$$

A decoupled system of linear equations for each precipitate is obtained, which describes the change of its radius and its composition according to:

$$\sum_{j=1}^{n+1+p_k} A_{ij} y_j = B_i \quad (75)$$

For further details on the model and the coefficients of the matrices A_{ij} and B_i are described in refs. [135] and [140]. The variables y_j denote the rates $y_i \equiv \dot{c}_{ki}$ ($i=1, \dots, n$), $y_{n+1} \equiv \dot{\rho}_k$ and the Lagrange multipliers $y_{n+1+j} \equiv \nu_{kj}$ ($j=1, \dots, p_k$). The latter are related to stoichiometric constraints of the precipitates.

The evolution of all precipitates in the system with time is obtained from numerically integrating the set of equations 75. The mathematical formulation of this new model allows simulating even complex precipitation reactions such as precipitation sequences with meta-stable phases, which is demonstrated in following chapters (5.1.3, 5.2.1, 5.2.2 and 6.3).

4.2.4 Example of a precipitate kinetic simulation.

Fig. 31 shows the results of an ageing simulation of a simple model system containing Fe, 0,1wt% C and 0,1wt% Mo. The matrix phase is Ferrite, the precipitate phase is cementite nucleating on dislocations. The dislocation density is chosen to be $1 \cdot 10^{10} \text{m}^{-2}$. The number of precipitate classes considered is 100 and the interfacial energy is assumed to be 18Jm^{-2} . When the 600°C isothermal ageing starts the supersaturated matrix contains no precipitates.

The diagrams in Fig. 31 a) beginning with the top are: Cementite phase fraction f , mean radius R and critical radius R_{crit} , total number of precipitates N and nucleation rate J , Carbon content in the matrix C_{Matrix} and the number of available nucleation sites N_{ns} . At certain simulation times, named state 1 to 6, the precipitation distributions are displayed in the figures b) to f) and g), respectively.

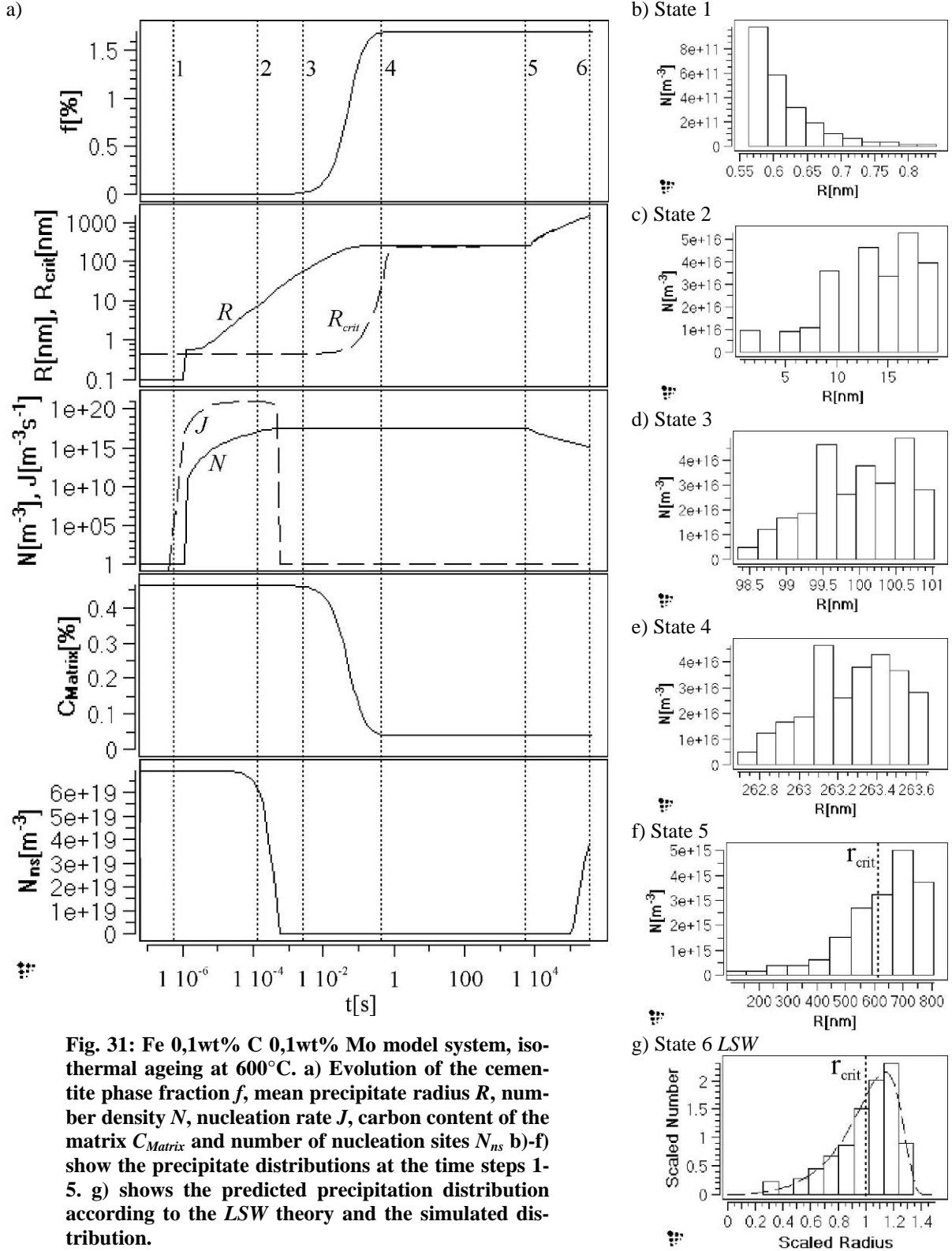


Fig. 31: Fe 0,1wt% C 0,1wt% Mo model system, isothermal ageing at 600°C. a) Evolution of the cementite phase fraction f , mean precipitate radius R , number density N , nucleation rate J , carbon content of the matrix C_{Matrix} and number of nucleation sites N_{ns} b)-f) show the precipitate distributions at the time steps 1-5. g) shows the predicted precipitation distribution according to the LSW theory and the simulated distribution.

After the incubation time is reached nucleation starts and the nucleation rate J raises rapidly. While J has a strong positive gradient the mean radius stays low due to the constantly formed precipitates with a radius of about 0,55nm (R_0). Therefore the precipitation distribution is left shifted as shown in Fig. 31 b), because at every time step more stable nuclei are formed.

The growth is characterised by the highest rate of the mean radius and a considerable difference between the mean radius and the critical radius. Furthermore the number density rises when growth is overlapping with nucleation or stays constant during pure growth. Due to the flux of elements from the matrix to the precipitates the supersaturation decreases significantly (C_{Matrix}), as a consequence ΔG^* rises according to equation 54 and 55. J reaches its maximum, the steady state nucleation rate level (state 2). J drops to zero and N stays constant, until coarsening starts, when the nucleation sites are saturated ($N_{NS}=0$). When pure growth is dominating the kinetic reaction R shows a gradient of 0,5 in the double logarithmic scale as predicted by the parabolic growth law for spherical precipitates [141] (state 3). As can be seen in Fig. 31 d) the precipitation distribution corresponding to this state is symmetric or even slightly right shifted and in total shifted to larger radii. At the end of the growth regime the supersaturation and the growth rate drop. Parallel the critical radius converges to the mean radius.

The phase fraction has then reached the equilibrium value which stays almost constant in the further process. Between growth and coarsening the kinetic reaction is in a transient stage. This stage is characterized by no change of f , R , and N but a rearrangement of the precipitate distribution. When the matrix is depleted from carbon and molybdenum the system energy can only further be lowered by dissipating excess surface energy. Every precipitate class with a radius below R_{crit} dissolves and feeds back elements into the matrix. The precipitate classes larger than R_{crit} grow by picking up the solute atoms from the small precipitates. Thereby the precipitate distribution is reorganized and gains a *LSW* shape (state 5, Fig. 31 f)).

During interfacial energy driven coarsening precipitates are actually dissolved and N is lowered. Parallel the mean radius R rises as described in equation 47. The precipitate distribution is shifted to larger radii but the shape stays constant as visualized in Fig. 31 g) and Fig. 28. There are nucleation sites available again $N_{NS}>0$ but there is not enough driving force for nucleation because of new precipitates.

4.3 Calculation of interfacial energy γ

The nearest neighbour, broken-bond approach introduced in chapter 3.3.1 is adapted and utilized in *MatCalc* to predict the chemical interfacial energy of precipitate phases in alloys. Becker [73] showed that the total enthalpy of a crystal, satisfying certain requirements, is the sum of all bond-energies in the crystal. Furthermore he explained that during the precipitation processes in a matrix bonds are broken and new bonds are established. This leads to a difference in the system enthalpy before and after kinetic reactions. Turnbull [74] generalized this approach and calculated the interfacial energy by means of the system enthalpy difference as shown in equation 38 (see chapter 3.3.1).

$$\gamma_c^0 = \frac{N_s \cdot z^* \cdot \Delta E^0}{N_A \cdot z_l} \quad (76)$$

N_s is the number of atoms per unit area on the surface of the precipitate, z^* is the number of crossbonds per surface-atom across the interface. ΔE^0 is the enthalpy of mixing for one mole of atoms. N_A is Avogadro's number and z_l is the number of nearest neighbours

in the precipitate. γ_c^0 is a mean value, because N_s , z^* and z_l may differ locally, depending on the orientation of the two adjoined crystal systems.

The precipitates considered in the kinetic simulations described in this work have mostly *fcc* structure. Therefore the number of nearest neighbours z_l of atoms on the corner of the *fcc* unit cell (Fig. 32) is derived: Every $1/8$ of an atom at the corner is connected to $3^{1/2}$ atoms. Therefore 1 atom is connected with 12 neighbours. Similar considerations reveal that the maximum number of nearest neighbours (coordination number) of an atom at the surface (z_s) is 9 for the [111] surface. This number may vary, depending on the orientation of the surface. The number of crossbonds $z^* = z_l - z_s$.

Tab. 4: Parameter for the calculation of the interfacial energy with the nearest neighbour, broken-bond method, considering a precipitate with *fcc* structure.

z_s [100]	8	nearest neighbours of an atom on a [100] surface
z_s [110]	7	nearest neighbours of an atom on a [110] surface
z_s [111]	9	nearest neighbours of an atom on a [111] surface
z_l	12	nearest neighbours in the precipitate bulk
z^* [100]	4	crossbonds across the [100] surface
z^* [110]	5	crossbonds across the [110] surface
z^* [111]	3	crossbonds across the [111] surface



Fig. 32: An *fcc* unit cell in the bulk.

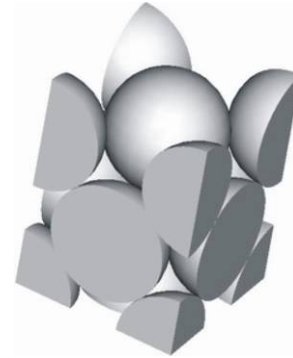


Fig. 33: An *fcc* unit cell with a surface on the [100] face.

MatCalc utilizes the atomic volume of the precipitate phase is to calculate the number of atoms on the surface N_s . The atomic volume $VPAU$ is available through the thermodynamic database. Only substitutional elements are considered with $VPAU$, interstitial elements are deliberately neglected, because they do not provide crossbonds.

$$N_s = \frac{1}{VPAU^{\frac{2}{3}}} \quad (77)$$

The difference of the system enthalpy (enthalpy of mixing) ΔE^0 is derived with *MatCalc*:

$$\Delta E^0 = \frac{\partial H_m}{\partial f} \quad (78)$$

Where H_m is the system enthalpy when the precipitate phase has a certain phase fraction f . The establishment of an interface is related to the rise of phase fraction. Therefore, the

correct enthalpy difference is the partial derivative of the system enthalpy with respect to the phase fraction. The complete equation to obtain the interfacial energy of a certain phase in a multi component multi phase system is given in equation 79. The other parameters for a precipitate with *fcc* structure are given in Tab. 4. It is assumed that no atom on the precipitate surface (fully coherent interface) has a broken bond, otherwise z^* would be lower than 3.

$$\gamma = \frac{z^*}{VPAU^{\frac{2}{3}} \cdot N_A \cdot z_l} \cdot \frac{\partial H_m}{\partial f} \quad (79)$$

The lowest value of 3 was chosen for z^* , arising from microstructural considerations. This is reasonable although not all interfaces have a [111] orientation and therefore have higher z^* values. On the other hand not all possible crossbonds are linked in real microstructures due to incoherency effects at the precipitate/matrix interface.

If a precipitate is located on a boundary or a dislocation line, the total interfacial energy of the system is increased by the precipitate on one hand and reduced by the loss of boundary area on the other hand. This fact is considered by introducing the „specific boundary interfacial energy” (*SBIE*). The situation is illustrated in Fig. 34. During growth of a precipitate located on a boundary the grain boundary area is reduced by an area equivalent to the circle A. Thus the energy balance for the shared grain boundary area demands a reduction of the interfacial energy of the precipitate by the product of A and *SBIE*. The same considerations go for the dislocation line.

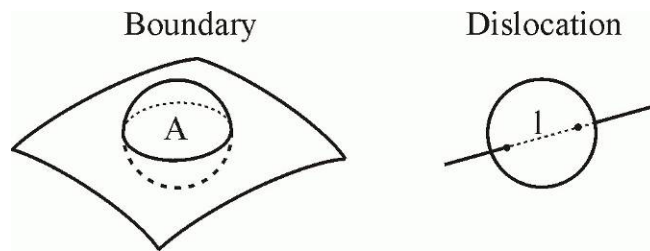


Fig. 34: Sketch of a precipitate located on a grain or subgrain boundary (left) and a precipitate located on a dislocation line (right). The energy equivalent to area A and length *l* respectively have to be considered when calculating the interfacial energies of precipitates.

4.3.1 Model systems

The results of the interfacial energy prediction over temperature of two binary model systems are presented, first a simple Fe-Cu alloy is shown. The considered phases are α -iron (*bcc*-structure) as the matrix phase and Cu-solid (*fcc*-structure) as the precipitate phase. Fig. 35 shows the phase fraction of the Cu phase as obtained by the temperature step calculation from 400°C to 900°C and the corresponding interfacial energy values.

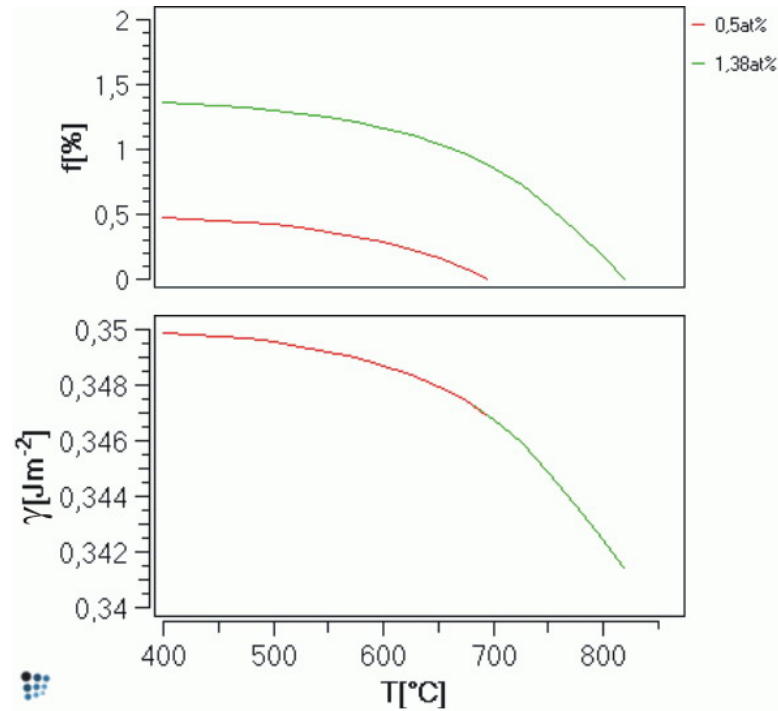


Fig. 35: Interfacial energy calculated with *MatCalc* for two different Cu fractions in a Fe-Cu alloy, utilizing the *SSOL 4* thermodynamic database.

Variations in composition show no influence on the interfacial energy in the Fe-Cu system, which can be seen in Fig. 35. Kampmann and Wagner [142] studied and simulated the isothermal Cu precipitation in a α -Fe matrix containing 1,38at% Cu at 500°C. They report that Cu precipitates change their crystal structure from *bcc* to *fcc* depending on their size. According to them, the interfacial energy of $0,27\text{Jm}^{-2}$ is reasonable when the precipitates are small with a *bcc* structure and a coherent interface between matrix and precipitate exists. When these precipitates grow and change to an *fcc* structure they enrich with Cu. From this instant on the interface is incoherent and the interfacial energy is reported to be $0,5\text{Jm}^{-2}$. In the available thermodynamic databases the Cu phase always has an *fcc* structure.

Li and co-workers [126] provide values for the interfacial energy of γ' precipitates in Ni-Al binary alloys. They report that the value of the interfacial energy for a Ni 12,5at% Al binary alloy is between $20 \cdot 10^{-3}$ and $24 \cdot 10^{-3}\text{Jm}^{-2}$. The calculation illustrated in Fig. 36 confirms this finding very well. It can also be seen that the interfacial energy of this Ni-Al alloy only weakly depends on the temperature and hence the phase fraction.

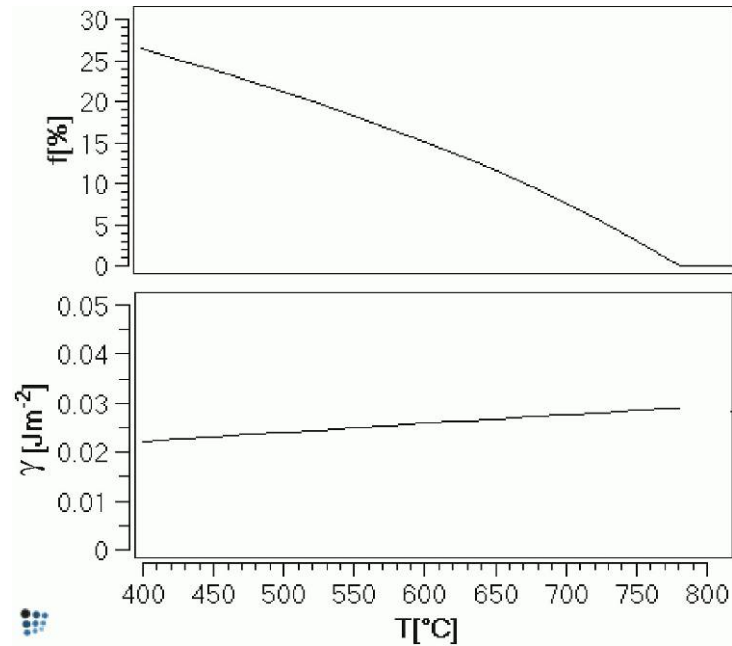


Fig. 36: A Ni-Al system with γ as precipitation phase in *fcc*. The γ values are calculated with *MatCalc* for 12,5 at% Al, utilizing the *Ni-Data* version 30 thermodynamic database.

4.3.2 Complex systems

Li et al. [126] investigated the coarsening of γ precipitates in industrial Ni-base alloys (*NIMONIC*, *INCONEL*, *UDIMET*). They also calculated the interfacial energies of these alloys. Fig. 37 shows the results of the calculated interfacial energy of γ in an *fcc* matrix of *NIMONIC 115* compared to the data presented by Li and co-workers. The parallel shift originates from a difference in the thermodynamic database used for the calculations. In the present work the *Ni-data* thermodynamic database version 30 was utilized.

Fig. 38 shows the values of the calculated interfacial energies of the stable phases of the steel *CB8* and the phase fraction diagram. The equilibrium calculation of this alloy is discussed in detail in chapter 6.2. The highest values are predicted for the boride M_3B_2 . Both MX phases, VN and NbC, as well as the AlN show quite similar values, the Laves phase has the lowest interfacial energy according to this calculation. The influence of the two different matrix phases can be seen very clearly. The carbides and nitrides have much lower values when they exist in an austenitic matrix phase, the M_3B_2 boride shows a little elevated values. The interfacial energy seems to drop slightly with rising temperature except for the BN and VN at elevated temperatures.

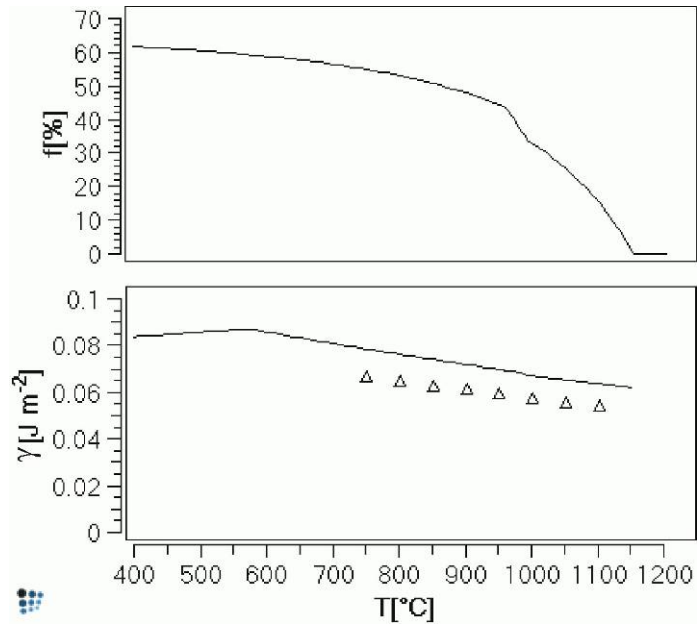


Fig. 37: Comparison of calculated interfacial energies of γ precipitates in the *fcc* matrix of *NIMONIC 115*. The triangles are published data by Li et al. [126].

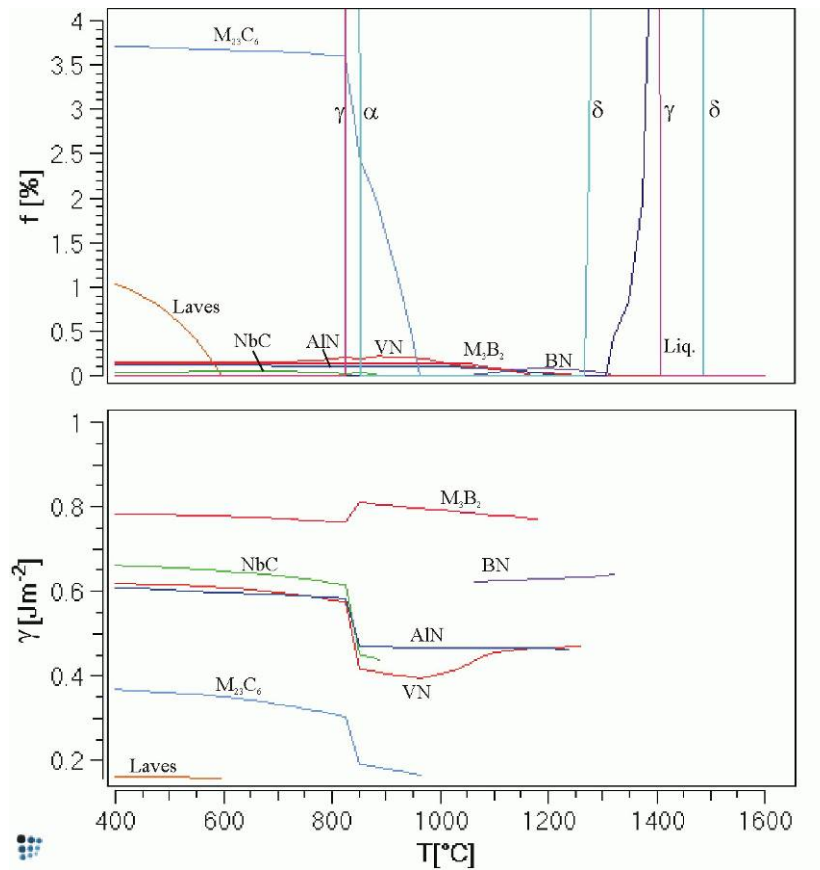


Fig. 38: Detail of the phase fraction diagram of the steel *CB8 heat 173* and the corresponding predicted specific chemical interfacial energies of the precipitates. Calculated utilizing *Fe-Data* [153] thermodynamic database.

5 Introductory simulations

In order to gain knowledge about the capability and possible weakness of the kinetic model introduced in chapter 4.2 when applying for kinetic simulations of highly complex alloys and heat treatments preliminary simulations are analysed and compared with published data. Beginning with the discussion of isothermal simulations of binary model systems finally the simulations of the thermal history of modern 9-12% Cr steels are presented in chapter 5.2 and 6.3.

5.1 Isothermal simulations

5.1.1 Fe-C system

Wepner [143] characterized the strain ageing effect of different binary Fe-C alloys. The specimens were annealed at different temperatures and the carbon precipitation measured by damping experiments.

Specimens of pure iron with up to 0,02%C and varying strain deformation up to 5% were thermally aged at temperatures between 38°C and 80°C. Wepner's investigations show that the precipitation of carbon in his specimens is based on two different effects that complement each other. The first mechanism is formation of *Cottrell atmospheres* around dislocations, the other mechanism is precipitation of cementite particles [144]. Cottrell and Bilby [145] studied the attachment of atoms on dislocations. During ageing the carbon atoms first move to the dislocations and form the *Cottrell cloud*. The higher the strain level and hence the dislocation density, the more dominating is the formation of the *Cottrell atmosphere*. Harper [146] extended their theory and provided equation 80 to calculate the fraction of carbon enriched in the vicinity of the dislocations.

$$q(t) = 1 - \exp \left[-2 \cdot L \cdot \left(\frac{\pi}{2} \right)^{1/3} \cdot \left(\frac{A \cdot D}{k \cdot T} \cdot t \right)^{2/3} \right] \quad (80)$$

L is the dislocation density, D the diffusion coefficient, k is the *Boltzmann* constant and T the absolute temperature. A is the interaction energy between dislocations and an atom, which is set to $3 \cdot 10^{-20}$ Jm according to reference [145].

Tab. 5: Simulation parameters for the precipitation kinetics simulation and for Harper's equation.

Cementite precipitation	C [wt%]	T [°C]	L [m ⁻²]	γ [Jm ⁻²] (calculated)
0% strain	0,015	38	$6 \cdot 10^{11}$	0,182
	0,016	80	$1,5 \cdot 10^{11}$	0,179
Harper, strain ageing	C [wt%]	T [°C]	L [m ⁻²]	f_{Equil} [%]
4,9% strained	0,015	38	$1 \cdot 10^{15}$	0,2788
4% strained	0,016	80	$9 \cdot 10^{14}$	0,2974

The combined kinetics of *Cottrell atmosphere* formation and cementite precipitation was analysed in detail for example by Kozeschnik [24]. From this results it was concluded that the published phase fraction data of two 0% strain specimens annealed at 38°C and 80°C respectively could be chosen for precipitation simulation. In the case of

0% strain the influence of the *Cottrell atmosphere* establishment is negligibly small, most of the precipitated carbon therefore forms carbides which can be predicted by the model implemented in *MatCalc*. The precipitation simulation presented earlier in [24] had been performed on the basis of the classical parabolic growth law. The kinetic simulation considered α -ferrite as matrix phase and cementite precipitates, which nucleate on dislocations. Wepner also provided data that correlate the applied strain and the dislocation density, based on various authors and measurement methods. The dislocation density was calculated and extrapolated.

$$f(t) = \left\{ 1 - \exp \left[- 2 \cdot L \cdot \left(\frac{\pi}{2} \right)^{1/3} \cdot \left(\frac{A \cdot N_A \cdot D}{R \cdot T} \cdot t \right)^{2/3} \right] \right\} \cdot f_{Equil} \quad (81)$$

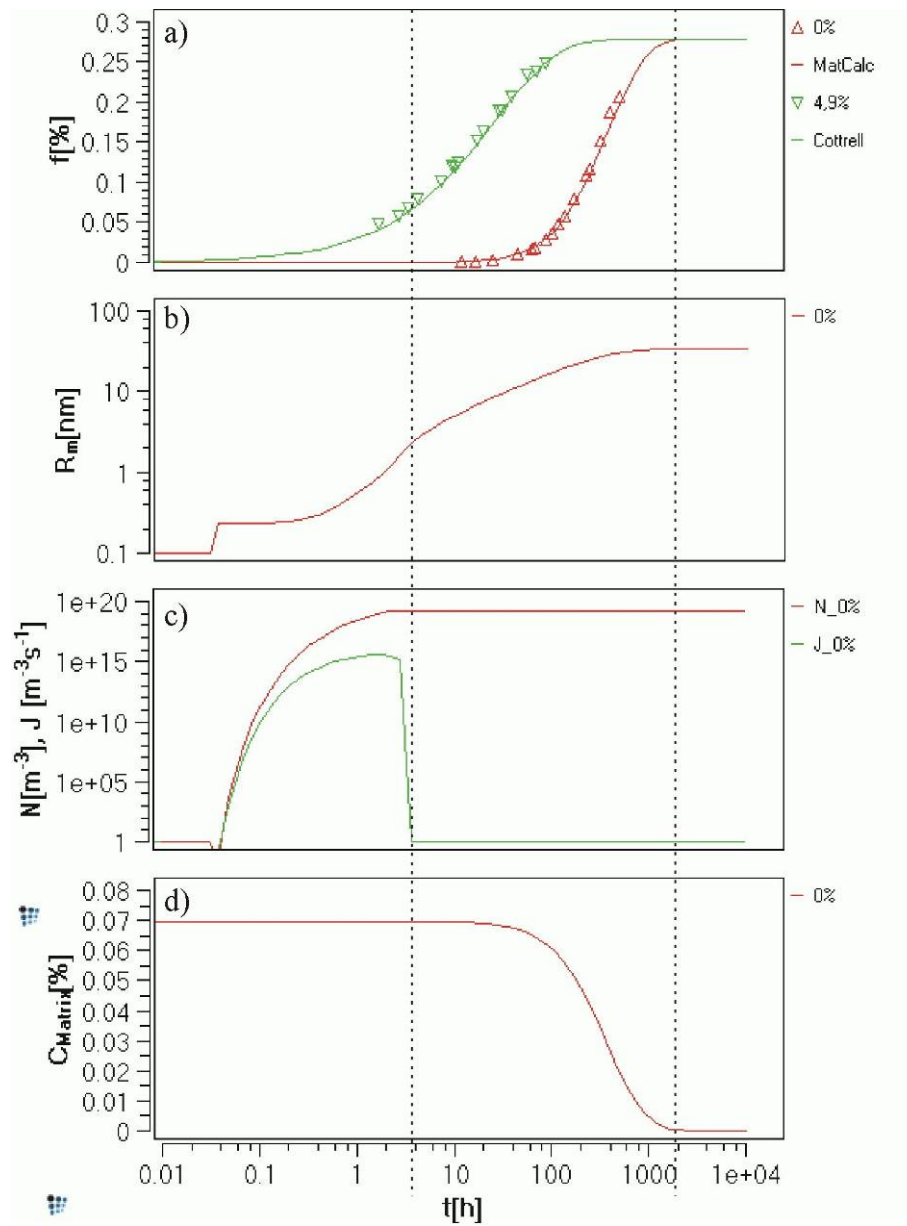


Fig. 39: a) Evolution of the phase fraction and published data points of the 38°C / 0% strain specimen. Predicted carbon precipitation due to strain ageing effect (Cottrell, 4,9% strain). b)-d) The mean radius R_m , the nucleation rate J and number density N and the C content of the matrix evolution of the cementite precipitates.

To predict the strain ageing effect too, equation 80 was adapted. Mainly the values are rescaled to the calculated equilibrium phase fraction of cementite as shown in equation 81.

The simulation parameters for both calculations are given in Tab. 5, the results for the 38°C simulation are given in Fig. 39. The nucleation starts at about 90s absolute simulation time, the nucleation rate J rises and reaches a maximum at about 2200s. Parallel the number density N rises, the maximum of formed precipitates is reached when the nucleation rate drops to zero, as can be seen in Fig. 39 c). The nucleation is terminated when all available nucleation sites are occupied. Physically a depleted zone is formed in the vicinity of each precipitate, which prevents nucleation. This is taken into account by prohibiting nucleation within a volume around each precipitate with a certain diameter (Inactive radius factor IRF , see chapter 4.2) In this case this diameter was set 30 times larger than the precipitate radius. All nucleation sites are saturated and no new precipitate can be formed after 4300s. Fig. 39 b) shows the evolution of the mean precipitate radius. The existing cementite precipitates grow immediately, first overlapped by nucleation.

During growth the carbon is depleted from the matrix to a fraction of $1,4 \cdot 10^{-12}\%$ (Fig. 39 d)). Growth stops at about 1900h absolute simulation time and the equilibrium phase fraction of cementite for 38°C is reached. The growth rate without overlapping nucleation satisfies the parabolic growth law (equ. 59 in chapter 4.1.2). During growth the phase fraction rises and fits excellent to the published data points as can be seen in Fig. 39 a). Similar explanations are valid for the 80°C simulations presented in Fig. 40.

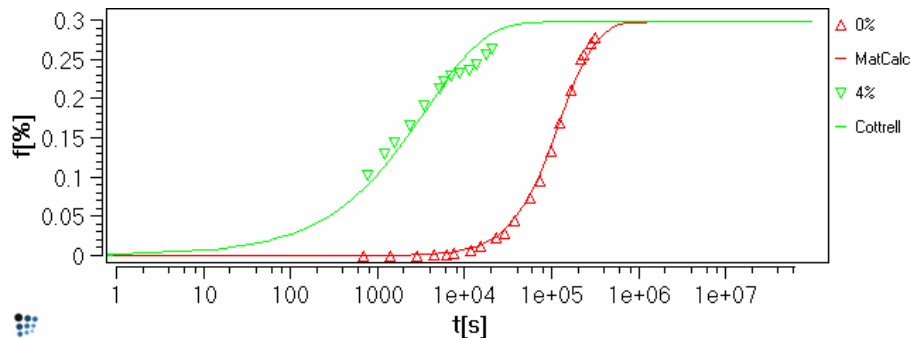


Fig. 40: shows the phase fraction evolution of the simulated 80°C / 0% strain specimen and the calculated phase fraction for the 4% strain specimen predicted by *Harper's equation*.

5.1.2 Fe-Cu system

The *Ostwald* ripening of spherical and rod-shaped Cu precipitates in an 1,5wt% Cu alloy aged between 600 and 750°C was examined by Monzen et al. [147]. They measured the precipitate size and the Cu concentration in the matrix. A precipitation kinetic simulation was performed at 650°C and 700°C and the results are compared with the published data.

The authors exactly describe the heat treatment they used to produce specimens with a defined precipitate distribution. The specimens were first solution heat treated and quenched in water. Then they aged the material at 650°C for 6h to precipitate Cu particles. Afterwards the material was rolled to 90% reduction and annealed at 750°C which caused a complete recrystallisation. In this condition the specimens contained spherical Cu precipitates with an average radius of 14nm. Then annealing was performed for up

to 300h at different temperatures to coarsen the initial precipitates. The hot rolled specimens developed spherical precipitates, in specimens that were aged without the previous rolling produce they were rod shaped. Only data of rolled specimens were simulated.

The *SSOL* Version *M* thermodynamic database was utilized for the simulation. In this database the Cu precipitate have an *fcc* structure and consist of 100% Cu. It has to be mentioned, that Cu precipitates in an iron matrix undergo a phase transformation when they reach a certain size. The large Cu precipitates have an *fcc* structure and consist of nearly 100% Cu, this condition is described by the used database.

Othens and co-workers [148] utilize high-resolution electron microscopy to investigate Cu-precipitates in α -Fe. They report that these precipitates change the crystal structure depending on the size. Precipitates with radii smaller than 2nm are coherent and have the *bcc* structure of Ferrite. Precipitates with radii between 2 and 9nm possess a twinned 9R structure and Cu particles larger than 9nm radius have a distorted *fcc* structure which continually changes to the *fcc* crystal structure of pure copper with rising radius.

Kampmann and Wagner [142] assumed this same phase transformation and have inferred on the basis of thermodynamic analysis, that Cu precipitate nucleate with a *bcc* configuration and a Cu-Fe mixed composition. They argue that precipitates with a radius of less than 0,3nm and a Cu-Fe composition show a lower nucleation barrier ΔG^* and therefore nucleate first. During growth a phase transformation of the Cu precipitates takes place to an *fcc* structure and a parallel enrichment with Cu. They observed highly Cu enriched particles with a radius larger than 0,5nm in a Fe 1,38at% Cu alloy after ageing at 500°C for 0,5h, this was proven with *SANS* investigations.

The data by Monzen et al. [147] chosen for simulation shows precipitates in the growth and coarsening regime with sizes larger than 14nm but there are no data available showing the early stages of the kinetic reaction. The first stable precipitate during simulation has a radius of 0,43nm. According to Kampmann and Wagner the structure of precipitates of this size is *bcc*. Hence a proposed phase transformation during early stages of the Cu precipitates (*fcc* structure, $X_{Cu}=1$) can not be considered. Fig. 41 shows the results of two versions of the kinetic simulation for the 650°C ageing data.

The data with index „1” show the results of simulation where the ageing treatment starts with a heating to the ageing temperature as it happens in reality when the specimens are put into the furnace. The heating rate was set to 3000K h^{-1} . Data set „2” directly starts with the aging simulation, assuming an instant heating to 650°C. The simulation „1” with heating up to the ageing temperature is explained first: The nucleation rate starts to rise when the temperature reaches about 582°C, the driving force for nucleation *DFM* has a value of about 13kJ at this point. It can be seen, that *DFM* drops with the rising temperature. According the *DFM* evolution, *J* 1 rises to a maximum at about 628°C, but due to the still rising temperature *J* 1 drops again.

When the ageing temperature is reached, indicated by the dotted line, the driving force reaches a value of about 9,5kJ and stays constant until the Cu content of the matrix begins to drop noticeable due to the growing precipitates. Nucleation stops (*J* = 0) when *DFM* has a value of about 5,7kJ, the maximum number of precipitate is reached, *N* 1 stays constant until coarsening begins. Meanwhile the radius and the phase fraction increased. The latter influences the value of the interfacial energy γ which increases slightly with *f*.

As can be seen the evolution of the mean radius is in good agreement with the experimental data points. To achieve this, the value of the interfacial energy was somewhat reduced to 98% of the calculated value. Although Monzen et al. [147] performed those experiments to investigate the coarsening behaviour of the precipitates; the calculation

in contrast shows that coarsening sets in significantly later and the measurements have been performed in the late growth stage and the transient region. Per definition coarsening starts when the critical radius R_c enters the precipitation distribution and smaller precipitates begin to dissolve (see Fig. 41).

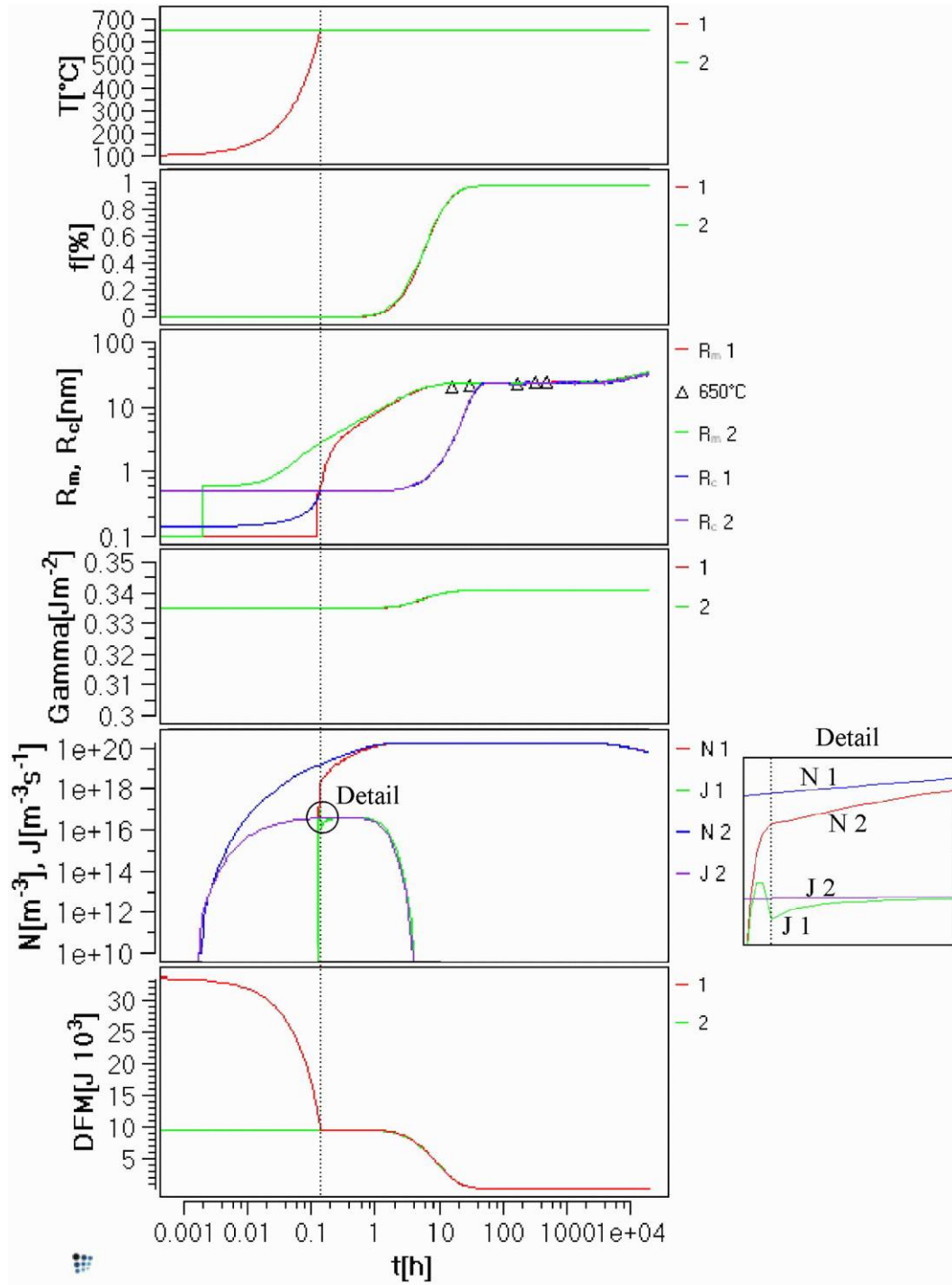


Fig. 41: The results of the precipitation kinetic simulation of Cu precipitates in Fe at 650°C. Beginning on the top: The temperature evolution, the phase fraction f , the mean radius R_m and the critical radius R_c , the calculated interfacial energy γ , the nucleation rate J and number of precipitates N , the driving force for nucleation DFM . The dotted line marks the end of the heating stage for dataset „1”.

Equation 82 describes the mean radius evolution over time, as discussed in chapter 4.1.

$$R^3(t) - R_0^3 = K_R^{LSW} \cdot t \quad (82)$$

The left side as well as the right side of this equation is shown in Fig. 42, where R_0 is set to 14nm as published by Monzen et al. The rate constant K_R^{LSW} for a multi-component, concentrated and ideal system [149] is given by:

$$K_R^{LSW} = \frac{8}{9} \cdot \frac{V_m^\beta \cdot \gamma}{\sum_{i=1}^c \left[\frac{(X_e^\beta - X_e^\alpha)^2}{X_e^\alpha \cdot D_\alpha \cdot \frac{1}{R \cdot T}} \right]} \quad (83)$$

V_m^β is the molar volume of the precipitate phase β , γ is the interfacial energy. X_e^β and X_e^α are the equilibrium concentrations of the elements i in the system, respectively. D_α is the chemical matrix diffusion coefficient of the element i , R and T have the usual meaning. This is the equation utilized in *MatCalc* to calculate the theoretical coarsening rate, the value in this case is $9,79 \cdot 10^{-31} \text{m}^3 \text{s}^{-1}$. As can be seen in Fig. 42, the simulated radius evolution ($R_m^3 - R_0^3$) asymptotically reaches the values of the theoretical coarsening ($K_R^{LSW} t$).

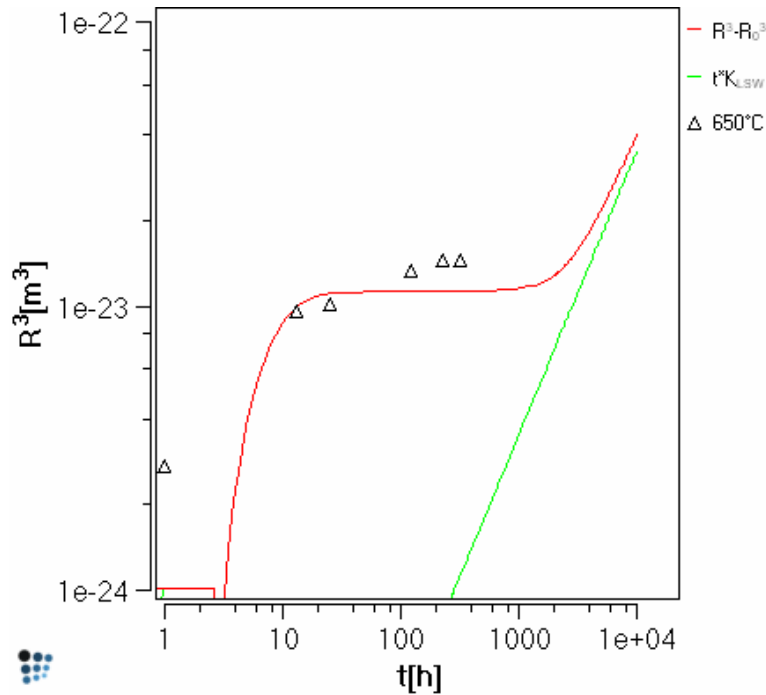


Fig. 42: This graph shows the cubed radius over time in double logarithmic scale. This is the usual way to illustrate the coarsening rate K_R^{LSW} .

5.1.3 Ageing simulation of two heat resistant Cr steels

The systems discussed in the previous chapters were binary and only consisted of two phases. Complex alloys, for example ferritic martensitic steels, contain many elements

and phases which typically undergo a series of solid-state phase transformations during fabrication. The mechanical properties as well as the creep resistance of these alloys are determined by the distribution of carbides and nitrides embedded in the martensitic matrix. During ageing of solution heat treated Cr steel, different carbides form and dissolve again in a precipitation sequence.

Robson and Bhadeshia [42] simulated the growth and dissolution of carbides (cementite, M_2X and $M_{23}C_6$) in complex Cr steels for power plant application at 600°C. They utilized an adapted *Johnson-Mehl-Avrami* approach to describe the rate at which phases precipitate during the isothermal ageing. They point out that it is essential to simulate the simultaneous kinetic reactions of all contributing precipitate phases as they are observed in a wide range of secondary hardening steels to understand the kinetic mechanisms and the influence of certain alloying elements and strategies.

Tab. 6: Composition of two heat resistant steels, in wt%.

	C	Cr	Mn	Mo	Ni	V	Fe
2¼% Cr 1% Mo	0,15	2,12	0,50	0,90	0,17	/	bal.
3% Cr 1,5% Mo	0,10	3,00	1,00	1,50	0,10	0,10	bal.

The same alloys as discussed in ref. [42] were simulated with *MatCalc* to investigate the kinetic model on precipitation sequences in complex multi component, multi phase, multi particle systems. Except for the chemical composition, all kinetic parameter (i.e. interfacial energies) were the same for all simulations to clarify the effect of the alloying elements and their balance. The composition of the two base-alloys is given in Tab. 6, the other parameter are shown in Tab. 7.

Tab. 7: Simulation parameter for both alloys.

	Matrix phase	Ferrite		
	Grain size [m]	100·10 ⁻⁶		
	Subgrainsize [m]	10·10 ⁻⁶		
	Dislocation density [m⁻²]	1·10 ¹⁴		
Kinetic parameter	M₂₃C₆	M₂X	Cementite	
Nucleation sites	Sub grain boundaries	dislocations	dislocations	
Number of nucleation sites [m ⁻³]	2,4 10 ²⁴	7,0 10 ²³	7,0 10 ²³	
γ [Jm ⁻²] used	0,21	0,19	0,12	
γ [Jm ⁻²] calculated	0,28-0,32	0,39-0,45	~0,16	

Robson and Bhadeshia used the number of nucleation sites and the interfacial energy as fit parameters to reproduce the published measurements from Klueh and Nasreldin [150] and Baker and Nutting [151], respectively. These investigations show a delayed formation of $M_{23}C_6$ in the 2¼% Cr steel and suppressed M_2X kinetics in the 3% Cr steel.

In this work the number of available nucleation sites was derived, as described in chapter 3.2.1. The other major parameter is the interfacial energy. Due to influences of grain boundaries and lattice misfits the effective interfacial energies can be smaller than the calculated values. During a parameter study these γ values were varied to obtain similar results as presented in ref. [42].

The simulations in this chapter start with an assumed supersaturated matrix containing no precipitates. From earlier calculations it is known that a heat treatment beginning with a quenching or a heating up to the actual simulation temperature shows different results, because the nucleation stage and the resulting precipitate distribution is strongly affected by the changing temperature during accelerated heating or quenching (see chapter 5.1.2). In the simulations discussed in this chapter cementite is dominant during the initial stages of the precipitation reaction. This phase develops to the coarsening stage before it is dissolved by the next carbide in the sequence. Effects originating from nucleation like a narrow precipitation distribution are vanished when coarsening is dominating. Therefore the instant start of the annealing at 600°C without heating up is accurate when only coarsening is analysed. The other carbides in the sequence (M_2X , $M_{23}C_6$) nucleate later anyway and would not be affected by the heating up process.

Heat treatment of 2¼% Cr steel

Despite the lowest driving force for nucleation cementite nucleates first with para-equilibrium composition, because of the shortest incubation time of about 1s in both alloys, see equation 56. This carbide already starts to coarsen before the other carbides occur in the precipitation sequence. Cementite is then partly dissolved during the formation of M_2X and later both carbides are dissolved due to $M_{23}C_6$ formation. The left column in Fig. 43 shows the results of the 2¼% Cr steel simulation compared to the results of the 3% Cr steel in the right column. In the top-row the phase fractions of the carbides with the published data by Robson and Bhadeshia are illustrated, the graphs below show the mean radii, the total number of precipitates and the driving forces for nucleation. The nucleation and growth stage of the cementite phase is not depicted in the graphs: The growth of cementite ends with a precipitate distribution with a mean radius of about 5nm radius and a total precipitate density of $4,5 \cdot 10^{22}m^{-3}$. Coarsening starts very early until at about 36s the M_2X phase nucleates which is the next phase in the sequence. M_2X shows the highest driving force for nucleation until about 4min and reaches a considerable phase fraction. This phase reaches the highest number of precipitates but they stay small in comparison to cementite and $M_{23}C_6$. The M_2X do not coarsen but are dissolved again by $M_{23}C_6$.

The M_2X carbides show a major composition change during the evolution which seems to be influenced by their own size and the concurrent $M_{23}C_6$ precipitation (Fig. 44, left column). Until the end of their growth stage they are Molybdenum rich which depletes the matrix of Mo. The graphs in Fig. 45 show the product of the phase fractions and element contents of the carbides to indicate where the alloying elements are dissolved. It can be seen that M_2X consumes up to 90% of the total Cr and 40% of the total Mo in the system.

After the M_2X phase fraction has reached the maximum of 2% and starts to dissolve the Mo is replaced with Cr. At about 7h the M_2X phase reaches the equilibrium composition predicted for 600°C of 47% Cr and 19% Mo. Shortly before the M_2X phase is dissolved again and the mean radius falls rapidly it enriches again with Mo.

The third and finally stable carbide in the sequence is $M_{23}C_6$. The nucleation of this Cr rich phase is first delayed by the concurrent formation of the M_2X . As described in the previous paragraph about 40% of the available Cr is consumed by this phase which can

be seen in Fig. 45 a). The driving force for nucleation of $M_{23}C_6$ is small due to the reduced amount of Cr and C available in the matrix, therefore the $M_{23}C_6$ kinetics is sluggish. First the M_2X carbide has to be dissolved to release the Cr and C before the phase fraction of $M_{23}C_6$ rises significantly. At the end of the simulation at 1000h the only remaining phase is the $M_{23}C_6$. The equilibrium composition for 600°C predicted by an equilibrium calculation is reached, as well as the equilibrium phase fraction. A prolonged simulation would show coarsening of the $M_{23}C_6$ precipitates.

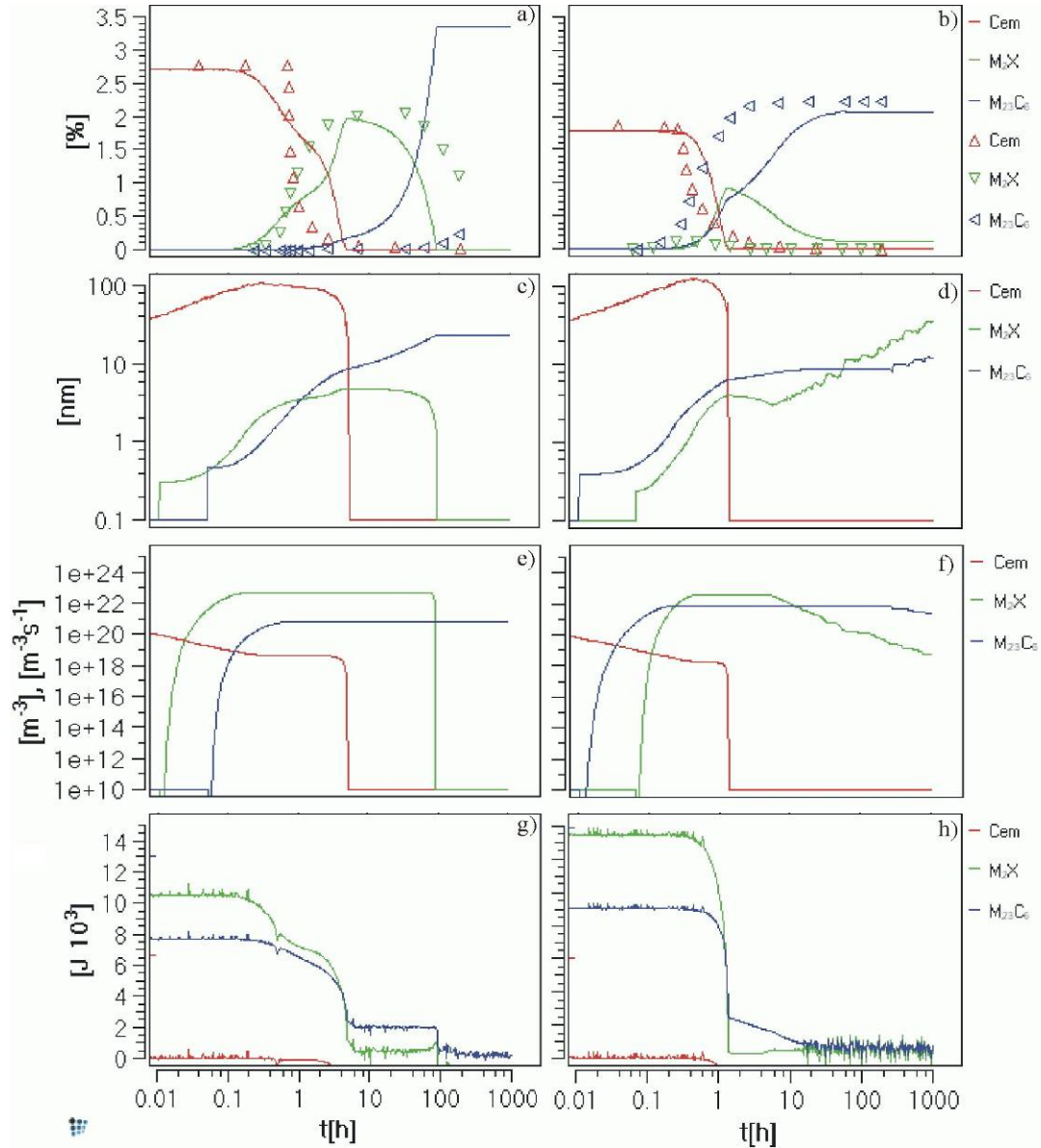


Fig. 43: The simulation results of both steels over time are shown. The left column depicts the 2 1/4% Cr steel, the right column the 3% Cr steel: a), b) are the phase fractions; c), d) are the mean radii; e), f) are the total precipitate numbers and g), h) are the driving forces for nucleation.

Fig. 45 g) shows that the element Ni is more or less dissolved in the matrix phase, as well as Mn. Cementite consists of Fe, nearly no excess alloying elements are dissolved in this carbide due to the para-equilibrium nucleation composition.

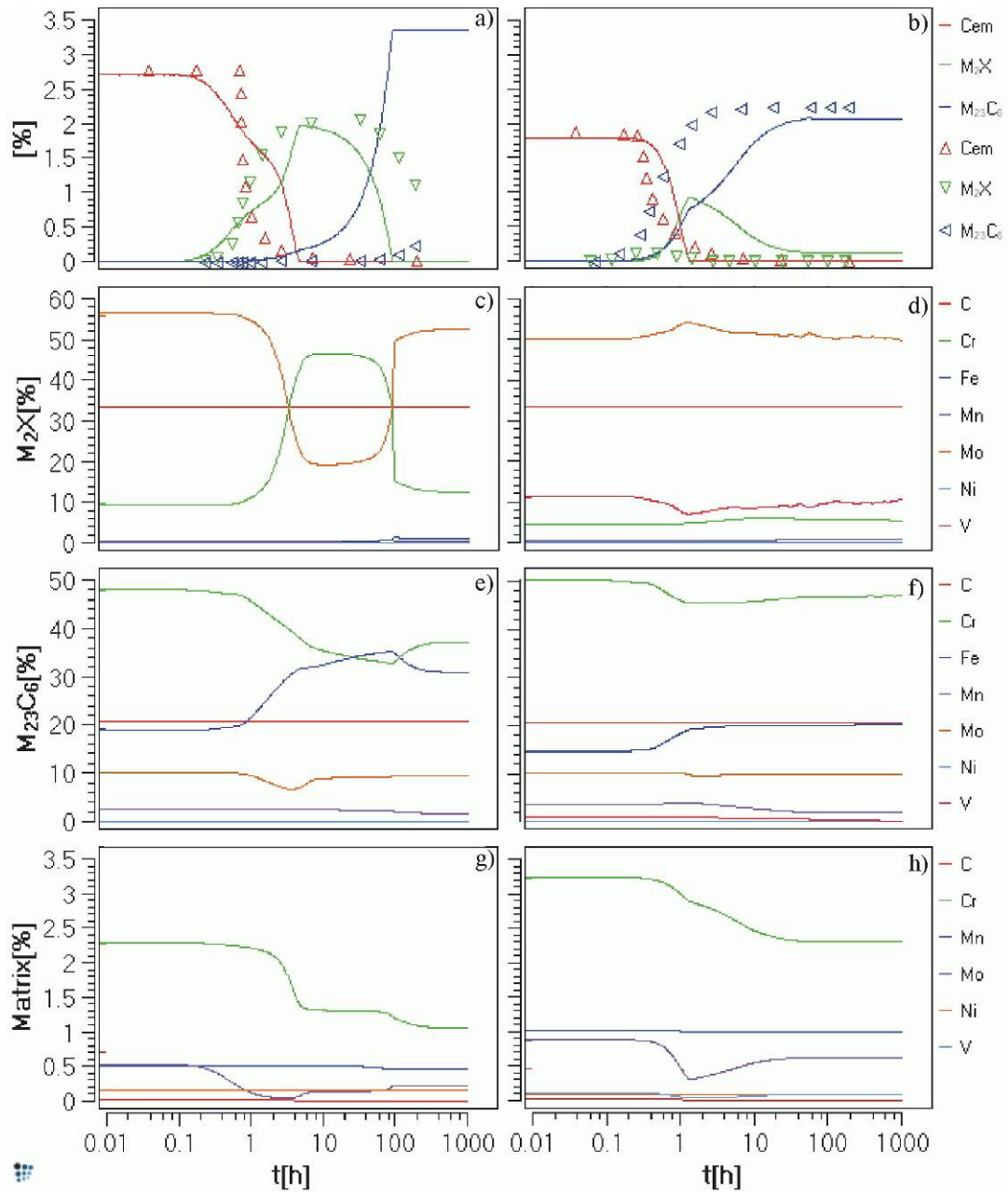


Fig. 44: The simulation results of both steels over time are shown. The left column depicts the 2 1/4% Cr steel, the right column the 3% Cr steel: a), b) are the phase fractions; c), d) the composition of the M_2X phase; e), f) the composition of the $M_{23}C_6$ phase and g), h) the composition of the Matrix phase.

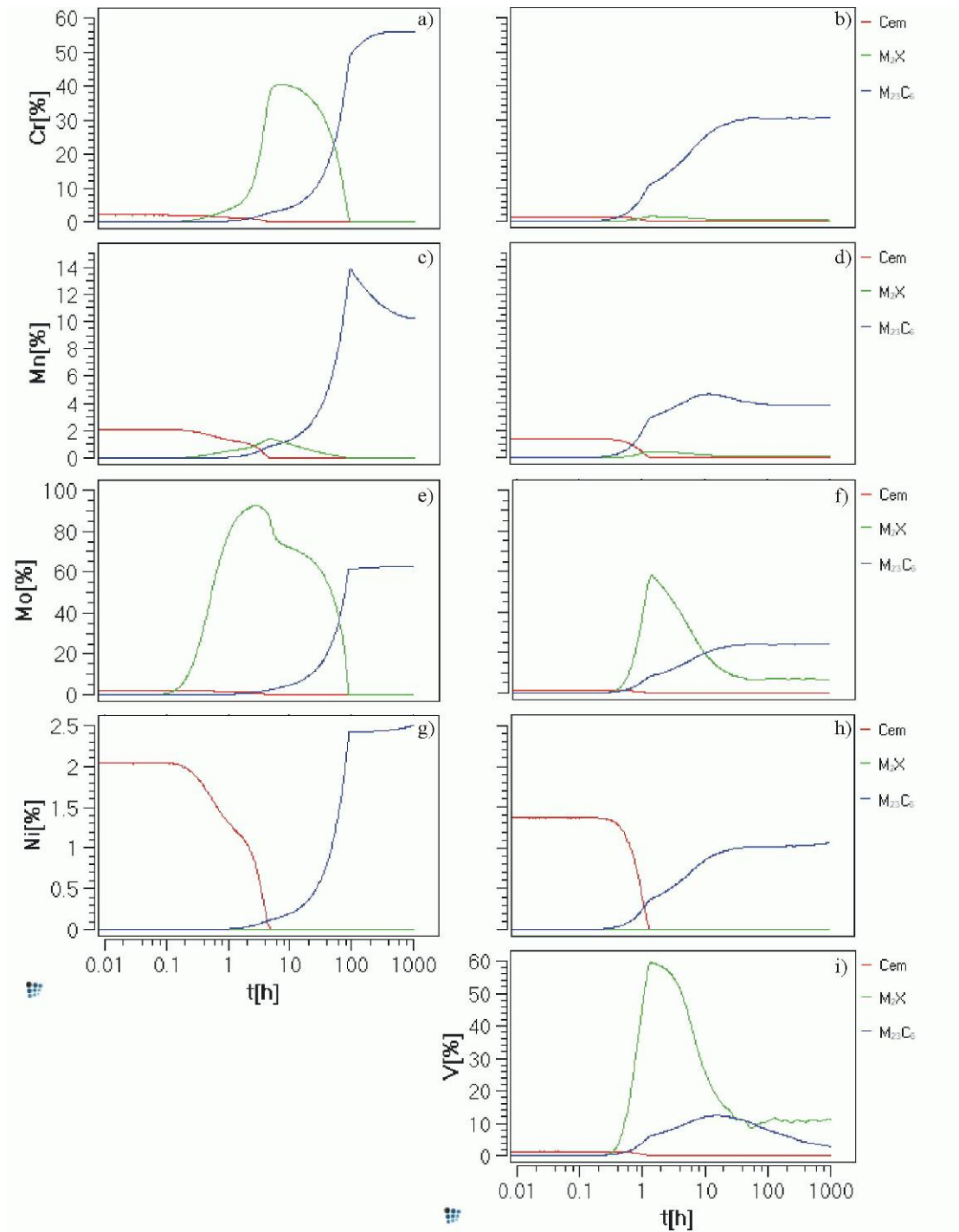


Fig. 45: The products of the phase fractions and element contents of the carbides over time are shown. The left column depicts the 2 1/4% Cr steel, the right column the 3% Cr steel. a), b) are the phase fractions multiplied with the Cr content; c), d) illustrates the Mn content; e), f) shows the Mo content; g), h) shows the Ni content and i) the V content.

Heat treatment of 3% Cr steel

As mentioned before, the simulation of the 3% Cr steel was performed with the same set of parameters as the simulation of the 2 1/4% Cr steel. Cementite with para-equilibrium composition is again the first carbide in the sequence but cementite is re-

placed by $M_{23}C_6$ and M_2X simultaneously. $M_{23}C_6$ nucleates 3min earlier than M_2X in the 3%Cr alloy due to the shorter incubation time (Tab. 8). The higher chromium content of 3wt% stabilises the $M_{23}C_6$ carbides and the lead of the $M_{23}C_6$ suppresses M_2X formation. The lower carbon content of 0,1wt% limits the maximum phase fractions of all carbides (Fig. 43 a) and b)).

Tab. 8: Calculated incubation times at the beginning of the simulation in seconds.

	$M_{23}C_6$	M_2X	Cementite
2¼% Cr 1% Mo	720	245	~1
3% Cr 1,5% Mo	351	1210	~1

The total number of M_2X is larger than the number of $M_{23}C_6$ because of the site saturation effect but they are smaller and therefore the phase fraction stays low. The M_2X phase can not absorb enough alloying elements to delay $M_{23}C_6$ formation.

The right column of Fig. 44 shows the composition evolution of the phases of the 3% Cr steel. There is a significant difference concerning the M_2X phase: This phase starts with a Mo rich composition as in the 2¼% Cr steel simulation but does not replace Mo with Cr. This could be another reason why $M_{23}C_6$ suppresses the M_2X formation, because Cr is available for $M_{23}C_6$ which raises the driving force. As illustrated in Fig. 45 b) about 30% of the available Cr is solved in the $M_{23}C_6$ phase and the rest stays in the matrix. According to this simulation the M_2X phase is stable in the 3% Cr steel, because of the higher molybdenum content of 1,5wt%. The M_2X phase fraction is lowered to the equilibrium amount of about 0,11%. The simulations published by Robson and Bhadeshia do not show a stable M_2X because they used a different thermodynamic database (Robson Bhadeshia: *MTDATA* [152], this work: *Fe-Data* [153]), which was not accessible in this work.

Composition variations

It is argued [42] that the increased C content of the 2¼%Cr alloy is responsible for the faster M_2X formation which retards $M_{23}C_6$.

To check the influence of Mo on the kinetics of the 2¼%Cr steel, simulations were performed with different compositions. An increased Mo content of 1,9wt% is compared with the nominal composition (0,9wt%) in Fig. 46 where no other parameters were changed. It is clearly visible that an increased Mo content accelerates the M_2X kinetics and stabilises this phase.

It seems that the beginning of the $M_{23}C_6$ nucleation is not further retarded. The discussed composition variation (Fig. 44 c)) is also influenced: Due to more Mo the Cr content of the M_2X phase only rises to about 20%, therefore more Cr is available for the $M_{23}C_6$ formation and the $M_{23}C_6$ phase fraction rises faster.

The influence of carbon on the kinetic reactions in the 3%Cr steel is depicted in Fig. 47. An increased C content of 0,15wt% leads to higher phase fractions of all carbides. In contrary to the published data of Robson and Bhadeshia, the kinetic reactions are not accelerated significantly. Due to the higher phase fraction of cementite, the dissolution lasts longer. It is obvious that M_2X reaches its maximum phase fraction with the disappearance of cementite. This leads to the consideration that M_2X is only stable as long as it is fed by the dissolving cementite.

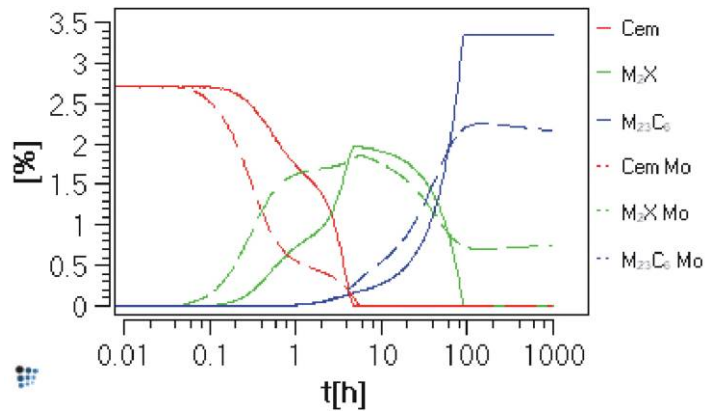


Fig. 46: The phase fractions of the 2¼%Cr steel with nominal composition as shown in Fig. 43 a) (solid lines) and with an increased Mo content of 1,9wt% (dashed lines).

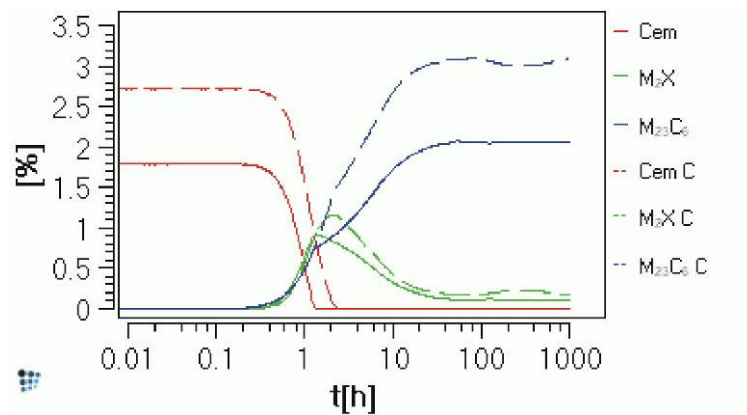


Fig. 47: The phase fractions of the 3%Cr steel with nominal composition as shown in Fig. 43 b) (solid lines) and with an increased C content of 1,5wt% (dashed lines).

A lowered Cr content of 1wt% in the 3%Cr steel suppresses the formation of $M_{23}C_6$ completely and further supports the M_2X kinetics, as illustrated in Fig. 48.

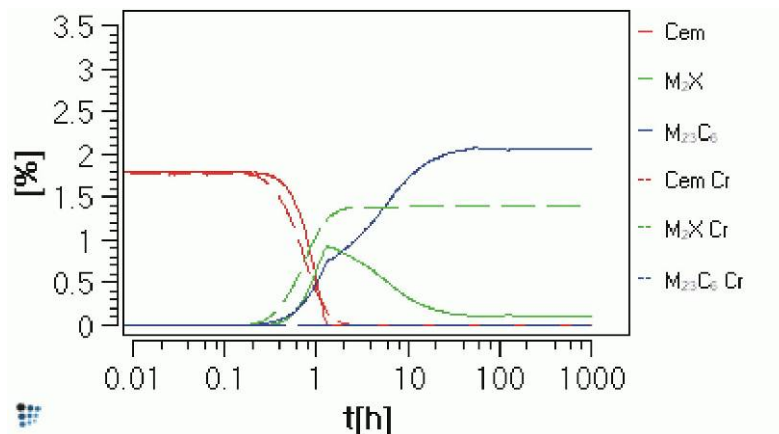


Fig. 48: The phase fractions of the 3%Cr steel with nominal composition as shown in Fig. 43 b) (solid lines) and with a lowered Cr content of 1wt% (dashed lines).

5.2 Heat treatments

5.2.1 Thermal history of P92

In the previous chapter, the isothermal annealing simulation of some alloys was introduced. In these cases the starting condition for the simulations was a supersaturated matrix containing no precipitates. During these simulations, the precipitates nucleate, grow, form a certain distribution and, if they do not dissolve again, finally coarsen. In the present chapter, the results of annealing simulations for steel *P92* are presented including a simplified preceding quality heat treatment. The *P92* is a modern 9-12% Cr steel for thermal power plant application with excellent creep behaviour; the composition is given in Tab. 9.

Gustafson, Hättestrand and co-workers [48, 154] intensively investigated a *P92* pipe supplied by Nippon Steel. The specimens were isothermally aged at 600°C and 650°C between 1000h and 26000h. Prior to annealing the pipe was austenitised (1070°C / 2h, air-cooled) and tempered (770°C / 2h, still air-cooled) [155]. The authors utilized the *EFTEM* method to quantify and identify size distributions of MX, $M_{23}C_6$ and Laves phase precipitates. Hättestrand and Andren did coarsening simulations utilizing *DICTRA* [154] and achieved good agreement with the measured data.

A precipitation kinetic simulation considering more precipitate phases was performed with *MatCalc*, to investigate the interaction of these phases. The simulation parameters are given in Tab. 10 and Tab. 11. The databases utilized are the *TCFE 3* [156] thermodynamic database in a modified version and the *MOB 2* diffusion database [157]. The miscibility gap existing between VN and NbC was artificially stabilized by varying the thermodynamic data describing the MX phases.

Tab. 9: Composition of the *P92* pipe, in wt% [48].

B	C	Cr	Mn	Mo	N	Nb	Ni	Si	V	W	Fe
0,001	0,11	8,96	0,46	0,47	0,05	0,07	0,06	0,04	0,20	1,84	bal.

The original thermodynamic parameter of the *TCFE 3* database describing the Laves phase were replaced by a set of parameters according to Kroupa [158]. These variations were first applied by Dimmler [8] to fit the Laves Phase fraction and the silicon content of the steel *CB8* to the actually measured values (see chapter 6.2).

During manufacturing heat treatment, 9-12% Cr steels undergo multiple γ / martensite and martensite / γ phase transformations. The pipe Gustafson and Hättestrand received was in „as-received” condition. The „as-received” condition describes the state in which the steel-processing industry delivers its products, ready for application or in order to be worked further. In the case of a steam power plant, „as-received” refers to the state when the service starts. Gustafson and Hättestrand performed an austenitisation and tempering treatment prior to the annealing. Due to the fact that the exact *Nippon Steel* manufacturing heat treatment including the complex hot rolling processes are unknown to the author, the present simulation starts at a certain state of the laboratory heat treatment performed by Gustafson and Hättestrand. Based on simulation experience the best state to start the simulation is cooling after austenitising. During austenitising the majority of the precipitate distributions dissolve or at least the phase fraction reach minima. In the present simulation it is assumed that all precipitate distributions dissolved during austenitising.

Tab. 10: Microstructural parameter of the matrix phases.

Matrix phase	Austenite	Ferrite
Grain size [m]	$100 \cdot 10^{-6}$	$100 \cdot 10^{-6}$
Subgrain size [m]	-	$0,1 \cdot 10^{-6}$
Dislocation density [m^{-2}]	$1 \cdot 10^{11}$	$1 \cdot 10^{14}$

The simulation starts at 1070°C with a supersaturated austenitic matrix cooling down to the martensite start temperature where the matrix transforms from austenite to martensite/ferrite. The temperatures M_s and A_f chosen in this simulation are 250°C and, according to an equilibrium calculation, 847°C , respectively. It has to be mentioned, that the matrix phase transformation is considered to happen instantaneously and the parent and product phase have the same chemical composition. During the following tempering and annealing, the temperature remains below A_f and the matrix phase stays martensitic/ferritic. It is further assumed that no major kinetic processes occur at temperatures below 250°C due to the sluggish diffusion of the atomic species.

Tab. 11: Nucleation sites of the precipitate phases depending on the matrix phase.

Thermal cycle	Matrix	$M_{23}C_6$	MX	Laves phase
1. Austenitising ($1070\text{-}250^{\circ}\text{C}$)	Austenite	GB	GB	GB
2. Tempering	Ferrite	GB, SGB	GB, SGB, Disl.	GB, SGB
3. Annealing				

The precipitates considered in the present simulations are the carbides/carbonitride NbC (MX), VN (MX) and $M_{23}C_6$ with the major constituents (Nb,V)(C,N), and $(\text{Fe,Cr})_{23}C_6$, respectively. The fourth precipitate phase considered in the simulation is Laves phase, which is an intermetallic phase of A_2B type. Its major constituents are Fe, W, Mo and Cr. The effective interfacial energies of all precipitate phases were calculated according to the procedure described in chapter 4.3, the values are reasonable. The number of precipitate classes considered was 25 for each kinetic phase.

Besides all thermodynamic differences, the two matrix phases provide different nucleation sites. The number of available nucleation sites is calculated over the assumed microstructure (Tab. 10) according to chapter 3.2.1.

Results and discussion of the complex heat treatment

In this simulation, the original heat treatment of the pipe by *Nippon Steel* is neglected. The laboratory heat treatment prior to annealing is simulated beginning with cooling from austenitising (complex simulation; CS).

Gustafson [48] points out, that the diffusion parameter for molybdenum in iron was adjusted to fit the simulation to experimental data. She also mentions that the diffusion coefficients assessed in the *MOB 2* may have an inaccuracy of the factor two, which has a great influence on the precipitation kinetic reactions.

In total three different MX populations are introduced during the simulation to reveal the influence of precipitation waves occurring during the multiple heating and cooling

operations. The first MX phases are the NbC and VN 1 which nucleate on austenite grain boundaries during cooling from austenitising. Beginning with reheating to tempering temperature the second VN phase is introduced (VN 2) and the nucleation of VN 1 is disabled. This is done to separate the existing VN precipitates during the simulation, which have a mean radius of about 10nm, and the newly nucleating VN precipitates. The growth of the VN 2 would be masked and interesting information about the precipitate evolution of the VN would be lost, although the simulation would provide correct results.

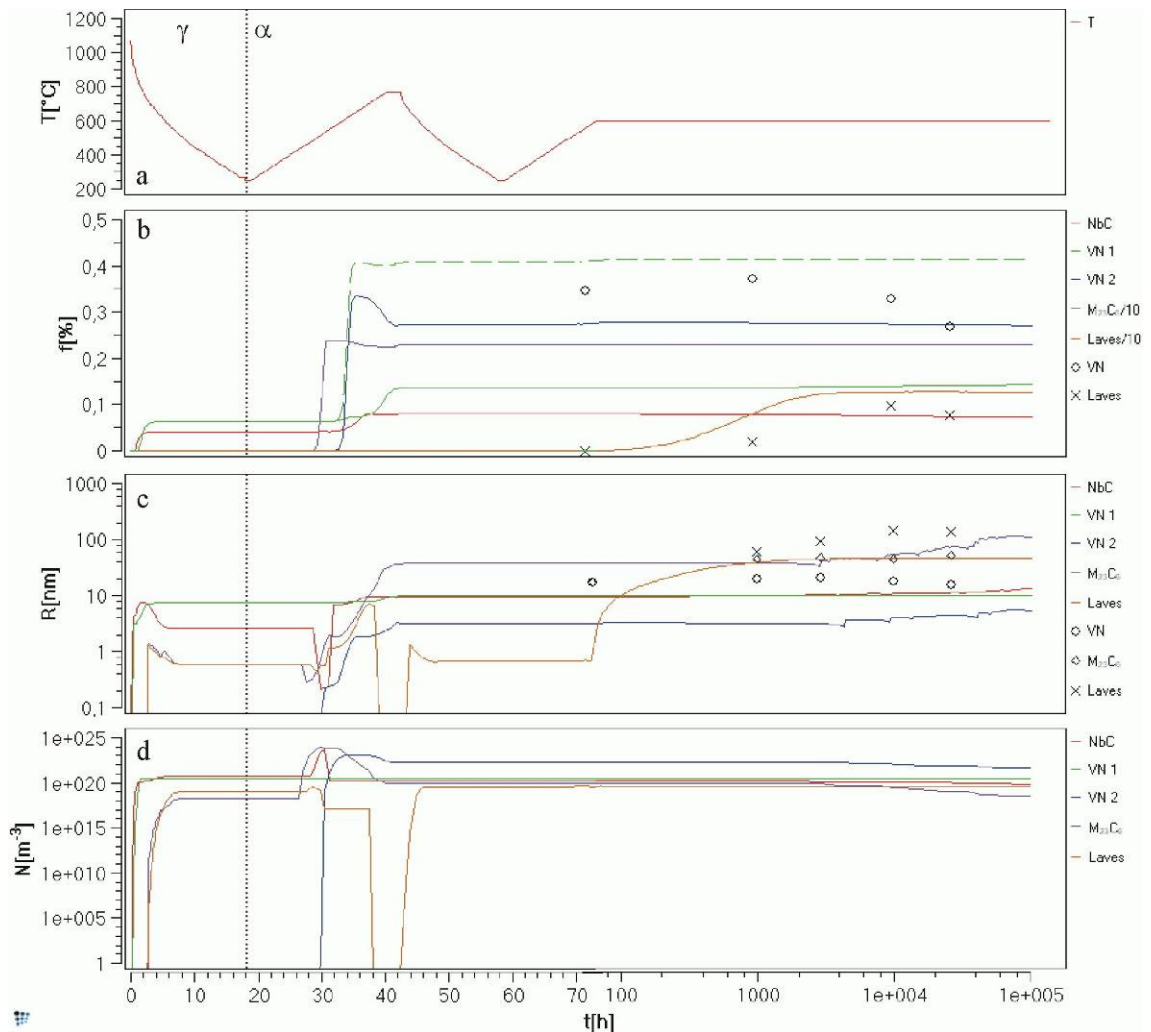


Fig. 49: Simplified thermal history of P92 type steel: Cooling from austenitising, tempering and annealing at 600°C. The experimental data points represent the phase fractions of VN and Laves phase and the mean radii of VN, $M_{23}C_6$ and Laves phase according ref. [126]. For better visualization the time scale is linear up to the beginning of annealing (~71h) and then logarithmic. The dotted lines indicate the matrix phase transformation from austenite to ferrite and vice versa. The green dashed line in the annealing section is the sum of the VN phase fractions.

Austenitising (1070°C – 250°C)

When the temperature decreases NbC and VN 1 precipitates nucleate and grow rapidly. The precipitates deplete the matrix from V, N and especially Nb which slows down the growth of the large NbC and VN 1.

Tempering (250°C – 770°C: 2h – 250°C)

During tempering, the NbC and VN 1 populations grow and the phase fraction increases. The newly introduced VN 2 precipitates first grow but show a coarsening behaviour overlapped by dissolution at the top temperature. The large VN 1 precipitates are more stable and grow on the expense of the much smaller VN 2 (*Gibbs Thomson* effect). The $M_{23}C_6$ precipitates coarsen which can clearly be seen in Fig. 49 b), c) and d). The phase fraction stays constant while the mean radius rises and the number density drops. As can be seen in Fig. 49 b), Laves phase does not reach important phase fractions, however it reaches a number density of about $3 \cdot 10^{19} m^{-3}$ but the mean radii stay well below 10nm. The agreement with the first set of data is good, if the split of the VN precipitates in two waves is considered.

Annealing (250°C – 600°C: $10^6 h$)

Already during tempering Laves phase precipitates nucleate and reach a mean radius of about 1nm in the „as-tempered” condition. The Laves phase population grows and the phase fraction reaches a noticeable level at about 1000h simulated annealing time with a simultaneous matrix depletion of Mo and W. The $M_{23}C_6$ and the VN 2 precipitates start to coarsen at about the same time. The VN 1 population slightly increases the phase fraction on the expense of the much smaller VN 2 precipitates due to the capillarity effect (*Gibbs Thomson* effect). According to this simulation no extensive coarsening of VN 1 takes place. After about 20000h of annealing, the NbC precipitates also start to coarsen.

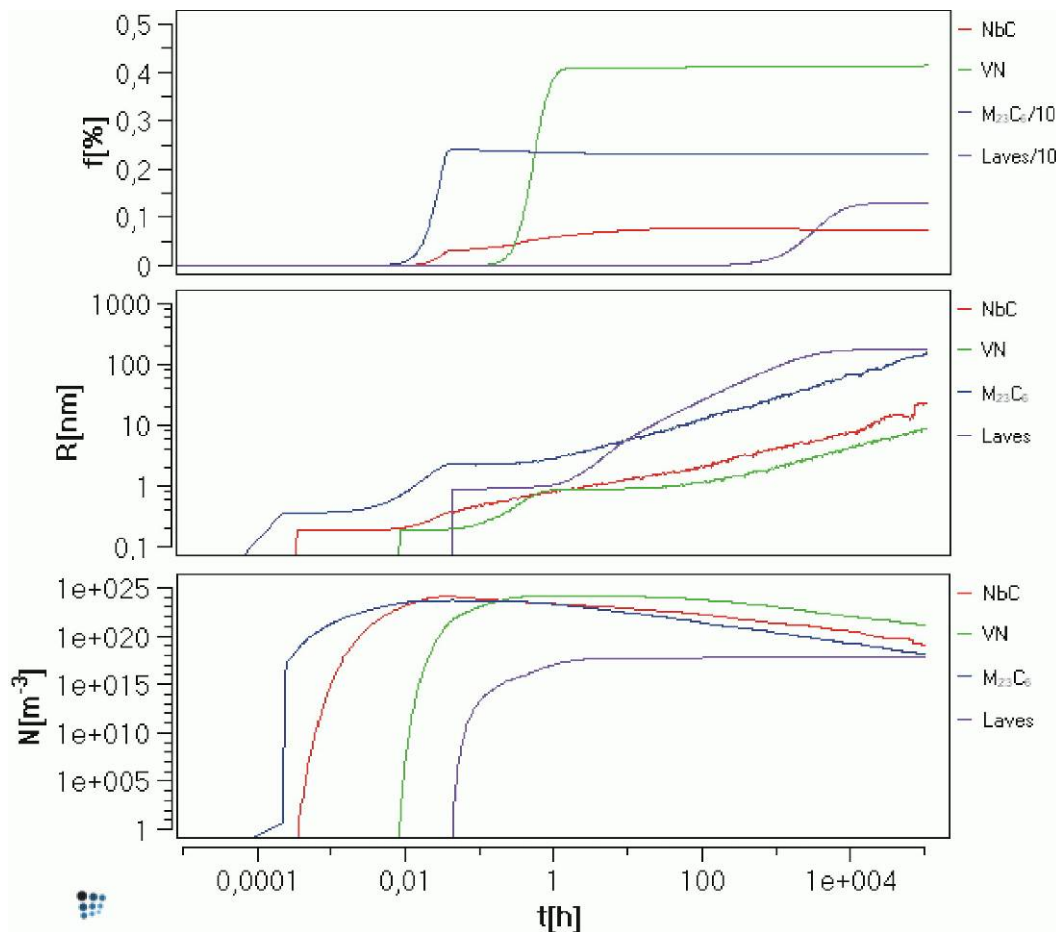


Fig. 50: Simple isothermal annealing simulation at 600°C of P92 type steel.

Results and discussion of the simple annealing simulation

Up to now, it was daily custom to perform annealing simulations isothermally. The reasons were mainly model restrictions. Following, such an isothermal simulation is discussed to be compared to the complex heat treatment simulation.

The simple isothermal simulation (IS) was performed with the same preconditions as the complex simulation described earlier in this chapter (Tab. 9 and Tab. 10). The IS assumes a supersaturated matrix containing no precipitates and the annealing starts directly at 600°C. A precipitation sequence develops as expected. During early stages the two carbide phases compete and the final phase fractions are reached after about 100 h, where the phase fraction of $M_{23}C_6$ is slightly lowered to the advantage of NbC and VN.

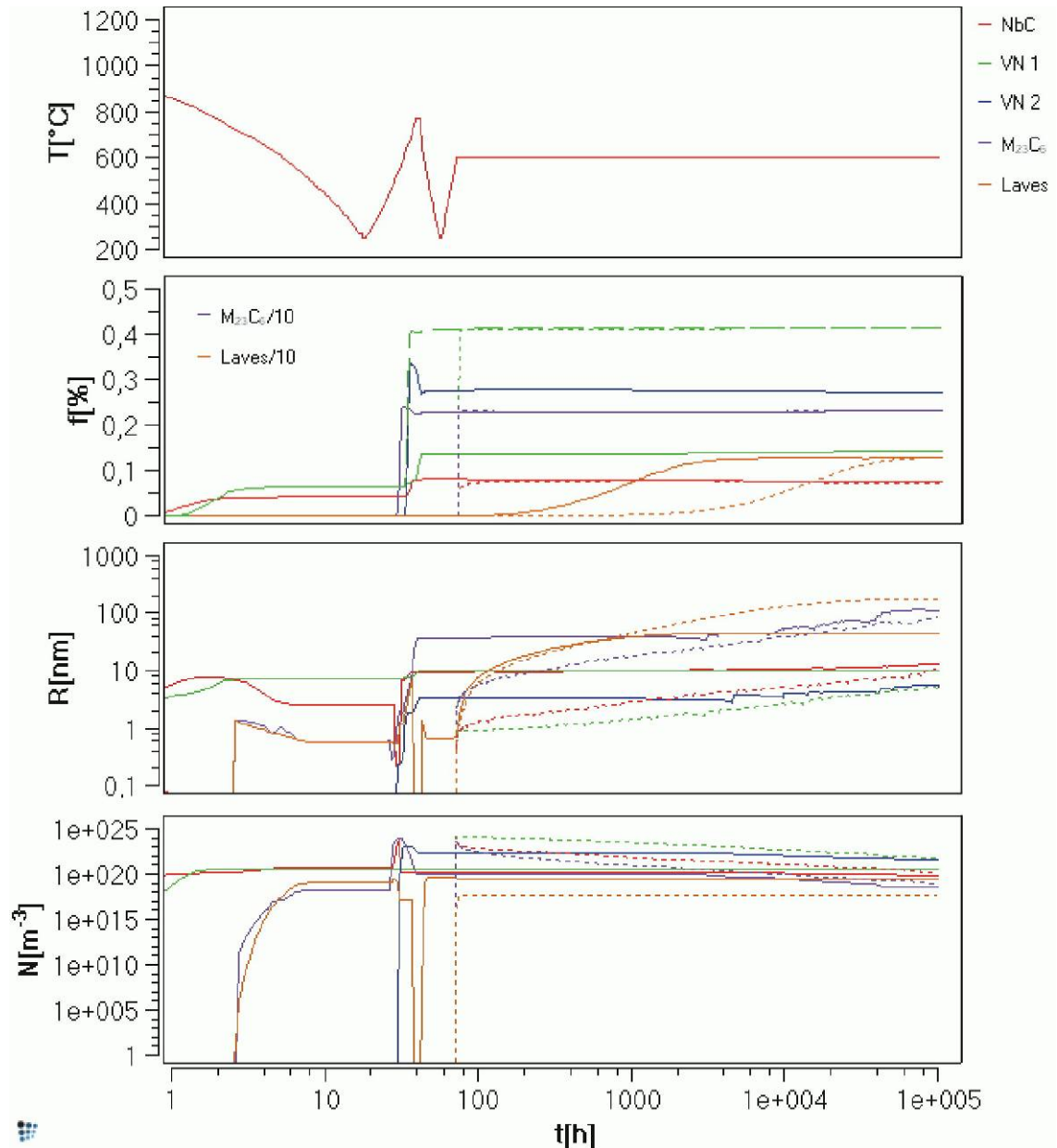


Fig. 51: The simulation of the thermal history as shown in Fig. 49 (full lines) compared with the simple isothermal annealing simulation at 600°C of P92 type steel Fig. 50 (dotted lines). The data of the isothermal simulation are time-shifted so that both annealing simulations start at the same time ($t \sim 71h$).

Comparing both simulations

Isothermal kinetic simulations are standard for academic use. Extremely useful information is gathered from various simulations pushing ahead both, insight in processes concerning phase transformation, and development of new alloys. Considering alloy development it is equally necessary to optimise the chemical composition as well as the heat treatment processes. By comparing the results of a simple isothermal simulation (IS) with the data obtained from the complex heat treatment simulation (CS) prior to the annealing the necessity to simulate the entire thermal history of a specimen as accurate as possible is illustrated (Fig. 51)

The data of the isothermal simulation are time-shifted so that both annealing simulations start at the same absolute simulation time ($t \sim 71\text{h}$). Some remarkable conclusions can be drawn:

- The phase fractions reach the same values, this is of course expected. The phase fractions of both VN waves in the complex simulation are summed up (dashed green line in Fig. 51) for comparability.
- After tempering in CS the Laves phase developed a mean radius of about 0,8nm and a total number of about $5 \cdot 10^{17} \text{m}^{-3}$ precipitates, no significant phase fraction is present. The Laves phase in IS reaches equivalent values for the radius but less number density. This denotes that the evolution of Laves phase is almost independent from the other precipitate reactions.
- The mean radius development of M_{23}C_6 populations are similar after about 9000h, as well as the number density evolution.
- The coarsening rates of all precipitates, except Laves phase, are expectedly equal for all phases. Nevertheless the coarsening starts much earlier in the IS and the NbC does not coarsen within the simulated time in the CS.
- The development of the MX precipitates is, in spite of everything, significantly different. The IS predicts more NbC precipitates with a much smaller mean radius. The size of the VN population is predicted to be much smaller at least up to 40000h.

Concluding it can be seen, that the results of both simulations coincide in expected areas. But the results differ too much with regard to creep simulation. Kinetic simulations will be a part of even more complex simulations considering local microstructural resolution describing damage mechanisms and material degradation during creep.

The „as-tempered” condition was generated by simulating the laboratory heat treatment with *MatCalc* prior to the annealing simulation. It can be shown that an annealing simulation needs a proper starting condition to meet the experimental data, and therefore needs no parameter fitting.

5.2.2 Thermal history of GX-12

The first complex kinetic simulation performed with *MatCalc* published, was the fabrication heat treatment and service simulation of the steel *G-X12 CrMoWVNbN 10 1 1* [159]. The publication can be found in the appendix (chapter 9.1). Since that time the precipitation kinetic model was further developed and new features, especially concerning nucleation, were introduced.

Knowledge about the precipitate evolution during the manufacturing process and service is of great importance for an optimization of the precipitate microstructure to improve the creep resistance of modern power plant materials. The work presented in

[159] demonstrates how the evolution of different precipitate populations in time can be modelled with computational thermodynamics and kinetics.

6 Precipitation kinetics of the *COST* steel *CB8*

In the *COST 522* program, many test melts were manufactured in the course of alloy design activities to improve the creep resistance, oxidation behaviour and to optimize the heat treatment parameters. One of these alloys is the steel *CB8*. After short creep tests this alloy showed excellent creep behaviour and it was decided to investigate this alloy in detail. Dimmler [8] received specimens in „as-received” condition from *voestalpine* foundry Linz. These specimens originated from a 100kg test-block (No. 1) which was fully heat treated together with a commercial casting. The time temperature evolution of this heat treatment is outlined in Fig. 52.

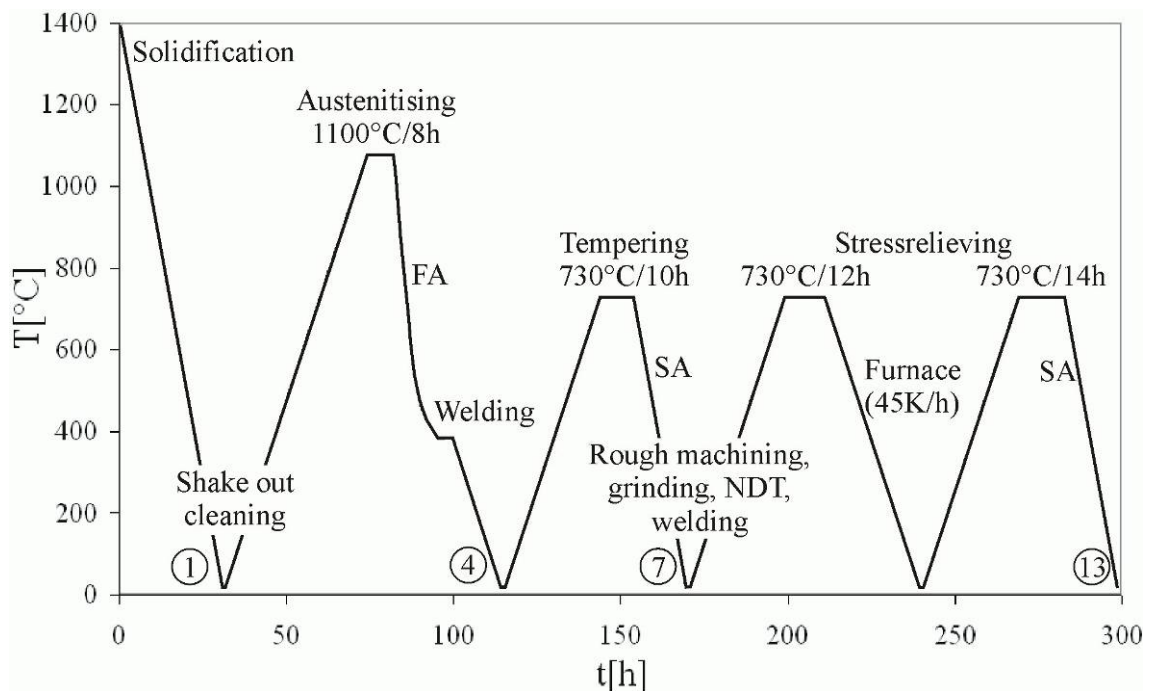


Fig. 52: An industrial heat treatment of a 9-12% Cr steel. The *CB8* specimens were heat treated according to this figure. The cooling rates are determined by the type of cooling: Forced air cooling (FA), still air cooling (SA) and mild cooling in a furnace were applied. The numbers represent specimen conditions (see Tab. 12) that were investigated by Plimon [29] and Sonderegger [30].

After the raw cast block is shaken out, the risers are cut. Before that a tempering at 720°C is necessary to relieve the high stresses in the martensitic material, otherwise cracks initiated in the risers could run through the whole cast-block. This step is not illustrated in Fig. 52. During austenitisation, segregation effects are levelled out and a more homogeneous microstructure is achieved. For example at 400°C the surface cracks are cut out and repair-welding is performed. After the tempering treatment the cast-block is machined and non destructive testing is performed and detected flaws are repaired. The stress relieving heat treatments further soften the martensitic material; in this case, after about 300h net heat treatment time, the „as-received” condition is obtained.

6.1 Experimental information

The specimens of the test-block 1 in „as-received” condition were creep tested up to 16000h at 650°C and varying stress levels in the laboratory of the *IWS**. The results of these investigations have been summarized and discussed by Dimmler [8]. To gain knowledge about the influence of each heat treatment step on the microstructure and the precipitate evolution, another test-block (No. 2) with the same chemical target composition was cast by *voestalpine*.

Tab. 12: Overview of the precipitate populations in the steel CB8 in different specimens; from Sonderegger [30].

Precipitate population	Found in specimen condition	Size (equivalent to diameter) [nm]	Shape	Location in the microstructure
NbC	After austenitising (No. 4, 7, 13)	30-100	Spherical, elliptical, cubic	Not specified
Mo-rich phase (not specified)	After austenitising (No. 4, 7, 13)	30-100 long, <10 width	Plates	Many parallel needles in the matrix
M ₂₃ C ₆	After tempering (No. 7, 13)	50-200	Not specified	Sub grain boundaries
VN	After tempering (No. 7, 13)	10-100	Compact or very flat	Sub grain boundaries
M ₇ C ₃	Just as-cast (No.1)	200	Spherical, elliptical	Prior austenite grain boundaries (<i>PAGB</i>)
Mo ₃ B ₂	As-cast to as-received (No. 1, 4, 7, 13)	200-10 ³ width, ≤10 ⁴ long	Elongated, spherical, elliptical	<i>PAGB</i> , segregated areas
Cr-rich phase, maybe M ₇ C ₃	After austenitising (No.4, 7, 13)	500	Irregular	Segregated areas
Laves-Phase	All exposed and crept specimens	100-800	Irregular	Sub grain boundaries
Modified Z phase	Specimens after about 16000h	100-200	Irregular	Sub grain boundaries

Cubic specimens of the second block were then heat treated in the *IWS* laboratory [29] according to the heat treatment of test-block 1 (see Fig. 52). The goal was to obtain the

* Institute for Material Science, Welding and Forming, Graz University of Technology, Graz, Austria

same microstructure and precipitate distribution in the „as-received” condition of test-block 2 to ensure comparability of the results with test-block 1. Single specimens were removed from the furnace during heat treatment and water-quenched at certain stages. Sonderegger [30] carefully investigated specimens in condition No. 1, 4, 7 and 13 according to Fig. 52 and creep tested specimens utilizing different optical- and electron-microscopical methods. Thereby, the evolution of the microstructure and the precipitate populations could be described over the whole lifetime. Subsequently, his results as relevant for the computer simulation are briefly summarized.

Specimen in „as-cast” condition (No. 1)

The microstructure of this specimen is martensitic with a fraction of retained austenite of about 0,8%. The prior austenite grain boundaries (*PAGB*) have a diameter between 0,5 and 2mm. The *EBS*D investigations show martensite lath packs containing 3 to 4 parallel laths with a typical width of about 1 μ m and a length of up to 100 μ m. The average size of the subgrain structures is also about 1 μ m and the whole microstructure shows a high dislocation density.

Presumably Mo_3B_2 particles are located on *PAGB* which show a cord structure, the length is below 10 μ m. Precipitates with a similar composition as these borides can be found in segregated areas within the microstructure. M_7C_3 with a size of about 200nm can be seen adjacent to the borides.

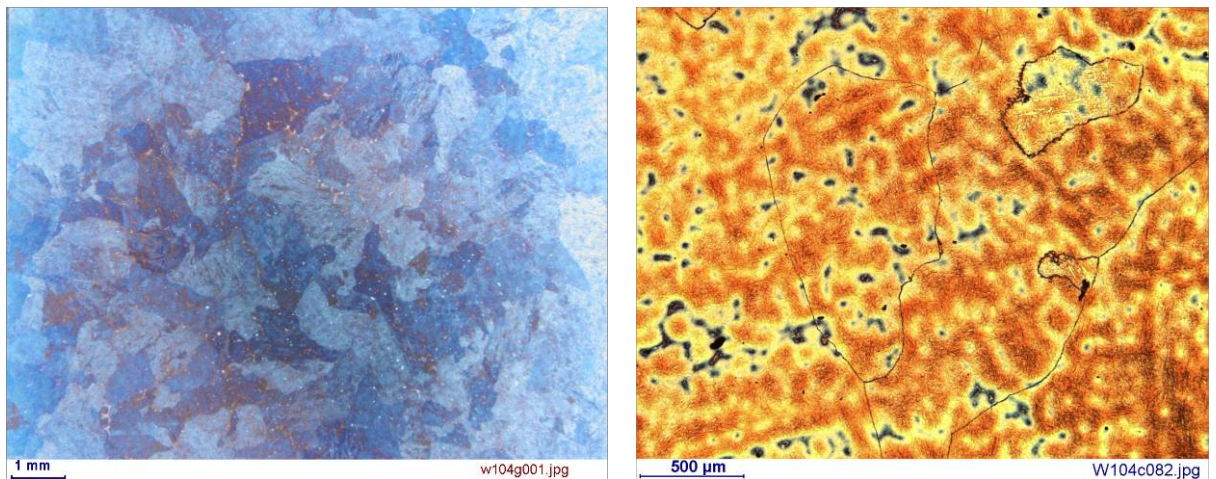


Fig. 53: Specimen „as-cast” condition. Light microscopy pictures, colour etched to identify the segregated areas and *PAGB*s [30].

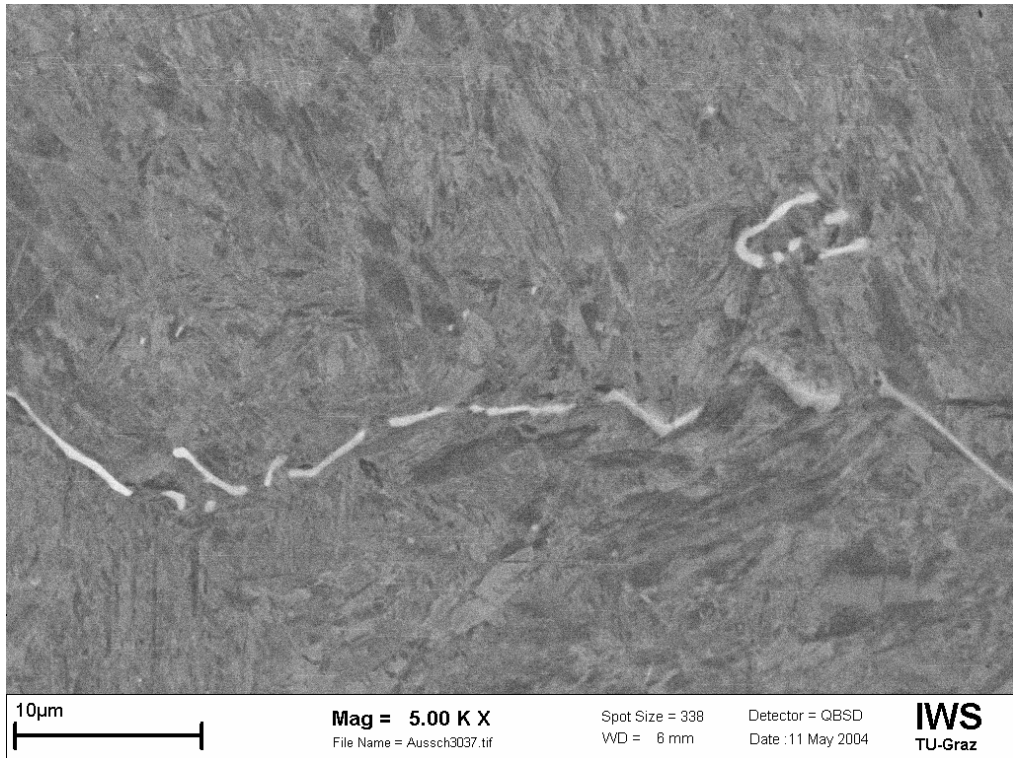


Fig. 54: Specimen in „as-cast“ condition. *TEM* image of a *PAGB* with cord shaped Mo_3B_2 [30].

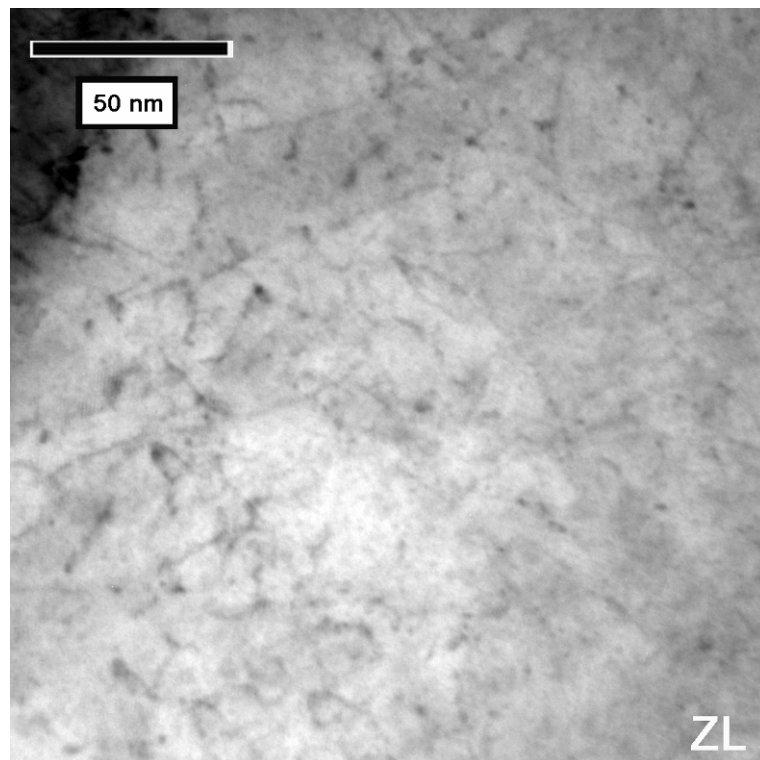


Fig. 55: Specimen in „as-cast“ condition. *TEM* bright field image, net-like high dislocation density [30].

Specimen in „austenitised“ condition (No. 4)

Specimen No. 4 does not show any retained austenite after the austenitising treatment and the segregated areas are more balanced in composition compared to condition No. 1. The martensite lath width stayed constant ($1\mu\text{m}$), the subgrain diameter slightly decreased to $0,8\mu\text{m}$. The borides at the *PAGBs* are vanished, instead Cr-rich precipitates, presumably M_7C_3 , occurred. These precipitates form a chain like structure and have an average diameter of about $0,5\mu\text{m}$. Small voids ($0,5\mu\text{m}$) can be found in the close vicinity of these carbides.

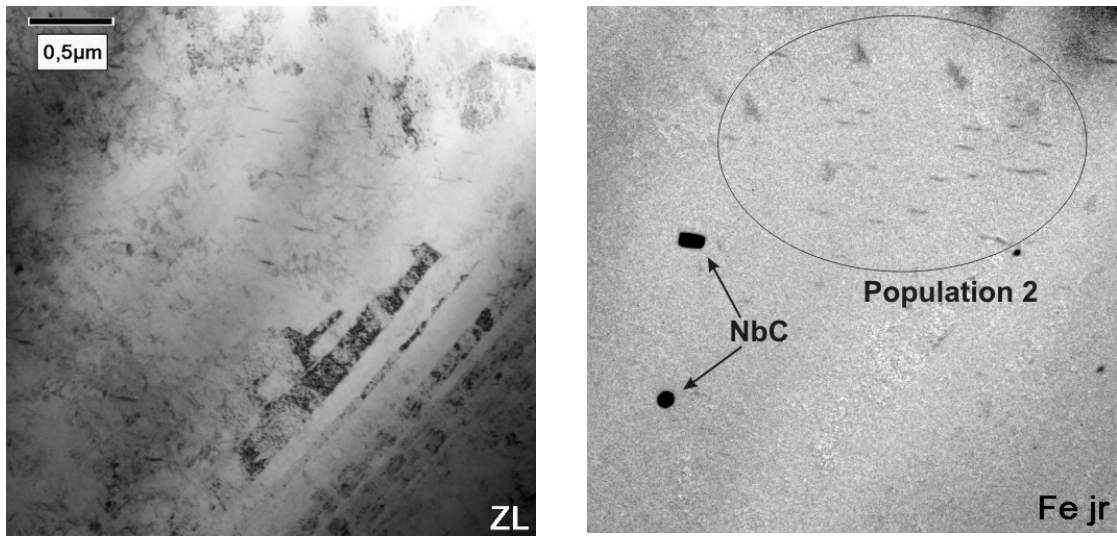


Fig. 56: Specimen in „austenitised“ condition. A *TEM* zero loss image on the left, the *Fe* jump ratio image on the right shows the isolated NbC and a group of Mo-rich needles [30].

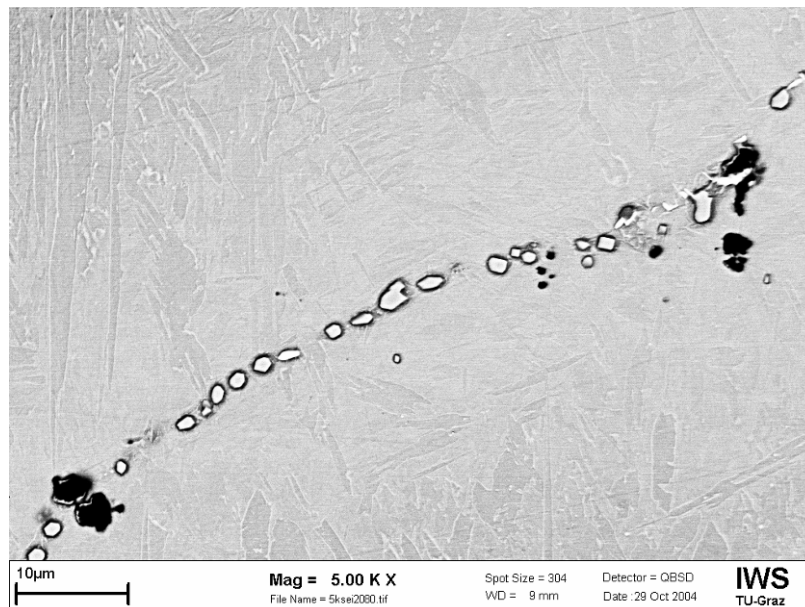


Fig. 57: Specimen in „austenitised“ condition. This *SEM* image shows the Cr-rich precipitates which form a chain and are presumed to be M_7C_3 [30].

Loose NbC particles can be found inside the matrix with no visible interaction with a grain or subgrain boundary. A small group of Mo-rich and needle shaped precipitates (named „Population 2” in Fig. 56) could be found exclusively in this specimen.

Specimen in „tempered” condition (No. 7)

Sonderegger reports a major change regarding the precipitation populations between the „austenitised” and „tempered” condition, whereas the matrix does not show significant changes. The martensite lath width and size of the sub grains stays nearly the same but the dislocation density drops significantly.

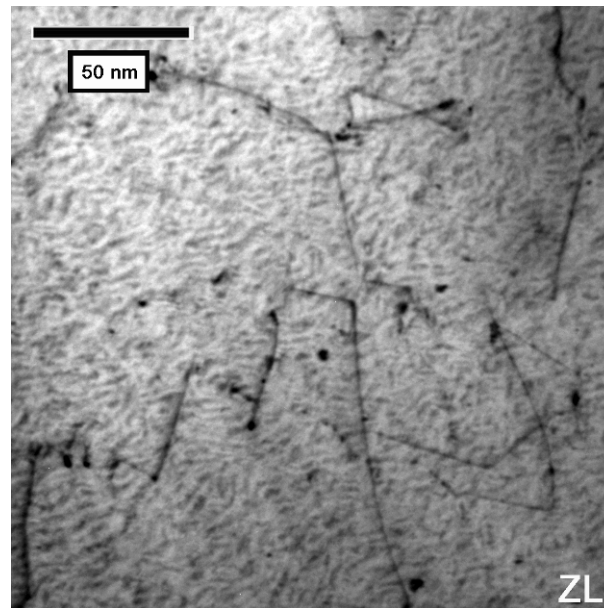


Fig. 58: Specimen in „tempered“ condition. This *TEM* image illustrates the structure of the dislocations [30].

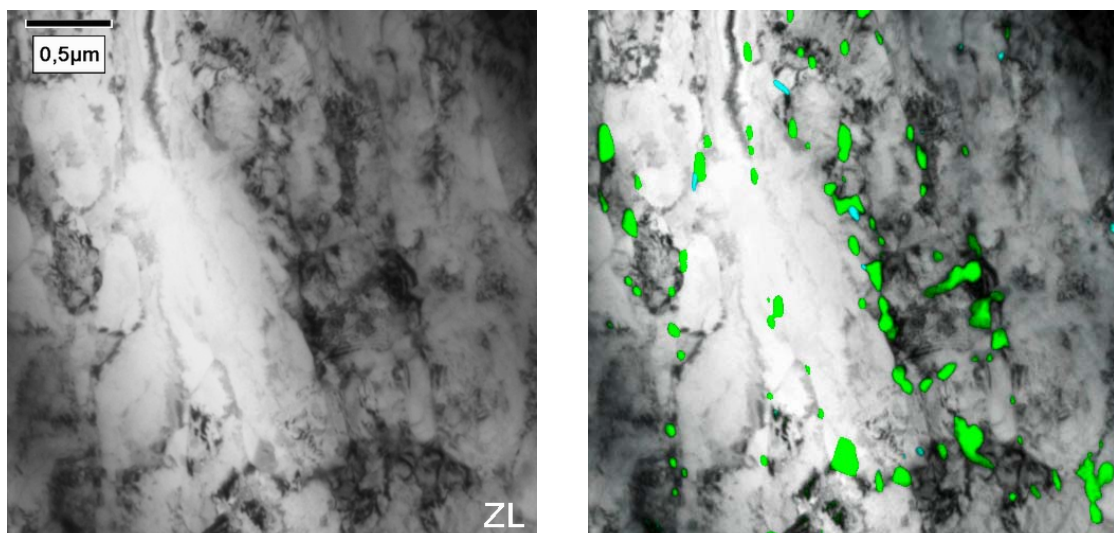


Fig. 59: Specimen in „tempered“ condition. The same *TEM* image is coloured to show the M₂₃C₆ precipitates (green) and the MX precipitates (cyan) [30].

Two new precipitate types occur, the Cr-rich $M_{23}C_6$ and vanadium-nitrides (MX). Both are located on martensite and subgrain boundaries and their volume fraction as well as their size already reaches values comparable to advanced heat treatment conditions. The NbC population did not change and the segregated areas have nearly disappeared.

Specimen in „as-received” condition (No. 13)

There were no major changes detected between this condition and the „tempered” condition. The martensite lath and subgrain structure did not change, the dislocation structure seems to be a little less distributed. Isolated sub grains show a high dislocation density and also sub grains without dislocations could be found. The segregated areas in the matrix are vanished. The $M_{23}C_6$ precipitates did grow/coarsen slightly, their number density is reduced by 25% and the mean diameter increased by 8% compared to the „austenitised” condition. The VN precipitates in contrast nucleate and grow, their number density increased by 10% and the mean diameter is 15-20% higher. Hence the volume fraction of the VN rose by 60%. The NbC precipitates do not change. According to Dimmler [8], the „as-received” condition contains already a small amount of Laves phase.

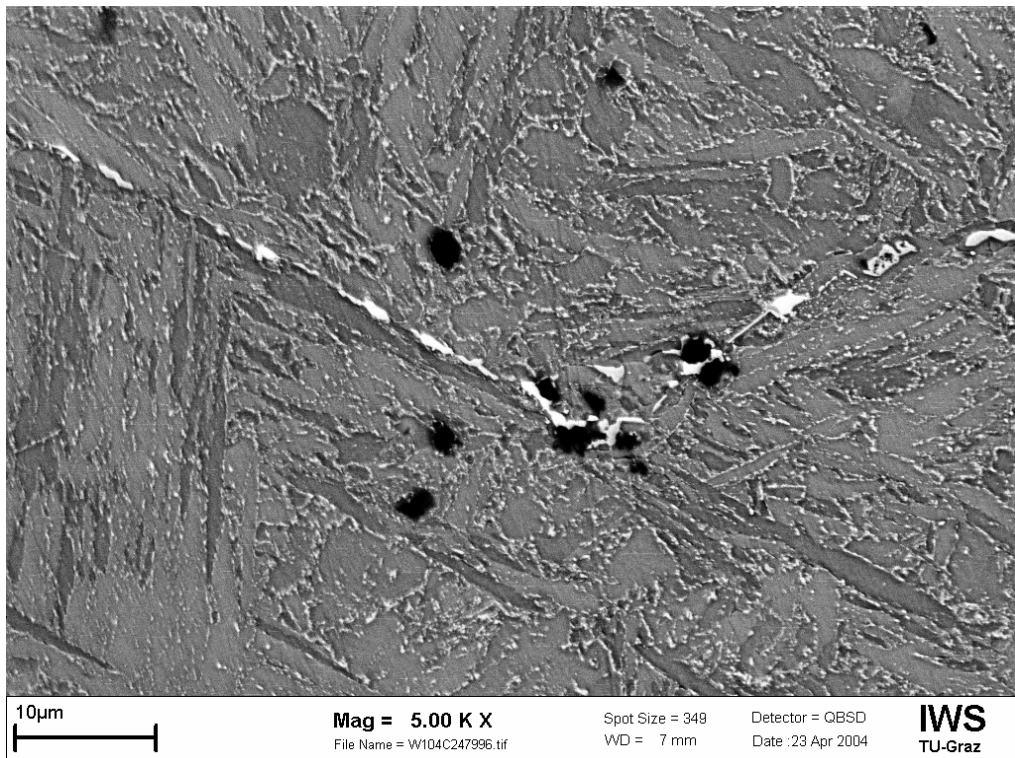


Fig. 60: Specimen in „as-received” condition. This SEM image shows Cr-rich precipitates at PAGBs (white) with adjacent voids (black) [30].

Specimens after creep testing and exposure at 650°C (2000h to 7000h)

Exposure refers to the head section of a creep specimen which is not loaded with mechanical stress but only temperature. Up to 7000h testing time the martensite lath width rises only slightly. The subgrain diameter of the exposed specimen-section does not change either. But the subgrain diameter of the creep loaded material in the gauge changes significantly from 0,7 to 1µm.

The investigations show growth/coarsening of the $M_{23}C_6$ precipitates, the mean diameter compared to the „as-received” condition is 20-30% higher and the number density is lowered by 20% in the exposed volume and 45% in the crept volume. The phase fraction of the $M_{23}C_6$ reaches values between 2,1 and 4,1% and further increases. The mean diameter of the VN precipitates stays constant between 50 and 70nm in both conditions, exposed and creep loaded. The number density of these MX particles in the specimen gauge is the same as in the „as-received” condition. The VN number density in the exposed specimen head increased by 90%, similar applies for the volume fraction.

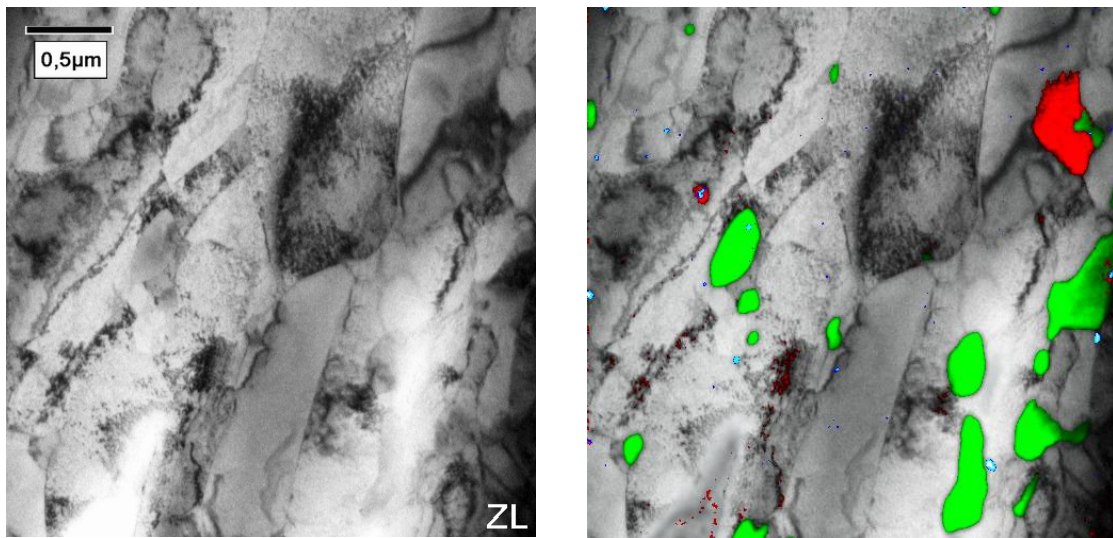


Fig. 61: TEM images of a creep loaded (100MPa) microstructure (gauge section) after 7000h. Slightly coarsened sub grains, decorated with $M_{23}C_6$ (green), VN (blue), Laves phase (red, right) and some NbC (red, left) [30].

Specimen after creep testing and exposure at 650°C (16000h)

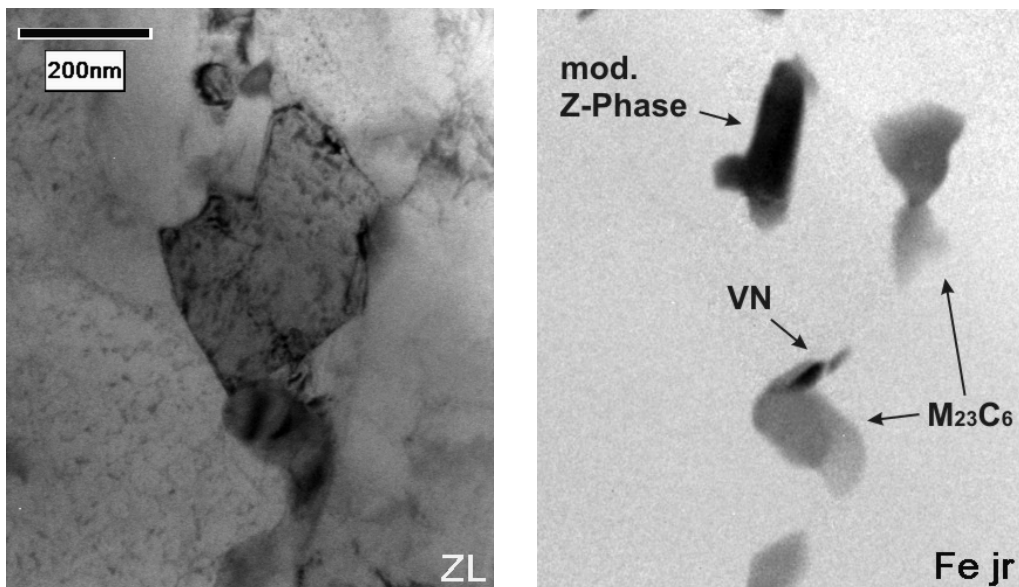


Fig. 62: TEM images of the exposed microstructure after 16564h at 650°C. Only few VN precipitates can be seen, also some modified Z phase precipitates [30].

16000h is the longest creep testing time of *CB8* specimens up to now. The differences in microstructure and precipitation distribution are significant and summarized below:

Tab. 13: Overview of the exposed and creep tested specimen conditions.

Exposed specimen section (head)	Creep loaded specimen section (gauge)
Sub grains	
No rise of the subgrain diameter (16564h).	Rapid growth of subgrain diameter from about 1 μ m after 7000h to 1,6 μ m (15802h/80MPa).
Martensite lath width	
No significant change in any exposed specimen.	The width changed from about 0,8 μ m at 7000h to about 1,1 μ m (15802h/80MPa).
M₂₃C₆	
The phase fraction stays about constant at 2%. Also the mean diameter of 123nm does not change a lot. The number density drops by 25%.	The phase fraction is constant at 2,9% and the mean diameter slightly increases to 159nm. The number of precipitates in the gauge drops significantly by 55% compared to the 7000h specimen. This coarsening behaviour is expected.
VN	
These MX precipitates dissolve, the volume fraction drops from 0,3% in the 7000h specimen to 0,06%. The mean radius slightly increases while the number density drops by a factor of 10.	The mean radius of the VN in the crept volume stays constant but the phase fraction of this phase is 12 times lower compared to the 7000h specimen. The reason for the dissolution could be the occurrence of Z phase.
Modified Z phase	
This phase has been detected first in this specimen condition. In the exposed head volume the Z phase is adjacent to the M ₂₃ C ₆ precipitates.	The Z phase occurs independent from other precipitates.
Laves phase	
Compared with the 7000h specimen there is no significant change, neither in the volume fraction (0,8%) nor in the mean diameter (250nm).	

6.2 Thermodynamic equilibrium analysis of the steel *CB8*

Thermodynamic equilibrium calculations are an accompanying part of modern material characterization and alloy designing. The following calculations support the understanding of the steel and bridge the gap between metallographic investigations and kinetic simulations. Based on the *CALPHAD* method [160] numerous thermodynamic databases are available describing the temperature and composition depending *Gibbs* free energy of phases in multi component multi phase systems. *MatCalc* and various thermodynamic databases were used to derive phase fraction diagrams for different composition variations and temperatures.

The databases used in the present work are:

- *SSOL Version M* (Standard database over the past years. Much experience in the field of 9-12% Cr steels [161])
- *SSOLA* (Update of Version M, very general, contains non-ideal solution phases within a framework of 78 elements [162])
- *Fe-Data* modified (for iron base alloys, contains B description in $M_{23}C_6$ [153])
- *TCFE 3* modified (for iron base alloys [156])

6.2.1 Thermodynamic equilibrium analysis (Fe-Data)

An alloy is considered to be in thermodynamic equilibrium if no driving force is present which effects a phase transformation towards an energetically lower condition. A system is in a meta-stable equilibrium if the driving forces are not high enough to reach the activation energy of the phase transformation towards an energetically lower condition. This thermodynamic equilibrium condition demands that the free *Gibb's* energy of the system is at a minimum.

Tab. 14: Composition of *CB8 heat 173* in wt%, Fe is balanced. The nominal composition range and the chemical composition of two laboratory melts are listed.

	Al	B	C	Co	Cr	Mn	Mo	N	Nb	Ni	Si	V
Nom.	0,010	0,0080	0,16	2,80	10,70	0,10	1,40	0,0150	0,050	0,10	0,20	0,18
Min.												
Nom.	0,020	0,0150	0,18	3,20	11,30	0,30	1,60	0,0300	0,070	0,20	0,30	0,22
Max.												
P	0,028	0,0112	0,17	2,92	10,72	0,20	1,40	0,0319	0,060	0,16	0,27	0,21
D	0,026	0,0106	0,17	2,94	10,86	0,20	1,41	0,0240	0,061	0,15	0,27	0,21

The steel grade *CB8* was investigated intensively at the institute of Material Science, Welding and Forming [8, 30]. Two laboratory scale melts, variants *D* and *P*, were supplied by *voestalpine* foundry Linz with minor variations in composition. All numerical simulations performed in this work are based on alloy version *P*.

Two databases were selected for the precipitation kinetic simulation, *Fe-Data* and modified *TCFE 3*. Both provide actual assessments and are considered to be most reliable. The *Fe-Data* was selected because this database considers Boron in the $M_{23}C_6$ carbides, which other databases do not up to now. The *TCFE 3* was utilized because of very good agreement with experimental data for the Cr steel *P92* (see chapter 5.2.1). First the thermodynamic equilibrium in a temperature range of 400 to 1600°C was investigated utilizing the *Fe-Data* database. In chapter 6.2.2 similar calculations utilizing the modified *TCFE 3* database are presented for comparison.

CB8 Phase fraction diagram

Fig. 63 shows the phase fraction f of each stable phase over temperature of the steel *CB8 heat 173 P*. The composition of this alloy is given in Tab. 14. An important fact is that steels of this type undergo two major transformations. At around 1450°C the δ -Ferrite matrix phase transforms to austenite and at about 850°C back to α -ferrite. The sum of all phase fractions except the matrix phases does not exceed 6% at any temperature.

The phase fraction diagram (Fig. 63) shall now be illustrated between 1600°C and 400°C: The boron-nitride (BN) has the highest solubility temperature of about 1320°C and is supposed to be a primary nitride. This phase is only stable down to 1050°C. Below about 1250°C the BN is gradually replaced by other boron-rich phases such as M_3B_2 . The next stable phases are a complex MX phase and the stoichiometric aluminum-nitride (AlN). The MX phase is a complex carbonitride containing the substitutional elements V, Nb, Cr, Mo and the interstitial elements C and N. The major constituents of the M_3B_2 are Mo, Cr and B. The next stable phase at a lower temperature is the $M_{23}C_6$ carbide with the major elements Cr, Fe, Mo and C. This carbide shows the highest phase fraction of all precipitate phases of about 3,7% at 400°C.

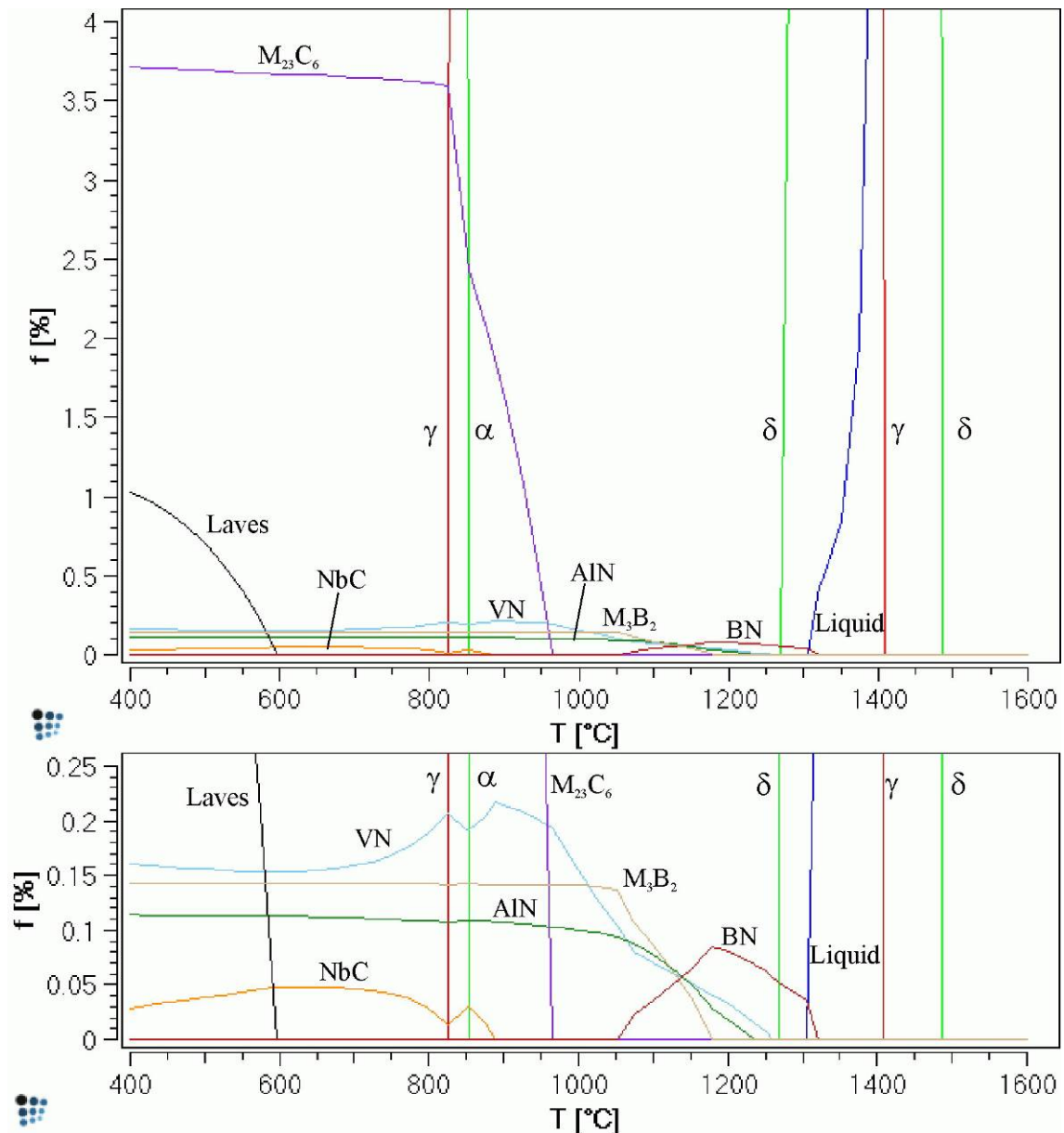


Fig. 63: Two details of the *CB8 heat 173 P* phase fraction diagram calculated using the *Fe-Data* database. The lower diagram shows the phases with a fraction lower than 0,25% in more detail.

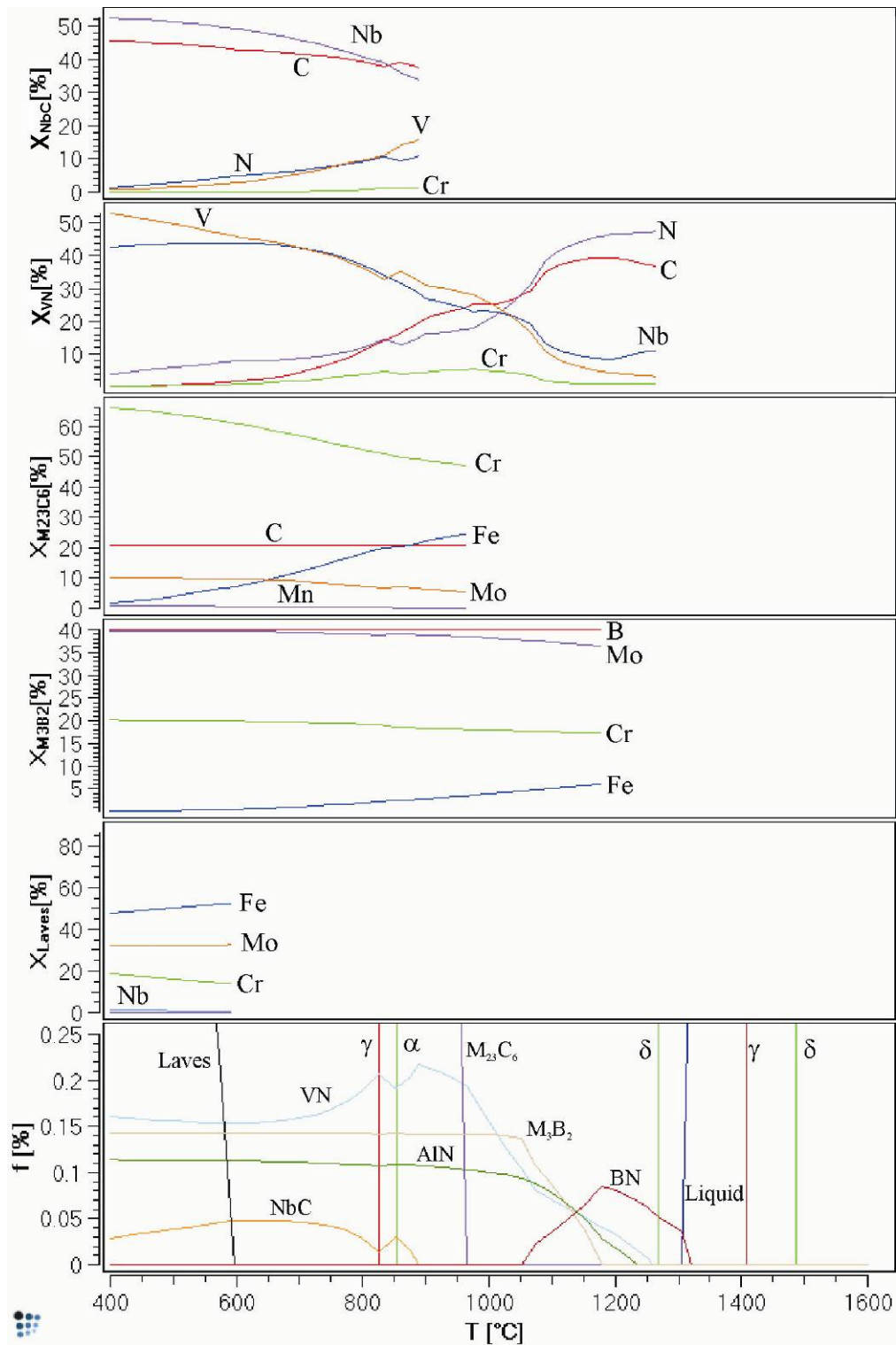


Fig. 64: The temperature dependent equilibrium composition of the phases MX (NbC), MX (VN), $M_{23}C_6$, M_3B_2 and Laves phase. Only major elements are shown in the temperature range where the phases are stable. For comparison the detail of the phase fraction diagram is shown again below. The calculation is based on the *Fe-Data* database. The composition graphs are only shown in the temperature ranges where the corresponding phase is stable.

Slightly above the A_3 temperature a second MX carbonitride appears. The steel *CB8* shows two variants of the MX phase forming a miscibility gap at lower temperatures.

This second MX phase is dominated by niobium and carbon and on the other hand contains less vanadium and nitrogen. Therefore this MX phase is named NbC. With the appearance of the NbC the MX phase with the higher solubility temperature changes its composition from a complex MX type to a vanadium and nitrogen rich phase, thus it is named VN. One can see that the phase fraction of the NbC is less than the phase fraction of the VN.

The calculated transformation temperature A_1 is about 825°C. Below this temperature the steel is fully ferritic.

At about 600°C the last of the stable phases occurs, the intermetallic Laves phase. This phase has an A_2B structure and contains mainly Fe, Mo and Cr, and reaches the second highest phase fraction amount of about 1% at 400°C.

Fig. 64 shows the variation of the composition of each of the considered phases. At lower temperatures the distinction between both variants of the MX phase intensifies. The VN phase depletes of Nb and C and vice versa. $M_{23}C_6$ enriches with Cr, depletes of Fe and gradually contains more Mo with decreasing temperature. The M_3B_2 phase shows a quite stable composition over temperature as well as the Laves phase. The phases shown in Fig. 64 contain only traces of the other alloying elements.

CB8 Phase diagrams

The nominal composition range as given in Tab. 14 represents the target composition range as obtained from the alloy design process. An industrial casting shows inhomogeneities in composition; hence the influences of variations in composition were investigated using thermodynamic equilibrium calculations. The fractions of elements with very high diffusivity, namely C, B and N, were changed one by one within a reasonable range. Additionally the Mo fraction was varied. The results are displayed in Fig. 65 to Fig. 68 where the dashed lines indicate composition *CB8 heat 173 P*. It has to be pointed out again, that these results are calculated using the *Fe-Data* thermodynamic database.

The phase diagram with varying carbon content can be seen in Fig. 65. Slight variations of the carbon content do not change the set of stable phases, major changes influence the solubility temperatures of phases. For example if the C fraction is lowered, the ferritic/austenitic two-phase region becomes wider for this alloy, because the A_1 temperature rises. Another effect is, that the δ -ferrite region widens with less carbon. It can be seen that even at a hypothetical carbon content of zero the *CB8* undergoes two major phase transformations and no δ -ferrite is predicted. The MX (NbC) phase is stable down to very low carbon contents, the same goes for $M_{23}C_6$. On the other hand the solubility temperature of the Laves phase is lowered with an increasing C content.

The phase diagram shown in Fig. 66 reveals that varying nitrogen content changes the solubility temperatures of some phases like BN, AlN, M_3B_2 and NbC. The miscibility gap mentioned above can be seen explicitly in this figure (areas 14, 16, 17 and 21), where the complex MX carbonitride splits into a VN and a NbC. If the nitrogen content is raised to more than 0,08 wt% an *hcp* phase would be stable (Cr_2N). Below a nitrogen content of about 0,015% BN is not stable. The solubility temperature of $M_{23}C_6$ seems to be virtually unsusceptible to variations of the N content. Although the AlN solubility temperature drops with lowered nitrogen, this phase is stable even at the lowest nitrogen contents.

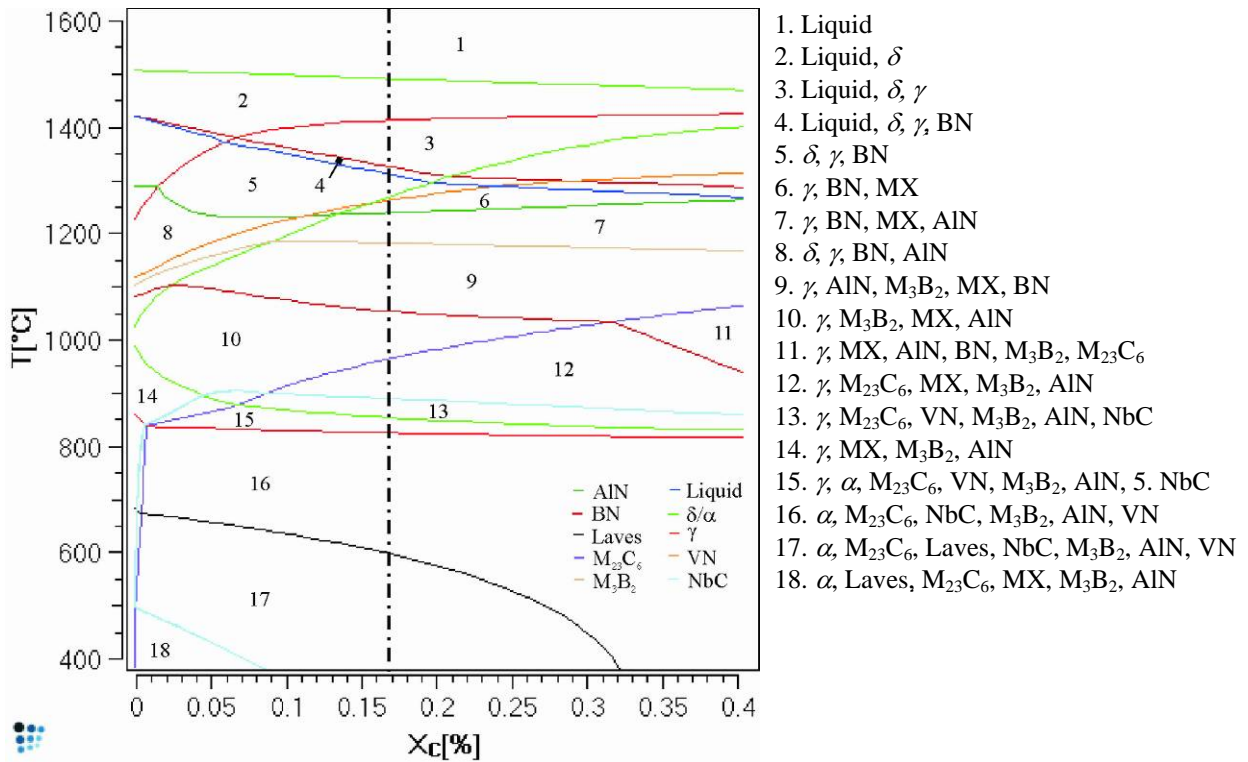


Fig. 65: Phase diagram of CB8 heat 173 P but varying Carbon content from 0 to 0,4wt%. The nominal composition contains 0,17wt% C (dash dotted line). The calculation is based on the Fe-Data database.

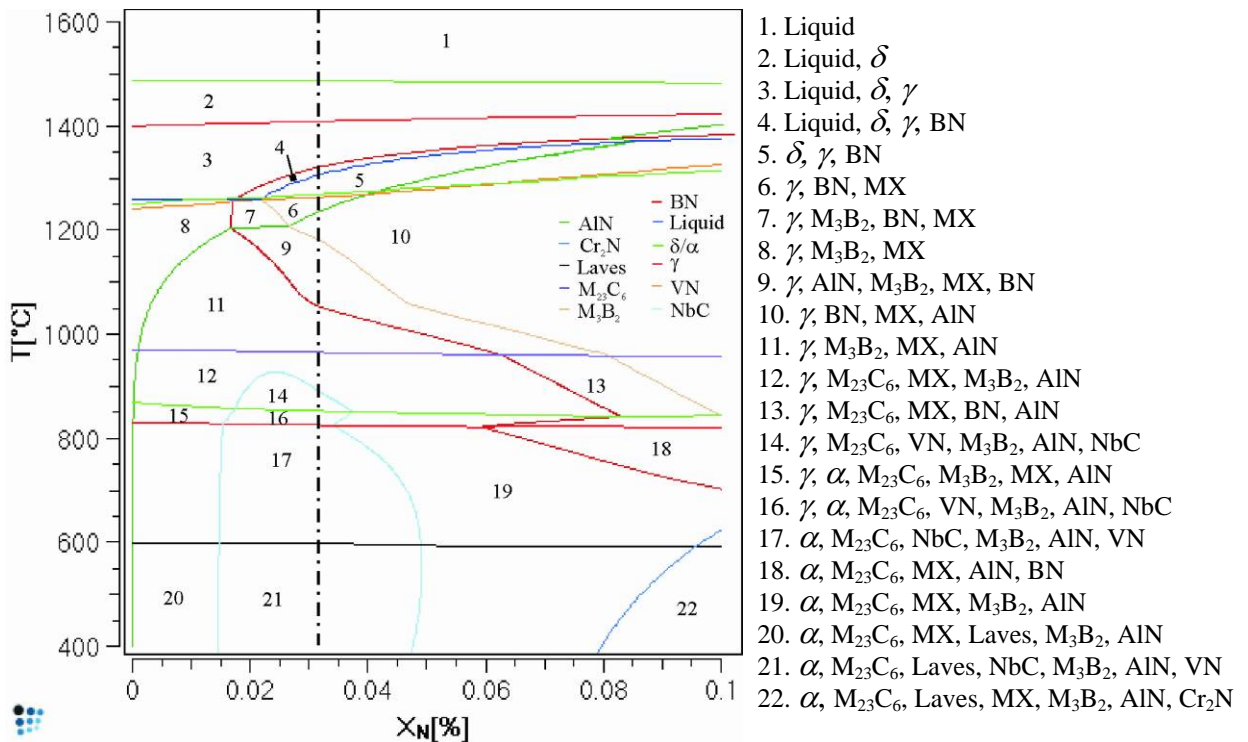


Fig. 66: Phase diagram of CB8 heat 173 P but varying nitrogen content from 0 to 0,1wt%. The nominal composition contains 0,0319wt% N (dash dotted line). The calculation is based on the Fe-Data database.

The phase diagram shown in Fig. 67 illustrates the results when boron is varied between 0 and 0,05wt%. It is interesting to see, that the borides form even at very low boron contents. The solubility temperature of the liquid phase and the Laves phase are lowered with increasing B content. It has to be pointed out that in industrial melts the maximum boron content is limited to about 0,015wt% or 150ppm due to non pressurised furnaces.

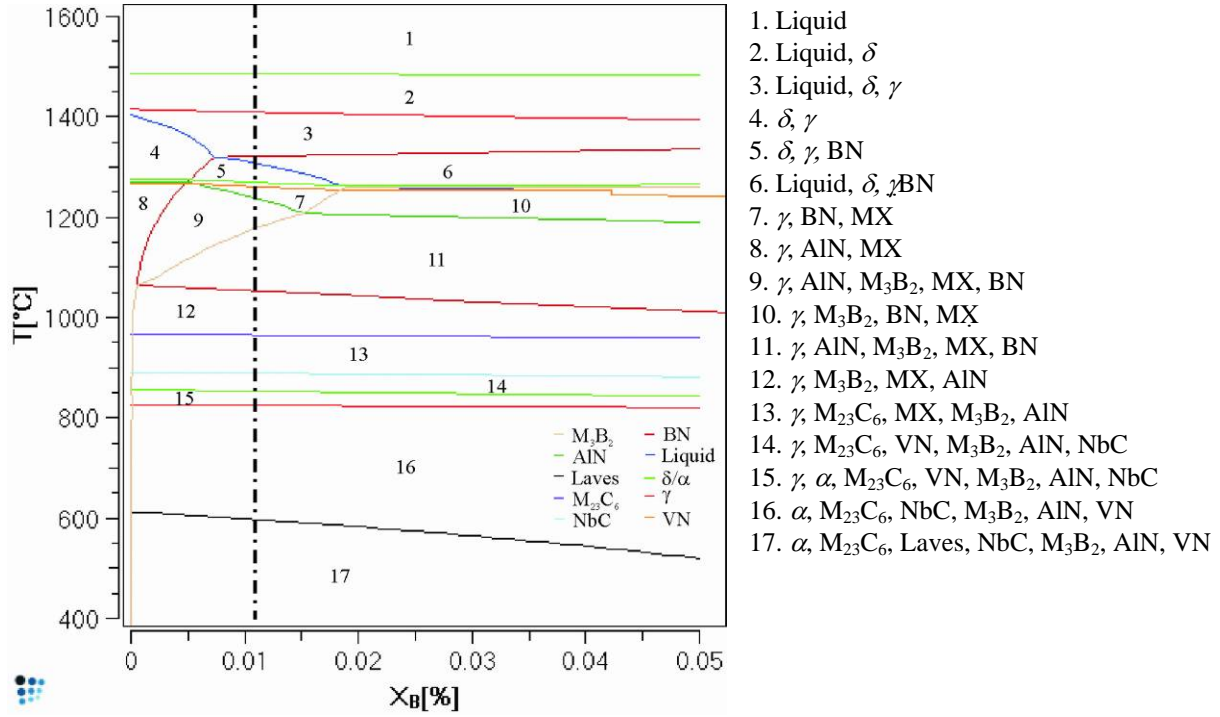


Fig. 67: Phase diagram of CB8 heat 173 P but varying Boron content from 0 to 0,05wt%. The nominal composition contains 0,0112wt% B (dash dotted line). The calculation is based on the Fe-Data database.

The molybdenum content was also varied up to 5wt%, the resulting phase diagram can be seen in Fig. 68. Molybdenum is added to these steels to stabilize ferrite and to increase the solid solution strengthening effect. This element forms carbides, like $M_{23}C_6$ together with chromium and at higher concentration also M_6C , which can be seen in the figure. If the molybdenum level is increased above about 4,5%wt this alloy does not transform completely into austenite, and residual δ -ferrite would be observed. A molybdenum concentration of 5wt% would lead to a calculated residual δ -ferrite fraction of about 8%. Mo also stabilises Laves phase, in this alloy it occurs when the Mo content exceeds about 0,75wt%. It is also worth mentioning that the M_3B_2 boride is stable down to a Mo content of about 0,25wt%. Due to the small M_3B_2 phase fraction the excess boron widens the region of the BN phase to much lower temperatures (about 750°C).

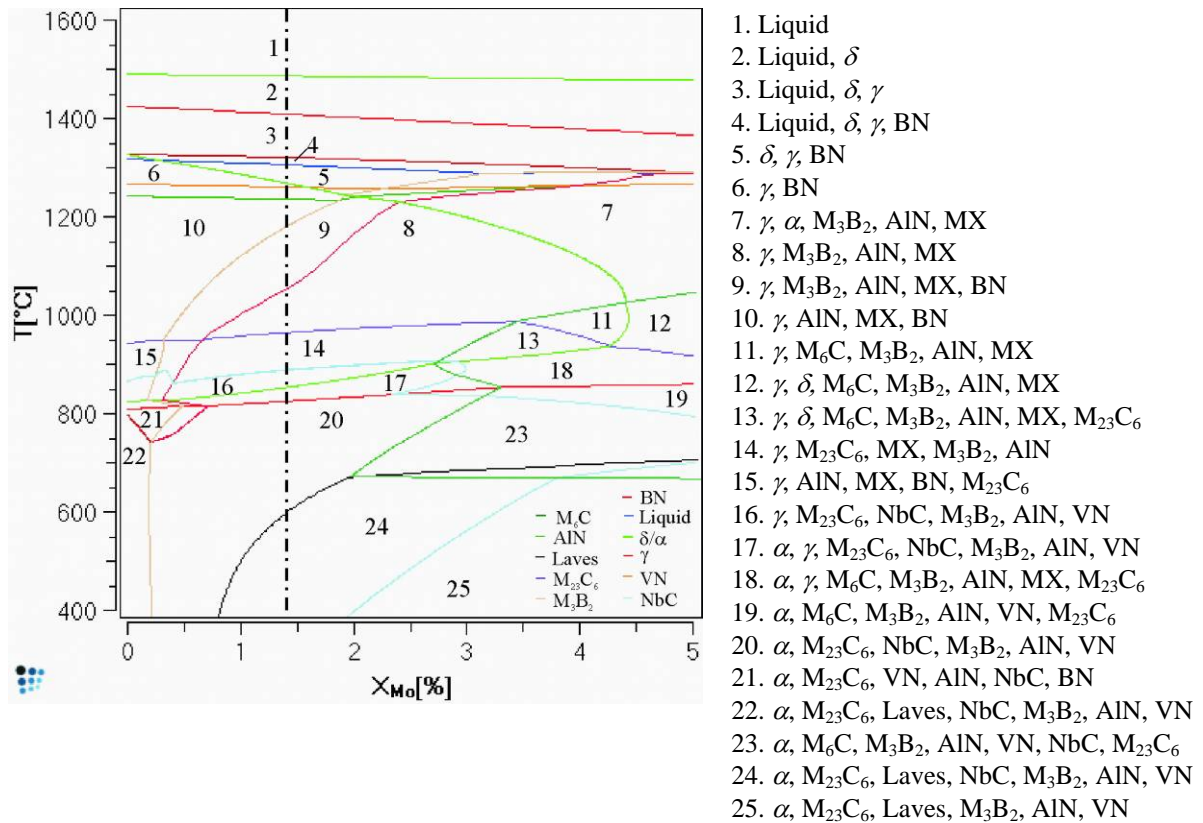


Fig. 68: Phase diagram of CB8 heat 173 P but varying molybdenum content from 0 to 5wt%. The nominal composition contains 1,4wt% Mo (dash dotted line). The calculation is based on the *Fe-Data* database.

Fig. 69 and Fig. 70 show the product of the phase fraction f and the element content X of the phase. This is one possibility to illustrate the influence of certain elements on the phase stability and composition and answers the question: Where is alloying element X ? Fig. 69 concentrates on the major MX forming elements V, Nb, C, and N. The NbC shows the highest concentration of niobium, also Laves phase contains a considerable amount of this element, especially at lower temperatures. The VN shows a higher solubility temperature and is the only stable MX phase between 900°C and 1250°C. Therefore this phase also contains Nb and C which form the NbC below 900°C. It is also worth to mention, that vanadium is the only element of the MX forming elements that is solved in the ferritic matrix in a considerable amount. The V/N ratio is apparently too high to incorporate all vanadium in the VN phase, the excess vanadium is therefore solved in Ferrite. Other facts are: AlN consumes about 45% of the available nitrogen and almost all carbon is dissolved in the $M_{23}C_6$ phase.

Fig. 70 concentrates on the elements Mn, Co, Cr, Mo, and B. Boron is believed to reduce the coarsening rate of $M_{23}C_6$ carbides [57] and to lower the grain boundary energy of the matrix phase, which stabilises the microstructure. Thermodynamic calculations can help to understand the boron influence by predicting where the boron is distributed in the microstructure. The borides occur down to a boron content of nearly zero, as shown in Fig. 67. Congruent to Fig. 70, boron is more or less dissolved in the borides, especially at lower temperatures, according to the calculation based on the *Fe-Data* thermodynamic database. The molybdenum is shared between the $M_{23}C_6$ carbide, the intermetallic Laves phase, M_3B_2 and ferrite. According to the Mo distribution Laves phase depletes ferrite from molybdenum. Co is not dissolved in any precipitate phases,

except a very small fraction contained in $M_{23}C_6$ near the A_1 temperature. Also about 80% of the alloyed chromium is solved in ferrite, the rest is predicted to be in $M_{23}C_6$, the same goes for manganese.

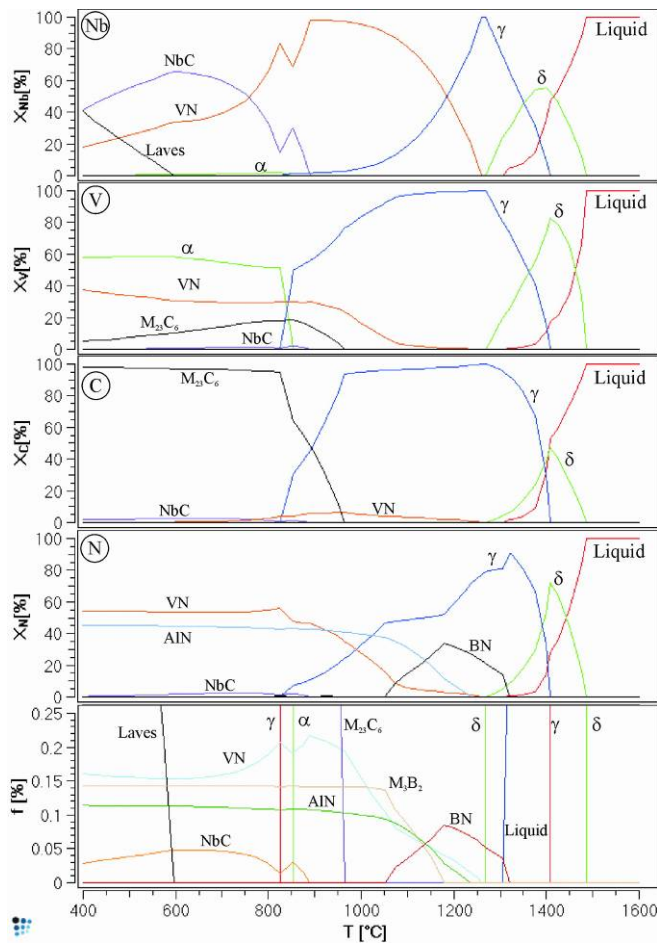


Fig. 69: The fraction of the elements Nb, V, C and N referred to the phase fraction of each phase. The values represent the product of the phase fraction f and the element content of the phase X normalized to 100%. Cb8 heat 173 P composition, based on *Fe-Data*.

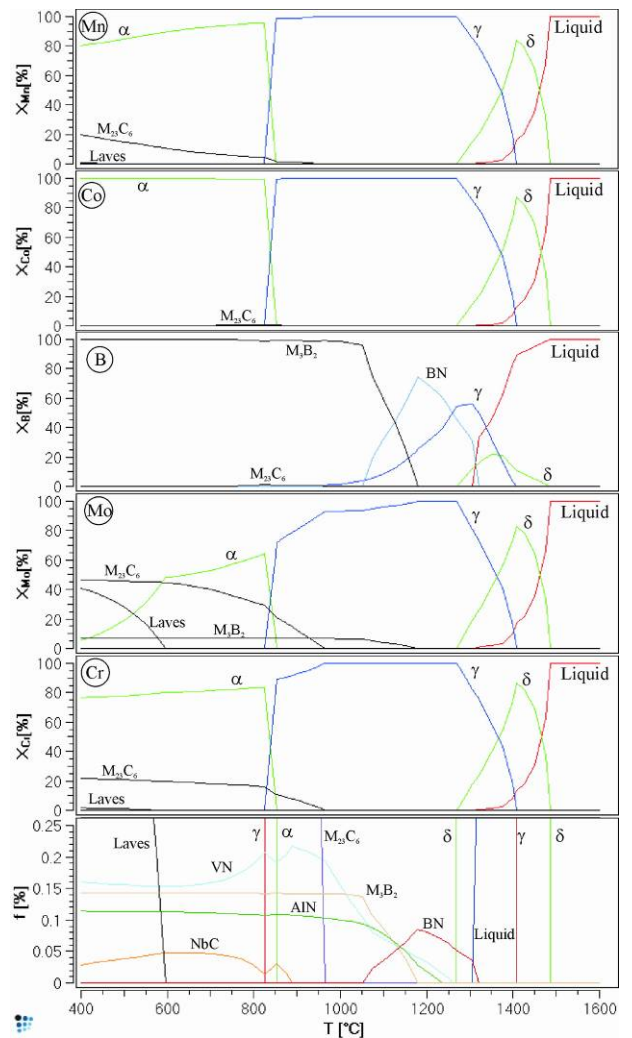


Fig. 70: As Fig. 69: The fraction of the elements Mn, Co, B, Mo and Cr referred to the phase fraction of each phase.

6.2.2 Comparing thermodynamic databases

A variety of thermodynamic databases is available to analyse iron based materials, the databases that have been used in the present work are summarized in Tab. 15. Not all databases describe the same phases. Particularly not every database contains boride phases, the Z phase or accurate descriptions of Laves phase. The element Boron was removed from the composition to be able to compare the results of all databases. The *SSOL version M* and *SSOL 4* thermodynamic database are the standard databases. More recent available databases for the field of ferritic steels are the *TCFE 3* and *Fe-Data*. The latter database contains a satisfactory set of boride describing parameters.

Tab. 15: Utilized thermodynamic databases

	<i>SSOL Vers. M mod.</i> [161]	<i>Fe-Data</i> [153]	<i>Kroupa</i> [158]	<i>TCFE 3 mod.</i> [156]
Boron	yes	yes	no	yes
Borides	M ₂ B tetra. Cr ₂ B ortho. Fe ₂ B ortho. Cr _a B _b	BN M ₃ B ₂ M ₂ B ortho. M ₂ B tetra.	no	BN B ₂ M Cr ₂ B ortho.
Z phase	Only in modified version	no	yes	Only in modified version
Status	Commercial	Commercial	Experimental	Commercial

Recently a new phase was found in specimens of creep resistant martensitic steels after long term creep tests, the modified Z phase. This stoichiometric phase of the form Cr(Nb, V)N was first assessed for thermodynamic databases by Kroupa, Danielsen and Hald [163]. The *Kroupa* database contains Z phase and also an improved description of Laves phase. The Z phase datasets [158] could be incorporated in the *SSOL* database too. More information about the Z phase can be found in chapter 3.2.2.

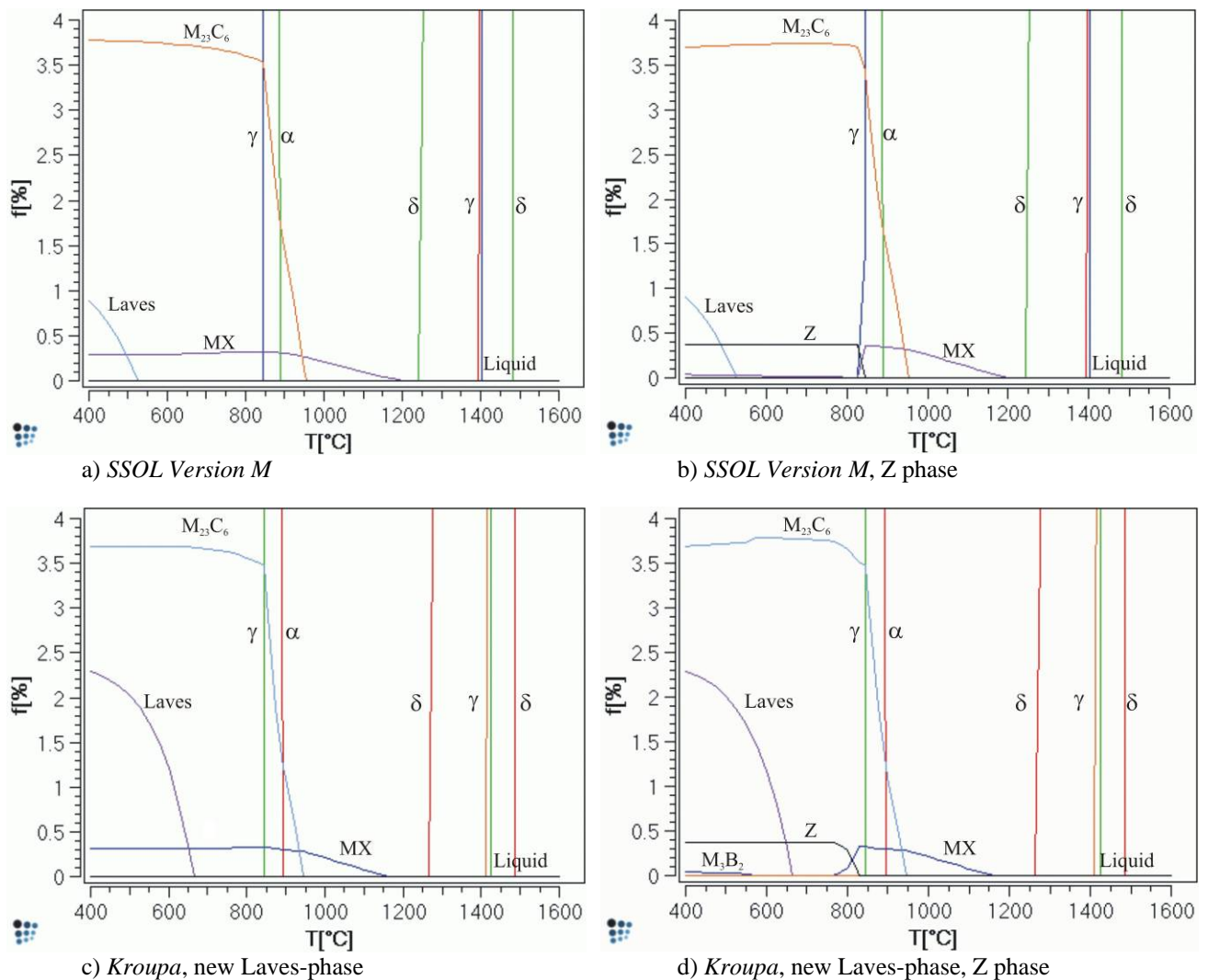


Fig. 71: (continued) Phase fraction diagram of CB8 heat 173 calculated with four different thermodynamic databases.

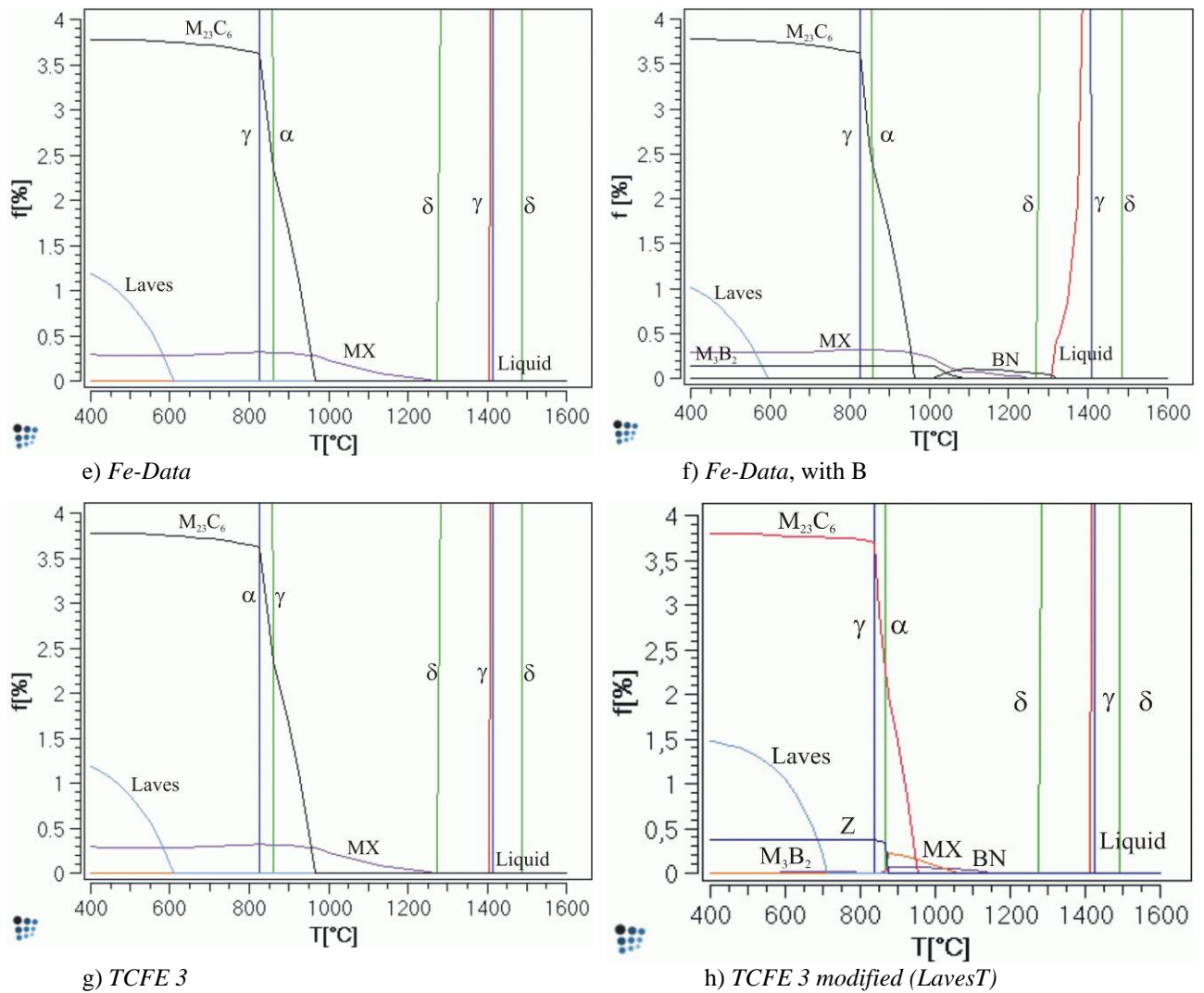


Fig. 71: Phase fraction diagram of CB8 heat 173 calculated with four different thermodynamic databases.

Fig. 71 a) to e) show phase fraction diagrams of the steel CB8 heat 173 P with the nominal composition as listed in Tab. 14 but without boron. Figure f) is very similar to the diagram in Fig. 63, showing the results including boron and the boride phases. To be as consistent as possible, in the phase fraction diagrams in Fig. 71 a)-f) only one complex MX phase is considered, because not all databases predict the miscibility gap between VN and NbC. The AlN phase was not considered in the calculations, because this phase is not available in all databases. Fig. 71 g) and h) show the phase fraction diagram predicted by the TCFE 3 in the original version and the modified version, respectively. Comparing the results of the SSOL version M database shown in a) and b) one can see that the Z phase replaces the MX phase almost over the entire ferrite region. At lower temperatures MX emerges marginally again as NbC which lowers the fraction of $M_{23}C_6$. The same effects can be seen in the phase fraction diagrams calculated with the Kroupa database (graphs c) and d)). The influence of the adapted new Laves phase are revealed by comparing the graphs a) to d) and the results presented in Fig. 63 and 64.

6.2.3 Thermodynamic equilibrium analysis (modified TCFE 3)

CB8 Phase diagrams

Two databases were selected for the precipitation kinetics simulation, *Fe-Data* and modified *TCFE 3*. Both provide actual assessments and are considered to be most reliable. In this case „modified” means that the description of Laves phase and MX phase was modified to show better agreement with experimental evidence in 9-12% Cr steels. According to the findings of Dimmler [8] the Laves phase description provided by Kroupa [158] is much more reliable in the area of 9-12% Cr-steels. Also the miscibility gap which exists between NbC and VN is pronounced by varying the SE-parameter. Otherwise a distinction between NbC and VN during the kinetic simulation is not possible, but the microstructural investigations reveal the two separated MX phases (see chapter 6.1). The equilibrium calculation results based on the modified *TCFE 3* database are introduced now and compared with the results based on the *Fe-Data*. The differences between the two databases in the range of Laves phase is the variation in composition, the higher phase fraction and the higher solubility temperature.

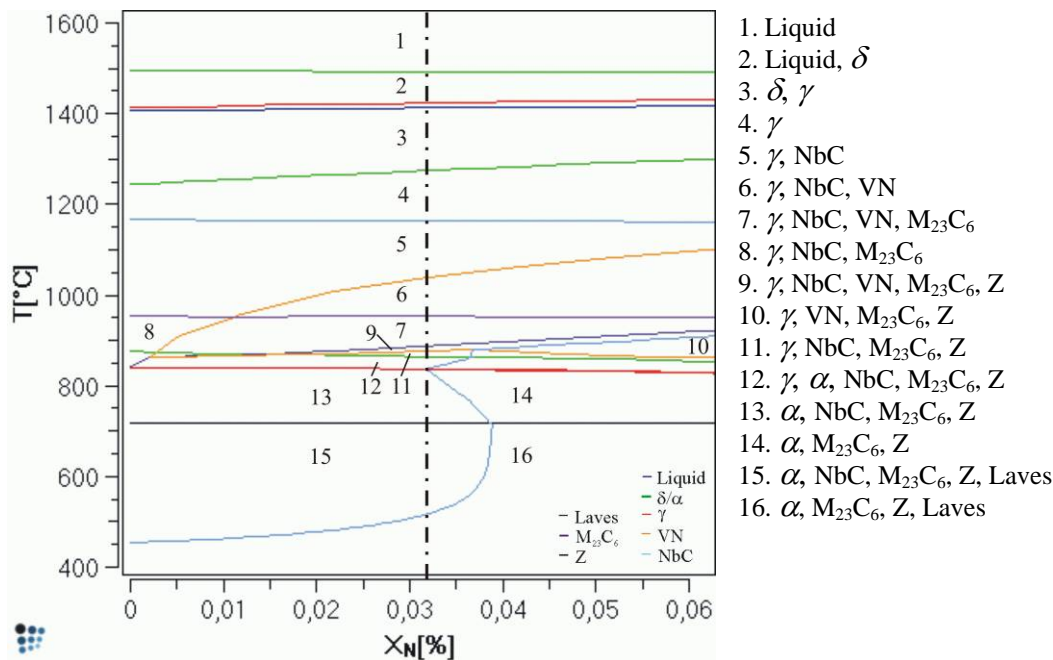


Fig. 72: Phase diagram of CB8 heat 173 P but varying nitrogen content from 0 to 0,06wt%. The nominal composition contains 0,0319wt% N (dash dotted line). The calculation is based on the modified TCFE 3 database.

Fig. 72 shows the phase diagram of CB8 with varying nitrogen content from 0 to 0,06wt% calculated utilizing the modified *TCFE 3* database. It is noteworthy that the Z phase is stable even at a system composition containing only traces of N. Below about 0,002wt% nitrogen the VN are not stable and the upper solubility temperature increases with the N content. The lower solubility temperature is demanded by the solubility of the Z phase. The upper solubility temperature NbC of about 1160°C is not influenced by the N content. The lower solubility temperature, in contrary, strongly varies with the N content. Above about 0,035wt% nitrogen, Z phase consumes also most of the Nb and besides VN also NbC dissolves when Z phase is stable.

CB8 Phase fraction diagram

Fig. 73 shows the results of the temperature step calculation of *CB8* based on the modified *TCFE 3* database.

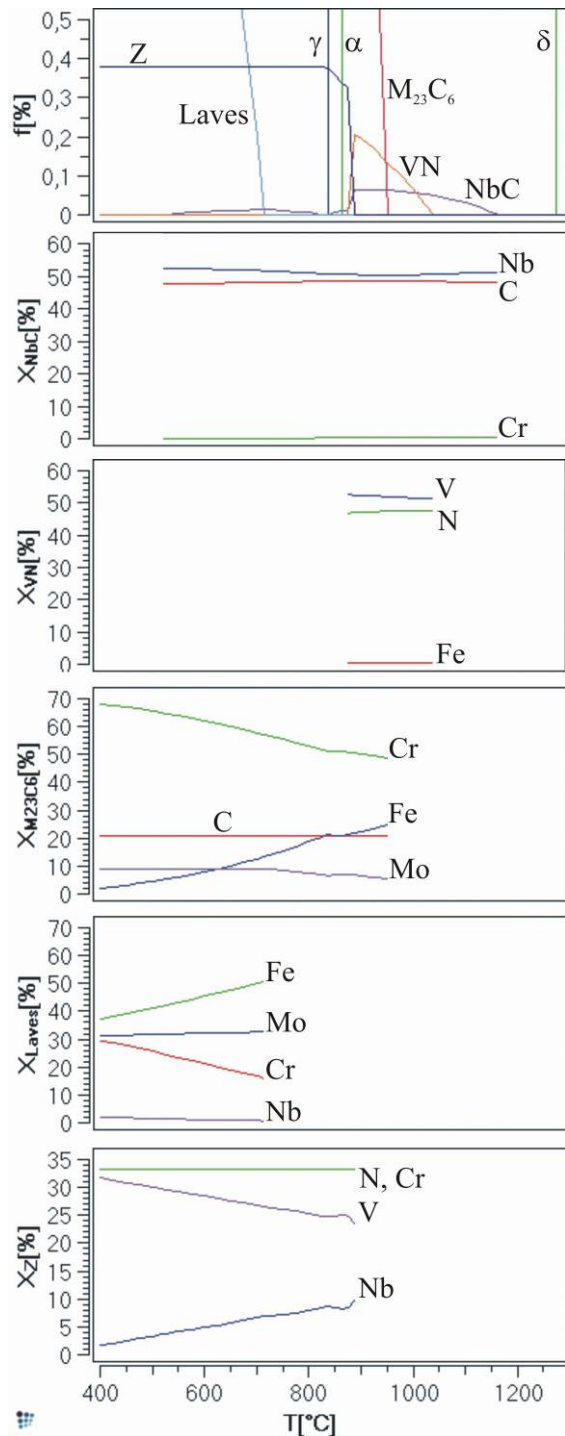


Fig. 73: The temperature dependent equilibrium composition of the phases NbC, VN, $M_{23}C_6$, M_3B_2 , Laves phase and Z phase. Only major elements are shown in the temperature range where the phases are stable. For comparison the detail of the phase fraction diagram is shown again below. The calculation is based on the *Fe-Data* database.

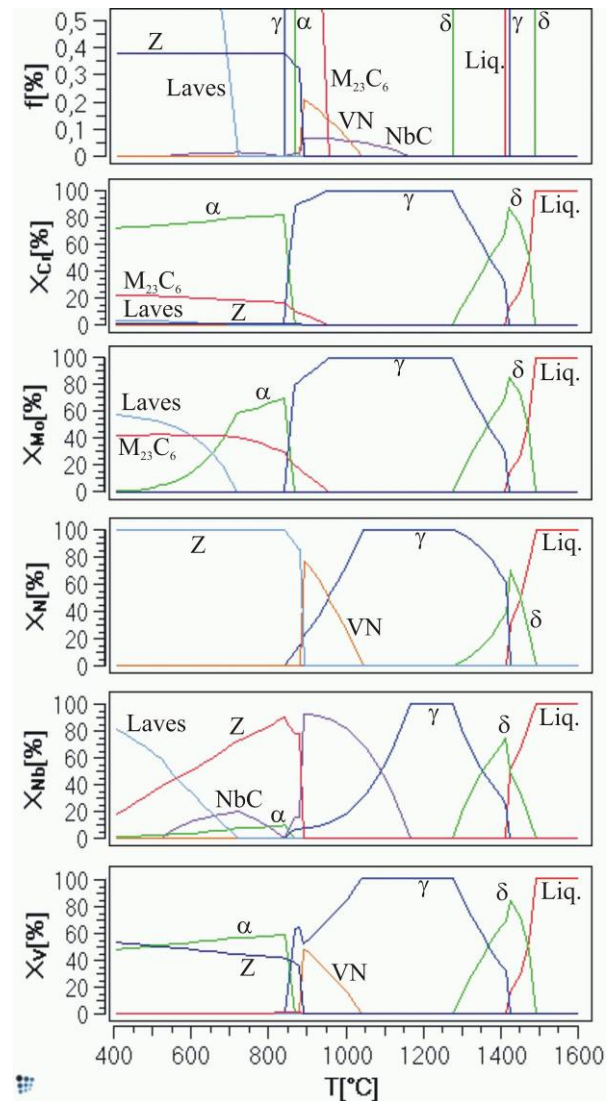


Fig. 74: The fraction of the elements Cr, Mo, N, Nb and V referred to the phase fraction of each phase. The values represent the product of the phase fraction f and the element content of the phase X normalized to 100%. *Cb8 heat 173 P* composition, based on *Fe-Data*. The calculation is based on the *Fe-Data* database.

The $M_{23}C_6$ and the Laves phase show a similar composition as predicted by the *Fe-Data* database (see Fig. 64). The Z phase consists of equal amounts of Cr and N. This phase also contains vanadium which displaces the niobium at lower temperatures. Fig. 74 illustrates the distribution of the elements in the phases (see Fig. 69 for comparison). It is worth mentioning that all nitrogen is allocated in Z phase, as well as remarkable amounts of niobium. Despite the influence of Z phase, the predictions of modified *TCFE 3* and *Fe-Data* with modified Laves do not show significant difference.

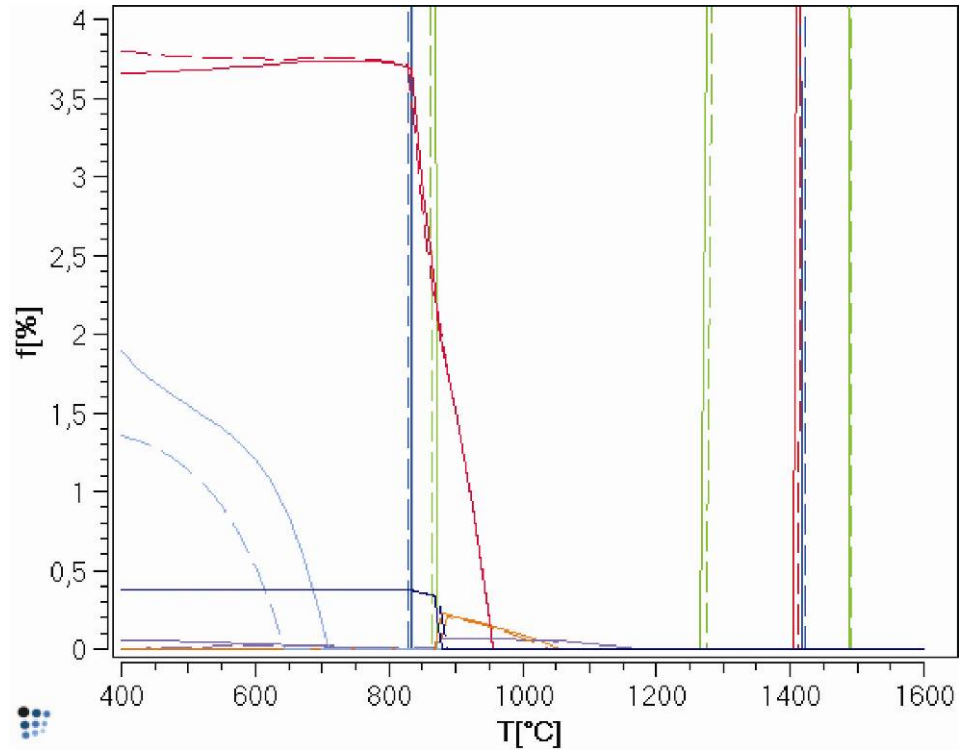


Fig. 75: Two variants of the phase fraction diagram of steel *CB8 heat 173 P*. The dashed lines represent the phase fractions calculated without silicon, the full lines are the same data as illustrated in Fig. 71 h). The calculation is based on the *Fe-Data* database.

6.2.4 Calculated interfacial energies γ

The changes performed on the thermodynamic data discussed in chapter 6.2 also influence the value of calculated interfacial energies (compare with 4.3.2). However, the modified *TCFE 3* database was utilized for the precipitation kinetic simulations of *CB8* (see chapter 6.3). Fig. 76 shows the results utilizing the modified *TCFE 3* database (full lines) and the original *TCFE 3* database (dashed lines). On the left side the influence of Z phase is illustrated, the results considering Z phase are represented by the dotted lines, without Z phase full lines.

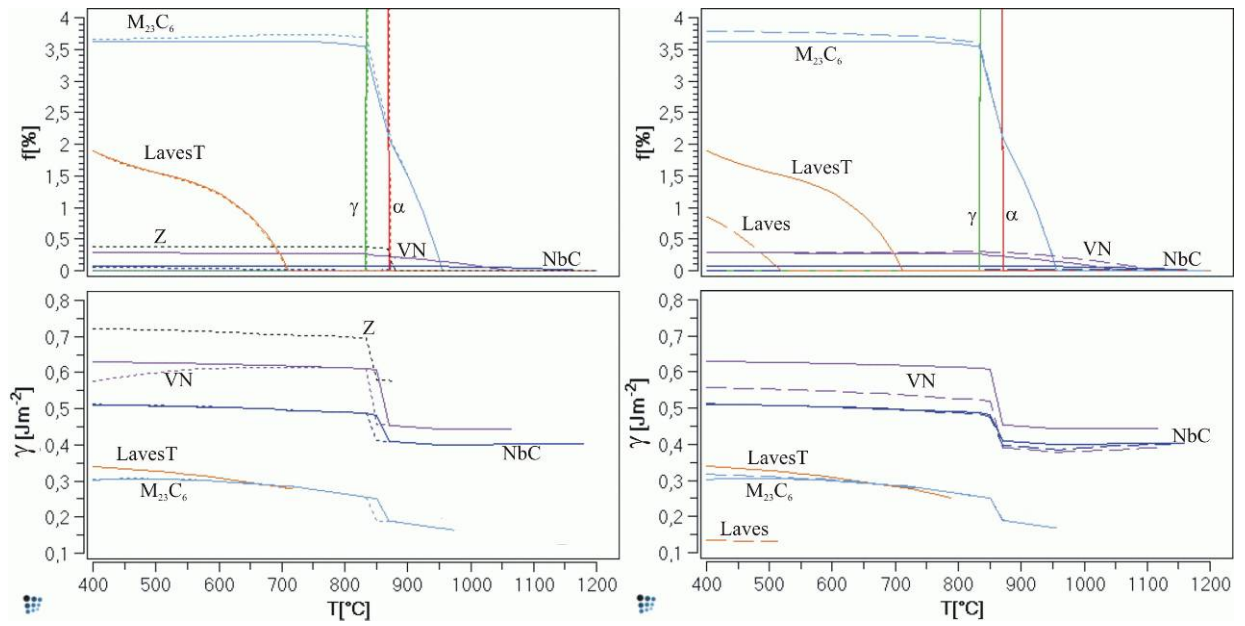


Fig. 76: Detail of the phase fraction diagram of the steel *CB8 heat 173* and the corresponding predicted specific chemical interfacial energies of the precipitates. Calculated utilizing *TCFE 3* thermodynamic database and the modified *TCFE 3*.

6.2.5 Microsegregation – Scheil-Gulliver simulation

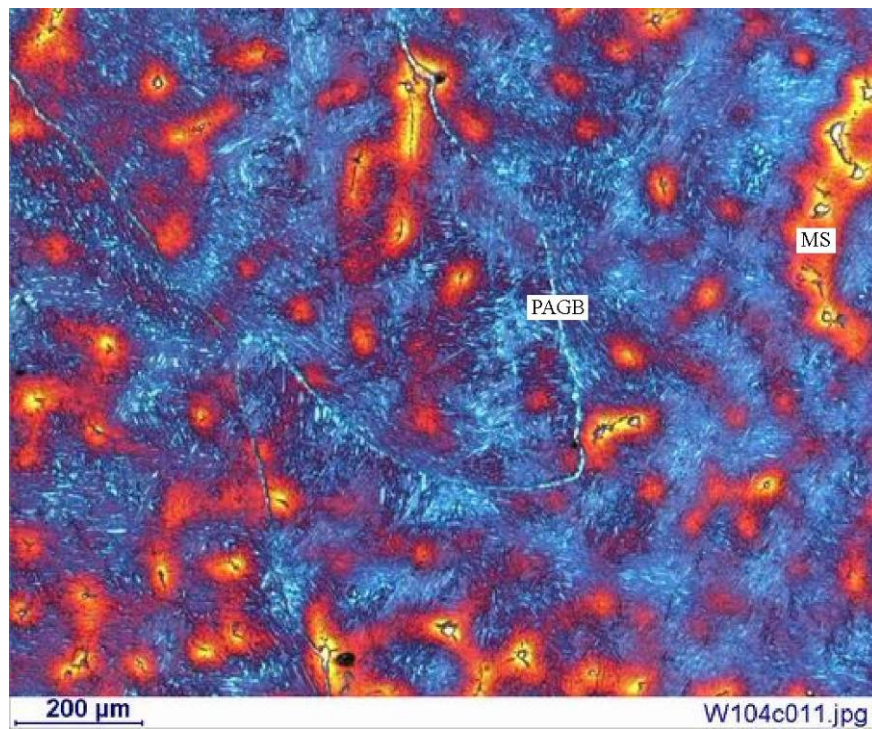


Fig. 77: Light microscopy image of a colour etched specimen of *CB8 heat 173 P* in as-cast condition. Inhomogeneities in composition appear in different colours (*MS*), also visible are prior austenite grain boundaries (*PAGB*).

The investigations of colour etched specimens in as-cast condition (see chapter 6.1) reveal a highly inhomogeneous microstructure consisting of martensitic grains surrounded by inhomogeneous regions (blue colour in Fig. 77) strongly segregated interdendritic regions originating from casting (Fig. 53). Due to the composition difference between the regions different precipitate phases form. In order to assess the possible influence of these segregations on the whole kinetic process in the early stages it is necessary to analyse the matrix composition and the phase fraction of potential precipitate phases. This task can be achieved by means of a modified Scheil-Gulliver analysis [164, 165].

The *Scheil-Gulliver* method allows calculating the fraction and composition of all phases during solidification step by step from the liquidus temperature to the temperature where solidification of the residual liquid phase occurs. In this case the residual fraction at final solidification was assumed to be 5%. According to the *Scheil-Gulliver* hypothesis, illustrated in Fig. 78, a solidifying liquid with the initial composition C_0 is slightly under cooled.

Consequently, a certain fraction of solid is formed with a composition of $C_{S,1}$ with the remaining liquid phase with the composition $C_{L,1}$. Both phases are in local equilibrium following the lever rule. From that instant on the composition of the solid phase, concerning the substitutional atoms, is frozen due to assumption of very slow diffusion in the solid phase. The interstitial elements boron, carbon and nitrogen are assumed to be nevertheless highly mobile in the liquid phase as well as the solid phase. Therefore these elements achieve overall equilibrium (liquid and solid phases) due to back-diffusion from the liquid phase into the solid phase [166]. This process occurs repeatedly, enriching the solid phase as well as the liquid phase with solute during cooling (Fig. 78: $C_{L,i}$ and $C_{S,i}$).

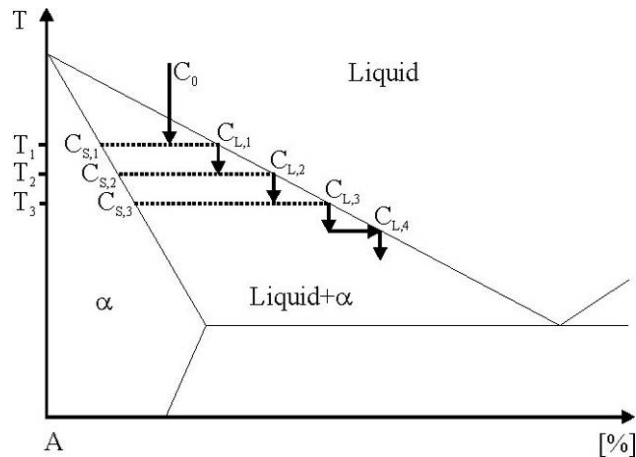


Fig. 78: Scheme of *Scheil* solidification of a hypothetic alloy. During solidification the actual liquid phase, beginning with C_0 , is under cooled and solidifies according to the lever-rule enriching both phases with solute [167].

When the solidification ends, the microstructure of the solid phase shows a composition gradient from the regions where the solidification started (centre of the dendrite) to the areas where the last liquid solidified (outer shell of the dendrite). The composition of the residual liquid at final solidification corresponds to the composition of the interdendritic regions. It should be noted that the Scheil-Gulliver analysis yields an upper limit of segregation since the substitutional elements also have a finite mobility and have some potential of back-diffusion.

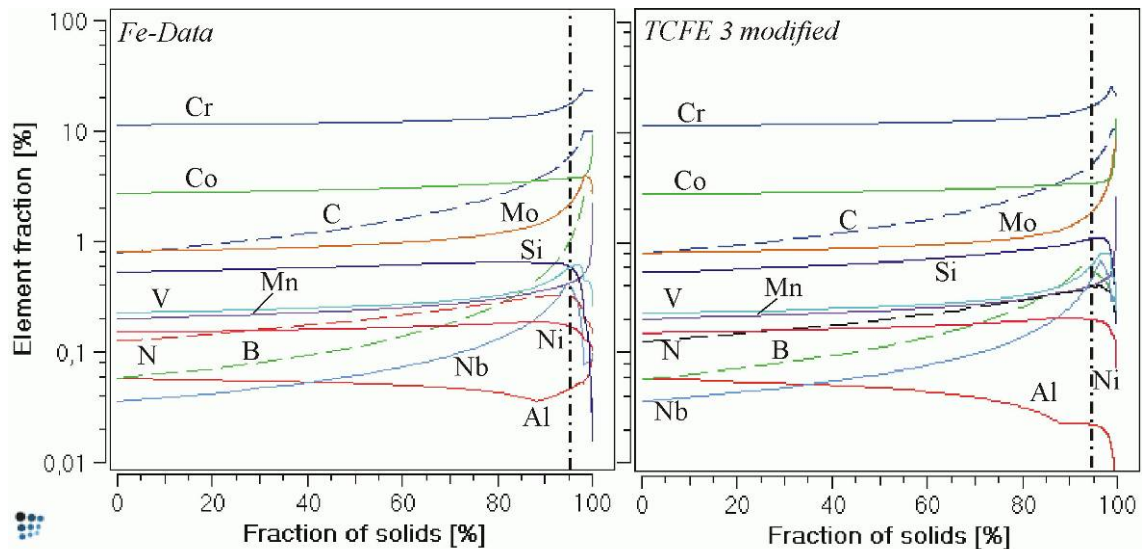


Fig. 79: Scheil calculation *CB8 heat 173 P* utilizing the *Fe-Data* thermodynamic database: Composition of the liquid phase, 5% residual liquid phase fraction indicated by dash dotted line.

As a result of the *Scheil-Gulliver* calculation the composition of a hypothetical alloy representing the segregated regions is achieved. As described, during cooling the remaining liquid enriches with certain elements while the liquid phase fraction decreases. The results of the calculation are shown in Fig. 79, where the element content in the liquid phase is given over the phase fraction of the sum of all solid phases. At a liquid phase fraction of 5% (dash dotted line) spontaneous solidification of the residual liquid with no further changes in composition is assumed. The last 5% of liquid is highly enriched with Cr, Co, Nb and V, see Tab. 16.

Tab. 16: *CB8 heat 173 P* composition and the hypothetical compositions of the residual melt with a phase fraction of 5%, Fe is balanced. The interstitial atoms boron, carbon and nitrogen are assumed to diffuse fast enough to reach the equilibrium condition. For this reason these elements are set to nominal composition for the hypothetical alloy.

wt%	Al	B	C	Co	Cr	Mn	Mo	N	Nb	Ni	Si	V
Hyp. <i>Fe-Data</i>	0,023			4,16	16,97	0,43	3,85		0,72	0,19	0,32	0,55
Hyp. <i>TCFE 3</i>	0,011	0,0112	0,17	3,80	16,17	0,42	3,43	0,0319	0,82	0,22	0,57	0,59
<i>CB8 heat 173 P</i>	0,028			2,92	10,72	0,20	1,40		0,06	0,16	0,27	0,21

The phase fraction diagrams representing this hypothetical segregation dominated compositions can be seen in Fig. 80. In contrast to the nominal *CB8 heat 173*, the segregated regions do not undergo the full phase transformation δ - γ - α . These regions probably consist of up to 98% δ -ferrite according to the present analysis based on the modified *TCFE 3* database. The results obtained from the *Fe-Data* based simulation predict about 70% δ -ferrite. The phase fractions of Laves phase are about the same, the *Fe-Data* based calculation predicts slightly more $M_{23}C_6$.

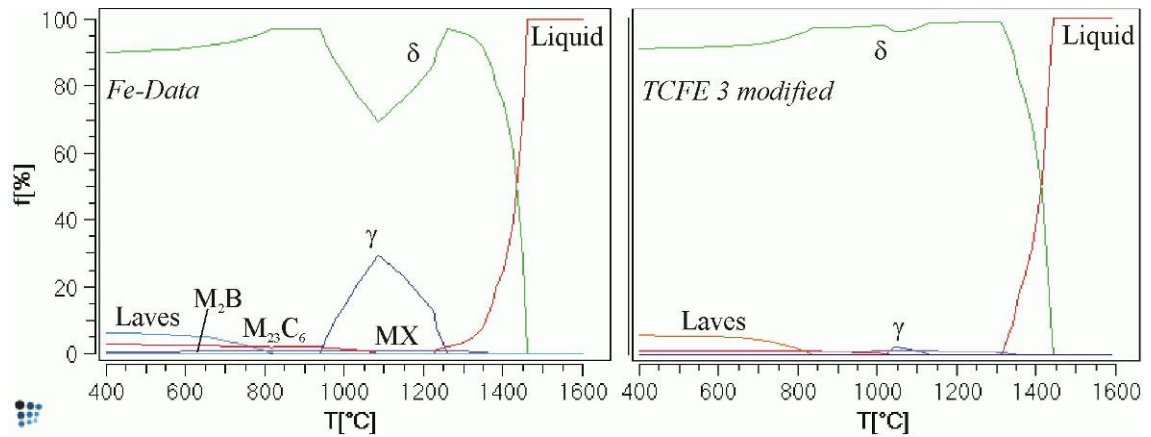


Fig. 80: Phase fraction diagrams based on hypothetical compositions as a result of modified Scheil-Gulliver calculations with 5% liquid fraction left. Utilizing thermodynamic databases: Left side the *Fe-Data*, right side *TCFE 3 modified*.

Concluding it can be assumed that the segregated regions do not influence the kinetic simulations presented in chapter 6.3 because they are relatively small compared with the not-segregated volume and they do not significantly dilute the matrix from any element. Moreover, the consecutive heat treatments and the phase transformation during austenitisation level out much of the initial segregation after casting. In the heat treated condition, the segregated regions have almost disappeared.

6.3 Thermal history of *CB8*

The steel *CB8* is a test-melt designed during the *COST 522* project to develop 9-12% Cr steels for application in 650°C *USC* steam power plants. Achieving a highly stable microstructure consisting of a tempered martensitic matrix strengthened by finely dispersed precipitates is the overall goal [168]. This ideal microstructure is reached by combining a sophisticated composition and a complex heat treatment consisting of austenitisation, annealing and a two step tempering. The simulations presented here help to understand the linked microstructural changes during manufacturing and service of 9-12% Cr steels. A basic version of these results is already published [169].

Tab. 17: Composition utilized in the kinetic simulation of the steel *CB8* in wt%.

Al	C	Co	Cr	Mn	Mo	N	Nb	Ni	Si	V	Fe
0,028	0,17	2,92	10,72	0,20	1,40	0,0319	0,06	0,16	0,27	0,21	bal.

A precipitation kinetic simulation of *CB8* with the composition given in Tab. 17 was performed with *MatCalc*. It has to be mentioned that boron, which is alloyed in *CB8*, was neglected due to unsatisfactory description in the database. The utilized databases are the *TCFE 3* [156] thermodynamic database in a modified version and the *MOB 2* diffusion database [157]. There is a need to simulate Z phase, because the breakdown of long term creep stability of a number of 9-12%Cr steels is thought to be caused by the precipitation of this recently discovered phase. Z phase dissolves MX precipitates, especially VN, and does not contribute to the precipitate strengthening effect due to its large size and low number density. The thermodynamic parameters for this phase [163] are still under development. This issue will be treated in detail by Holzer [170] who is performing currently a parameter study for Z phase incorporated in the present simulation.

6.3.1 Numerical Simulation

During a typical manufacturing procedure, 9-12% Cr steels undergo multiple austenite/martensite and martensite/austenite phase transformations, see chapter 6 for the time temperature evolution.

When the simulation starts at 1400°C, all elements are assumed to be in solid solution. The austenitic ingot cools down to martensite start temperature M_S and starts to transform. M_S is set to be 350°C in this case. In the simulations it is assumed that the transformation from austenite to martensite and back is occurring instantaneously and the parent and product phase have the same chemical composition. Furthermore, the precipitate population does not change during this transformation. It is also assumed that no noticeable kinetic processes occur at temperatures below M_S due to the sluggish diffusion of all atomic species.

During austenitising, a transformation back to austenite starts at the measured A_I transformation temperature of 847°C [29]. The material transforms to martensite again when cooling down after austenitisation. During the subsequent heat treatment and service the temperature stays below A_I and the matrix phase remains martensitic/ferritic.

During the simulation, all precipitates interact with each other by exchanging atoms with the matrix phase. 100 precipitate classes were considered for each precipitate phase. The interaction of six precipitate phases with the matrix phase is considered in the present simulation: The intermetallic Laves phase and Z phase with the major constituents Fe, W, Mo, Cr and Nb, N, V respectively. The carbides and carbonitrides are NbC (MX), VN (MX), M_7C_3 and $M_{23}C_6$ with the major constituents (Nb,V)(C,N), $(Fe,Cr)_7C_3$ and $(Fe,Cr)_{23}C_6$, respectively. Earlier simulations investigating the precipitation sequence in this group of steels (chapter 5.1.3) showed that cementite contributes but is dissolved by the other carbides and hence does not influence the precipitate microstructure of the other precipitate phases. Therefore this phase was not considered here to increase clarity.

Tab. 18: Microstructural parameter of the matrix phases.

Matrix phases	Austenite	Ferrite
Grain size [m]	100 10^{-6}	100 10^{-6}
Subgrain size [m]	/	0,1 10^{-6}
Subgrain elongation factor	/	100
Dislocation density [m^{-2}]	1 10^{11}	1 10^{14}
GB [Jm^{-2}]	0,24	0,24
Specific boundary interfacial energy	SGB [Jm^{-2}]	0,24
	Disl. [Jm^{-1}]	0,0

It has to be pointed out that the investigations (see chapter 6.1) show a miscibility gap in the complex MX phase, i.e. separate Nb/C rich precipitates and V/N rich MX precipitates. This fact was taken into account by artificially stabilizing the miscibility gap by varying the thermodynamic data of the corresponding precipitate phases. The exact procedure can be found in the print out of the script in chapter 9.2.2. Also the original thermodynamic parameters of the *TCFE 3* database describing Laves phase were replaced by a set of parameters according to Kroupa [158]. These variations were first

applied in thermodynamic equilibrium calculations presented by Dimmler [8] to fit the Laves Phase fraction of steel *CB8* to the actually measured values. Apparently the original thermodynamic data describe the tungsten-rich Laves phase very well, which could be confirmed by the simulation of steel *P92* (chapter 5.2.1). The Laves phase in *CB8* is based on molybdenum which slightly affects the simulation.

Tab. 18 summarizes important simulation parameters describing the matrix phases. The grain size, actually the prior austenite grain size, was set to a diameter of 100 μ m according to findings of Dimmler [8] and Sonderegger [30], as well as the subgrain size which is connected to the martensite lath width.

Tab. 19: Nucleation sites of the precipitate phases depending on the matrix phase. Abbreviations: *GB* grain boundary, *SGB* subgrain boundary, *D* dislocations.

Thermal cycle	Matrix	$M_{23}C_6$	M_7C_3	MX (NbC, VN)	Laves phase	Z phase
1. Casting						
2.2. Austenizing (847-1070-350°C)	Austenite	GB	GB	GB	GB	GB
2.1. Austenizing (350-847°C)						
3. Annealing & Tempering	Ferrite	GB, SGB	GB, SGB	GB, SGB, D	GB, SGB	GB, SGB, D
4. Service						

The diffusivities inside the precipitates are assumed to be 1% of the diffusion coefficients in the matrix. This is reasonable because of the much lower defect density inside the precipitates compared to the matrix. The model in its current status does not take composition gradients inside the precipitates into account. However, during the kinetic processes the matrix phase and precipitate phases vary the composition. Such variations imply a mass flux by diffusion inside the precipitate to and from the interface. Hence, the larger the precipitate the longer it takes to change the composition of the spherical volume, which may influence the whole set of chemical potentials. Anyhow, the heating rates and cooling rates of this simulation are small enough that no such effect became aware to the author.

The effective interfacial energies of all precipitate phases were calculated according to the procedure introduced in chapter 4.3; the values are displayed in Fig. 82. To support the nucleation of Laves phase the calculated interfacial energy of this phase was reduced by 25%. In order to moderate Z phase, the interfacial energy of which was increased to 125%.

Another kinetic parameter is the inactive radius factor *IRF* influencing the nucleation. The *IRF* was set to 5 for every precipitate phase (see chapter 4.2 for details). The nucleation sites are thus disabled in a spherical volume five times the diameter around each precipitate.

Connected to the matrix microstructure is the type of nucleation site, an important parameter for the simulations. Available nucleation sites are homogeneous sites (bulk, *B*) or heterogeneous sites, such as dislocations (*D*), grain boundaries (*GB*) or subgrain boundaries (*SGB*). How many sites are actually available is defined by the microstructural parameters grain size, subgrain size and dislocation density (see chapter 3.2.1).

6.3.2 Results and Discussion

To compare the numerical results and experimental data, specimens were simulated in a laboratory furnace according to the industrial heat treatment, beginning with austenitisa-

tion. Specimens were removed from the furnace and water-quenched at certain stages during the heat treatment. Phase fractions and precipitate distributions were measured. The results of the metallographic investigations have been summarized in chapter 6.1.

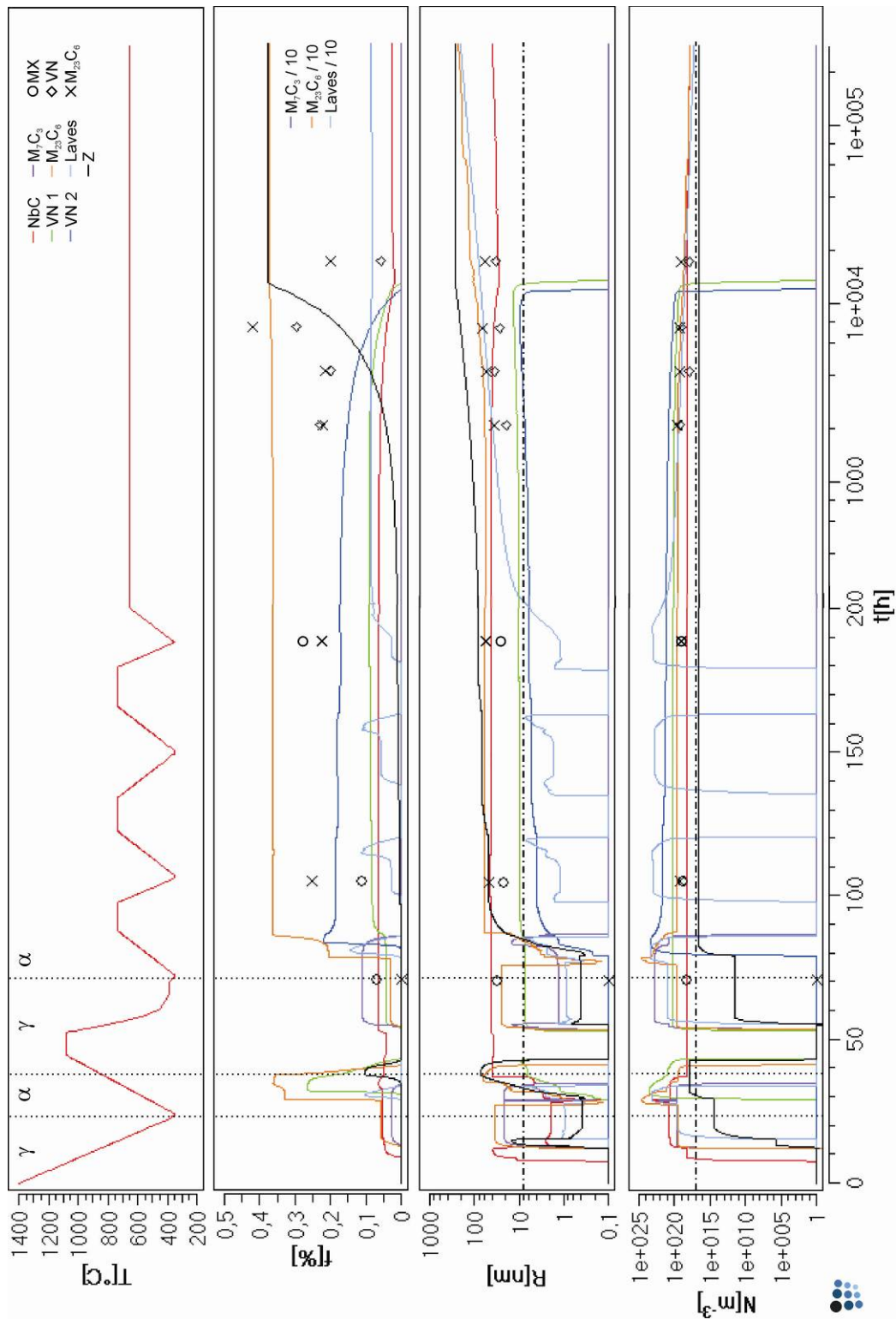


Fig. 81: This figure shows the time-temperature history and the corresponding graphs for precipitate phase fraction, mean radius and number density. The data points represent experimental values for the MX and $M_{23}C_6$ phases. The dash dotted line indicates the experimental identification and detection limit for the *EFTEM* method. The time scale is linear up to 200h afterwards logarithmic.

The various precipitates that occur in the course of the fabrication process are located on distinct microstructural sites. For instance, during casting, the first precipitates nucleating are the NbC carbides, occurring at the austenite grain boundaries. During subsequent reheating, other NbC precipitates and VN precipitates nucleate on the martensite lath boundaries and on dislocations. After austenitising and during tempering, a third wave of MX precipitates nucleates. In order to monitor separately the evolution of these different populations, one NbC and two VN (1 and 2) precipitate phases are introduced in the simulation. Besides their difference in thermodynamics, they are characterized by different conditions for nucleation.

Casting (1400°C – 350°C)

The simulation starts at 1400°C in an austenitic matrix containing no precipitates. While the material continuously cools down with 45K/h to martensite start temperature the NbC carbides nucleate first at about 1000°C and start to occupy the majority of their available grain boundary nucleation sites.

The next precipitate phases nucleating at about 840°C are the $M_{23}C_6$ and M_7C_3 carbides and the Z phase. The carbides stop nucleating due to nucleation site saturation (Fig. 82). Just below 700°C the Laves phase also starts to nucleate. Due to sluggish diffusion at lower temperatures, the kinetic processes slow down considerably below 650°C and practically stop at about 500°C. This effect is clearly visible in the graphs in Fig. 81; all lines run horizontally indicating that the precipitate microstructure does not change. At 350°C the first part of the simulation stops and the matrix phase is changed from austenite to ferrite without changing the existing precipitate distributions. At this instant the $M_{23}C_6$ reached the highest phase fraction value of about 0,5%; the NbC phase fraction is about 0,05% and the M_7C_3 phase fraction is even lower at about 0,025%.

Laves and Z phase do exist, but their phase fractions are very low, also the mean radius of these two phases is lower than 1nm. Due to their size and the low number density ($N < 4 \cdot 10^{15} \text{ m}^{-3}$) they are usually not easily detected by electron microscopy methods. The horizontal dash dotted line in the mean radius graph and number density graph (Fig. 81) indicates the detection and identification limit of the *EFTEM* method.

Austenitising (350°C – 1080°C for 8h – 350°C), stress relieving 385°C for 7h)

At the beginning of the austenitisation the matrix is switched from austenite to ferrite without changing the precipitate distribution or the composition. Due to the martensite lath structure and the high dislocation density more nucleation sites are available in Ferrite. The austenitic matrix in the configuration utilized here offers a number of nucleation sites in the order of 10^{24} m^{-3} , whereas the ferritic/martensitic matrix provides up to 10^{26} m^{-3} . The mobility of atoms rises with the temperature and due to high driving forces all precipitate phases (attached to the domain „Ferrite”) start to nucleate at about 550°C. At about 29h absolute simulation time $M_{23}C_6$ carbides saturate the available nucleation sites, they start to coarsen immediately. The newly introduced carbonitride phase VN 1 quickly develops a high number density and reaches a phase fraction of about 0,25%. NbC and M_7C_3 have already reached the maximum phase fraction during casting and adjust to the rising temperature and equivalent phase fraction. Laves phase is the first precipitate phase to reach the solubility temperature and dissolves completely at approximately 550°C. Thereby Cr and Mo is fed back into the matrix which boosts the $M_{23}C_6$ population to a phase fraction of 3,5% just below the A_1 temperature.

When A_1 is reached the matrix phase is changed to austenite. $M_{23}C_6$ and VN 1 show a mean radius and number density evolution determined by coarsening overlapped with dissolution. Elements available due to the dissolution of VN 1 are incorporated in Z

phase initially, which likewise dissolves shortly after. The smaller precipitates of the NbC population also dissolve and the phase fraction is reduced to the equilibrium phase fraction at austenitisation temperature. During cooling all phases nucleate and grow again. As observed during casting the $M_{23}C_6$ phase saturates the available nucleation sites as well as the VN 1 population. That circumstance retards the phase fraction increase slightly and sole growth is the determining mechanism.

Originally the austenitisation temperature was set to 1100°C, but the actual treatment of the specimens in the laboratory of the *IWS* was performed at 1080°C, which was also simulated. The nonlinear cooling was taken over from measured values during fabrication of a comparable industrial casting at *voestalpine* foundry Linz.

Process annealing, tempering 1, tempering 2 (each at 730°C for 10h, 12h and 14h)

Reheating during process annealing produces similar mean radii and number densities of all precipitate populations compared to reheating to austenitising, except NbC and of course VN 2 which is newly introduced. The mean radius of the NbC population is about 40nm in the „as austenitised” condition compared to about 2nm in the „as-cast” condition because these carbonitrides did not dissolve during austenitisation.

The precipitation microstructure developing during process annealing does not change significantly during the following tempering steps, nevertheless these tempering treatments are essential for manufacturing. Laves phase shows a nearly identical cycle of nucleation, growth and dissolution without coarsening at all three heat treatment steps. Z phase and VN 1 grow, overlapped by coarsening, on the expense of the smaller VN 2 population (*Gibbs Thomson* effect) on one hand and a higher thermodynamic stability (Z phase) on the other hand. It is interesting to note that during every heat treatment step new $M_{23}C_6$ precipitates are formed, but due to their small size the mean radius and number density in Fig. 81 do not change noticeable. Anyhow, the result is a multimodal distribution of $M_{23}C_6$ precipitates which can be seen in Fig. 84 g). According to this simulation Z phase already exists in the „as-received” condition, even though only with a small phase fraction. The author is not aware that this fact was reported up to now, a possible reason is the rather low number density of Z phase of about $5 \cdot 10^{16} \text{m}^{-3}$ and thus discovery is rather unlikely.

Service (350°C – 650°C for $2 \cdot 10^5 \text{h}$)

In the „as-received” condition the Laves phase mean radius is about 1nm, this population starts to coarsen at the service temperature and reaches a mean radius of about 200nm at the end of the simulated period of 280000h (~32a). During service Z phase first grows and increases its phase fraction on the expense of VN 1, VN 2 and also NbC. Parallel VN 1, VN 2 and NbC coarsen overlapped by dissolution, where the VN 2 precipitates dissolve faster due to their smaller radii compared to VN 1 (*Gibbs Thomson* effect). Global equilibrium is reached after about $2 \cdot 10^4 \text{h}$ (~2,3a) where the VN populations are dissolved completely and Z phase as well as the residual NbC population reach the equilibrium phase fraction. Beyond this moment the residual precipitate populations coarsen otherwise the individual compositions stay constant (see Fig. 83).

Notes

The simulation shows good agreement with the investigations in general. Due to some unavoidable simplifications, some simulation results in the early stages of the heat treatment show differences to the findings presented in ref. [30]. These deviations are limited and cancel out during the austenitisation simulation. The deviations originate in

the segregation of the real microstructure in the „as-cast” condition which is not considered in the computer simulation.

The measured mean diameter of the M_7C_3 in the „as-cast” condition is 200nm, the simulated mean diameter is only 40nm. According to Sonderegger [30] these precipitates are located in segregated areas which have different matrix composition and therefore provide different driving forces (discussed in chapter 6.1). This circumstance is not considered in the simulation, the matrix is assumed to be perfectly homogenous in composition at any time. The simulated mean diameter of the M_7C_3 after austenitising shows good agreement with the results from Sonderegger who also reports that the matrix composition shows nearly no segregations any more at this instant. The tempered martensitic matrix is approximated with ferrite in the simulation, because of lack of data in the thermodynamic database for martensite. This approximation is reasonable at the latest after the austenitisation simulation.

Interfacial energy and nucleation site saturation

A strongly affecting parameter for kinetic simulations is the interfacial energy γ of the precipitate matrix interface. This energy directly influences nucleation and coarsening. Since the critical energy for forming a nucleus is proportional γ^3 , small variations in γ can highly enhance the formation of a phase or completely suppress it.

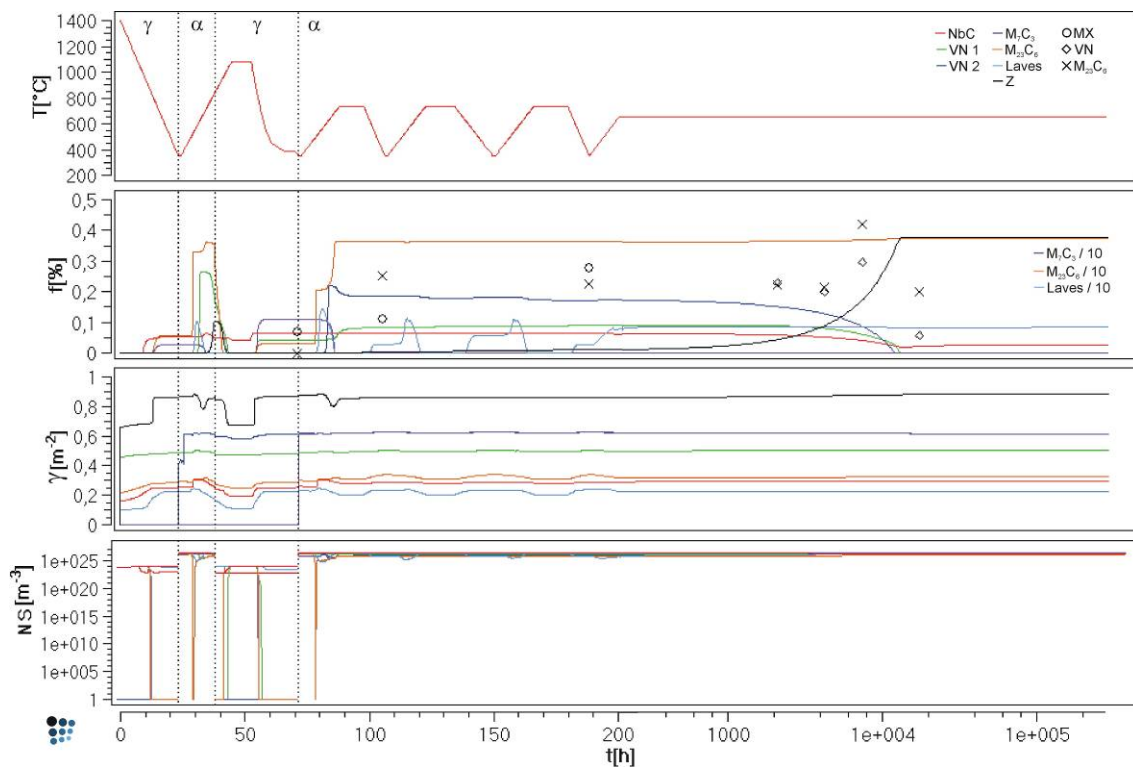


Fig. 82: This figure shows the time-temperature history and the corresponding graphs for precipitate phase fraction, calculated interfacial energies and available nucleation sites for every precipitate phase. Due to programming reasons the interfacial energies are calculated when the precipitate phase is attached to a domain. Therefore the interfacial energy values of VN 1 and VN 2 rises vertically after casting and austenitising, respectively.

It was the intention of the author to use the same set of parameters for all complex heat treatment simulations (compare with chapter 5.2.1) and to reduce the interventions via parameter variations to a minimum. Nevertheless the interfacial energies of Laves phase and Z phase were multiplied with constant factors to meet experimental results more precisely. The calculated interfacial energy of Laves phase was reduced by 25% in order to promote nucleation. Otherwise the number density and as a result also the phase fraction of Laves phase would be too small. The interfacial energy values of Z phase is increased by 25% because otherwise this phase would be too dominant. It has to be pointed out that the thermodynamic descriptions of both phases, especially Z phase, are still uncertain considering 9-12% Cr steels. These interventions will probably obsolete when the assessment of thermodynamic parameters is more reliable.

Evolution of the precipitate and matrix composition during simulation

Fig. 83 illustrates the variations in composition of the major precipitate phases and matrix phase. The driving forces for the kinetic processes strongly depend on the supersaturation of the matrix and the temperature of course. In general the composition of all precipitate phases is temperature dependent. Fig. 83 i) indicates that the individual heat treatment steps similarly affect the matrix composition.

The evolution of the composition of Laves phase seems to be only temperature dependent and uninfluenced by other kinetic reactions. No element diluted in Laves phase is significantly depleted in the matrix and hence the driving force is not limited due to declining supersaturation. This is illustrated for example by the trace of silicon in the matrix (Fig. 83 i)). The composition of Laves phase shows that the Fe content rises with the temperature and parallel the Si and Cr content decreases.

All other phases evidently interact with each other especially the carbides. The first nucleation limiting processes is the site saturation of NbC and $M_{23}C_6$ and then the depletion of the matrix from C and N in the „as-cast” and later the „as austenitised” condition. A significant drop in the C content can be seen when the $M_{23}C_6$ phase fraction rises during reheating to the austenitising temperature.

The nucleus composition of $M_{23}C_6$ is identical with the equilibrium composition at the corresponding temperature. During cooling to the M_S temperature the composition does not change significantly because of too small mobilities at low temperatures. Above a temperature of about 700°C the diffusivities are fast enough so that the composition of $M_{23}C_6$ precipitates reaches nearly identical values as predicted by equilibrium calculations. The major variation in composition of $M_{23}C_6$ is the changing Fe/Cr ratio. Observing the NbC composition (Fig. 83 c)) reveals, that there are no significant variations concerning the chemical composition. The C/Nb ratio just slightly shifts depending on the temperature. The composition of this phase is quite stable over the whole temperature range and no massive material transport via diffusion processes is necessary.

Similar considerations hold true for the Z phase. During the dissolution of the two VN precipitate populations vanadium is fed back into the matrix and instantly incorporated in Z phase, thereby the V/Nb ratio of Z phase increases.

The fact that both VN populations have nearly identical compositions during the heat treatment supposes that the composition is not significantly depending on the precipitate size. Instead the actual matrix composition and the temperature are responsible for the variations of the V/N ratio.

During service at 650°C every stable precipitate phase reaches the composition and phase fraction predicted by thermodynamic equilibrium calculation.

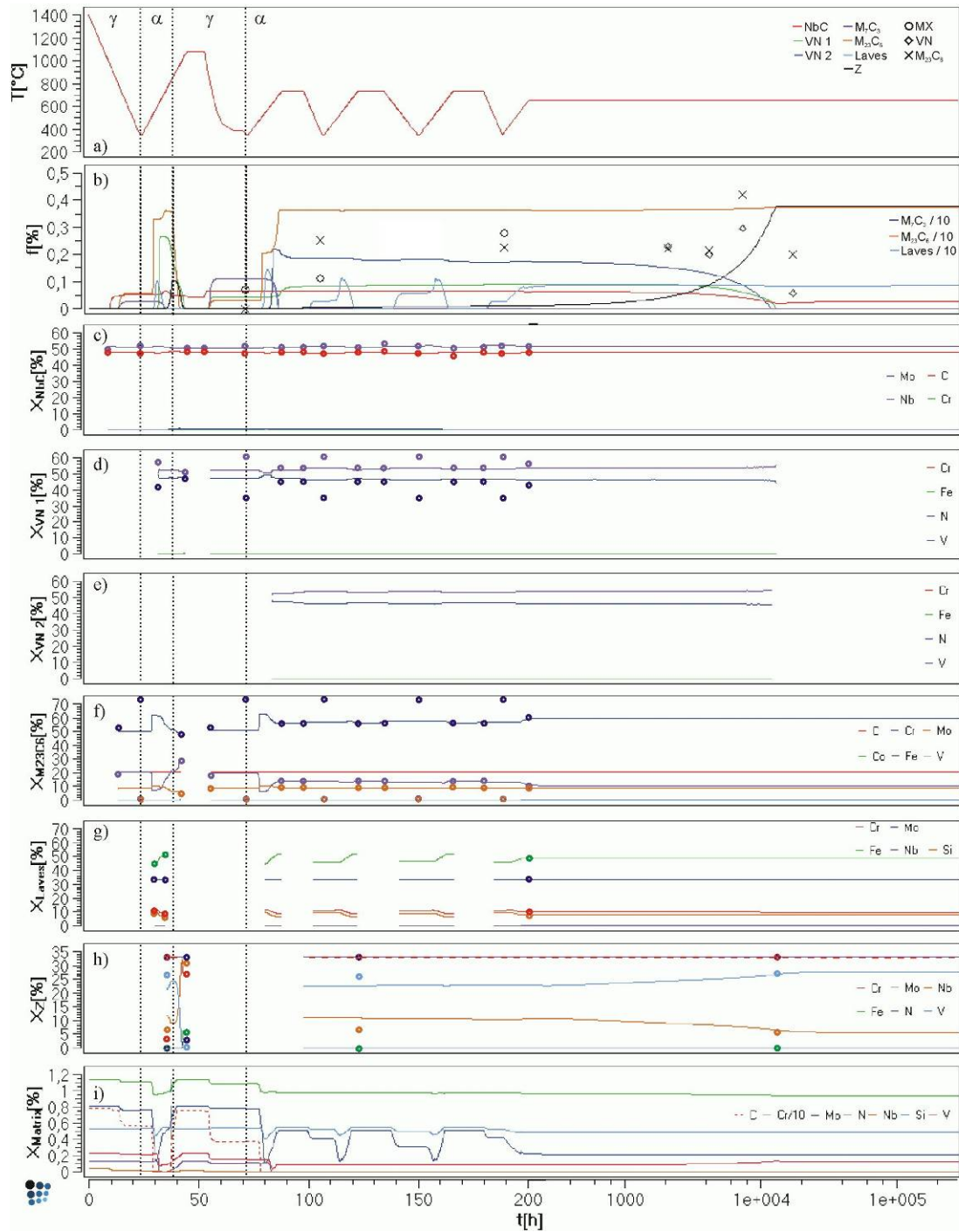


Fig. 83: This figure shows the time-temperature history and the corresponding graphs for precipitate phase fraction and the composition of the NbC, VN 1, VN 2, $M_{23}C_6$, Laves phase, Z phase and matrix phase. Only major elements are displayed. The coloured circles represent the equilibrium composition at the corresponding temperature.

Precipitate populations

In the present simulation the number of precipitate classes is 100 in order to display the influence of nucleation, growth and coarsening on the precipitate distribution. Fig. 84 shows distributions of $M_{23}C_6$ and Laves phase at certain stages during heat treatment

and service. Comparing Fig. 84 a) and b) illustrates a typical precipitate distribution in the growing stage partly overlapped with nucleation.

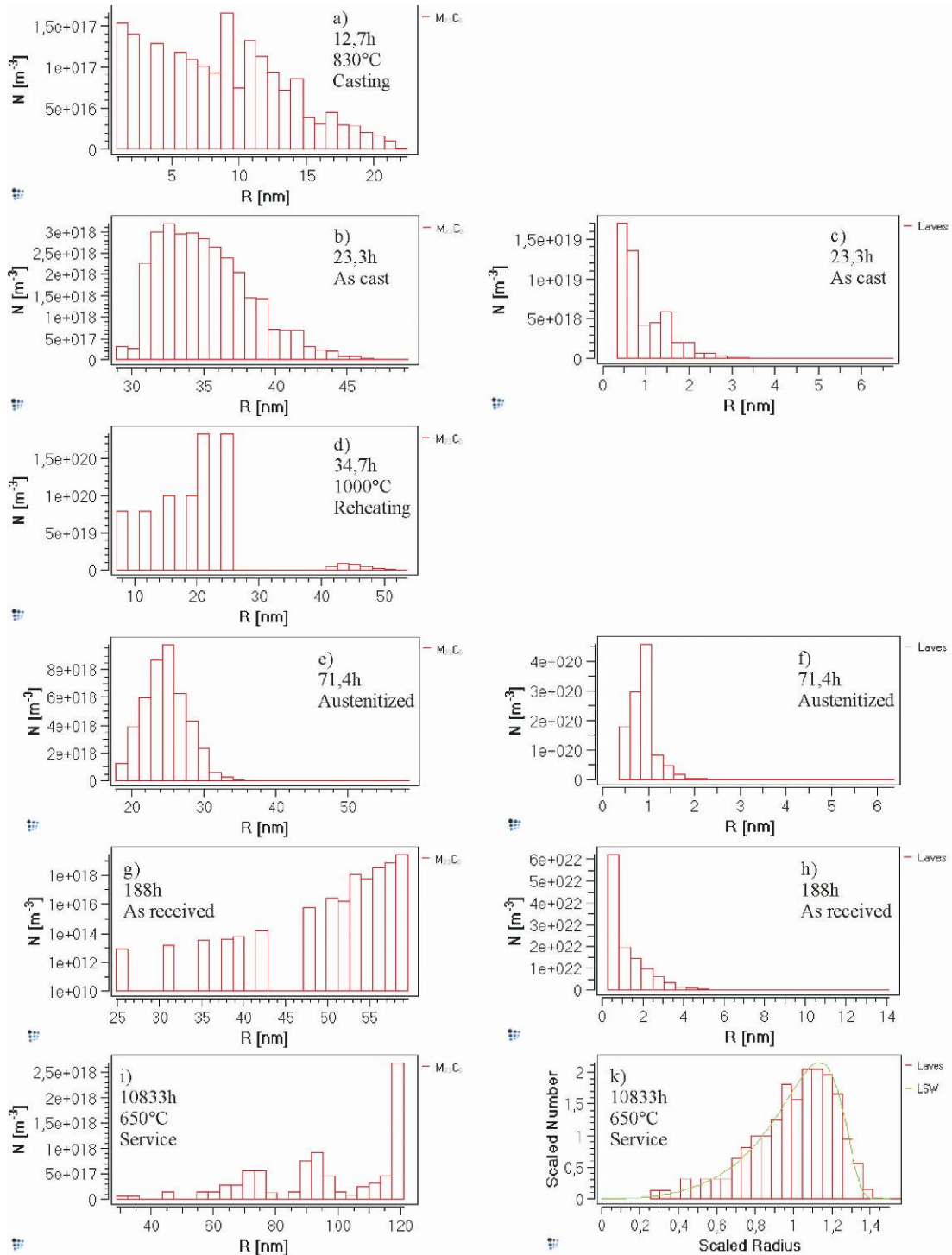


Fig. 84: These figures show the precipitation distributions of $M_{23}C_6$ and Laves phase at different times.

The left-shifted distribution in Fig. 84 a) is typical for the nucleation stage, where in Fig. 84 b) the nucleation rate already decreases because the smallest precipitates are not the most numerous. In the case of $M_{23}C_6$ the nucleation was reduced due to the depletion of the matrix with necessary elements like carbon and nucleation site saturation.

The Laves phase distribution is still left-shifted in the „as-cast” condition (Fig. 84 c)), because nucleation went on to low temperatures as the supersaturation of the matrix was still high regarding elements dissolved in Laves phase.

During reheating of the „as-cast” material nucleation of additional $M_{23}C_6$ precipitates is observed and parallel the existing precipitates grow. The resulting precipitate distributions are multimodal (Fig. 84 d)). At 1080°C during austenitisation the $M_{23}C_6$ precipitates dissolve completely and nucleate again while cooling down which leads to similar distributions as in „as-cast” condition (Fig. 84 e)), the same goes for Laves phase (Fig. 84 f)). At the end of the heat treatment in the „as-received” condition, the simulated precipitate distribution of $M_{23}C_6$ is again multimodal due to the repeated heating and cooling operations and hence nucleation processes during tempering. The number axis N in Fig. 84 g) is scaled logarithmically to emphasise the multimodal characteristic of the $M_{23}C_6$ population. A group of small precipitates ($25\text{nm} < R < 45\text{nm}$) is outnumbered at least 100 times by a group of large precipitates with a radius up to 60nm. Laves phase is completely dissolved during every heat treatment step and starts from scratch again afterwards. Therefore Laves phase only exists as a monomodal left-shifted distribution, typical for growth.

During service at 650°C for some thousand hours the Laves distribution changes to a *LSW* distribution as predicted by kinetic theory (chapter 4.1.3). The green line illustrates the envelope predicted by classical *LSW* theory for dilute binary systems. Complex alloys with significant phase fractions, like the one simulated here, develop precipitate distributions which are significantly broader than classical *LSW* (compare Fig. 84 k)). Considering $M_{23}C_6$ the simulated service time does not suffice to blur the multi-modal effect and therefore a typical *LSW* distribution is not achieved. Anyhow the $M_{23}C_6$ population coarsens, which can be seen on the mean radius trace depicted in Fig. 81.

Comparing coarsening rates

Desirable properties of a stable microstructure for high temperature application are low coarsening rates of the precipitates preserve a good creep resistance. The coarsening rates (see chapter 5.1.1 [149]) can be compared with the theoretical temporal power law:

$$R^3(t) - R^3(t_0) = K_R^{LSW} \cdot t \quad (84)$$

$$K_R^{LSW} = \frac{8}{9} \cdot \frac{V_m^\beta \cdot \gamma}{\sum_{i=1}^c \left[\frac{(X_e^\beta - X_e^\alpha)^2}{X_e^\alpha \cdot D_\alpha \cdot \frac{1}{R \cdot T}} \right]} \quad (85)$$

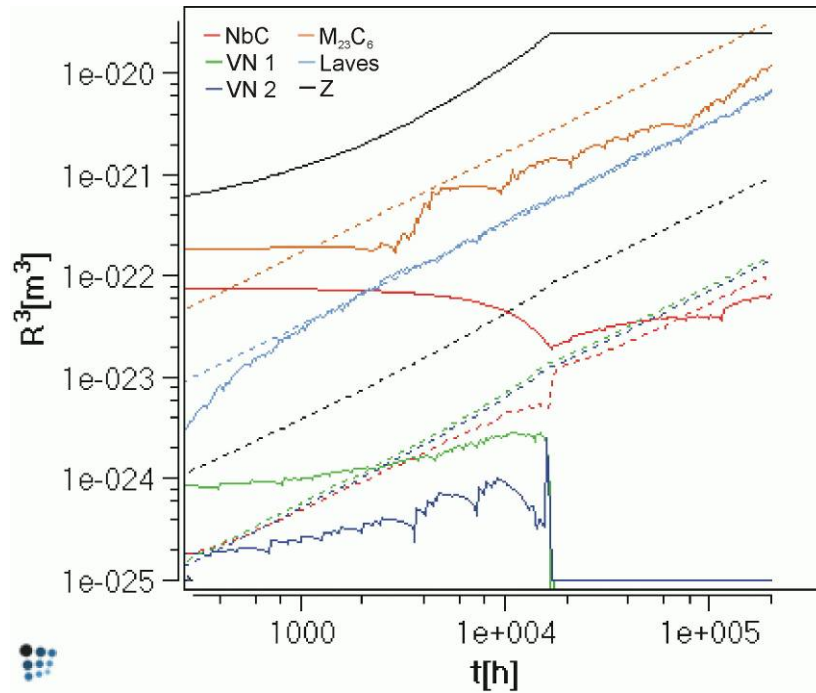


Fig. 85: The solid lines represent the simulated mean radii to the power of three. The dashed lines represent the coarsening gradients obtained from equation 85. The coarsening rates can be predicted analytically with satisfying accuracy for even complex systems.

Inserting the simulated mean radii into the equation above leads to Fig. 85 where the calculated coarsening rates are compared with the simulated coarsening. Only the gradients are of interest, the values for mean radii at the beginning of the service $R(t_0)$ are set to zero. It can be seen that Laves phase and $M_{23}C_6$ show excellent agreement with the theoretical value K_R . The other populations grow (Z phase) or dissolve (VN, NbC) overlapped by dissolution which changes the coarsening rates. After global equilibrium is reached at about $2 \cdot 10^4$ h the coarsening rate of NbC is also predicted correctly with K_R . Z phase is in the transient region between growth and coarsening until the end of the simulated time span.

6.3.3 Comparing two cooling rates from austenitising

The major benefit of computer simulations in this field is the possibility to gain knowledge about the influence of parameter variations, i.e. different compositions or heat treatment parameters on the microstructure and hence the properties of the component. A large casting like a turbine casing represents a geometrically complex component with different wall thicknesses and therefore inhomogeneous temperature distributions during heat treatment. It is possible to simulate the influence of different cooling rates by means of kinetic simulations. It has to be pointed out that only different cooling rates after austenitisation were considered to keep the influence limited. Anyway, the cooling conditions are more equal during casting due to the insulation effect as a result of sand in the casting mould.

The cooling rate after austenitising is not linear and therefore a cooling rate can not be given. Anyway, the linearised value of the slow cooling rate is about 40K/h and the linearised rate of the fast cooling rate is about 45K/h.

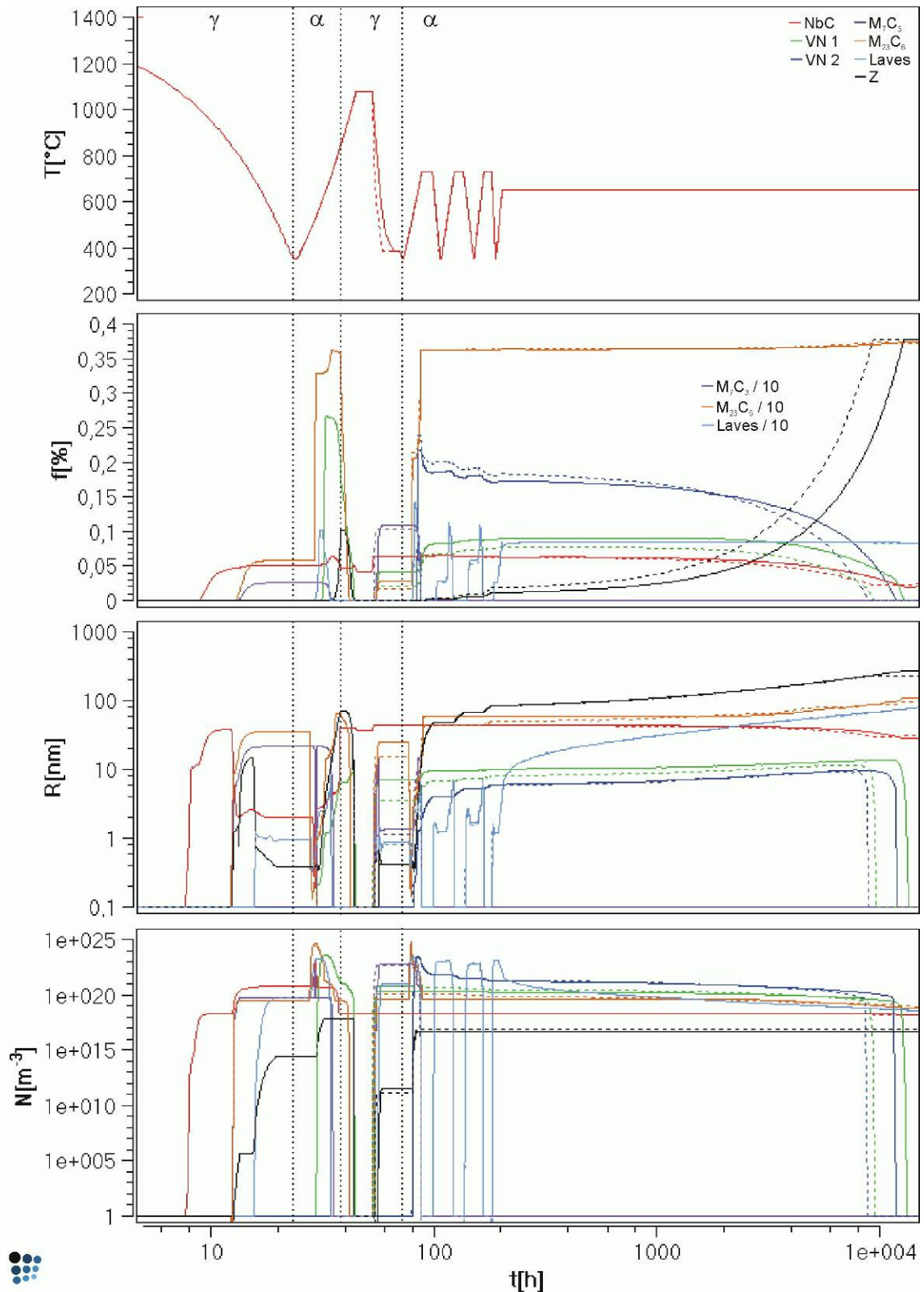


Fig. 86: Two simulations with different cooling rates after austenitising are compared. The solid lines represent the simulation discussed in detail above. The dashed lines represent the results for the same heat treatment except the faster cooling from austenitising temperature to stress relieving at 385°C.

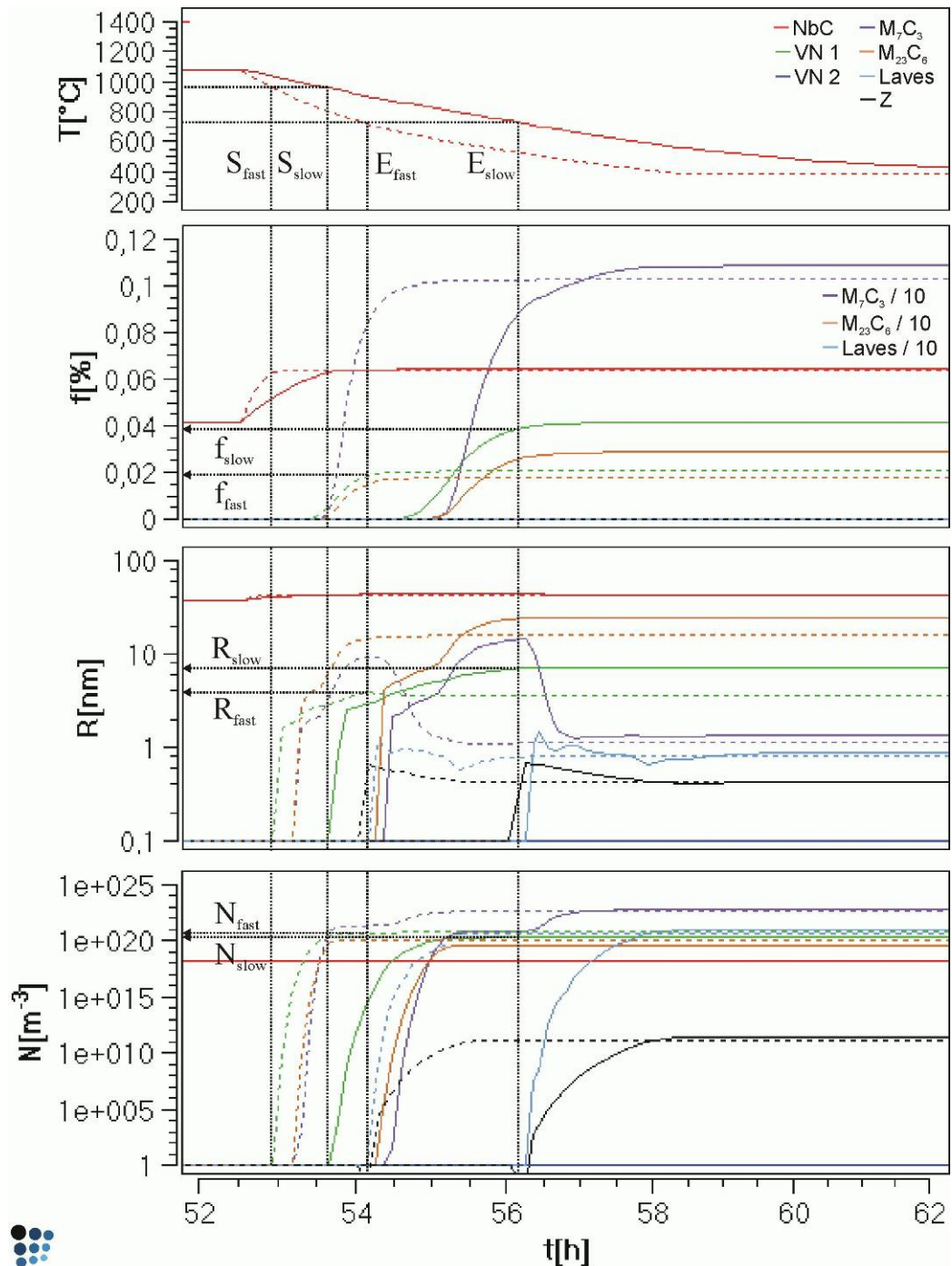


Fig. 87: A detail of Fig. 86, showing the cooling from austenitising to 385°C only. The solid lines represent the slow cooling rate, the dashed lines represent the fast cooling rate. The dashed lines represent the results for the same heat treatment except the faster cooling from austenitising temperature.

The difference between slow and fast cooling rates is exemplified by means of the VN 1 population, where the period of nucleation, overlapped with growth, is observed. Beginning S and end E of nucleation happen at the same temperature in both cases because due to the cooling rates no undercooling effects occur. The period of nucleation lasts longer for the slower cooling rate and during this time the precipitates also grow larger. Therefore less precipitates nucleate but the phase fraction reaches about twice the value. The processes are very similar for all precipitate phases.

As a result of a rapid cooling after austenitising the phase fractions of all precipitate phases except NbC are smaller. During reheating to annealing more VN 2 precipitates nucleate, compensating the lower VN 1 phase fraction. Thus the VN precipitates are smaller and consequently their dissolution due to increasing γ phase is finished about 5000h earlier. From that instant on the precipitation kinetic reactions are very similar to the reference simulation.

6.3.4 Comparing two austenitisation temperatures

The temperature level and duration of austenitisation is an issue often discussed. The goal is to homogenize the microstructure of the components. This includes dissolving the majority of the precipitates formed during casting, acquiring an ideal martensite lath structure, homogenising the matrix composition and parallel preventing austenite grain growth.

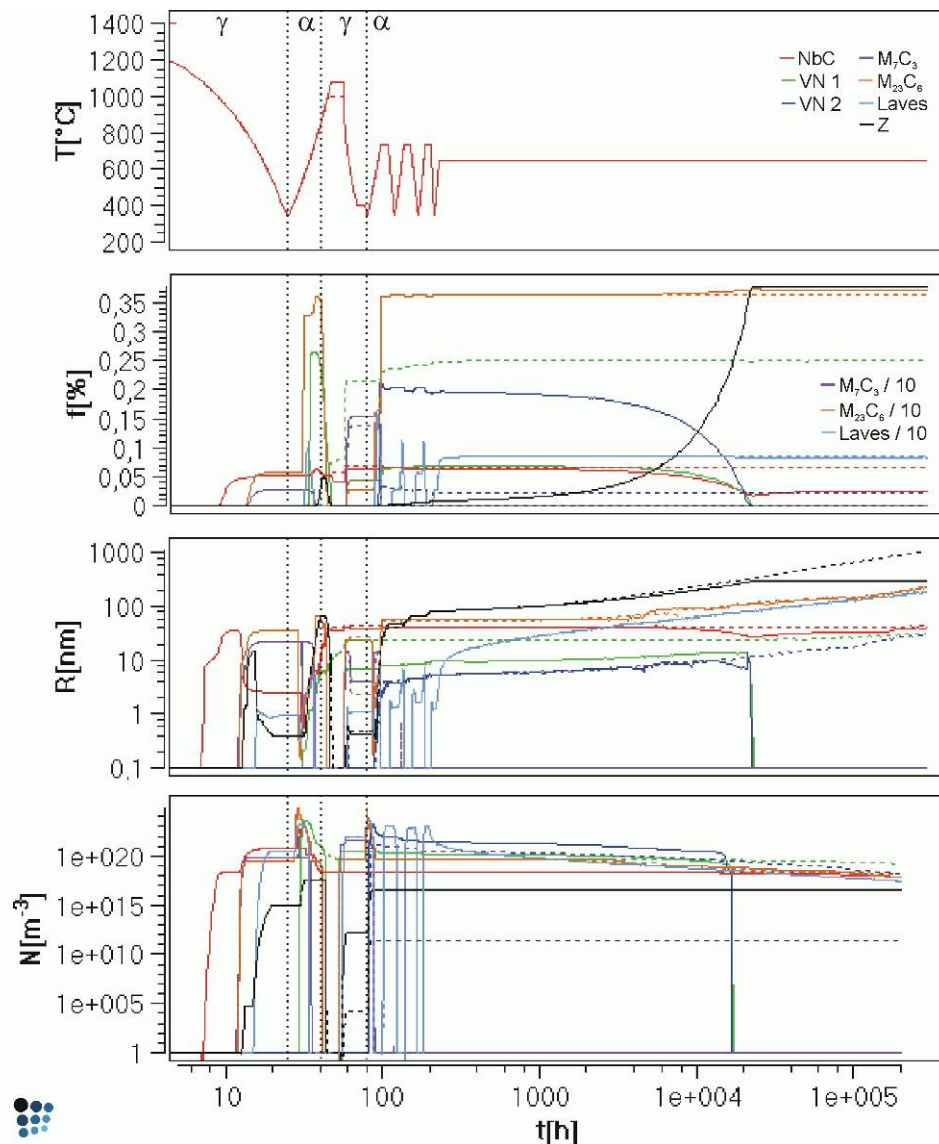


Fig. 88: The results of two simulations with different austenitisation temperatures are compared. The major difference is that Z phase precipitation can be retarded when the austenitisation temperature is reduced from 1080°C to 1000°C. The dashed lines represent the results for the same heat treatment except the lower austenitising temperature.

Fig. 88 shows the results for the simulation with an austenitisation treatment at 1080°C, as discussed before, compared to the results of an austenitisation treatment at 1000°C. Most conspicuous is the effect on Z phase. According to this simulation the Z phase kinetics is slowed down remarkably and the phase fraction does not reach noticeable levels before about 270000h (~31a). Z phase is not suppressed, but the maximum number density reached in the „as-received” condition is reduced by 10^5 times to 10^{12}m^{-3} .

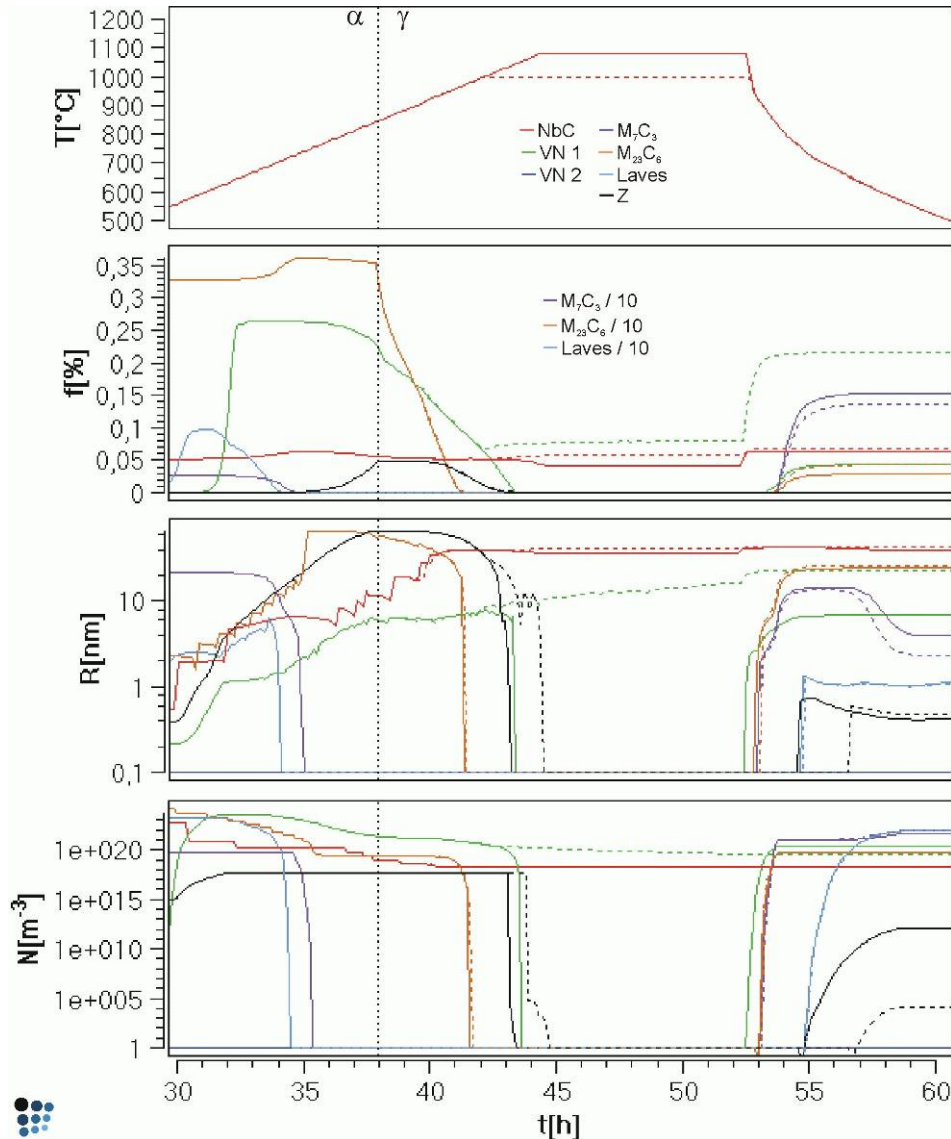


Fig. 89: A detail of Fig. 88, showing the high temperature section of austenitisation only. By reducing the austenitisation temperature well below the solubility temperature of VN, the formation of Z phase can be retarded. The dashed lines represent the results for the same heat treatment except the lower austenitising temperature.

These precipitates grow and coarsen very similar to the reference simulation, they even grow larger up to $2 \mu\text{m}$ in diameter at the end of the simulation. Z phase does not contribute to the precipitate hardening effect due to its size but dissolves preferred VN precipitates. If the VN population is not dissolved completely during austenitisation elements like vanadium nitrogen and niobium are not available to such an extent and hence the driving force for nucleation of Z phase is strongly reduced and the incubation time extended. The VN precipitates not dissolved at 1000°C coarsen which can be seen in

Fig. 89. During annealing the second VN population develops but expectedly does not reach equal values as in the reference simulation. As a result of the *Gibbs Thomson* effect the VN 1 phase fraction is slightly increased on the expense of VN 2 during tempering.

A reduction of the austenitisation temperature to 1000°C would therefore provide a more stable microstructure during service and the preferable MX phases are preserved beyond the design live of a power plant component of 200000h. On the other hand the VN population develops a larger mean radius which would reduce the precipitate hardening effect.

6.3.5 Comparing two annealing/tempering temperatures

The level of process annealing and tempering temperature is usually set in the range of 730°C for martensitic chromium steels. The idea of the three-step heat treatment is to soften the martensitic microstructure and to develop a finely dispersed precipitation microstructure. Anyhow, the temperature level is in proportion to the monetary and technical effort and therefore a lower tempering temperature would be appreciated.

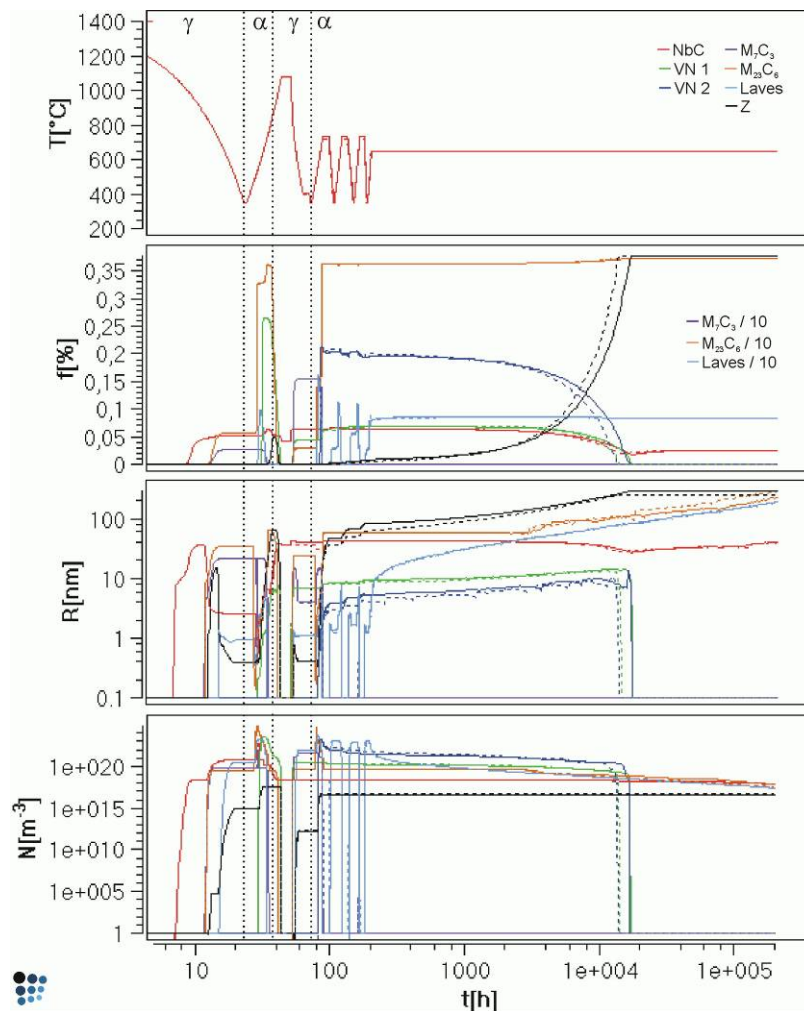


Fig. 90: The results of two simulations with different annealing/tempering temperatures are compared. The size of the VN 2 precipitates is smaller, therefore they dissolve faster and hence Z phase grows accelerated. The dashed lines represent the results for the same heat treatment except the lower annealing- and tempering temperature.

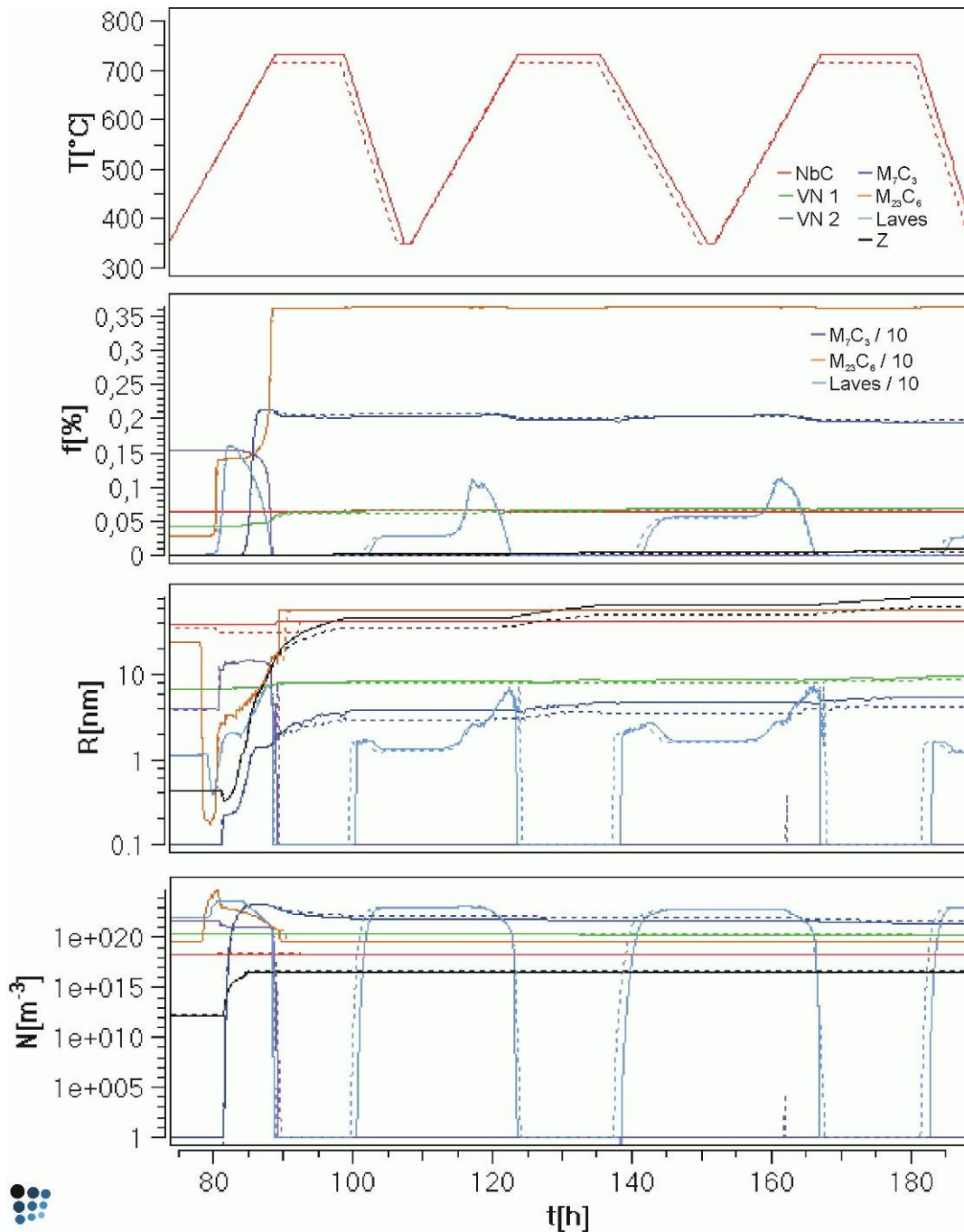


Fig. 91: A detail of Fig. 90, showing the annealing and two step tempering only. Due to the lower temperature of 715°C compared to 730°C the growth rates of the precipitate are reduced. The „as-received” condition is therefore determined by a finer precipitate microstructure. The dashed lines represent the results for the same heat treatment except the lower annealing- and tempering temperature.

A simulation was carried out with a reduced tempering temperature of 715°C and compared to the reference simulation. Less precipitates are dissolved at the lower temperature and the mean radii are smaller. The smaller VN 2 precipitates are faster dissolved by the Z phase during service which therefore shows a higher growth rate. After about 3000h simulation time the phase fraction of Z phase rises significantly faster. From this point of view a lowered tempering temperature is not favourable.

6.3.6 Comparing two service temperatures

Although the aspired service temperature for the steel *CB8* is 650°C, a simulation was performed with a service temperature at 675°C presenting the results in Fig. 92. Laves phase does not reach the same level of phase fraction compared to the reference simulation at 650°C because this phase has not reached the equilibrium phase fraction in the „as-received” condition. Due to the higher temperature the motilities of all atomic species are obviously enhanced and thus all kinetic processes are accelerated: The VN populations are fully dissolved after 6000h which is about half the time span compared to the service at 650°C. All growth and coarsening rates are higher; the consequence is an accelerated degradation of the microstructure and limited service time.

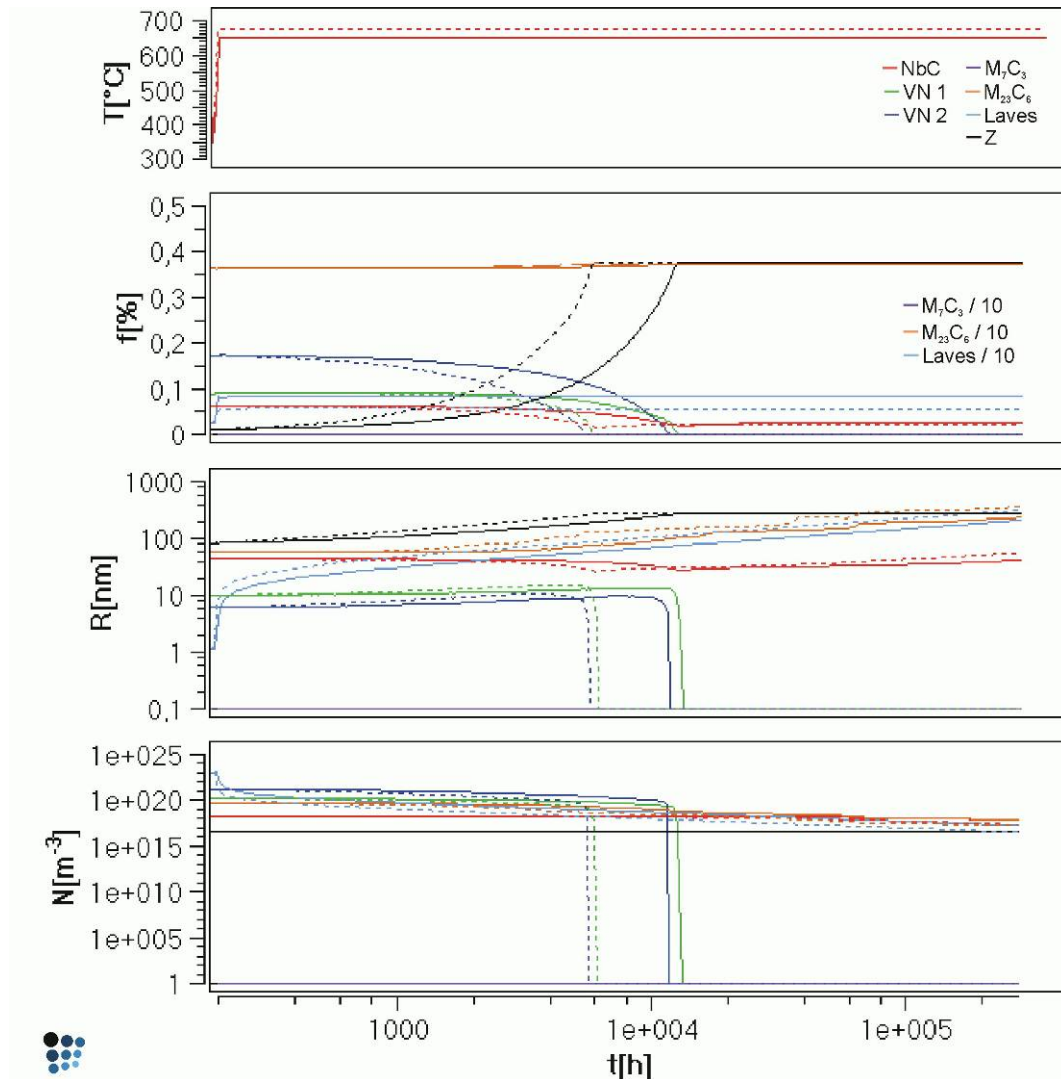


Fig. 92: The results of two simulations with different service temperatures at 650°C and 675°C respectively are compared. The graphs show the service only. The dashed lines represent the results for the same heat treatment except the higher service temperature.

On the other hand it can be seen that moderate overheating for a short time, planned or accidentally, would have no particular influence on the precipitate microstructure. The agreement between simulation and experiment is promising, in particular because the simulations have been performed without major adjustment parameters which were

utilized for two highly complex alloys (*P92* and *CB8*) which show partly different kinetic behaviour.

7 Summary, Conclusions, Outlook

Knowledge about the precipitate evolution during the manufacturing process and service is of great importance for an optimization of the precipitate microstructure to improve the creep resistance of modern power plant materials. The present work demonstrates how the evolution of different precipitate populations in time can be modelled with computational thermodynamics and kinetics. The basis of the simulations is given by thermodynamic and diffusional databases, combined with classical nucleation theory, which is adapted to apply to multi-component systems and a new model for the simulation of the evolution of precipitates in complex systems.

In general, modelling promises to be a tool for a variety of problems in materials science under the absolute prerequisite of a physically reliable basis of the models and „secure” materials data, e.g., for equilibrium thermodynamics and kinetic calculations. To provide real advance in the development of creep resistant materials, simultaneously, additional statistical analysis on basis of a large extent of carefully accessed experimental data is more than ever necessary.

With the novel model for simulation of the precipitation kinetics in complex alloys, the drawback of a limited number of elements, phases and particles of the previous models is overcome. It seems possible now that the amount, distribution and chemical composition of stable and meta-stable phases can be predicted by computational methods from the chemical composition and the process parameters such as the time/temperature history during production. Corresponding research is currently going on at the IWS with high emphasis.

A comprehensive R&D strategy has been introduced at the IWS, which covers the experimental characterisation of the creep behaviour up to refined microstructure investigations and advanced modelling. Through the multidisciplinary character of the approach, a comprehensive understanding of the mechanism operating during creep in 9-12% Cr steels can be achieved.

On the other hand, our investigations suggest that the problem of creep in these complex alloys has to be investigated on the local scale also, i.e. including nucleation and growth conditions of precipitates or the influence of deformation on the precipitation kinetics in general. Further topics are preferential orientations of precipitates and thus anisotropic mechanistic effects, inhomogeneities and texture in the microstructure. In the new microstructural modelling approach, these mechanisms can be taken into account.

A proposed usage of the software *MatCalc*, as it is available now, is to optimize alloy compositions with regard to phase fractions and coarsening rates by means of the equilibrium thermodynamic module which requires only slightest computation time. Basing on these alloy predictions kinetic simulations allow to optimise the heat treatment parameters. Joined with specialised investigation methods the time for development of new alloys with specific properties will be reduced.

The results presented in this thesis prove amongst other findings, that two important parameters for kinetic simulations can be predicted independently. The effective interfacial energies γ and the number of available nucleation sites N_S are usually fit-parameters. γ influences the whole kinetic process especially nucleation of precipitates. These energies can be calculated by means of thermodynamic databases and microstructural parameters based on a nearest neighbour, broken-bond approach. The available nucleation sites N_S determine the initial maximum number of precipitates and thus have a determining influence on the final microstructure.

Furthermore comparison of simple and complex heat treatment processes stresses that it is inevitable to simulate the full manufacturing heat treatment prior to the isothermal service simulation. It has to be pointed out, that isothermal simulations of highly complex alloys have to start from proper starting conditions (microstructure) and thus appropriate assumptions are necessary. By starting a kinetic simulation with casting, the „as-received” condition is generated individually and the heat treatment parameters can be optimised. This ability opens the kinetic simulations with the *SFFK* model to R&D application.

8 Bibliography

- [1] I. Paul „Super Critical Coal Fired Power Plants; A technology Being successfully Deployed in Developing Countries” <http://www.worldbank.org>
- [2] „Umweltbericht 98, Kapitel 6 Der Treibhauseffekt“ 1998, Verbund - Austrian Power Trading AG
- [3] G. Dimmler, P. Weinert, H. Cerjak „Investigations and analysis on the stationary creep behaviour of 9-12% chromium ferritic martensitic steels” Proc. 7th Liège Conf., Materials for Advanced Power Engineering 2002, Liège, 2002, pp. 1539-1550
- [4] H. Cerjak, G. Dimmler, P. Hofer, E. Kozeschnik, E. Letofsky, C. Pein, J. Rajek, B. Schaffernak, B. Sonderegger, P. Weinert „A Comprehensive Approach to the Development and Improvement of 9-12% Cr Steels - Report, Status & Outlook” Proc. 4th International Conference on Advances in Materials Technology for Fossil Power Plants, Hilton Head Island, SC USA, 2004, pp. 919-940
- [5] Sir Oliver Lyle „The Efficient Use of Steam” Her Majesty’s Stationery Office, 1947
- [6] R. Blum, R. W. Vanstone „Materials Development in Thermie Project for 700°C USC Plant” 8th Ultra-steel Workshop, Tsukuba, Japan, 2004
- [7] G. Kukutschki „Sammlung und Auswertung der Materialdaten von Stählen für Gas- und Dampfturbinenrotoren anhand eines Eigenschaftsprofils“ Diploma thesis, Graz University of Technology, Graz, 2003
- [8] G. Dimmler „Quantifizierung der Kriech- und Zeitstandfestigkeit von 9-12% Cr Stählen auf mikrostruktureller Basis“ Ph.D. thesis, Graz University of Technology, Graz, 2003
- [9] H. K. D. H. Bhadeshia, A. Strang, D. J. Gooch „Ferritic power plant steels: remnant life assessment and approach to equilibrium“ International Materials Reviews, Vol. 43, No. 2, 1998, pp. 45-69
- [10] F. Abe, S. Nakazawa, H. Araki, T. Noda „The role of microstructural instability on creep behaviour of a low radioactivation martensitic 9Cr-2W steel“ Metall. Trans, Vol. 23 A, 1992, pp. 469-477
- [11] F. Abe „Creep rates and Strengthening Mechanisms in Tungsten-Strengthened 9Cr Steels” Materials Science and Engineering, A319-321, 2001, pp. 770-773
- [12] S. Spigarelli, E. Cerri, E. Evangelista, P. Bianchi, Proc. 6th Liège Conference, Materials for Advanced Power Engineering 1998, Liège, Belgium, 1998, pp. 539-548
- [13] P. Polcik „Modellierung des Verformungsverhaltens der warmfesten 9-12% Chromstähle im Temperaturbereich von 550-650°C“ Ph.D. thesis, Erlangen, Shaker Verlag, 1998
- [14] L. Kloc, V. Sklenicka „Transition from power-law to viscous creep behaviour of P-91 type heat-resistant steel” Materials Science and Engineering, 1997, pp. 962-965
- [15] R. Hanus „Advanced 9-12% Cr Cast Steel Grades, Research - Foundry Process Development - Quality - Experience“ Proc. 4th International Conference on Advances in Materials Technology for Fossil Power Plants, Hilton Head Island, SC USA, 2004, pp. 457-471

- [16] G. Zeiler, W. Meyer, K. Spiradek, J. Wosik „Experiences in Manufacturing and Long-Term Mechanical & Microstructural Testing on 9-12% Chromium Steel Forgings for Power Generation Plants” Proc. 4th International Conference on Advances in Materials Technology for Fossil Power Plants, Hilton Head Island, SC USA, 2004, pp. 223-236
- [17] E. Letofsky „Das Verhalten von Schweißverbindungen moderner Kraftwerkswerkstoffe“ Ph.D. thesis, Graz University of Technology, Graz, 2001
- [18] E. Letofsky, H. Cerjak „Microstructure Aspects of Creep Resistant Welded Joints” International Conference on Advanced Structural Steels ICASS 2002, Tsukuba, Japan, 2002
- [19] B. Scarlin, T. U. Kern, M. Staubli „The European Efforts in Material Development for 650°C USC Power Plants – COST522” Proc. 4th International Conference on Advances in Materials Technology for Fossil Power Plants, Hilton Head Island, SC USA, 2004, pp. 81-100
- [20] B. Scarlin, R. Vanstone, R. Gerdes „Materials development for ultrasupercritical steam turbines” Proc. 4th International Conference on Advances in Materials Technology for Fossil Power Plants, Hilton Head Island, SC USA, 2004, pp. 51-67
- [21] P. Hofer, „Mikrostrukturelle Analyse als Basis für die Entwicklung neuer Kraftwerkswerkstoffe am Beispiel von G-X12 CrMoWVNbN 10-1-1“, Ph.D. thesis, Graz University of Technology, Graz, 1999
- [22] K. Kaneko, S. Matsumura, A. Sadakata, K. Fujita, W.-J. Moona, S. Ozaki, N. Nishimura, Y. Tomokiyo „Characterization of carbides at different boundaries of 9Cr-steel” Materials Science and Engineering A 374, 2004, pp. 82–89
- [23] T. Weidinger „Adaptierung einer Hochtemperatur-Belastungseinrichtung für die Rasterelektronenmikroskopie mit Unterstützung von Finite-Elemente-Modellierung“, Diploma thesis, Graz University of Technology, Graz, 2002
- [24] E. Kozeschnik „Thermodynamische Berechnung der Phasengleichgewichte und der Ausscheidungskinetik in metallischen Werkstoffen“ Ph.D. thesis, Graz University of Technology, Graz, 1997
- [25] B. Schaffernak „Charakterisierung von 9-12% Cr Stählen mittels thermodynamischer Modellrechnungen“ Ph.D. thesis, Graz University of Technology, Graz, 2000
- [26] P. Weinert „Modellierung des Kriechverhaltens von ferritisch/martensitischen 9-12% Cr Stählen auf mikrostruktureller Basis“ Ph.D. thesis, Graz University of Technology, Graz, 2001
- [27] E. Kozeschnik, B. Buchmayr, Proc. Mathematical Modelling of Weld Phenomena 5, ed.: H. Cerjak, Institute of Materials, London, 2001, pp. 349-361
- [28] G. Dimmler, P. Weinert, H. Cerjak „Investigations and analysis on the stationary creep behaviour of 9-12% chromium ferritic martensitic steels” Proc. 7th Liège Conf., Materials for Advanced Power Engineering 2002, Liège, 2002, pp. 1539-1550
- [29] S. W. Plimon „Simulation of an industrial heat treatment and accompanying microstructural investigation of a modern 9-12% chromium steel” Diploma thesis, Graz University of Technology, Graz, 2004
- [30] B. Sonderegger „Characterisation of the Substructure of Modern Power Plant Steels Using the EBSD - Method” Ph.D. thesis, Graz University of Technology, Graz, 2005

- [31] K. Thornton, J. Ågren, P. W. Voorhees „Modelling the evolution of phase boundaries in solids at the meso- and nano-scales” *Acta Materialia*, Vol. 51, 2003, pp. 5675-5710
- [32] J. O. Andersson, L. Höglund, B. Jönsson, J. Ågren „Fundamentals and Applications of Ternary Diffusion” New York, NY, Ed.: G. R. Purdy, Pergamon Press, 1990, p. 153
- [33] J. Lee, *Theor. Appl. Fract. Mech.*, Vol. 33, 2000, pp. 207-217
- [34] F. Soisson, G. Martin, *Phys. Rev. B*, Vol. 62, 2000, pp. 203-214
- [35] M. Asta, *Acta Mater*, Vol. 44, 1996, pp. 4131-4136
- [36] J. W. Cahn, J. E. Hilliard. *J. Chem. Phys.*, Vol. 28, 1958, p. 258
- [37] M. Avrami, *J. Chem. Phys*, Vol. 7, 1939, p. 1103
- [38] M. Avrami, *J. Chem. Phys*, Vol. 8, 1940, p. 212
- [39] M. Avrami, *J. Chem. Phys*, Vol. 9, 1941, p. 177
- [40] W. A. Johnson, R. F. Mehl, *Transactions of the American Institute of Mining and Metallurgical Engineers*, Vol. 135, 1939, p. 416
- [41] A. Kolmogorov „A statistical theory for the recrystallization of metals.” *Akad. nauk SSSR, Izv., Ser. Matem.* 1, 1937, p. 355
- [42] J. D. Robson, H. K. D. H. Bhadeshia „Kinetics of precipitation in power plant steels” *Calphad*, Vol. 20, 4, 1996, pp. 447-460
- [43] J. D. Robson, H. K. D. H. Bhadeshia „Modelling Precipitation Sequences in Power Plant Steels. Part 1” *Mater. Sci. Techn.*, Vol. 13 (8), 1997, pp. 631-639
- [44] N. Fujita, H. K. D. H. Bhadeshia „Precipitation Reactions in 3Cr1,5Mo Power Plant Steel” *Inst. of Mater.*, London, in: *Advanced Heat Resistant Steel for Power Generation*, edited by R. Viswanathan, J. Nutting, 1998, p. 233
- [45] R. H. Davies, A. T. Dinsdale, J. A. Gisby, J. A. J. Robinson, S. M. Martin, *Calphad*, Vol. 26, 2002, pp. 229-271
- [46] R. Kampmann, R. Wagner, in: „*Decomposition of Alloys: The early Stages*” edited by: P. Haasen, V. Gerold, R. Wagner, M. F. Ashby, Oxford, Pergamon press, 1984, pp. 91-103
- [47] J. Ågren, *Scripta Metall.*, Vol. 20, 1986, pp. 1507-1510
- [48] Å. Gustafson, M. Hättestrand „Coarsening of precipitates in an advanced creep resistant 9% chromium steel-quantitative microscopy and simulations” *Materials Science and Engineering*, Vol. A333, 2002, pp. 279-286
- [49] A. Schneider, G. Inden „Simulation of kinetics of precipitation reactions in ferritic steels” *Acta Materialia*, Vol. 53, 2005, pp. 519-531
- [50] Lord Kelvin (Sir William Thomson) „On the Division of Space with Minimum Partitional Area” *Philosophical Magazine*, Vol. 24, No. 151, 1887, p. 503
- [51] F. Abe, H. Araki, *Materials Science and Technology*, Vol. 8, 1992, pp. 767-773
- [52] J. H. Woodhead, A. G. Quarell, *J. Iron Steel Inst.*, Vol. 203, 1965, pp. 605-620
- [53] S. G. Hong, W. B. Lee, C. G. Park „The effects of tungsten addition on the microstructural stability of 9Cr-Mo Steels” *Journal of Nuclear Materials*, Vol. 288, 2001, pp. 202-207
- [54] Y. Hosoi, N. Wade, T. Urita, *Trans Iron Steel Inst.*, Vol. 26, 1986, p. 30
- [55] H. K. D. H. Bhadeshia „Martensitic Transformations: Crystallography and Nucleation” *Encyclopedia of Materials Science: Science and Technology*, Eds.: K. Buschow, R. W. Cahn, M. C. Flemings, B. Ilschner, E. J. Kramer, S. Mahajan, Pergamon Press, Elsevier Science, ISBN 0-08-0431526, 2001, pp. 5203-5206
- [56] K. J. Irvine, F. B. Pickering „High-Strength 12% Chromium Steels” 1964

- [57] F. Abe „Alloy Design of Creep and Oxidation Resistant 9Cr Steels for Thick Section Boiler Components Operating at 650°C” Proc. 4th International Conference on Advances in Materials Technology for Fossil Power Plants, Hilton Head Island, SC USA, 2004, pp. 273-289
- [58] T. Horiuchi, M. Igarashi, F. Abe „Improved Utilization of Added B in 9%Cr Heat-Resistant Steels Containing W” ISIJ International, Vol. 42, 2002, pp. 67-71
- [59] N. Takahashi, T. Fujita „The Effect of Boron on the Long Period Creep Rupture Strength of Modified 12% Chromium Heat Resistant Steel” ISIJ International, Vol. 16, 1976, pp. 606-613
- [60] Z. Kubon, V. Foldyna, V. Vodarek, Proc. 4th international Charles Parsons turbine conference „Advances in Turbine Materials, Design and Manufacturing“ Eds.: A. Strang, W. M. Banks, R. D. Conroy, M. J. Goulette, The Institute of Materials, London, 1997, pp. 309-321
- [61] B. A. Senior „The precipitation of Laves’ phase in 9Cr1Mo steels” Mat. Sci. Eng., Vol 119 A, 1989, pp. L5-L8
- [62] H. Danielsen, J. Hald „Z phase in 9-12% Cr Steels” Proc. 4th International Conference on Advances in Materials Technology for Fossil Power Plants, Hilton Head Island, SC USA, 2004, pp. 876-889
- [63] J. W. Gibbs, The Scientific Papers of J. Willard Gibbs, Vol. 1, Longmans-Green, London, 1906, p. 55
- [64] H. Ibach „The role of surface stress in reconstruction, epitaxial growth and stabilization of mesoscopic structures” Surface Science Reports, Vol. 29, 1997, pp. 193-263
- [65] L. E. Murr, Interfacial Phenomena in Metals and Alloys, Addison-Wesley Publishing Company, 1975, ISBN 0-201-04884-1
- [66] R. Shuttleworth, Proc. Phys. Soc., Ser. A, Vol. 63, 1950, p. 444
- [67] G. Wulff, Z. Kristallogr., Vol. 34, 1901, p. 449
- [68] K. E. Easterling, D.A. Porter „Phase Transformations in Metals and Alloys” Chapman & Hall, 1996, p. 149
- [69] J. W. Martin, R. D. Doherty, B. Cantor „Stability of microstructure in metallic systems” 2nd edition, Cambridge Univ. Press, 1997, Cambridge UK
- [70] F. R. N. Nabarro, Proc. Roy. Soc, Vol. A175, 1940, p. 519
- [71] J. K. Lee, D. M. Barnett, H. I. Anderson, Metall. Trans., Vol. 8A, 1977, p. 963
- [72] W. L. Bragg, E. J. Williams, Proc. Roy. Soc. London 145, 1934, p. 699
- [73] R. Becker, Ann. Phys., Vol. 32, 1938, pp. 128-140
- [74] D. Turnbull, Impurities and Imperfections, ASM, Cleveland OH, 1955, pp. 121-143
- [75] T. Nishizawa, I. Ohnuma, K. Ishida, Journal of Phase Equilibria, Vol. 22, No. 3, 2001, pp. 269-275
- [76] I. S. Servi, D. Turnbull „Thermodynamics and Kinetics of Precipitation in the Copper-Cobalt System” Acta Metallurgica, Vol. 14, 1966, pp. 161-169
- [77] U. R. Katter „The thermodynamic modelling of multicomponent phase equilibria” JOM, 1997, pp. 14-19
- [78] M. Hillert „A solid-solution model for inhomogeneous systems” Acta Metallurgica, Vol. 9, No. 6, 1961, pp. 525-535
- [79] G. J. Shiflet, Y. W. Lee, H. I. Aaronson, K. C. Russell „A Re-Assessment of the Comparison of Classical Homogeneous Nucleation Theory and Experiment In Cu-Co Alloys” Scripta Metallurgica, Vol. 15, 1981, pp. 719-722

- [80] Y. W. Lee, K. C. Russel, H. I. Aaronson „On the evaluation of the molar regular solution constant” *Scripta Metallurgica*, Vol. 15, 1981, pp. 723-726
- [81] C. Wagner, *Thermodynamics of Alloys*, Addison-Wesley, Reading MA, 1965, p. 35
- [82] J. W. Cahn, J. E. Hilliard „Free Energy of a Nonuniform System. I. Interfacial Energy“ *J. Chem. Phys.*, Vol. 28, No. 2, 1958, pp. 258-267
- [83] Y. W. Lee, H. I. Aaronson „Anisotropy of coherent interphase boundary energy” *Acta Metallurgica*, Vol. 28, 1980, pp. 539-548
- [84] Z.-G. Yang, M. Enomoto „Discrete lattice plane analysis of Baker-Nutting related B1 compound/ferrite interfacial energy” *Materials Science and Engineering A*, Vol. 332, No. 1-2, 2002, pp. 184-192
- [85] Z.-G. Yang, M. Enomoto „Calculation of the Interfacial Energy of B1-Type Carbides and Nitrides with Austenite” *Metall Mater Trans A*, Vol. 32A, 2001, pp. 267-273
- [86] A. R. Miedema, F. J. A. den Broeder „On the Interfacial Energy in Solid-Liquid and Solid-Solid Metal Combinations” *Z. Metallkd.* 70, 1979, pp. 14-20
- [87] A. R. Miedema „Surface Energies of Solid Metals” *Z. Metallkd.*, Vol. 69, 1978, pp. 287-292
- [88] A. R. Miedema, R. Boom „Surface Tension and Electron Density of Pure Liquid Metals” *Z. Metallkde.*, Vol. 69, 1978, pp. 183-190
- [89] P. H. Leo, J. Hu „Continuum Modelling of Noncoherent Interfaces” *Solid - Solid Transformations*, W. C. Johnson, J. M. Howe, D. E. Laughlin, W. A. Soffa, *The Minerals, Metals & Materials Society*, 1994, pp. 1103-1108
- [90] M. Kahlweit „Zur Berechnung der Grenzflächenspannung zwischen zwei Phasen eines binären Systems” *Zeitschrift für Physikalische Chemie Neue Folge*, Vol. 34, 1962, pp. 163-181
- [91] Z. M. Wang, G. J. Shiflet „Heterogeneous Nucleation of δ' on Dislocations in a Dilute Aluminium-Lithium Alloy” *Metall Mater Trans A*, Vol. 27A, 1996, pp. 1599-1609
- [92] Y. Gotoh, S. Entani, H. Kawanzowa „Interfacial energy calculation of bcc/fcc interface” *Surface Science* 507-510, 2002, pp. 401-405
- [93] P. Wynblatt „Comparison between modelling and experimental measurements of interfacial properties” *Applied Surface Science* Vol. 219, 2003, pp. 39-46
- [94] A. Landa, P. Wynblatt, E. Johnson, U. Dahmen „Computer simulation of Pb/Al interfaces“ *Acta Materialia*, Vol. 48, No. 10, 2000, pp. 2557-2563
- [95] L. G. Hector Jr., D. J. Siegel, J. Adams „Atomistic Simulation of Adhesion and Adhesive Transfer at Metal/Metal-Oxide Interfaces „Proceedings: Integration of Material, Process, and Product Design, Seven Springs PA, 1998, pp. 39-46
- [96] K. Rapcewicz, B. Chen, B. Yakobson, J. Bernholc „Consistent methodology for calculating surface and interface energies” *Physical-Review-B-Condensed-Matter*, Vol. 57 No. 12, 1998, pp. 7281-7291
- [97] I. Tanaka, M. Mizuno, S. Nakajyo, H. Adachi „Importance of metal-metal bondings at the interface of MgO and 3d-transition metals” *Acta Materialia*, Vol. 46, No. 18, 1998, pp. 6511-6520
- [98] D. Gupta „Diffusion, Solute Segregations and Interfacial Energies in Some Material: An Overview” *Interface Science*, Vol. 11, 2003, pp. 7-20
- [99] F. Spaepen „A Structural Model for the Solid-Liquid Interface in Monoatomic Systems” *Acta Metallurgica*, Vol. 23, 1975, pp. 729-743

- [100] F. Spaepen, R. B. Meyer „The Surface Tension in a Structural Model for the Solid-Liquid Interface” *Scripta Metallurgica*, Vol. 10, 1976, pp. 257-263
- [101] D. Holland-Moritz „On the energy of the interface between a melt and quasi-crystalline and polytetrahedral phases” *Journal of Non-Crystalline Solids*, 250-252, 1999, pp. 839-843
- [102] T. Nishizawa, I. Ohnuma, K. Ishida „Correlation between Interfacial Energy and Phase Diagram in Ceramic-Metal Systems” *Journal of Phase Equilibria*, Vol. 22, No. 3, 2001, pp. 269-275
- [103] R. M. Digilov „Solid-liquid interfacial tension in metals: correlation with the melting point” *Physica B* 352, 2004, pp. 53-60
- [104] J. A. V. Butler, *Proc. R. Soc. A* 135, 1932, pp. 348-375
- [105] Z. Qiao, L. Yan, Z. Cao, Y. Xie „Surface tension prediction of high-temperature melts” *Journal of Alloys and Compounds* 325, 2001, pp. 180-189
- [106] J. Lee, K. Morita „Evaluation of Surface Tension and Adsorption for Liquid Fe-S Alloys” *ISIJ International*, Vol. 42, No. 6, 2002, pp. 588-594
- [107] R. Pichaa, J. Vrestala, A. Kroupa „Prediction of alloy surface tension using a thermodynamic database” *Computer Coupling of Phase Diagrams and Thermochemistry*, in press
- [108] T. Ueda, T. Tanaka, S. Hara „Thermodynamic Evaluation of Surface Tension of Molten Salt Mixtures in Alkali Halides, Nitrate, Carbonate and Sulphate Systems” *Z. Metallkd.*, Vol. 90, No. 5, 1999, pp. 342-347
- [109] T. Tanaka, K. Hack, S. Hara „Use of Thermodynamic Data to Determine Surface Tension and Viscosity of Metallic Alloys” *MRS Bulletin*, 1999, pp. 45-50
- [110] T. Tanaka, J. Lee „Application of Thermodynamic Databases to Evaluate Physico-Chemical Properties in Materials Production and Development” in: *Proc. CIMTEC 2002-10th International Ceramics Congress and 3rd Forum on New Materials*, Florenz 2002
- [111] T. Tanaka, S. Hara „Application of Thermodynamic Databases to Evaluation of Interfacial Tension between Liquid Steels and Molten Slags” *Z. Metallkd.*, Vol. 90, No. 5, 1999, pp. 348-354
- [112] T. Tanaka, S. Hara „Thermodynamic Evaluation of Nano-Particle Binary Alloy Phase Diagrams” *Z. Metallkd.*, Vol. 92, No. 11, 2001, pp. 1236-1241
- [113] T. Tanaka, S. Hara „Thermodynamic Evaluation of Binary Phase Diagrams of Small Particle Systems” *Z. Metallkd.*, Vol. 92, No. 5, 2001, pp. 467-472
- [114] T. Tanaka, K. Hack, S. Hara „Calculation of Surface Tension of Liquid Bi-Sn Alloy using Thermochemical Application Library ChemApp” *Calphad*, Vol. 24, No. 4, 2000, pp. 465-474
- [115] T. Tanaka, K. Hack, T. Iida, S. Hara „Application of Thermodynamic Databases to the Evaluation of Surface Tensions of Molten Alloys, Salt Mixtures and Oxide Mixtures” *Z. Metallkd.*, Vol. 87, No. 5, 1996, pp. 380-389
- [116] T. Tanaka, S. Hara „Thermodynamics of Surface Tension of Molten Salt Mixtures” *Electrochemistry*, Vol. 67, No. 6, 1999, pp. 573-580
- [117] H. Jones „The Surface Energy of Solid Metals” *Metal Sci. Journal*, Vol. 5, 1971, pp. 15-18
- [118] W. R. Tyson „Surface energies of solid metals” *Canadian Metallurgy Quarterly*, Vol. 14, No. 4, 1975, pp. 307-314

- [119] J. B. Hess „Measurement of Solid:Solid Interfacial Energies” Metal Interfaces, A Seminar on Metal Interfaces held during the 33. National Metal Congress and Exposition, ASM, Cleveland OH, 1952, pp. 134-152
- [120] S. Schmauder, P. Binkele „Atomistic computer simulation of the formation of Cu-precipitates in steels” Computational Materials Science, Vol. 24, 2002, pp. 42-53
- [121] I. M. Lifshitz, V. V. Slyozov „The kinetics of precipitation from supersaturated solid solutions“ Journal of Physics and Chemistry of Solids, Vol. 19, 1961, pp. 35-50
- [122] C. Wagner, Z. Elektrochem., Vol. 65, 1961, p. 581
- [123] A. J. Ardell „Interfacial Free Energies and Solute Diffusivities from Data on Ostwald Ripening” Interface Science, Vol. 3, 1995, pp. 119-125
- [124] S. Polat, M. A. Dvorack, H. Chen „An in situ X-ray diffraction study of precipitation from a supersaturated solid solution: The γ' precipitate in a Ni-12.5% Si alloy” Acta Metallurgica, Vol. 33, 1985, pp. 2175-2183
- [125] C. Marsh, H. Chen „An In Situ X-Ray Diffraction Study of Precipitation from a Supersaturated Solid Solution: The γ' Precipitate in a Ni-12,5at.% Al Alloy” Acta Metallurgica et Materialia, Vol. 38, 1990, pp. 2287-2298
- [126] X. Li, N. Saunders, A. P. Miodownik „The Coarsening Kinetics of γ' Particles in Nickel-Based Alloys” Metall. Mater. Trans. A, Vol. 33A, 2002, pp. 3367-3373
- [127] H. Jones „The Grain Boundary Term in Surface Energy Measurement by Zero Creep” Scripta Metallurgica, Vol. 6, 1972, pp. 423-430
- [128] L. E. Murr, G. I. Wong, R. J. Horylev „Measurement of Interfacial Free Energies and Associated Temperature Coefficients in 304 Stainless Steel” Acta Metallurgica, Vol. 21, 1973, pp. 595-604
- [129] R. Wagner, R. Kampmann, P. W. Voorhees „Homogeneous Second-Phase Precipitation” in: G. Kostortz „Phase Transformations in Materials” Wiley-VCH Publishing Company, 2001, ISBN 3-527-30256-5
- [130] R. Becker, W. Döring, Ann. Phys. Vol. 24, 1935, p. 719
- [131] K. C. Russell, Adv. Colloid Interface Sci., Vol. 13, 1980, p. 205
- [132] J. K. Tien, P. G. Shewmon, J. S. Foster, Scripta Metall, Vol. 7, 1973, p. 1171
- [133] D. Fan, S. P. Chen, L.-Q. Chen, P. W. Voorhees „Phase-field simulation of 2-D Ostwald ripening in the high Vol. fraction regime“ Acta Materialia, Vol. 50, 2002, pp. 1895-1907
- [134] S. P. Marsh, M. E. Glicksman „Kinetics of phase coarsening in dense systems“ Acta Materialia, Vol. 44, 1996, pp. 3761-3771
- [135] J. Svoboda, F.D. Fischer, P. Fratzl, E. Kozeschnik „Modeling of kinetics in multi-component multi-phase systems with spherical precipitates: I: Theory” Materials Science and Engineering A, Vol. 385, No. 1-2, 2004, p. 166
- [136] E. Kozeschnik, J. Svoboda, P. Fratzl, F.D. Fischer „Modelling of kinetics in multi-component multi-phase systems with spherical precipitates: II: Numerical solution and application” Materials Science and Engineering A, Vol. 385, No. 1-2, 2004, p. 157
- [137] J. Ågren, F. H. Hayes, L. Höglund, U. R. Kattner, B. Legendre, R. Schmid-Fetzer. “Applications of computational thermodynamics” Vol. 93, No. 2, 2002, pp. 128-142
- [138] E. Kozeschnik, J.Svoboda, F. D. Fischer „Modeling of precipitation in multi-component multi-particle multi-phase systems” Modeling, Control, and Optimi-

- zation in Ferrous and Nonferrous Industry, edited by: F. Kongoli, B.G. Thomas, K. Sawamiphakdi, ISBN: 0-87339-561-1, 2003, pp. 429-434
- [139] K. C. Russell „Nucleation in Solids: The induction and steady state effects“ Adv. Coll. Interf. Sci., Vol. 13, 1980, pp. 205-318
- [140] E. Kozeschnik, J. Svoboda, F. D. Fischer „Modified evolution equations for the precipitation kinetics of complex phases in multi-component systems“ Calphad, Vol. 28, No. 4, 2004, pp. 379-382
- [141] C. J. Zener „Theory of Growth of Spherical Precipitates From Solid Solution“ J. Appl. Phys. 20, 1949, p. 950
- [142] R. Kampmann, R. Wagner „Phase Transformations in Fe-Cu-Alloys - SANS-Experiments and Theory“ Proceedings of an IFF-ILL Workshop, Jülich, BRD, 1985, pp. 73-77
- [143] W. Wepner „Dämpfungsmessung an schwach gereckten Eisen-Kohlenstoff-Legierungen“ Acta Metallurgica, Vol. 5, 1957, pp. 703-710
- [144] A. H. Cottrell „Dislocations and plastic flow in crystals“ Oxford University Press, London, 1953
- [145] A. H. Cottrell, B. A. Bilby „Dislocation Theory of Yielding and Strain Aging of Iron“ Proc. Phys. Soc., Series A 62, 1949, pp. 49-62
- [146] S. Harper „Precipitation of Carbon and Nitrogen in Cold-Worked Alpha-Iron“ Phys. Rev., Vol. 83, No. 4, 1951, pp. 709-712
- [147] R. Monzen, K. Takada, K. Matsuda „Coarsening kinetics of Cu particles in an Fe.1.5% Cu alloy“ Z. Metallkd., Vol. 94, 2003, p. 11
- [148] P. J. Othens, M. L. Jenkins, G. D. W. Smith „High-resolution electron microscopy studies of the structure of Cu precipitates in α -Fe“ Philos. Mag. A, Vol. 70, 1994, pp. 1-24
- [149] J. Ågren, M. T. Clavaguera-Mora, J. Golcheski, G. Inden, H. Kumar, C. Sigli „Workshop on applications of computational thermodynamics“ Calphad, Vol. 24, No. 1, 2000, pp. 41-54
- [150] R. L. Klueh, A. M. Nasreldin, Metallurgical Transactions A, Vol. 18 A, 1987, p. 1279
- [151] R. G. Baker, J. Nutting, Journal of the Iron and Steel Institute, Vol. 192, 1959, pp. 257-268
- [152] MTDATA: Metallurgical Thermochemistry Group, National Physical Laboratory, Teddington, London, 1998
- [153] Fe-DATA, thermodynamic database, copyright AEA Technology, OX11 0QJ Didcot, UK
- [154] M. Hättestrand, H. O. Andren „Evaluation of particle size distribution of precipitates in a 9% chromium steel using energy filtered transmission electron microscopy“ Micron, Vol. 32, 2001, pp. 789-797
- [155] R. Faulkner, Y. F. Yin „Microstructural Modelling for Creep Strength Prediction in Ferritic Steels“ Proc. 4th International Conference on Advances in Materials Technology for Fossil Power Plants, Hilton Head Island, SC USA, 2004, pp. 890-903
- [156] TCFE, solution database, copyright Thermo-Calc AB, SE-113 47 Stockholm, Sweden
- [157] A. Engström, MOB 2 mobility database, Thermo-Calc AB, SE-113 47 Stockholm, Sweden, 1998
- [158] A. Kroupa, IPM Brno, private communication

- [159] J. Rajek, E. Kozeschnik, H. Cerjak „Simulation of precipitation in a complex 9-12% Cr steel for modern steam power plants” Modeling, Control, and Optimization in Ferrous and Nonferrous Industry, Eds. F. Kongoli, B. G. Thomas, and K. Sawamiphakdi, ISBN: 0-87339-561-1, 2003, pp. 435-440
- [160] N. Saunders, A. P. Miodownik „CALPHAD (Calculated Phase Diagrams): A Comprehensive Guide“ Elsevier Science & Technology Books, Pergamon Press Inc., ISBN 0080421296, 1998
- [161] SSOL Vers. M solution database, copyright Thermo-Calc AB, SE-113 47 Stockholm, Sweden
- [162] SSOL 4 solution database, copyright Thermo-Calc AB, SE-113 47 Stockholm, Sweden
- [163] H. Danielsen, J. Hald „Z phase in 9-12% Cr steels“ ISSN 0282-3772, Värmeforsk Service AB, Stockholm, 2004
- [164] E. Scheil, Z. Metallkd., Vol. 34, 1942, p. 70
- [165] G. M. Gulliver, J. Inst. Met., Vol. 9, 1913, p. 120
- [166] E. Kozeschnik „A Scheil-Gulliver Model with Back-Diffusion Applied to the Micro Segregation of Chromium in Fe-Cr-C Alloys” Met. Mater. Trans., Vol. 31A, 2000, pp. 1682-1684
- [167] N. Saunders, X. Li, A. P. Miodownik, J.-P. Schillé „Modelling of the Thermo-physical and Physical Properties for Solidification of Al-Alloys” Light Metals 2003, Ed.: P. Crepeau TMS, 2003
- [168] J. Hald, S. Straub, Proc. 6th Liege Conference of Materials for Advanced Power Engineering, Part I, Forschungszentrum, Jülich, 1998, p. 155
- [169] J. Rajek, E. Kozeschnik, H. Cerjak „Computer Simulation of Precipitation in a Complex 9-12% Cr-Steel during fabrication heat treatment” Proc. 4th International Conference on Advances in Materials Technology for Fossil Power Plants, Hilton Head Island, SC USA, 2004, pp. 941-947
- [170] I. Holzer, Ph.D. thesis, Graz University of Technology, Graz, work in progress

9 Appendix

9.1 Thermal history of GX-12

This paper was published in the proceedings of „Modeling, Control, and Optimization in Ferrous and Nonferrous Industry From” from the Materials Science & Technology TMS conference held in Chicago, Illinois, November 9 to 12 in 2003 [159].

Simulation Of Precipitation In A Complex 9-12% Cr Steel For Modern Steam Power Plants

J. Rajek¹, E. Kozeschnik^{1,2} and H. Cerjak¹

¹ Graz University of Technology, Institute for Materials Science,
Welding and Forming, 8010 Graz, Austria

² Materials Center Leoben, 8700 Leoben, Austria

Keywords: Precipitation kinetics, heat treatment, power plant steels, simulation

Abstract

The novel multi-component, multi-particle, multi-phase precipitation model developed recently is used to predict the precipitation kinetics in complex 9-12% Cr steels investigated within the European COST 522 project. These steels are used for tubes, pipes, casings and rotors in USC (ultra super critical) steam power plants for the 21st century. In the computer simulations, the evolution of the precipitate microstructure is monitored over the entire production heat treatment starting with the casting process, including austenizing, several annealing treatments and in-service conditions. The main interest lies on the concurrent growth and coarsening interaction of different types of precipitates.

Introduction

In fossil fired steam power plants, 9-12% Cr-steels are used as turbine casings, steam pipes and tubes and rotor forgings. To meet ecological and economical requirements, like reducing the CO₂ exhaust and improving the efficiency, increased steam parameters with a steam temperature up to 650 °C and pressure up to 250 bar are necessary. The present 9-12% Cr-steels, developed in the US, Europe (COST 522) and Japan, use well balanced mechanisms to resist these service conditions. To optimize creep-resistance, precipitation hardening with carbides and nitrides and solid solution strengthening (Mo, Mn, W dissolved in the martensitic matrix) are applied. The idea behind this strategy is, that precipitates on the grain- and subgrain boundaries work as obstacles for the movement of dislocations and pin down grain boundaries. A stable microstructure, with minimized precipitate coarsening, minimal grain growth and dislocation recovery is aspired. To achieve this goal, fundamental knowledge about the effects of the alloying elements and the heat treatment on the evolution of the precipitate population is necessary.

During heat treatment, precipitates can form and dissolve again, thereby affecting the kinetics of other types of precipitates. It can be shown, that every stage in the manufacturing process of a complex martensitic 9-12% Cr steel can have influences on the materials properties during service. To achieve a favorable microstructure, the optimization of the heat treatment of these steels should start at very early stages of the production process. By optimizing the thermal cycle parameters mentioned before, the best possible combination of precipitate radii, number density and phase fraction can be obtained.

To carry out the numerical simulations, the software *MatCalc* [1], which is developed at the Graz University of Technology, is applied. For detailed information, please refer to ref. [2].

Numerical Simulation

In a typical manufacturing procedure, these steels undergo several austenite/ferrite phase transformations. The austenitic ingot cools down to martensite start temperature and starts to transform into martensite. During austenizing, a transformation back to austenite starts at the A_1 -transformation temperature. During cooling, the material transforms to martensite again. During the following heat treatments, the temperature does not reach A_1 again and the matrix phase remains martensitic/ferritic. The precipitates that are considered in the present simulations are the carbides $M_{23}C_6$ and MX with the major constituents $(Fe,Cr)_{23}C_6$ and $(Nb,V)C$, respectively. These carbides have face centered cubic structure. The third precipitate phase that is considered in the simulation is Laves phase, which is an intermetallic phase of A_2B type and with hexagonal structure. Its major constituents are Fe, W, Mo and Cr.

During the simulation, all precipitates interact with each other by exchanging atoms with the matrix phase. This process is controlled by the multi-component diffusivities of all elements, which is available through kinetic databases, such as the mobility database of the software package DICTRA [3]. The thermodynamic parameters for calculation of the chemical potentials are taken from the IWS_steel database [4].

A very important parameter of the simulations is the type of heterogeneous nucleation site. Available sites are dislocations, grain boundaries and subgrain boundaries. How many sites are actual available is defined by the parameters grain size, subgrain size and dislocation density. For simplicity, the grain size and subgrain size are chosen to be the same for both matrix phases, the values are typical for annealed martensitic/ferritic structures. Table 1 summarizes all kinetic parameters that were used in the simulations.

Table 1: Kinetic parameters for the precipitates and the matrix phases.

Matrix phase		Austenite	Ferrite		
Grain size [m]		$100 \cdot 10^{-6}$	$100 \cdot 10^{-6}$		
Subgrainsize [m]		$5 \cdot 10^{-6}$	$5 \cdot 10^{-6}$		
Dislocation density [$1/m^2$]		$1 \cdot 10^{11}$	$1 \cdot 10^{14}$		
Thermal cycle	Matrix	Kinetic parameters	$M_{23}C_6$	MX	Laves phase
Casting, austenizing (825-250°C)	Austenite	Nucleation site	SGB	SGB	SGB, $M_{23}C_6$
		γ [J/m^2]	0.11	0.15	0.05
Austenizing (250-825°C), heat treatment, service	Ferrite	Nucleation site	SGB	SGB, dislocation	SGB, $M_{23}C_6$
		γ [J/m^2]	0.15	0.17	0.05

The interfacial energy γ of the precipitates directly influences nucleation and coarsening. Whereas γ enters the coarsening rate linearly [5], nucleation is affected in a much stronger way. Since the critical energy for forming a nucleus is proportional γ^3 , small variations in γ can highly enhance the formation of a phase or completely suppress it.

In the simulations it is assumed that the transformation from austenite to martensite and back is happening instantaneously and the parent and product phase have the same chemical composition. The precipitate population does not change during this transformation. When the simulation starts at 1200°C all elements are assumed to be in solid solution. It is further assumed that no kinetic processes occur at temperatures below 250°C due to the sluggish diffusion of the atomic species.

Results and Discussion

Casting (1.200°C – 250°C)

The simulation starts at 1200°C in an austenitic matrix containing no precipitates. While the material continuously cools down (60K/h) to martensite-start-temperature (250°C), the MX carbides nucleate first at the highest temperature and start to occupy the majority of the available grain boundary nucleation sites. At about 850°C, the $M_{23}C_6$ carbides start to nucleate. Due to decreased diffusion capability at lower temperatures, the kinetic processes slow down considerably below 650°C. This effect is clearly visible in the graphs (see figure 1).

Austenizing (250°C – 1.100°C/12h – 250°C)

At the beginning of the austenizing process, the precipitate population after casting is moved into a ferritic matrix. Reheating is performed up to the previously calculated equilibrium transition temperature A_1 of 825°C. Up to about 550°C, diffusion processes are too slow to cause major changes in the precipitate microstructure. Above this temperature, MX precipitates nucleate. At elevated temperatures, the existing $M_{23}C_6$ precipitates start to grow initially until they finally dissolve again after passing their equilibrium solubility temperature. The volume fraction of the MX precipitates decreases to their equilibrium volume fraction, which is less than half the amount that was present after casting.

When the temperature decreases again, nucleation of new $M_{23}C_6$ precipitates at the sub-grainboundaries is observed. The existing MX precipitates grow; no nucleation is assumed to occur in this stage because the dislocation density is rather low due to the annealing process.

It is interesting to note that there is also a small amount of laves phase precipitating. The precipitates have a very small radius, though, and they dissolve again completely in the following annealing steps.

Process annealing (550°C/20h), Tempering 1 (730°C/12h), Tempering 2 (720°C/9h)

The graphs in figure 1 clearly show that the fraction $M_{23}C_6$ and MX increase considerably during process annealing. The total number of the MX precipitates increases significantly, as does the mean radius. When the temperature reaches 730°C during tempering 1, the $M_{23}C_6$ equilibrium phase fraction is approached and it almost stays constant throughout the rest of the heat treatment procedure. However, the onset of *Ostwald* ripening for the MX and $M_{23}C_6$ precipitates can be observed in the graphs during tempering 1 and 2, where the number density decreases simultaneously to an increase of the mean radius.

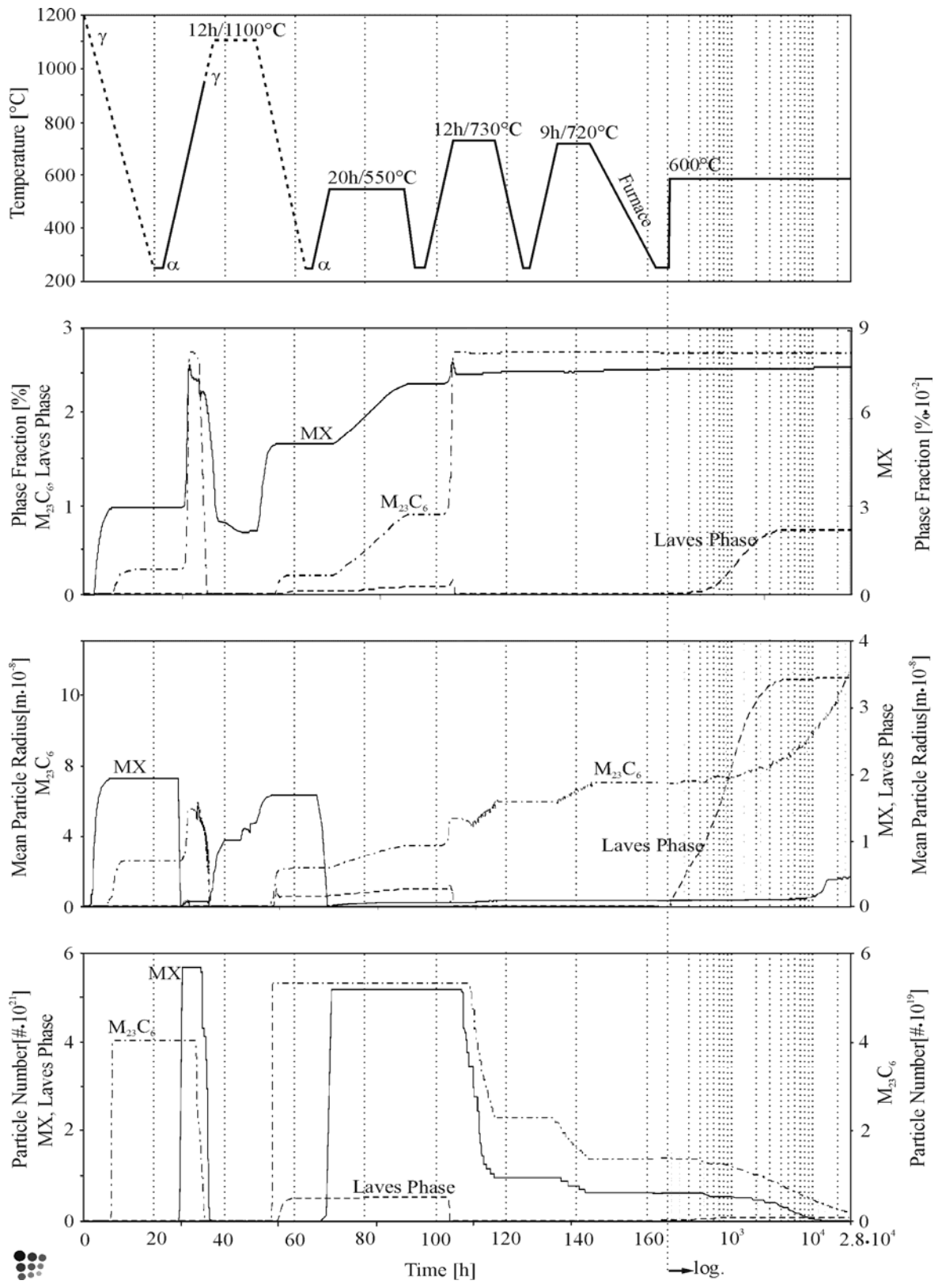


Figure 1: This figure shows the time-temperature history and the corresponding graphs for phase fraction, mean precipitate radius and number density. The time scale is linear until service starts at an absolute time of 164.8h. The 34000h service simulation is plotted in logarithmic scale. The mean radius and number density graphs have different y-axis scales for better visualization.

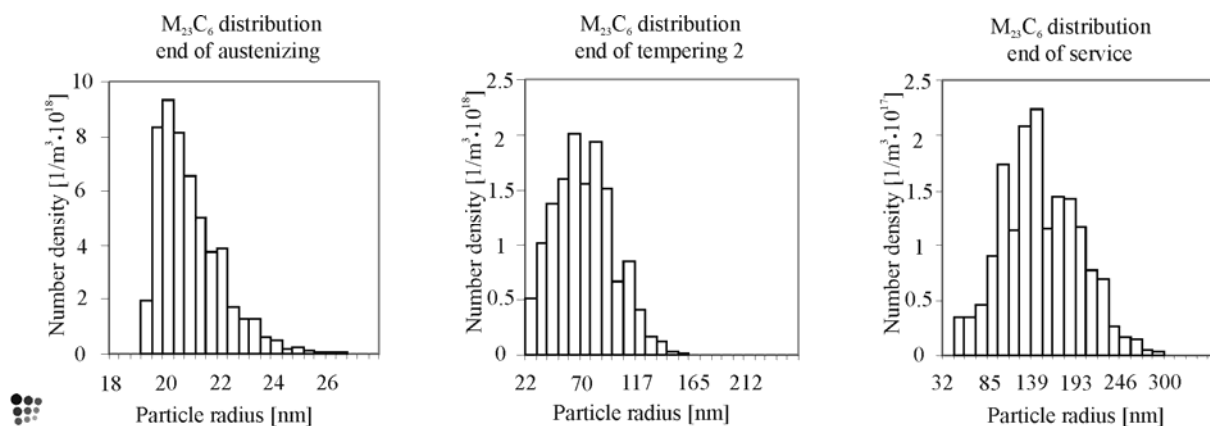


Figure 2: Precipitate distribution of $M_{23}C_6$ at three stages are shown. Rearrangement from a left-shifted to a more symmetric distribution is observed with annealing time.

Service (600°C/34000h)

During service at 600°C, both $M_{23}C_6$ and MX precipitates undergo *Ostwald* ripening. The mean radius of these precipitates increases and the number density decreases due to the consumption of smaller precipitates by larger ones. Figure 2 shows the calculated precipitate distribution at different steps of the thermal history.

After a few hundred hours, Laves phase precipitation starts and proceeds up to approximately 5000h. Within the time span of the simulation, no coarsening of laves phase precipitates is observed. The time when laves phase appears in the simulation of the service conditions correlates well with experimental observations, since no laves phase was found directly after heat treatment whereas a considerable number of laves precipitates were present after 976h [6]. The fact that laves phase appears only after a few hundred hours of service is due to the long incubation period for this type of precipitate. Calculations based on classical nucleation theory (see also ref. [2]) predict that the incubation time is in the order of 200-300h.

Summary and Outlook:

Knowledge about the precipitate evolution during the manufacturing process and service is of great importance for an optimization of the precipitate microstructure to improve the creep resistance of modern power plant materials. The present work demonstrates how the evolution of different precipitate populations in time can be modeled with computational thermodynamics and kinetics. The basis of the simulations is given by thermodynamic and diffusional databases, combined with classical nucleation theory, which is adapted to apply to multi-component systems, and a new model for the simulation of the evolution of precipitates in complex systems.

Acknowledgement

This work was part of the European COST522 activity and it was supported by the Austrian Science Fund (FWF). Financial support of the Kplus program of the Austrian Government is also gratefully acknowledged.

References

1. E. Kozeschnik and B. Buchmayr, *Mathematical Modelling of Weld Phenomena 5* (London, Institute of Materials, Book 734, 2001), 349-361.
2. ibid. E. Kozeschnik, J. Svoboda, F.D. Fischer, *Modelling of precipitation in multi-component, multi-particle, multi-phase systems*.
3. J. O. Andersson, et al., *Fundamentals and Applications of Ternary Diffusion* (New York, NY: G.R. Purdy (ed.), Pergamon Press, 1990), 153.
4. E. Kozeschnik and W. Rindler, Graz University of Technology, Institute for Materials Science, Welding and Forming, unpublished research, 2001.
5. I. M. Lifshitz, V. V. Slyozov, *J. Phys. Chem. Solids*, 19 (1962), 35.
6. P. Hofer, „Microstructural analysis as basis of the development of new materials for power plants conducted on G-X12 CrMoWVNbN 10-1-1” (Ph.D. thesis, Graz University of Technology, 1999), 185.

9.2 Scripts

MatCalc can be controlled either by a graphical user interface, a command line window or by executing script files. A script contains all commands to setup and run a simulation in a logical order; scripts are also a reliable method to document the parameter settings of a simulation.

9.2.1 Thermal history of P92

Master script

The system is set up utilizing *MatCalc* scripts. In total five scripts are used to simulate the complete thermal history. These scripts are loaded and executed in the correct order (batch processing) by the master script.

```
$ MatCalc batch script for P92 simulation
$ Script 1 and 2 are executed one after the other

$ change working directory ...
$ '.' = set to path of last file operation
set-working-directory .

$ _____
run P92_600_1_austenitising_setup.mcs
start-precipitate-simulation

$ _____
run P92_600_2_annealing.mcs
start-precipitate-simulation
```

System setup and austenitising (P92_600_1_austenitising_setup.mcs)

The first script defines the alloy system, reads the necessary databases, and creates the matrix- and the precipitate phases, the tables containing the experimental data and finally all plots for visualization. In this particular case some parameter of the thermodynamic database are also edited to stabilize the miscibility gap between NbC and VN. The austenitising simulation is finished when the corresponding end-time is reached, in this case 63000s or 17,5h.

```
$ P92_600_1_austenitising_setup
$ 2005-04-23
$ MatCalc script version 1, MatCalc version 5.11

new-workspace

$ Some information about the simulation
set-workspace-info Simulation of steel P92; experimental data from annealing at 600°C
set-workspace-info +
set-workspace-info +Experimental data published in:
set-workspace-info +M. Hättstrand, H.-O. Andren
set-workspace-info +Evaluation of particle size distribution of precipitates
set-workspace-info +in a 9% chromium steel using energy filtered TEM
set-workspace-info +Micron, Vol. 32, 2001, pp. 789-797
set-workspace-info +Thermodynamic database: TCFE 3_mod (modified for Cr-steels)
set-workspace-info +
set-workspace-info +Phase data for Lavest modified to have the same phase fraction at
set-workspace-info +650°C than obtained by Dimmler G., i.e., 0.2% 'as-received', 0.8%
set-workspace-info +'equilibrium'
set-workspace-info +
set-workspace-info +also modified td parameters of MX precipitates to make sure that the
set-workspace-info + major constituents remain consistent, i.e. NbC remains NbC and VN
set-workspace-info + remains VN. Otherwise the composition of the MX carbides/nitrides
set-workspace-info + switches during HT. Moreover, numerical stability is drastically
set-workspace-info +increased!
```

```

$ setup thermodynamics, diffusion etc. _____
open-thermo-database TCFE3_mod.tdb

select-elements C Cr Fe Mn Mo N Nb Ni Si V W
select-phase bcc_a2 fcc_al m23c6 lavest
set-reference-element fe

read-thermodyn-database

enter-composition wp c=0,11 cr=8,96 mn=0,46 mo=0,47 n=0,05 nb=0,07 ni=0,06 si=0,04 v=0,2
enter-composition wp w=1,84

$ define some variables that are used later _____

set-variable-value time 63000
set-variable-value x_scale 1
set-variable-value ipdcf 0,01 $ Diffusion coeff. in prec., factor of matrix diffusion
set-variable-value npc 25 $ Number of precipitate classes
set-variable-value irf 1 $ inactive radius factor
set-variable-value ssprl 400 $ Linear storage interval

$ Define NbC and VN precipitate phases _____
create-new-phase fcc_al e
change-phase-status fcc_al#01 m :Nb:C:
change-phase-status fcc_al#02 m :V:N:

$ Stabilize the miscibility gap between NbC and VN
$ change parameter in fcc parent phases
$ add penalty term for opposite side of miscibility gap: NbC
EDIT_PARAMETER a t G(fcc_al#01,V:N;0) 298,16 +100000; 6000 N
EDIT_PARAMETER a t G(fcc_al#01,V:C;0) 298,16 +100000; 6000 N
EDIT_PARAMETER a t G(fcc_al#01,NB:N;0) 298,16 +100000; 6000 N
$ add penalty term for opposite side of miscibility gap: VN
EDIT_PARAMETER a t G(fcc_al#02,NB:C;0) 298,16 +100000; 6000 N
EDIT_PARAMETER a t G(fcc_al#02,NB:N;0) 298,16 +100000; 6000 N
EDIT_PARAMETER a t G(fcc_al#02,V:C;0) 298,16 +100000; 6000 N

$ read diffusion data and physical constants
read-mobility-database mobility_v21
read-physical-database PhysData.pdb

$ setup precipitation simulation _____

$ 1. precipitate domains and microstructure parameter

create-precipitate-domain Austenite $ austenite as prec. domain = matrix
set-precipitation-parameter Austenite x fcc_al $ matrix phase of domain is FCC_A1
set-precipitation-parameter Austenite d 1e11 $ dislocation density
set-precipitation-parameter Austenite g 100e-6 $ grain diameter
set-precipitation-parameter Austenite l 1 $ grain elongation factor

create-precipitate-domain Ferrite
set-precipitation-parameter Ferrite x bcc_a2
set-precipitation-parameter Ferrite d 1e14
set-precipitation-parameter Ferrite g 100e-6
set-precipitation-parameter Ferrite l 1
set-precipitation-parameter Ferrite s 0,1e-6 $ subgrain diameter (lath-width)
set-precipitation-parameter Ferrite o 100 $ sub grain elongation factor

$ 2. tables for heat treatment _____

create-global-table ht_600

$ Austenitising
add-table-entry ht_600 0 1070
add-table-entry ht_600 400 1024
add-table-entry ht_600 1080 948
add-table-entry ht_600 3132 872
add-table-entry ht_600 5760 796
add-table-entry ht_600 9360 720
add-table-entry ht_600 15120 644
add-table-entry ht_600 22680 558
add-table-entry ht_600 31680 473
add-table-entry ht_600 41400 400
add-table-entry ht_600 41400 400
add-table-entry ht_600 63000 250

```

```

$ Tempering
add-table-entry ht_600 66600      250
add-table-entry ht_600 141480     770
add-table-entry ht_600 148680     770
add-table-entry ht_600 149080     720
add-table-entry ht_600 154520     644
add-table-entry ht_600 162080     558
add-table-entry ht_600 171080     473
add-table-entry ht_600 180800     400
add-table-entry ht_600 202400     250

```

```

$ Annealing
add-table-entry ht_600 206000     250
add-table-entry ht_600 256400     600
add-table-entry ht_600 3,6e8      600

```

\$ 3. tables containing experimental data

```

create-global-table r_m23c6_600_annealed
add-table-entry r_m23c6_600_annealed 57,2      17,9
add-table-entry r_m23c6_600_annealed 1057,2    47,3
add-table-entry r_m23c6_600_annealed 3057,2    49,8
add-table-entry r_m23c6_600_annealed 10057,2   45,6
add-table-entry r_m23c6_600_annealed 26057,2   54,4

```

```

create-global-table r_vn_600_annealed
add-table-entry r_vn_600_annealed 57,2      17,9
add-table-entry r_vn_600_annealed 1057,2    20,5
add-table-entry r_vn_600_annealed 3057,2    21,1
add-table-entry r_vn_600_annealed 10057,2   19
add-table-entry r_vn_600_annealed 26057,2   16,5

```

```

create-global-table r_laves_600_annealed
add-table-entry r_laves_600_annealed 57,2      0
add-table-entry r_laves_600_annealed 1057,2    62
add-table-entry r_laves_600_annealed 3057,2    93,5
add-table-entry r_laves_600_annealed 10057,2   145
add-table-entry r_laves_600_annealed 26057,2   137

```

```

create-global-table f_vn_600_annealed
add-table-entry f_vn_600_annealed 57,2      3,49E-03
add-table-entry f_vn_600_annealed 1057,2    3,73E-03
add-table-entry f_vn_600_annealed 10057,2   3,30E-03
add-table-entry f_vn_600_annealed 26057,2   2,69E-03

```

```

create-global-table f_laves_600_annealed
add-table-entry f_laves_600_annealed 57,2      0,00E+00
add-table-entry f_laves_600_annealed 1057,2    2,06E-04
add-table-entry f_laves_600_annealed 10057,2   9,83E-04
add-table-entry f_laves_600_annealed 26057,2   7,77E-04

```

\$ 4. precipitates

```

create-new-phase m23c6 p
set-precipitation-parameter m23c6_p0 c npc      $ particle classes
set-precipitation-parameter m23c6_p0 d Austenite $ domain
set-precipitation-parameter m23c6_p0 i 0       $ interfacial energy
set-precipitation-parameter m23c6_p0 l 1e100   $ interface mobility (high , no data)
set-precipitation-parameter m23c6_p0 e 0       $ elastic energy (zero, no data)

```

```

$ Nucleation sites for "Austenite" prec. domain
set-precipitation-parameter m23c6_p0 n s g
set-precipitation-parameter m23c6_p0 n n t     $ nucl. model: Becker-Doering time dep
set-precipitation-parameter m23c6_p0 n c o     $ nucleus comp: ortho equilibrium
set-precipitation-parameter m23c6_p0 n i y     $ Nucleation site saturation: use=yes
set-precipitation-parameter m23c6_p0 n r irf   $ Nucleation site saturation: inactive ra-
radius factor
set-precipitation-parameter m23c6_p0 n a m     $ atomic attachment: max time concept
set-precipitation-parameter m23c6_p0 n m i     $ incub time model: interface control
set-precipitation-parameter m23c6_p0 n t 1.0   $ incubation time constant
set-precipitation-parameter m23c6_p0 n u 1.0   $ nucleation constant

```

```

set-precipitation-parameter m23c6_p0 s d r ipdcf $ diffusion in precipitate: fixed ratio
set-precipitation-parameter m23c6_p0 s i r ipdcf $ interstitial diffusion in precipi-
tate: fixed ratio
set-precipitation-parameter m23c6_p0 s m l     $ Matrix diffusion enhancement factor

```

```

create-new-phase fcc_al#01 p $ NbC _____
$ make sure, miscibility gap is wide open :-)
$ add penalty term for opposite side of miscibility gap: NbC
EDIT_PARAMETER a t G(fcc_al#01_p0,V:N;0) 298,16 +100000; 6000 N
EDIT_PARAMETER a t G(fcc_al#01_p0,V:C;0) 298,16 +100000; 6000 N
EDIT_PARAMETER a t G(fcc_al#01_p0,NB:N;0) 298,16 +100000; 6000 N

set-precipitation-parameter fcc_al#01_p0 c npc
set-precipitation-parameter fcc_al#01_p0 d Austenite
set-precipitation-parameter fcc_al#01_p0 i 0
set-precipitation-parameter fcc_al#01_p0 l 1e100
set-precipitation-parameter fcc_al#01_p0 e 0

set-precipitation-parameter fcc_al#01_p0 n s g
set-precipitation-parameter fcc_al#01_p0 n n t
set-precipitation-parameter fcc_al#01_p0 n c o
set-precipitation-parameter fcc_al#01_p0 n i y
set-precipitation-parameter fcc_al#01_p0 n r irf
set-precipitation-parameter fcc_al#01_p0 n a m
set-precipitation-parameter fcc_al#01_p0 n m i
set-precipitation-parameter fcc_al#01_p0 n t 1.0
set-precipitation-parameter fcc_al#01_p0 n u 1.0

set-precipitation-parameter fcc_al#01_p0 s d r ipdcf
set-precipitation-parameter fcc_al#01_p0 s i r ipdcf
set-precipitation-parameter fcc_al#01_p0 s m l

create-new-phase fcc_al#02 p $ VN_1 _____
$ add penalty term for opposite side of miscibility gap: VN
EDIT_PARAMETER a t G(fcc_al#02_p0,NB:C;0) 298,16 +100000; 6000 N
EDIT_PARAMETER a t G(fcc_al#02_p0,NB:N;0) 298,16 +100000; 6000 N
EDIT_PARAMETER a t G(fcc_al#02_p0,V:C;0) 298,16 +100000; 6000 N

set-precipitation-parameter fcc_al#02_p0 c npc
set-precipitation-parameter fcc_al#02_p0 d Austenite
set-precipitation-parameter fcc_al#02_p0 i 0
set-precipitation-parameter fcc_al#02_p0 l 1e100
set-precipitation-parameter fcc_al#02_p0 e 0

set-precipitation-parameter fcc_al#02_p0 n s g
set-precipitation-parameter fcc_al#02_p0 n n t
set-precipitation-parameter fcc_al#02_p0 n c o
set-precipitation-parameter fcc_al#02_p0 n i y
set-precipitation-parameter fcc_al#02_p0 n r irf
set-precipitation-parameter fcc_al#02_p0 n a m
set-precipitation-parameter fcc_al#02_p0 n m i
set-precipitation-parameter fcc_al#02_p0 n t 1.0
set-precipitation-parameter fcc_al#02_p0 n u 1.0

set-precipitation-parameter fcc_al#02_p0 s d r ipdcf
set-precipitation-parameter fcc_al#02_p0 s i r ipdcf
set-precipitation-parameter fcc_al#02_p0 s m l

create-new-phase fcc_al#02 p $ VN_2 _____
$ add penalty term for opposite side of miscibility gap: VN
EDIT_PARAMETER a t G(fcc_al#02_p1,NB:C;0) 298,16 +100000; 6000 N
EDIT_PARAMETER a t G(fcc_al#02_p1,NB:N;0) 298,16 +100000; 6000 N
EDIT_PARAMETER a t G(fcc_al#02_p1,V:C;0) 298,16 +100000; 6000 N

set-precipitation-parameter fcc_al#02_p1 c npc
set-precipitation-parameter fcc_al#02_p1 d none
set-precipitation-parameter fcc_al#02_p1 i 0
set-precipitation-parameter fcc_al#02_p1 l 1e100
set-precipitation-parameter fcc_al#02_p1 e 0

set-precipitation-parameter fcc_al#02_p1 n s n
set-precipitation-parameter fcc_al#02_p1 n n t
set-precipitation-parameter fcc_al#02_p1 n c o
set-precipitation-parameter fcc_al#02_p1 n i y
set-precipitation-parameter fcc_al#02_p1 n r irf
set-precipitation-parameter fcc_al#02_p1 n a m
set-precipitation-parameter fcc_al#02_p1 n m i
set-precipitation-parameter fcc_al#02_p1 n t 1.0
set-precipitation-parameter fcc_al#02_p1 n u 1.0

set-precipitation-parameter fcc_al#02_p1 s d r ipdcf
set-precipitation-parameter fcc_al#02_p1 s i r ipdcf

```

```

set-precipitation-parameter fcc_al#02_p1 s m 1

create-new-phase lavest p $ Laves phase _____
set-precipitation-parameter lavest_p0 c npc
set-precipitation-parameter lavest_p0 d Austenite
set-precipitation-parameter lavest_p0 i cie$lavest_p0
set-precipitation-parameter lavest_p0 l 1e100
set-precipitation-parameter lavest_p0 e 0

set-precipitation-parameter lavest_p0 n s g
set-precipitation-parameter lavest_p0 n n t
set-precipitation-parameter lavest_p0 n c o
set-precipitation-parameter lavest_p0 n i y
set-precipitation-parameter lavest_p0 n r irf
set-precipitation-parameter lavest_p0 n a m
set-precipitation-parameter lavest_p0 n m i
set-precipitation-parameter lavest_p0 n t 1.0
set-precipitation-parameter lavest_p0 n u 1.0

set-precipitation-parameter lavest_p0 s d r ipdcf
set-precipitation-parameter lavest_p0 s i r ipdcf
set-precipitation-parameter lavest_p0 s m 1

$ Simulation setup _____

set-temperature-celsius 1070      $ define something
set-automatic-startvalues         $ equilibrium calculation, reasonable values
$scalcequilibrium                 $ start with some equilibrium

set-sim-parameter e time          $ simulation end time
set-sim-parameter t t ht_600 10  $ T-control from table
set-sim-parameter s r            $ simulation starting conditions: reset
set-sim-parameter c w y          $ convergence control: weighted diffusion coeff. = on
set-sim-parameter c o y          $ convergence control: oscillation damping = on
set-sim-parameter c d 0,03       $ convergence control: dfm-compensation 3%
set-sim-parameter c m 1e-4       $ convergence control: mass-balance tolerance
set-sim-parameter u 100          $ update windows every n steps
set-sim-parameter r l ssprl      $ store results in buffer: linear time steps, var. ssprl

$ visualization _____

new-gui-window pl

$ define values for default x-axis (will be used by all plots)
set-gui-window-property . X stepvalue/3600 $ default x-value: time in hours
set-gui-window-property . s u y           $ use default x-axis for all plots: yes
set-gui-window-property . s t t[h]        $ default x-axis title
set-gui-window-property . s y log         $ default x-axis type: logarithmic scaling
set-gui-window-property . s s x_scale..   $ default x-axis scaling: range from x_scale
..
set-gui-window-property . y col_no_symb   $ default style sheet for plots

$ for first plot:
$ add series that displays Temperature
set-plot-option . s n b t$c             $ add series
set-plot-option . s m -1 t$c T          $ define series legend
set-plot-option . a y 1 t T[°C]         $ y-axis title

$ create second plot and define props (phase fractions)
create-new-plot x .
set-plot-option . s n b f$fcc_al#01_p0   $ add series
set-plot-option . s m -1 f$fcc_al#01_p0 NbC $ define series legend
set-plot-option . s n b f$fcc_al#02_p0
set-plot-option . s m -1 f$fcc_al#02_p0 VN_1
set-plot-option . s n b f$fcc_al#02_p1
set-plot-option . s m -1 f$fcc_al#02_p1 VN_2
set-plot-option . s n b f$m23c6_p0/10
set-plot-option . s m -1 f$m23c6_p0/10 M<sub>23</sub><sub>C<sub>6</sub>/10
set-plot-option . s n b f$lavest_p0/10
set-plot-option . s m -1 f$lavest_p0/10 Laves/10
set-plot-option . s n t f_vn_600_annealed $ add table containing exp. data
set-plot-option . s m -1 f_vn_600_annealed VN
set-plot-option . s n t f_laves_600_annealed
set-plot-option . s m -1 f_laves_600_annealed Laves
set-plot-option . a y 1 t f[%] $ y-axis title
set-plot-option . a y 1 f 100 $ multiply with 100 to show phase fractions in percent

```

```

$ create third plot and define props (mean radius)
create-new-plot x .
set-plot-option . s n b r_mean$fcc_al#01_p0*1e9
set-plot-option . s m -1 r_mean$fcc_al#01_p0*1e9 NbC
set-plot-option . s n b r_mean$fcc_al#02_p0*1e9
set-plot-option . s m -1 r_mean$fcc_al#02_p0*1e9 VN_1
set-plot-option . s n b r_mean$fcc_al#02_p1*1e9
set-plot-option . s m -1 r_mean$fcc_al#02_p1*1e9 VN_2
set-plot-option . s n b r_mean$m23c6_p0*1e9
set-plot-option . s m -1 r_mean$m23c6_p0*1e9 M<sub>23</sub>C<sub>6</sub>
set-plot-option . s n b r_mean$lavest_p0*1e9
set-plot-option . s m -1 r_mean$lavest_p0*1e9 Laves
set-plot-option . s n t r_vn_600_annealed
set-plot-option . s m -1 r_vn_600_annealed VN
set-plot-option . s n t r_m23c6_600_annealed
set-plot-option . s m -1 r_m23c6_600_annealed M<sub>23</sub>C<sub>6</sub>
set-plot-option . s n t r_laves_600_annealed
set-plot-option . s m -1 r_laves_600_annealed Laves
set-plot-option . a y l t R[nm]
set-plot-option . a y l y log
set-plot-option . a y l s 0,1..
set-plot-option . l r

$ create fourth plot and define props (nucleation rate and number density)
create-new-plot x .
set-plot-option . s n b num_part$fcc_al#01_p0
set-plot-option . s m -1 num_part$fcc_al#01_p0 NbC
$set-plot-option . s n b nucl_rate_btdt$fcc_al#01_p0
$set-plot-option . s m -1 nucl_rate_btdt$fcc_al#01_p0 J_NbC
set-plot-option . s n b num_part$fcc_al#02_p0
set-plot-option . s m -1 num_part$fcc_al#02_p0 VN_1
$set-plot-option . s n b nucl_rate_btdt$fcc_al#02_p0
$set-plot-option . s m -1 nucl_rate_btdt$fcc_al#02_p0 J_VN_1
set-plot-option . s n b num_part$fcc_al#02_p1
set-plot-option . s m -1 num_part$fcc_al#02_p1 VN_2
$set-plot-option . s n b nucl_rate_btdt$fcc_al#02_p1
$set-plot-option . s m -1 nucl_rate_btdt$fcc_al#02_p1 J_VN_2
set-plot-option . s n b num_part$m23c6_p0
set-plot-option . s m -1 num_part$m23c6_p0 M<sub>23</sub>C<sub>6</sub>
$set-plot-option . s n b nucl_rate_btdt$m23c6_p0
$set-plot-option . s m -1 nucl_rate_btdt$m23c6_p0 J_M<sub>23</sub>C<sub>6</sub>
set-plot-option . s n b num_part$lavest_p0
set-plot-option . s m -1 num_part$lavest_p0 Laves
$set-plot-option . s n b nucl_rate_btdt$lavest_p0
$set-plot-option . s m -1 nucl_rate_btdt$lavest_p0 J_Laves
set-plot-option . a y l t N[m<sup>-3</sup>]
set-plot-option . a y l y log
set-plot-option . a y l s 1..
set-plot-option . l r

$ move window to new position and resize
move-gui-window . 20 20 600 800
update-gui-window . $ Update the GUI window

new-gui-window p5 $ New precipitation distribution plot window
set-gui-window-property . m y

set-plot-option . s n p fcc_al#01_p0 $ Show the precipitation distribution
set-plot-option . s m -1 fcc_al#01_p0 NbC
set-plot-option . s n p fcc_al#02_p0
set-plot-option . s m -1 fcc_al#02_p0 VN_1
set-plot-option . s n p fcc_al#02_p1
set-plot-option . s m -1 fcc_al#02_p1 VN_2
set-plot-option . s n p m23c6_p0
set-plot-option . s m -1 m23c6_p0 M<sub>23</sub>C<sub>6</sub>
set-plot-option . s n p lavest_p0
set-plot-option . s m -1 lavest_p0 Laves
set-plot-option . a x l t Scaled Radius
set-plot-option . a y l t Scaled Number
set-plot-option . a x l s 0..1,499

$ define a function for LSW distribution
set-function-expression LSW x^2*(3/(3+x))^(7/3)*((3/2)/(3/2-x))^(11/3)*exp(-x/(3/2-x))^4/9
set-plot-option . s n f LSW 0..1,5 $ add to plot

$ in this histogram plot: scale radius and frequency for comparison with theoretical

```

```

$ steady-state distribution (LSW)
set-plot-option . h r y $ scale radius
set-plot-option . h f y $ scale frequency

$ next plots are precipitate distributions for all phases
create-new-plot p .
set-plot-option . s n p fcc_al#01_p0
set-plot-option . s m -1 fcc_al#01_p0 NbC
set-plot-option . a x l t R [nm]
set-plot-option . a y l t N [m<sup>-3</sup>]
set-plot-option . a x l s 0..
set-plot-option . a x l f 1e9
set-plot-option . l r

create-new-plot p .
set-plot-option . s n p fcc_al#02_p0
set-plot-option . s m -1 fcc_al#02_p0 VN_1
set-plot-option . a x l t R [nm]
set-plot-option . a y l t N [m<sup>-3</sup>]
set-plot-option . a x l s 0..
set-plot-option . a x l f 1e9
set-plot-option . l r

create-new-plot p .
set-plot-option . s n p fcc_al#02_p1
set-plot-option . s m -1 fcc_al#02_p1 VN_2
set-plot-option . a x l t R [nm]
set-plot-option . a y l t N [m<sup>-3</sup>]
set-plot-option . a x l s 0..
set-plot-option . a x l f 1e9
set-plot-option . l r

create-new-plot p .
set-plot-option . s n p m23c6_p0
set-plot-option . s m -1 m23c6_p0 M<sub>23</sub>C<sub>6</sub>
set-plot-option . a x l t R [nm]
set-plot-option . a y l t N [m<sup>-3</sup>]
set-plot-option . a x l s 0..
set-plot-option . a x l f 1e9
set-plot-option . l r

create-new-plot p .
set-plot-option . s n p lavest_p0
set-plot-option . s m -1 lavest_p0 Laves
set-plot-option . a x l t R [nm]
set-plot-option . a y l t N [m<sup>-3</sup>]
set-plot-option . a x l s 0..
set-plot-option . a x l f 1e9
set-plot-option . l r

$ move window to new position and resize
move-gui-window . 600 30 390 900
update-gui-window . $ Update the GUI window

$ move output window to new position and resize
move-gui-window 0 0 700 900 270
move-gui-window 0 show $ make output window the active foreground window

```

Tempering and annealing (P92_600_2_annealing.mcs)

The main difference of this script is a change in data handling. During the simulation of the manufacturing (total 56,2h), the state was stored every 400s simulated time. This is reasonable because the detail of the record is high enough and the file-size is in the range of some megabytes. In this condition the precipitate structure is quite stable and during the isothermal annealing simulation for 3,6 10⁸h the precipitate populations are changing slowly. Therefore a logarithmic recording method is utilized. The moment t_i of saving a data-set is calculated according to:

$$t_{i+1} = t_i \cdot SF \quad (86)$$

This method turned out to be precise and the file size is below ½ gigabyte if *SF* is set from 1,02 to 1,05.

```
$ P92, annealing
$ MatCalc script version 1

set-variable-value time 3,6e8

set-precipitation-parameter m23c6_p0 d Ferrite
$ Nucleation sites for "Ferrite" prec. domain
set-precipitation-parameter m23c6_p0 n s gs

set-precipitation-parameter fcc_al#01_p0 d Ferrite
$ Nucleation sites for "Ferrite" prec. domain
set-precipitation-parameter fcc_al#01_p0 n s gsd

set-precipitation-parameter fcc_al#02_p0 d Ferrite
$ Nucleation sites for "Ferrite" prec. domain
set-precipitation-parameter fcc_al#02_p0 n s n

set-precipitation-parameter fcc_al#02_p1 d Ferrite
$ Nucleation sites for "Ferrite" prec. domain
set-precipitation-parameter fcc_al#02_p1 n s gsd

set-precipitation-parameter lavest_p0 d Ferrite
$ Nucleation sites for "Ferrite" prec. domain
set-precipitation-parameter lavest_p0 n s gs

set-sim-parameter e time
set-sim-parameter t t ht_600 10
set-sim-parameter s n
set-sim-parameter a y
set-sim-parameter r g 1.02
```

9.2.2 Thermal history of CB8

The purpose of the scripts is explained in chapter 9.2.1. The simulation of the complete thermal history considering 25 precipitate classes lasts about 20min. utilizing a standard notebook (*Intel Centrino* 1,4MHz with 512MB memory).

Master script

```
$ MatCalc batch script for CB8 simulation

$ MUST change working directory ...
$ '.' = set to path of last file operation
set-working-directory .

$ _____
run cb8_173_1_setup_casting.mcs
start-precipitate-simulation

$ _____
run cb8_173_2_reheating.mcs
start-precipitate-simulation

$ _____
run cb8_173_3_austenitising.mcs
start-precipitate-simulation

$ _____
run cb8_173_4_ht.mcs
start-precipitate-simulation

$ _____
run cb8_173_5_service.mcs
start-precipitate-simulation
```

System setup and casting simulation (CB8_173_1_setup_casting.mcs)

```
$ CB8 heat 173 IWS, TCFE 3_mod
$ MatCalc script version 1
$ This is a script for MatCalc version 5.1

new-workspace

set-workspace-info CB8 with
set-workspace-info +Al B C Co Cr Fe Mn Mo N Ni Nb Si V
set-workspace-info +Ferrite Austenite; NbC, M7C3, M23C6, Laves (from casting),
set-workspace-info +VN_1 (from HT_slow), to separate MX waves, the nucleation of
set-workspace-info +NbC is disabled after casting, VN_1 are introduced during reheating,
set-workspace-info +VN_2 are introduced in HT
set-workspace-info +
set-workspace-info +Thermodynamic database: TCFE 3_mod (modified for Cr-steels)
set-workspace-info +
set-workspace-info +Phase data for LavesT modified to have the same phase fraction at
set-workspace-info +650°C than obtained by Dimmler G., i.e., 0.2% as-received, 0.8%
set-workspace-info +'equilibrium'
set-workspace-info +Interfacial energy of LavesT reduced to 75%, otherwise not enough
set-workspace-info +precipitates nucleate. Interfacial energy of Z increased to 125%
set-workspace-info +
set-workspace-info +Also modified td parameters of MX precipitates to make sure that the
set-workspace-info +major constituents remain consistent, i.e. NbC remains NbC and VN
set-workspace-info +remains VN. Otherwise the composition of the MX carbides/nitrides
set-workspace-info +switches during HT. Moreover, numerical stability is drastically
set-workspace-info +increased!

$ thermodynamic database ...
open-thermo-database TCFE3_mod.tdb

$ select elements and phases
select-elements C Co Cr Fe Mn Mo N Nb V
select-elements Al Si Ni
select-phase bcc_a2 fcc_al lavest m7c3 m23c6 zet
set-reference-element fe

$ read ...
read-thermodyn-database

$ system setup
enter-composition wp c=0,17 co=2,92 cr=10,72 mn=0,2 mo=1,4 n=0,0319 nb=0,06 v=0,21
enter-composition wp al=0,028 si=0,27 ni=0,16

$ create additional MX carbide and define major constituents acc. to miscibility gap
create-new-phase fcc_al e
change-phase-status fcc_al#01 m :Nb:C:
change-phase-status fcc_al#02 m :V:N:

$ make sure, miscibility gap is wide open :-)
$ change parameter in fcc parent phases
$ add penalty term for opposite side of miscibility gap: NbC
EDIT_PARAMETER a t G(fcc_al#01,V:N;0) 298,16 +100000; 6000 N
EDIT_PARAMETER a t G(fcc_al#01,V:C;0) 298,16 +100000; 6000 N
EDIT_PARAMETER a t G(fcc_al#01,NB:N;0) 298,16 +100000; 6000 N
$ add penalty term for opposite side of miscibility gap: VN
EDIT_PARAMETER a t G(fcc_al#02,NB:C;0) 298,16 +100000; 6000 N
EDIT_PARAMETER a t G(fcc_al#02,NB:N;0) 298,16 +100000; 6000 N
EDIT_PARAMETER a t G(fcc_al#02,V:C;0) 298,16 +100000; 6000 N

$ read diffusion data and physical constants
read-mobility-database mobility_v21
read-physical-database PhysData.pdb

set-variable-value time 84000
set-variable-value x_scale 1
set-variable-value ipdcf 0,01 $ diffusion coefficient in precipitates
set-variable-value npc 100 $ number of precipitate classes
set-variable-value ssprl 400 $ linear storage interval
set-variable-value mie 0.24 $ matrix interfacial energies
set-variable-value irf 5 $ inactive radius factor

$ precipitate domains (austenite and ferrite)
create-precipitate-domain Austenite $ Austenite as prec. domain = matrix
```

```

set-precipitation-parameter Austenite x fcc_a1 $ matrix phase of domain „Austenite“
set-precipitation-parameter Austenite d le11 $ dislocation density
set-precipitation-parameter Austenite g 100e-6 1 $ grain diameter
set-precipitation-parameter Austenite n g mie $ interfacial energy of grain boundary
set-precipitation-parameter Austenite n s mie $ interf. energy of subgrain boundary

```

```

create-precipitate-domain Ferrite
set-precipitation-parameter Ferrite x bcc_a2
set-precipitation-parameter Ferrite d le14
set-precipitation-parameter Ferrite g 100e-6 1
set-precipitation-parameter Ferrite s 0,1e-6 100 $ subgrain diameter (lath-width)
set-precipitation-parameter Ferrite n g mie $ interfacial energy of grain boundary
set-precipitation-parameter Ferrite n s mie $ interf. energy of subgrain boundary

```

\$ Heat treatment, slow cooling rate after austenitising _____

```
create-global-table ht_slow
```

\$ Casting

```

add-table-entry ht_slow 0 1400
add-table-entry ht_slow 84000 350

```

\$ Reheating

```

add-table-entry ht_slow 87600 350
add-table-entry ht_slow 137300 847

```

\$ Austenitising

```

add-table-entry ht_slow 160600 1080
add-table-entry ht_slow 189400 1080
add-table-entry ht_slow 191340 1018
add-table-entry ht_slow 195480 893
add-table-entry ht_slow 199260 800
add-table-entry ht_slow 203184 700
add-table-entry ht_slow 207576 600
add-table-entry ht_slow 211716 530
add-table-entry ht_slow 218700 452
add-table-entry ht_slow 236590 385
add-table-entry ht_slow 252790 385
add-table-entry ht_slow 257830 350

```

\$ HT

```

add-table-entry ht_slow 261430 350
add-table-entry ht_slow 316150 730
add-table-entry ht_slow 352150 730
add-table-entry ht_slow 382550 350
add-table-entry ht_slow 386150 350
add-table-entry ht_slow 440870 730
add-table-entry ht_slow 484070 730
add-table-entry ht_slow 538790 350
add-table-entry ht_slow 542390 350
add-table-entry ht_slow 597110 730
add-table-entry ht_slow 647510 730
add-table-entry ht_slow 677910 350

```

\$ Service

```

add-table-entry ht_slow 721110 650
add-table-entry ht_slow 58321110 650

```

\$ Experimental data _____

\$ value divided by 100 to compensate the scaling factor

```

create-global-table f_mx
add-table-entry f_mx 6.75E+01 7.30E-04
add-table-entry f_mx 1.02E+02 1.14E-03
add-table-entry f_mx 1.80E+02 2.79E-03

```

```
create-global-table r_mx
```

```

add-table-entry r_mx 6.75E+01 3.15E+01
add-table-entry r_mx 1.02E+02 2.30E+01
add-table-entry r_mx 1.80E+02 2.70E+01

```

```
create-global-table n_mx
```

```

add-table-entry n_mx 6.75E+01 3.07E+18
add-table-entry n_mx 1.02E+02 8.61E+18
add-table-entry n_mx 1.80E+02 1.73E+19

```

\$ value divided by 1000 to compensate the scaling factors

```

create-global-table f_m23c6
add-table-entry f_m23c6      6.75E+01      0.00E+00
add-table-entry f_m23c6      1.02E+02      2.55E-03
add-table-entry f_m23c6      1.80E+02      2.28E-03
add-table-entry f_m23c6      2.00E+03      2.25E-03
add-table-entry f_m23c6      4.03E+03      2.15E-03
add-table-entry f_m23c6      7.06E+03      4.20E-03
add-table-entry f_m23c6      1.66E+04      2.00E-03

create-global-table r_m23c6
add-table-entry r_m23c6      6.75E+01      0.00E+00
add-table-entry r_m23c6      1.02E+02      5.01E+01
add-table-entry r_m23c6      1.80E+02      5.40E+01
add-table-entry r_m23c6      2.00E+03      3.73E+01
add-table-entry r_m23c6      4.03E+03      5.78E+01
add-table-entry r_m23c6      7.06E+03      7.00E+01
add-table-entry r_m23c6      1.66E+04      6.17E+01

create-global-table n_m23c6
add-table-entry n_m23c6      6.75E+01      0.00E+00
add-table-entry n_m23c6      1.02E+02      2.33E+19
add-table-entry n_m23c6      1.80E+02      1.77E+19
add-table-entry n_m23c6      2.00E+03      5.61E+19
add-table-entry n_m23c6      4.03E+03      2.28E+19
add-table-entry n_m23c6      7.06E+03      2.15E+19
add-table-entry n_m23c6      1.66E+04      1.90E+19

$ value divided by 100 to compensate the scaling factor
create-global-table f_vn
add-table-entry f_vn          2.00E+03      2.30E-03
add-table-entry f_vn          4.03E+03      2.00E-03
add-table-entry f_vn          7.06E+03      3.00E-03
add-table-entry f_vn          1.66E+04      6.00E-04

create-global-table r_vn
add-table-entry r_vn          2.00E+03      2.10E+01
add-table-entry r_vn          4.03E+03      3.90E+01
add-table-entry r_vn          7.06E+03      2.80E+01
add-table-entry r_vn          1.66E+04      3.47E+01

create-global-table n_vn
add-table-entry n_vn          2.00E+03      3.10E+19
add-table-entry n_vn          4.03E+03      1.40E+18
add-table-entry n_vn          7.06E+03      1.60E+19
add-table-entry n_vn          1.66E+04      1.50E+18

$ Create precipitate phases _____
create-new-phase m23c6 p $ M23C6
set-precipitation-parameter m23c6_p0 c npc      $ particle classes
set-precipitation-parameter m23c6_p0 d Austenite $ domain
set-precipitation-parameter m23c6_p0 i 0        $ use calculated interfacial energy
set-precipitation-parameter m23c6_p0 l 1e100    $ interface mobility
set-precipitation-parameter m23c6_p0 e 0        $ strain energy

$ Nucleation sites for „Austenite“ prec. domain
set-precipitation-parameter m23c6_p0 n s g      $ nucleation site=grain boundary
set-precipitation-parameter m23c6_p0 n n t      $ nucl. model: Becker-Doering time dep
set-precipitation-parameter m23c6_p0 n c o      $ nucleus comp: ortho equilibrium
set-precipitation-parameter m23c6_p0 n i y      $ nucleation site saturation: use=yes
set-precipitation-parameter m23c6_p0 n r irf    $ nuc. site saturation: inactive radius=irf
set-precipitation-parameter m23c6_p0 n a m      $ atomic attachment: max time concept
set-precipitation-parameter m23c6_p0 n m i      $ incub time model: interface control
set-precipitation-parameter m23c6_p0 n t 1.0    $ incubation time constant
set-precipitation-parameter m23c6_p0 n u 1.0    $ nucleation constant

set-precipitation-parameter m23c6_p0 s d r ipdcf $ diffusion in precipitate factor
set-precipitation-parameter m23c6_p0 s i r ipdcf $ interstitial diff. in precipitate
factor
set-precipitation-parameter m23c6_p0 s m 1      $ matrix diffusion enhancement factor

$ _____
create-new-phase fcc_al#01 p $ NbC
$ add penalty term for opposite side of miscibility gap: NbC
EDIT_PARAMETER a t G(fcc_al#01_p0,V:N;0) 298,16 +100000; 6000 N
EDIT_PARAMETER a t G(fcc_al#01_p0,V:C;0) 298,16 +100000; 6000 N
EDIT_PARAMETER a t G(fcc_al#01_p0,NB:N;0) 298,16 +100000; 6000 N

```

```

set-precipitation-parameter fcc_al#01_p0 c npc
set-precipitation-parameter fcc_al#01_p0 d Austenite
set-precipitation-parameter fcc_al#01_p0 i 0
set-precipitation-parameter fcc_al#01_p0 l 1e100
set-precipitation-parameter fcc_al#01_p0 e 0

set-precipitation-parameter fcc_al#01_p0 n s g
set-precipitation-parameter fcc_al#01_p0 n n t
set-precipitation-parameter fcc_al#01_p0 n c o
set-precipitation-parameter fcc_al#01_p0 n i y
set-precipitation-parameter fcc_al#01_p0 n r irf
set-precipitation-parameter fcc_al#01_p0 n a m
set-precipitation-parameter fcc_al#01_p0 n m i
set-precipitation-parameter fcc_al#01_p0 n t 1.0
set-precipitation-parameter fcc_al#01_p0 n u 1.0

set-precipitation-parameter fcc_al#01_p0 s d r ipdcf
set-precipitation-parameter fcc_al#01_p0 s i r ipdcf
set-precipitation-parameter fcc_al#01_p0 s m l

$
-----
create-new-phase fcc_al#02 p $ VN_1
$ add penalty term for opposite side of miscibility gap: VN
EDIT_PARAMETER a t G(fcc_al#02_p0,NB:C;0) 298,16 +100000; 6000 N
EDIT_PARAMETER a t G(fcc_al#02_p0,NB:N;0) 298,16 +100000; 6000 N
EDIT_PARAMETER a t G(fcc_al#02_p0,V:C;0) 298,16 +100000; 6000 N

set-precipitation-parameter fcc_al#02_p0 c npc
set-precipitation-parameter fcc_al#02_p0 d none
set-precipitation-parameter fcc_al#02_p0 i 0
set-precipitation-parameter fcc_al#02_p0 l 1e100
set-precipitation-parameter fcc_al#02_p0 e 0

set-precipitation-parameter fcc_al#02_p0 n s n
set-precipitation-parameter fcc_al#02_p0 n n t
set-precipitation-parameter fcc_al#02_p0 n c o
set-precipitation-parameter fcc_al#02_p0 n i y
set-precipitation-parameter fcc_al#02_p0 n r irf
set-precipitation-parameter fcc_al#02_p0 n a m
set-precipitation-parameter fcc_al#02_p0 n m i
set-precipitation-parameter fcc_al#02_p0 n t 1.0
set-precipitation-parameter fcc_al#02_p0 n u 1.0

set-precipitation-parameter fcc_al#02_p0 s d r ipdcf
set-precipitation-parameter fcc_al#02_p0 s i r ipdcf
set-precipitation-parameter fcc_al#02_p0 s m l

$
-----
create-new-phase fcc_al#02 p $ VN_2
$ add penalty term for opposite side of miscibility gap: VN
EDIT_PARAMETER a t G(fcc_al#02_p1,NB:C;0) 298,16 +100000; 6000 N
EDIT_PARAMETER a t G(fcc_al#02_p1,NB:N;0) 298,16 +100000; 6000 N
EDIT_PARAMETER a t G(fcc_al#02_p1,V:C;0) 298,16 +100000; 6000 N

set-precipitation-parameter fcc_al#02_p1 c npc
set-precipitation-parameter fcc_al#02_p1 d none
set-precipitation-parameter fcc_al#02_p1 i 0
set-precipitation-parameter fcc_al#02_p1 l 1e100
set-precipitation-parameter fcc_al#02_p1 e 0

set-precipitation-parameter fcc_al#02_p1 n s n
set-precipitation-parameter fcc_al#02_p1 n n t
set-precipitation-parameter fcc_al#02_p1 n c o
set-precipitation-parameter fcc_al#02_p1 n i y
set-precipitation-parameter fcc_al#02_p1 n r irf
set-precipitation-parameter fcc_al#02_p1 n a m
set-precipitation-parameter fcc_al#02_p1 n m i
set-precipitation-parameter fcc_al#02_p1 n t 1.0
set-precipitation-parameter fcc_al#02_p1 n u 1.0

set-precipitation-parameter fcc_al#02_p1 s d r ipdcf
set-precipitation-parameter fcc_al#02_p1 s i r ipdcf
set-precipitation-parameter fcc_al#02_p1 s m l

$
-----
create-new-phase m7c3 p $ M7C3
set-precipitation-parameter m7c3_p0 c npc

```

```

set-precipitation-parameter m7c3_p0 d Austenite
set-precipitation-parameter m7c3_p0 i 0
set-precipitation-parameter m7c3_p0 l 1e100
set-precipitation-parameter m7c3_p0 e 0

set-precipitation-parameter m7c3_p0 n s g
set-precipitation-parameter m7c3_p0 n n t
set-precipitation-parameter m7c3_p0 n c o
set-precipitation-parameter m7c3_p0 n i y
set-precipitation-parameter m7c3_p0 n r irf
set-precipitation-parameter m7c3_p0 n a m
set-precipitation-parameter m7c3_p0 n m i
set-precipitation-parameter m7c3_p0 n t 1.0
set-precipitation-parameter m7c3_p0 n u 1.0

set-precipitation-parameter m7c3_p0 s d r ipdcf
set-precipitation-parameter m7c3_p0 s i r ipdcf
set-precipitation-parameter m7c3_p0 s m 1

$ _____
create-new-phase lavest p $ Laves phase
set-precipitation-parameter lavest_p0 c npc
set-precipitation-parameter lavest_p0 d Austenite
set-precipitation-parameter lavest_p0 i cie$lavest_p0*0.75
set-precipitation-parameter lavest_p0 l 1e100
set-precipitation-parameter lavest_p0 e 0

set-precipitation-parameter lavest_p0 n s g
set-precipitation-parameter lavest_p0 n n t
set-precipitation-parameter lavest_p0 n c o
set-precipitation-parameter lavest_p0 n i y
set-precipitation-parameter lavest_p0 n r irf
set-precipitation-parameter lavest_p0 n a m
set-precipitation-parameter lavest_p0 n m i
set-precipitation-parameter lavest_p0 n t 1.0
set-precipitation-parameter lavest_p0 n u 1.0

set-precipitation-parameter lavest_p0 s d r ipdcf
set-precipitation-parameter lavest_p0 s i r ipdcf
set-precipitation-parameter lavest_p0 s m 1

create-new-phase zet p $ Z phase
set-precipitation-parameter zet_p0 c npc
set-precipitation-parameter zet_p0 d Austenite
set-precipitation-parameter zet_p0 i cie$zet_p0*1.4 $ interfacial energy was increased
by 40%
set-precipitation-parameter zet_p0 l 1e100
set-precipitation-parameter zet_p0 e 0

set-precipitation-parameter zet_p0 n s g
set-precipitation-parameter zet_p0 n n t
set-precipitation-parameter zet_p0 n c o
set-precipitation-parameter zet_p0 n i y
set-precipitation-parameter zet_p0 n r irf
set-precipitation-parameter zet_p0 n a m
set-precipitation-parameter zet_p0 n m i
set-precipitation-parameter zet_p0 n t 1.0
set-precipitation-parameter zet_p0 n u 1.0

set-precipitation-parameter zet_p0 s d r ipdcf
set-precipitation-parameter zet_p0 s i r ipdcf
set-precipitation-parameter zet_p0 s m 1

$ simulation setup _____

set-temperature-celsius 1400 $ define something
set-automatic-startvalues $ initiate equilibrium calculation (estimate variables)
$calc-equilibrium $ start with some equilibrium

set-sim-parameter e time $ simulation end time
set-sim-parameter t t ht_slow 10 $ T-control from table
set-sim-parameter s r $ simulation starting conditions: reset
set-sim-parameter c w y $ convergence control: weighted diffusion coef. = on
set-sim-parameter c o y $ convergence control: oscillation damping = on
set-sim-parameter c d 0,03 $ convergence control: dfm-compensation 3%
set-sim-parameter c m 1e-4 $ convergence control: mass-balance tolerance
set-sim-parameter u 100 $ update windows every n steps

```

```

set-sim-parameter r l ssprl      $ store results in buffer: Linear steps = ssprl in s

$ create output windows, plots etc. _____

new-gui-window pl

$ Define values for default x-axis (will be used by all plots)
set-gui-window-property . X stepvalue/3600 $ default x-value: time in hours
set-gui-window-property . s u y          $ use default x-axis for all plots: yes
set-gui-window-property . s t t[h]       $ default x-axis title
set-gui-window-property . s y log        $ default x-axis type: logarithmic scaling
set-gui-window-property . s s x_scale..  $ default x-axis scaling: From x_scale to end

$ Temperature
set-plot-option . s n b t$c           $ add series
set-plot-option . s m -1 t$c T        $ define series legend
set-plot-option . a y l t T[°C]      $ y-axis title

$ Phase fractions
create-new-plot x .
set-plot-option . s n b f$fcc_al#01_p0      $ add series
set-plot-option . s m -1 f$fcc_al#01_p0 NbC $ rename series legend
set-plot-option . s n b f$fcc_al#02_p0
set-plot-option . s m -1 f$fcc_al#02_p0 VN_1
set-plot-option . s n b f$fcc_al#02_p1
set-plot-option . s m -1 f$fcc_al#02_p1 VN_2
set-plot-option . s n b f$m7c3_p0/10
set-plot-option . s m -1 f$m7c3_p0/10 M<sub>7</sub>C<sub>3</sub>/10
set-plot-option . s n b f$m23c6_p0/10
set-plot-option . s m -1 f$m23c6_p0/10 M<sub>23</sub>C<sub>6</sub>/10
set-plot-option . s n b f$lavest_p0/10
set-plot-option . s m -1 f$lavest_p0/10 Laves/10
set-plot-option . s n b f$zet_p0
set-plot-option . s m -1 f$zet_p0 Z
set-plot-option . s n t f_mx           $ add table with experimental values
set-plot-option . s m -1 f_mx MX      $ rename table
set-plot-option . s n t f_vn
set-plot-option . s m -1 f_vn VN
set-plot-option . s n t f_m23c6
set-plot-option . s m -1 f_m23c6 M<sub>23</sub>C<sub>6</sub>/10
set-plot-option . a y l t f[%]       $ change y-axis title
set-plot-option . a y l f 100       $ multiply with 100 to show phase fractions in percent

$ Mean radii
create-new-plot x .
set-plot-option . s n b r_mean$fcc_al#01_p0*1e9
set-plot-option . s m -1 r_mean$fcc_al#01_p0*1e9 NbC
set-plot-option . s n b r_mean$fcc_al#02_p0*1e9
set-plot-option . s m -1 r_mean$fcc_al#02_p0*1e9 VN_1
set-plot-option . s n b r_mean$fcc_al#02_p1*1e9
set-plot-option . s m -1 r_mean$fcc_al#02_p1*1e9 VN_2
set-plot-option . s n b r_mean$m7c3_p0*1e9
set-plot-option . s m -1 r_mean$m7c3_p0*1e9 M<sub>7</sub>C<sub>3</sub>
set-plot-option . s n b r_mean$m23c6_p0*1e9
set-plot-option . s m -1 r_mean$m23c6_p0*1e9 M<sub>23</sub>C<sub>6</sub>
set-plot-option . s n b r_mean$lavest_p0*1e9
set-plot-option . s m -1 r_mean$lavest_p0*1e9 Laves
set-plot-option . s n b r_mean$zet_p0*1e9
set-plot-option . s m -1 r_mean$zet_p0*1e9 Z
set-plot-option . s n t r_mx
set-plot-option . s m -1 r_mx MX
set-plot-option . s n t r_vn
set-plot-option . s m -1 r_vn VN
set-plot-option . s n t r_m23c6
set-plot-option . s m -1 r_m23c6 M<sub>23</sub>C<sub>6</sub>
set-plot-option . a y l t R[nm]
set-plot-option . a y l y log
set-plot-option . a y l s 0,1..
set-plot-option . l r

$ Number densities
create-new-plot x .
set-plot-option . s n b num_part$fcc_al#01_p0
set-plot-option . s m -1 num_part$fcc_al#01_p0 NbC
set-plot-option . s n b num_part$fcc_al#02_p0
set-plot-option . s m -1 num_part$fcc_al#02_p0 VN_1
set-plot-option . s n b num_part$fcc_al#02_p1

```

```

set-plot-option . s m -1 num_part$fcc_a1#02_p1 VN_2
set-plot-option . s n b num_part$m7c3_p0
set-plot-option . s m -1 num_part$m7c3_p0 M<sub>7</sub>C<sub>3</sub>
set-plot-option . s n b num_part$m23c6_p0
set-plot-option . s m -1 num_part$m23c6_p0 M<sub>23</sub>C<sub>6</sub>
set-plot-option . s n b num_part$lavest_p0
set-plot-option . s m -1 num_part$lavest_p0 Laves
set-plot-option . s n b num_part$zet_p0
set-plot-option . s m -1 num_part$zet_p0 Z
set-plot-option . s n t n_mx
set-plot-option . s m -1 n_mx MX
set-plot-option . s n t n_vn
set-plot-option . s m -1 n_vn VN
set-plot-option . s n t n_m23c6
set-plot-option . s m -1 n_m23c6 M<sub>23</sub>C<sub>6</sub>
set-plot-option . a y l t N[m<sup>-3</sup>]
set-plot-option . a y l y log
set-plot-option . a y l s l..
set-plot-option . l r

$ Matrix composition
create-new-plot x .
set-plot-option . s n b x$bcc_a2$c$%wt
set-plot-option . s m -1 x$bcc_a2$c$%wt C
set-plot-option . s n b x$bcc_a2$cr$%wt
set-plot-option . s m -1 x$bcc_a2$cr$%wt Cr
set-plot-option . s n b x$bcc_a2$mo$%wt
set-plot-option . s m -1 x$bcc_a2$mo$%wt Mo
set-plot-option . s n b x$bcc_a2$n$%wt
set-plot-option . s m -1 x$bcc_a2$n$%wt N
set-plot-option . s n b x$bcc_a2$nb$%wt
set-plot-option . s m -1 x$bcc_a2$nb$%wt Nb
set-plot-option . s n b x$bcc_a2$si$%wt
set-plot-option . s m -1 x$bcc_a2$si$%wt Si
set-plot-option . s n b x$bcc_a2$v$%wt
set-plot-option . s m -1 x$bcc_a2$v$%wt V
set-plot-option . a y l t X<sub>Matrix</sub>[%]
set-plot-option . a y l y lin
set-plot-option . a y l s ..1,2
set-plot-option . a y l f 100
set-plot-option . l r

create-new-plot x .
set-plot-option . s n b x$fcc_a1$c$%wt
set-plot-option . s m -1 x$fcc_a1$c$%wt C
set-plot-option . s n b x$fcc_a1$cr$%wt
set-plot-option . s m -1 x$fcc_a1$cr$%wt Cr
set-plot-option . s n b x$fcc_a1$mo$%wt
set-plot-option . s m -1 x$fcc_a1$mo$%wt Mo
set-plot-option . s n b x$fcc_a1$n$%wt
set-plot-option . s m -1 x$fcc_a1$n$%wt N
set-plot-option . s n b x$fcc_a1$nb$%wt
set-plot-option . s m -1 x$fcc_a1$nb$%wt Nb
set-plot-option . s n b x$fcc_a1$si$%wt
set-plot-option . s m -1 x$fcc_a1$si$%wt Si
set-plot-option . s n b x$fcc_a1$v$%wt
set-plot-option . s m -1 x$fcc_a1$v$%wt V
set-plot-option . a y l t X<sub>Matrix</sub>[%]
set-plot-option . a y l y lin
set-plot-option . a y l s ..1,2
set-plot-option . a y l f 100
set-plot-option . l r

$ move window to new position and resize
move-gui-window . 20 20 600 800
update-gui-window . $ Update the GUI window

new-gui-window p5 $ New precipitation distribution plot window, scaled version
set-gui-window-property . m y

set-plot-option . s n p fcc_a1#01_p0 $ Show the precipitation distribution
set-plot-option . s m -1 fcc_a1#01_p0 NbC
set-plot-option . s n p fcc_a1#02_p0
set-plot-option . s m -1 fcc_a1#02_p0 VN_1
set-plot-option . s n p fcc_a1#02_p1
set-plot-option . s m -1 fcc_a1#02_p1 VN_2
set-plot-option . s n p m7c3_p0

```

```

set-plot-option . s m -1 m7c3_p0 M<sub>7</sub>C<sub>3</sub>
set-plot-option . s n p m23c6_p0
set-plot-option . s m -1 m23c6_p0 M<sub>23</sub>C<sub>6</sub>
set-plot-option . s n p lavest_p0
set-plot-option . s m -1 lavest_p0 Laves
set-plot-option . s n p zet_p0
set-plot-option . s m -1 zet_p0 Z
set-plot-option . a x l t Scaled Radius
set-plot-option . a y l t Scaled Number
set-plot-option . a x l s 0..1,499

$ define a function for LSW distribution
set-function-expression LSW x^2*(3/(3+x))^(7/3)*((3/2)/(3/2-x))^(11/3)*exp(-x/(3/2-x))*4/9
set-plot-option . s n f LSW 0..1,5 $ add to plot

$ in this histogram plot: scale radius and frequency for comparison with theoretical
$ steady-state distribution (LSW)
set-plot-option . h r y $ scale radius
set-plot-option . h f y $ scale frequency

$ next plots are precipitate distributions for all phases

create-new-plot p .
set-plot-option . s n p fcc_al#01_p0
set-plot-option . s m -1 fcc_al#01_p0 NbC
set-plot-option . a x l t R [nm]
set-plot-option . a y l t N [m<sup>-3</sup>]
set-plot-option . a x l s 0..
set-plot-option . a x l f 1e9
set-plot-option . l r

create-new-plot p .
set-plot-option . s n p fcc_al#02_p0
set-plot-option . s m -1 fcc_al#02_p0 VN_1
set-plot-option . a x l t R [nm]
set-plot-option . a y l t N [m<sup>-3</sup>]
set-plot-option . a x l s 0..
set-plot-option . a x l f 1e9
set-plot-option . l r

create-new-plot p .
set-plot-option . s n p fcc_al#02_p1
set-plot-option . s m -1 fcc_al#02_p1 VN_2
set-plot-option . a x l t R [nm]
set-plot-option . a y l t N [m<sup>-3</sup>]
set-plot-option . a x l s 0..
set-plot-option . a x l f 1e9
set-plot-option . l r

create-new-plot p .
set-plot-option . s n p m7c3_p0
set-plot-option . s m -1 m7c3_p0 M<sub>7</sub>C<sub>3</sub>
set-plot-option . a x l t R [nm]
set-plot-option . a y l t N [m<sup>-3</sup>]
set-plot-option . a x l s 0..
set-plot-option . a x l f 1e9
set-plot-option . l r

create-new-plot p .
set-plot-option . s n p m23c6_p0
set-plot-option . s m -1 m23c6_p0 M<sub>23</sub>C<sub>6</sub>
set-plot-option . a x l t R [nm]
set-plot-option . a y l t N [m<sup>-3</sup>]
set-plot-option . a x l s 0..
set-plot-option . a x l f 1e9
set-plot-option . l r

create-new-plot p .
set-plot-option . s n p lavest_p0
set-plot-option . s m -1 lavest_p0 Laves
set-plot-option . a x l t R [nm]
set-plot-option . a y l t N [m<sup>-3</sup>]
set-plot-option . a x l s 0..
set-plot-option . a x l f 1e9
set-plot-option . l r

```

```

create-new-plot p .
set-plot-option . s n p zet_p0
set-plot-option . s m -1 zet_p0 Z
set-plot-option . a x 1 t R [nm]
set-plot-option . a y 1 t N [m<sup>-3</sup>]
set-plot-option . a x 1 s 0..
set-plot-option . a x 1 f 1e9
set-plot-option . l r

$ move window to new position and resize
move-gui-window . 600 30 390 900
update-gui-window . $ Update the GUI window

$ move output window to new position and resize
move-gui-window 0 0 700 900 270
move-gui-window 0 show $ make output window the active foreground window

```

Austenitising simulation (CB8_173_2_reheating.mcs)

The batch-script reads this script after the casting simulation is finished. Scripts 2 to 5 have the same function. They move the precipitate populations between the matrix phases (domains) and fit the precipitate phases to the actual matrix phase. In this case the matrix phase is changed from austenite to ferrite because the casting simulation ends at the assumed martensite start temperature. Due to the martensitic microstructure more nucleation sites are selected, for example sub grains and dislocations. Finally the simulation end-time is postponed to the point in the heat treatment when the next interruption is necessary. In this case 155300s absolute simulation time, at this instant the transformation temperature A_1 is reached and the next script is executed.

```

$ CB8 IWS, reheating after casting
$ MatCalc script version 1

set-variable-value time 137300

$ Shift the precipitate distributions from „Austenite“ to „Ferrite“
$ Change the nucleation sites and the interfacial energies acc. to the new matrix phase

set-precipitation-parameter m23c6_p0 d Ferrite
$ Nucleation sites for „Ferrite“ prec. domain
set-precipitation-parameter m23c6_p0 n s gs

set-precipitation-parameter fcc_al#01_p0 d Ferrite
$ Nucleation sites for „Ferrite“ prec. domain
set-precipitation-parameter fcc_al#01_p0 n s gsd

set-precipitation-parameter fcc_al#02_p0 d Ferrite
$ Nucleation sites for „Ferrite“ prec. domain
set-precipitation-parameter fcc_al#02_p0 n s gsd

set-precipitation-parameter fcc_al#02_p1 d none
$ Nucleation sites for „Ferrite“ prec. domain
set-precipitation-parameter fcc_al#02_p1 n s n

set-precipitation-parameter zet_p0 d Ferrite
$ Nucleation sites for „Ferrite“ prec. domain
set-precipitation-parameter zet_p0 n s gsd

set-precipitation-parameter m7c3_p0 d Ferrite
$ Nucleation sites for „Ferrite“ prec. domain
set-precipitation-parameter m7c3_p0 n s gs

set-precipitation-parameter lavest_p0 d Ferrite
$ Nucleation sites for „Ferrite“ prec. domain
set-precipitation-parameter lavest_p0 n s gs

set-sim-parameter e time
set-sim-parameter t t ht_slow 10 $ Select the table for this T(t)
set-sim-parameter s n
set-sim-parameter r l sspr1
set-sim-parameter a y $ Activate the „append to buffer“ option

```

Austenitising simulation (CB8_173_3_austenitising.mcs)

Similar to the prior script, the matrix phase is switched back to austenite and the nucleation sites are selected accordingly.

```
$ CB8 IWS, austenizing after reheating
$ MatCalc script version 1

set-variable-value time 257830

set-precipitation-parameter m23c6_p0 d Austenite
$ Nucleation sites for „Austenite“ prec. domain
set-precipitation-parameter m23c6_p0 n s g

set-precipitation-parameter fcc_al#01_p0 d Austenite
$ Nucleation sites for „Austenite“ prec. domain
set-precipitation-parameter fcc_al#01_p0 n s g

set-precipitation-parameter fcc_al#02_p0 d Austenite
$ Nucleation sites for „Austenite“ prec. domain
set-precipitation-parameter fcc_al#02_p0 n s g

set-precipitation-parameter fcc_al#02_p1 d none
$ Nucleation sites for „Austenite“ prec. domain
set-precipitation-parameter fcc_al#02_p1 n s n

set-precipitation-parameter zet_p0 d Austenite
$ Nucleation sites for „Ferrite“ prec. domain
set-precipitation-parameter zet_p0 n s g

set-precipitation-parameter m7c3_p0 d Austenite
$ Nucleation sites for „Austenite“ prec. domain
set-precipitation-parameter m7c3_p0 n s gs

set-precipitation-parameter lavest_p0 d Austenite
$ Nucleation sites for „Austenite“ prec. domain
set-precipitation-parameter lavest_p0 n s gs

set-sim-parameter e time
set-sim-parameter t t ht_slow 10
set-sim-parameter s n
set-sim-parameter r l ssprl
set-sim-parameter a y
```

Heat treatment simulation (CB8_173_4_ht.mcs)

```
$ CB8 IWS, heat treatment
$ MatCalc script version 1

set-variable-value time 677910

set-precipitation-parameter m23c6_p0 d Ferrite
$ Nucleation sites for „Ferrite“ prec. domain
set-precipitation-parameter m23c6_p0 n s gs

set-precipitation-parameter fcc_al#01_p0 d Ferrite
$ Nucleation sites for „Ferrite“ prec. domain
set-precipitation-parameter fcc_al#01_p0 n s gsd

set-precipitation-parameter fcc_al#02_p0 d Ferrite
$ Nucleation sites for „Ferrite“ prec. domain
set-precipitation-parameter fcc_al#02_p0 n s n

set-precipitation-parameter fcc_al#02_p1 d Ferrite
$ Nucleation sites for „Ferrite“ prec. domain
set-precipitation-parameter fcc_al#02_p1 n s gsd

set-precipitation-parameter zet_p0 d Ferrite
$ Nucleation sites for „Ferrite“ prec. domain
set-precipitation-parameter zet_p0 n s gsd

set-precipitation-parameter m7c3_p0 d Ferrite
$ Nucleation sites for „Ferrite“ prec. domain
set-precipitation-parameter m7c3_p0 n s gs
```

```
set-precipitation-parameter lavest_p0 d Ferrite
$ Nucleation sites for „Ferrite“ prec. domain
set-precipitation-parameter lavest_p0 n s gs
```

```
set-sim-parameter e time
set-sim-parameter t t ht_slow 10
set-sim-parameter s n
set-sim-parameter r l ssprl
set-sim-parameter a y
```

Annealing simulation (CB8_173_5_service.mcs)

```
$ CB8 IWS, service
$ MatCalc script version 1
```

```
set-variable-value time 58321110
```

```
set-precipitation-parameter m23c6_p0 d Ferrite
$ Nucleation sites for „Ferrite“ prec. domain
set-precipitation-parameter m23c6_p0 n s gs
```

```
set-precipitation-parameter fcc_al#01_p0 d Ferrite
$ Nucleation sites for „Ferrite“ prec. domain
set-precipitation-parameter fcc_al#01_p0 n s gsd
```

```
set-precipitation-parameter fcc_al#02_p0 d Ferrite
$ Nucleation sites for „Ferrite“ prec. domain
set-precipitation-parameter fcc_al#02_p0 n s n
```

```
set-precipitation-parameter fcc_al#02_p1 d Ferrite
$ Nucleation sites for „Ferrite“ prec. domain
set-precipitation-parameter fcc_al#02_p1 n s gsd
```

```
set-precipitation-parameter zet_p0 d Ferrite
$ Nucleation sites for „Ferrite“ prec. domain
set-precipitation-parameter zet_p0 n s gsd
```

```
set-precipitation-parameter m7c3_p0 d Ferrite
$ Nucleation sites for „Ferrite“ prec. domain
set-precipitation-parameter m7c3_p0 n s gs
```

```
set-precipitation-parameter lavest_p0 d Ferrite
$ Nucleation sites for „Ferrite“ prec. domain
set-precipitation-parameter lavest_p0 n s gs
```

```
set-sim-parameter e time
set-sim-parameter t t ht_slow 10
set-sim-parameter s n
set-sim-parameter r l ssprl
set-sim-parameter a y
set-sim-parameter r g 1.02
```

9.3 Maybe unfamiliar...

A binary Fe 1wt% Cu alloy was annealed at 600°C until the end of the coarsening reaction was reached (Fig. 93). The end is determined when only one precipitate is left and per definition coarsening can not go on. The time until only one precipitate is left is about $5,5 \cdot 10^{18}$ a - today it is assumed that the universe has an age of about 10^{16} a. Assuming furthermore that this reaction started with the big bang, which is not possible because Fe and Cu had to be bred in the core of stars first, the annealing at 600°C needs to go on 5500 times longer than the age of our universe until one precipitate is left. It is also uncertain that the elementary particles will exist and interact in the same way in the future as today. Therefore the assessment of the thermodynamic data will eventually be inaccurate. Anyhow, the single sphere inside the 1m^3 cube of ferrite would have a diameter of 238,9mm and a volume of 7,14 litre.

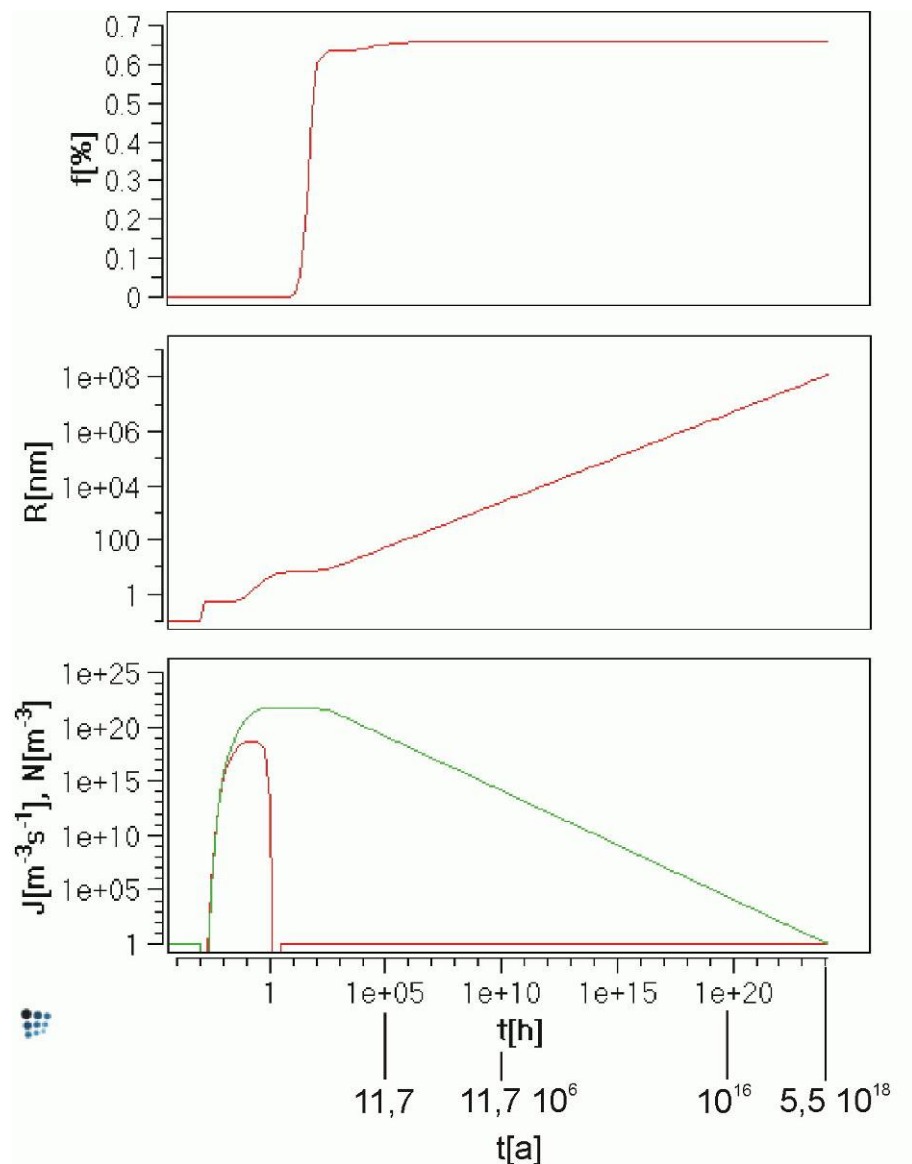


Fig. 93: Hypothetic simulation of Cu precipitation in 1m^3 of an Fe 1wt% Cu alloy until only one precipitate is left.